

PROCEEDINGS OF SPIE



SPIE—The International Society for Optical Engineering

Laser Optics 2000

High-Power Gas Lasers

Oleg B. Danilov

Editor

26–30 June 2000

St. Petersburg, Russia

Organized by

Institute for Laser Physics (Russia)

All-Russia Scientific Center, S.I. Vavilov State Optical Institute

General Physics Institute, Russian Academy of Sciences

P.N. Lebedev Physical Institute, Russian Academy of Sciences

A.F. Ioffe Physico-Technical Institute, Russian Academy of Sciences

Russian National Center of Laser Physics, St. Petersburg State University

St. Petersburg Institute of Fine Mechanics and Optics (Russia)

Scientific Council on Coherent and Nonlinear Optics, Russian Academy of Sciences

SPIE—The International Society for Optical Engineering

SPIE Russia Chapter

OSA—Optical Society of America

ROS—Rozhdestvensky Optical Society (Russia)

Government of St. Petersburg (Russia)

ISTC—International Scientific and Technological Center

20010927 025

DISTRIBUTION STATEMENT A
Approved for Public Release
Distribution Unlimited



Volume 4351

REPORT DOCUMENTATION PAGE

Form Approved OMB No. 0704-0188

Public reporting burden for this collection of information is estimated to average 1 hour per response, including the time for reviewing instructions, searching existing data sources, gathering and maintaining the data needed, and completing and reviewing the collection of information. Send comments regarding this burden estimate or any other aspect of this collection of information, including suggestions for reducing this burden to Washington Headquarters Services, Directorate for Information Operations and Reports, 1215 Jefferson Davis Highway, Suite 1204, Arlington, VA 22202-4302, and to the Office of Management and Budget, Paperwork Reduction Project (0704-0188), Washington, DC 20503.

1. AGENCY USE ONLY (Leave blank)		2. REPORT DATE 14 September 2001	3. REPORT TYPE AND DATES COVERED Conference Proceedings	
4. TITLE AND SUBTITLE Laser Optics 2000: High-Power Gas Lasers (Volume 4351)			5. FUNDING NUMBERS F61775-00-WF	
6. AUTHOR(S) Conference Committee				
7. PERFORMING ORGANIZATION NAME(S) AND ADDRESS(ES) Institute for Laser Physics 12 Birzhevaya line St. Petersburg 199034 Russia			8. Performing Organization Report Number N/A	
9. SPONSORING/MONITORING AGENCY NAME(S) AND ADDRESS(ES) EOARD PSC 802 Box 14 FPO 09499-0200			10. SPONSORING/MONITORING AGENCY REPORT NUMBER CSP 00-5049	
11. SUPPLEMENTARY NOTES Conference Proceedings in five volumes. Proceedings of SPIE – The International Society for Optical Engineering, 26-30 June 2000, St. Petersburg, Russia. Volumes 4350 (Solid State Lasers), 4351 (High-Power Gas Lasers), 4352 (Ultrafast Optics and Superstrong Laser Fields), 4353 (Control of Laser Beam Characteristics and Nonlinear Methods for Wavefront Control), and 4354 (Semiconductor Lasers and Optical Communication), ISSN 0277-786X				
12a. DISTRIBUTION/AVAILABILITY STATEMENT Approved for public release; distribution is unlimited.			12b. DISTRIBUTION CODE A	
ABSTRACT (Maximum 200 words) The Final Proceedings for the Tenth Conference on Laser Optics, 26-30 June 2000. This is an interdisciplinary conference. Topics include generation of ultrashort light pulses, application of nonlinear correction techniques in adaptive optics and lasers, advanced methods of beam control and pointing; diode-pumped solid state lasers; high average power gas and solid-state lasers; and lasers in medicine and medical applications.				
14. SUBJECT TERMS EOARD, Adaptive optics, Gas lasers, Solid state lasers, Aberration correction			15. NUMBER OF PAGES Five bound volumes	
			16. PRICE CODE	
17. SECURITY CLASSIFICATION OF REPORT UNCLASSIFIED	18. SECURITY CLASSIFICATION OF THIS PAGE UNCLASSIFIED	19. SECURITY CLASSIFICATION OF ABSTRACT UNCLASSIFIED	20. LIMITATION OF ABSTRACT UL	



PROCEEDINGS OF SPIE

SPIE—The International Society for Optical Engineering

Laser Optics 2000

High-Power Gas Lasers

Oleg B. Danilov

Editor

26–30 June 2000

St. Petersburg, Russia

Organized by

Institute for Laser Physics (Russia) • All-Russia Scientific Center, S.I. Vavilov State Optical Institute • General Physics Institute, RAS • P.N. Lebedev Physical Institute, RAS • A.F. Ioffe Physico-Technical Institute, RAS • Russian National Center of Laser Physics, St. Petersburg State University • St. Petersburg Institute of Fine Mechanics and Optics (Russia) • Scientific Council on Coherent and Nonlinear Optics, RAS • SPIE—The International Society for Optical Engineering • SPIE Russia Chapter • OSA—Optical Society of America • ROS—Rozhdestvensky Optical Society (Russia) • Government of St. Petersburg (Russia) • ISTC—International Scientific and Technological Center

Supported by

Ministry of Science and Technical Policy of the Russian Federation • Ministry for Economics of the Russian Federation • Ministry of Education of the Russian Federation • Federal Agency for Conventional Weapons (Russia) • Russian National Foundation for Basic Research • SPIE—The International Society for Optical Engineering • Lawrence Livermore National Laboratory (USA) • European Office of Aerospace Research and Development (USA) • OSA—Optical Society of America • ISTC—International Scientific and Technological Center • Amada Corporation (Japan) • Jenoptic GmbH (Germany) • Corning Inc. (USA) • IRE-Polus Group (Germany)

Published by

SPIE—The International Society for Optical Engineering



Volume 4351

SPIE is an international technical society dedicated to advancing engineering and scientific applications of optical, photonic, imaging, electronic, and optoelectronic technologies.

AQ FOI-12-2759



The papers appearing in this book compose the proceedings of the technical conference cited on the cover and title page of this volume. They reflect the authors' opinions and are published as presented, in the interests of timely dissemination. Their inclusion in this publication does not necessarily constitute endorsement by the editors or by SPIE. Papers were selected by the conference program committee to be presented in oral or poster format, and were subject to review by volume editors or program committees.

Please use the following format to cite material from this book:

Author(s), "Title of paper," in *Laser Optics 2000: High-Power Gas Lasers*, Oleg B. Danilov, Editor, Proceedings of SPIE Vol. 4351, page numbers (2001).

ISSN 0277-786X
ISBN 0-8194-4041-8

Published by
SPIE—The International Society for Optical Engineering
P.O. Box 10, Bellingham, Washington 98227-0010 USA
Telephone 1 360/676-3290 (Pacific Time) • Fax 1 360/647-1445
<http://www.spie.org/>

Copyright© 2001, The Society of Photo-Optical Instrumentation Engineers.

Copying of material in this book for internal or personal use, or for the internal or personal use of specific clients, beyond the fair use provisions granted by the U.S. Copyright Law is authorized by SPIE subject to payment of copying fees. The Transactional Reporting Service base fee for this volume is \$15.00 per article (or portion thereof), which should be paid directly to the Copyright Clearance Center (CCC), 222 Rosewood Drive, Danvers, MA 01923 USA. Payment may also be made electronically through CCC Online at <http://www.directory.net/copyright/>. Other copying for republication, resale, advertising or promotion, or any form of systematic or multiple reproduction of any material in this book is prohibited except with permission in writing from the publisher. The CCC fee code is 0277-786X/01/\$15.00.

Printed in the United States of America.

Contents

- v *Laser Optics 2000 Program Committee*
- 1 **High-power XeCl laser system MELS-4k with a 25×25-cm output aperture** [4351-01]
V. F. Losev, N. G. Ivanov, Yu. N. Panchenko, A. G. Yastremsky, High Current Electronics Institute (Russia)
- 8 **Electron beam transport and foil stability in high-energy e-beam-pumped KrF lasers** [4351-02]
V. D. Zvorykin, S. V. Arlantsev, V. G. Bakaev, O. V. Rantsev, G. V. Sychugov, A. Yu. Tserkovnikov, P.N. Lebedev Physical Institute (Russia)
- 19 **Kinetic research of active mixtures of the XeF excimer laser with optical pumping** [4351-03]
V. P. Fokanov, A. B. Pavlov, Russian Scientific Ctr. of Applied Chemistry
- 29 **Nonlinear reflection of laser radiation in Xe-containing dense gas mixtures and cryogenic solutions** [4351-04]
A. P. Burtsev, V. V. Bertsev, V. N. Bocharov, St. Petersburg State Univ. (Russia)
- 34 **Nonlinear absorption and laser-induced damage of BaF₂, CaF₂, and Al₂O₃ at 248 nm** [4351-05]
N. V. Morozov, P. B. Sergeev, P.N. Lebedev Physical Institute (Russia)
- 40 **Simulation of mechanisms causing a nonlinear absorption of UV laser radiation in ionic crystals** [4351-06]
S. V. Kurbasov, P. B. Sergeev, P.N. Lebedev Physical Institute (Russia)
- 48 **Detuning characteristics of ionic anti-Stokes Raman laser** [4351-07]
S. A. Babin, S. I. Kablukov, S. V. Khorev, E. V. Podivilov, V. V. Potapov, D. A. Shapiro, M. G. Stepanov, Institute of Automation and Electrometry (Russia)
- 60 **New simulations for COIL lasers from the University of Illinois** [4351-08]
D. S. Stromberg, L. A. Fockler, D. L. Carroll, W. C. Solomon, Univ. of Illinois/Urbana-Champaign (USA)
- 72 **Current status of chemical oxygen-iodine laser research** [4351-09]
S. Rosenwaks, B. D. Barmashenko, D. Furman, E. Bruins, V. Rybalkin, Ben-Gurion Univ. of the Negev (Israel)
- 86 **Amplification of image brightness by means of the photodissociative iodine laser** [4351-10]
Ilg. V. Bagrov, O. B. Danilov, S. A. Tul'skii, A. P. Zhevlakov, Institute for Laser Physics (Russia)
- 92 **Possibility of realizing fullerene-oxygen-iodine laser with solar pumping (Sun-Light FOIL)** [4351-11]
O. B. Danilov, I. M. Belousova, A. A. Mak, V. Yu. Zaleskiy, V. A. Grigor'ev, A. V. Kris'ko, E. N. Sosnov, V. P. Belousov, Institute for Laser Physics (Russia)
- 99 **Technical proposals of industrial high-power CO lasers** [4351-12]
I. Ya. Baranov, Baltic State Technical Univ. (Russia)

- 104 **High-power high-optical-quality rf-excited slab CO₂ lasers** [4351-13]
A. I. Dutov, A. A. Kuleshov, S. A. Motovilov, N. A. Novoselov, N. L. Orlov, V. E. Semenov,
A. A. Sokolov, Institute for Laser Physics (Russia)
- 110 **About particularities of intensities distribution in a cross-section of powerful laser beams**
[4351-14]
V. A. Gurashvili, Troitsk Institute for Innovation and Fusion Research (Russia); P. V. Korolenko,
M.V. Lomonosov Moscow State Univ. (Russia); A. P. Napartovich, S. P. Pavlov, A. V. Rodin,
N. E. Sarkarov, Troitsk Institute for Innovation and Fusion Research (Russia); A. M. Zotov,
M.V. Lomonosov Moscow State Univ. (Russia)
- 117 **Construction and characterization of a CO₂ waveguide laser with a special electrode design for
materials processing** [4351-15]
J. L. Jiminéz Pérez, CICATA-IPN (Mexico); M. A. Algatti, Univ. Estadual Paulista (Brazil);
J. G. Mendoza-Alvarez, A. Cruz Orea, CICATA-IPN (Mexico) and CINVESTAV-IPN (Mexico)
- 123 **Energy parameters and resource of high-power pulse-periodical sealed-off TEA-CO₂ lasers**
[4351-16]
B. A. Kozlov, S. G. Fomin, Radio-Engineering Academy (Russia)
- 134 **Improvement of the optical quality of the free-vortex aerodynamic windows** [4351-17]
A. S. Boreisho, A. V. Trilis, Baltic State Technical Univ. (Russia); V. M. Khailov, R. I. Sericov,
Central Institute of Aircraft Engine Construction (Russia)
- 141 **Small-sized TEA-N₂ and TEA-Xe lasers with high average radiation power** [4351-18]
B. A. Kozlov, R. I. Ashurkov, Radio-Engineering Academy (Russia)
- 151 **IR lasers in a struggle against dangerous cosmic objects** [4351-19]
B. A. Kuzyakov, Moscow State Univ. of Technology (Russia)
- 159 **Influence of the competition of rotational-vibrational transitions on a two-wave CO₂ laser
generation mode** [4351-20]
V. O. Petukhov, V. A. Gorobets, B.I. Stepanov Institute of Physics (Belarus); K. V. Kozlov, Joint
Stock Co. Peleng (Belarus)
- 164 **Action of pulse-periodic and continuous IR radiation on light-controlled vanadium dioxide
mirrors** [4351-21]
O. B. Danilov, A. I. Sidorov, Institute for Laser Physics (Russia); D. H. Titterton, DERA (UK);
S. A. Tul'skii, I. L. Yachnev, A. P. Zhevlakov, Institute for Laser Physics (Russia)
- 171 **Efficient intracavity frequency doubling of CO₂ laser in nonlinear crystals** [4351-22]
V. O. Petukhov, V. A. Gorobets, S. Ya. Tochitsky, B.I. Stepanov Institute of Physics (Belarus);
K. V. Kozlov, Joint Stock Co. Peleng (Belarus)
- 176 **Stochastic and order phase structures in active medium flow of gas-dynamic laser** [4351-23]
V. O. Kovalevsky, V. V. Lobachev, Baltic State Technical Univ. (Russia)
- 186 *Author Index*

Laser Optics 2000 Program Committee

Chair

Artur A. Mak, Institute for Laser Physics (Russia)

Vice-Chairs

Alexander A. Andreev, Institute for Laser Physics (Russia)

Vladimir Yu. Venediktov, Institute for Laser Physics (Russia)

Scientific Secretary

A. F. Vassil'yev, Institute for Laser Physics (Russia)

Members

Zhores I. Alferov, A.F. Ioffe Physico-Technical Institute (Russia)

Pavel A. Apanasevich, B.I. Stepanov Institute of Physics (Belarus)

Sergey N. Bagaev, Institute for Laser Physics (Russia)

Nikolai G. Basov, P.N. Lebedev Physical Institute (Russia)

Yuri D. Berezin, Institute for Laser Physics (Russia)

Viktor I. Bespalov, Institute of Applied Physics (Russia)

Ernest V. Boiko, Military Medical Academy (Russia)

F. V. Bunkin, General Physics Institute (Russia)

Oleg B. Danilov, Institute for Laser Physics (Russia)

Eugeni M. Dianov, General Physics Institute (Russia)

Sergei A. Dimakov, Institute for Laser Physics (Russia)

Alexander V. Dotsenko, Corning Scientific Center (Russia)

Valentin Gapontsev, IPG Laser GmbH (Germany)

Yu. D. Golyaev, Research and Development Institute Polyus (Russia)

Vyacheslav M. Gordienko, M.V. Lomonosov Moscow State University (Russia)

Serguei A. Gurevich, A.F. Ioffe Physico-Technical Institute (Russia)

Valerii P. Kandidov, M.V. Lomonosov Moscow State University (Russia)

Yakov I. Khanin, Institute of Applied Physics (Russia)

I. V. Kovsh, Laser Association (Russia)

O. N. Krohin, P.N. Lebedev Physical Institute (Russia)

Vladimir V. Lyubimov, Institute for Laser Physics (Russia)

Alexander A. Manenkov, General Physics Institute (Russia)

Yuri T. Mazurenko, S.I. Vavilov State Optical Institute (USA)

Anatoly P. Napartovich, Troitsk Institute for Innovation and Fusion Research (Russia)

Anatoly N. Oraevsky, P.N. Lebedev Physics Institute (Russia)

Vladislav Ya. Panchenko, Scientific Research Center for Technological Lasers (Russia)

Pavel P. Pashinin, General Physics Institute (Russia)

G. T. Petrovskiy, S.I. Vavilov State Optical Institute (Russia)

N. N. Rozanov, Institute for Laser Physics (Russia)

Alexander S. Rubanov, B.I. Stepanov Institute of Physics (Belarus)

Marat S. Soskin, Institute of Physics (Ukraine)

Victor A. Serebryakov, Institute for Laser Physics (Russia)
Ivan A. Shcherbakov, General Physics Institute (Russia)
Vladimir E. Sherstobitov, Institute for Laser Physics (Russia)
Leonid N. Soms, Institute for Laser Physics (Russia)
V. B. Smirnov, St. Petersburg State University (Russia)
Anatoli P. Sukhorukov, M.V. Lomonosov Moscow State University (Russia)
Vladimir I. Ustyugov, Institute for Laser Physics (Russia)
V. V. Valuev, GPO Almaz (Russia)
V. N. Vasilev, St. Petersburg State Institute of Fine Mechanics and Optics (Russia)
Evgeny A. Viktorov, Institute for Laser Physics (Russia)
Vadim P. Veiko, St. Petersburg State Institute of Fine Mechanics and Optics (Russia)
Vladimir E. Yashin, Institute for Laser Physics (Russia)
Georgii M. Zverev, Research and Development Institute Polyus (Russia)

High power XeCl laser system "MELS-4k" with a 25x25 cm output aperture

V. F. Losev, N. G. Ivanov, Yu. N. Panchenko and A.G.Yastremsky

Gas Laser Laboratory, High Current Electronics Institute SB RAS,
4, Akademicheskoy ave., Tomsk, 634055, Russia
Fax (382 2)259410, e-mail: losev@hcei.tomsk.su

Abstract

High power XeCl laser system and experimental results of diffraction limited laser beam amplification are described. Beyond the preamplifier, the 5 cm x 6 cm laser beam contained 50% of the radiation energy in the diffraction core. At the output from the system an irradiation brightness of $2 \times 10^{14} \text{ W/cm}^2\text{cr}^{-1}$ was obtained. Minimum divergence near 0.05 mrad of output beam was restricted to turbulence of air and optics elements. A numerical model of the amplification of the radiation, taking into account the influence of the amplified spontaneous emission, was developed.

Keywords: excimer, laser beam, amplifier, divergence, intensity.

1. Introduction

An excimer lasers at present are most promising for achieving the high brightness in UV spectrum region. This is first because the excimer lasers emit at short wavelength and with a high intensity of the radiation. Second, there are no principal restrictions on the increase of the cross size of their active medium. An efficiency for the KrF and XeCl lasers up to 10% and 5% accordingly was realized. Many applications of laser radiation require simultaneously a high energy and a high coherence. One of the ways of obtaining such radiation involves its generation in laser systems.

High-power KrF laser systems ($\lambda = 248 \text{ nm}$) have now been created in a number of most developed countries. Studies of the generation of ultra-powerful laser radiation pulses and of the interaction of such radiation with matter are being prosecuted on such lasers within a framework of national programs. The best known of these are Ashura (Japan), Sprite и Titania (England), and Nike (USA) [1-3]. These laser systems have high apertures of tens centimetres and a radiation energy from 200 J to 1 kJ. A KrF laser system with a Garpun output module also exists in Russian (Physics Institute of the Russian Academy of Sciences, Moscow). The module has an 18 cm x 20 cm x 100 cm active volume excited by two electron beams [4]. It can generate a lasing pulse with a duration of 50 ns and an energy of 60 J.

In this paper the XeCl laser system MELS-4K ($\lambda = 308 \text{ nm}$) developed at the Institute of High-Current Electronics of the Siberian Division of the Russian Academy of Sciences (Tomsk) with an output amplifier aperture of 25 cm x 25 cm is described and the research results of a high quality beam formation is shown.

2. Apparatus and methods

The MELS-4K laser system incorporates a front end, a preamplifier, and main amplifier. The front end is an assembly of two electric-discharge XeCl lasers with a plasma sheet and having a 3 cm x 1.5

cm x 60 cm active volume (Fig.1). By varying the pump regimes in the lasers, it is possible to generate radiation pulses with an energy of 100 - 300 mJ and of 15-150 ns duration (FWHM). One of the lasers is

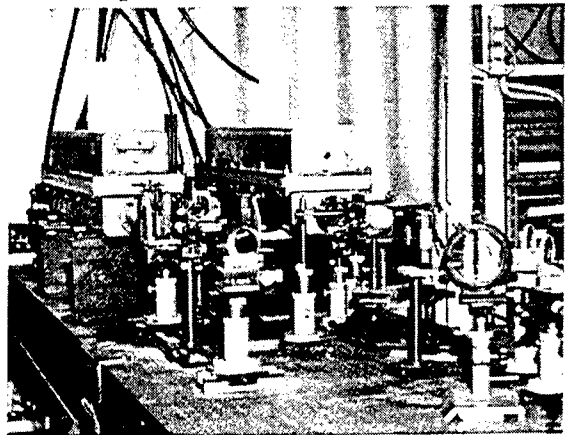


Fig.1 Laser system front end.

the master oscillator. The combination of a master oscillator with a second laser in various optical systems makes it possible to obtain different radiation parameters at the output from the front end. Thus, in the single-pass amplification regime the energy was $E = 15$ mJ, the spectral-line half-width is $\Delta\nu = 0.01$ cm⁻¹, $t = 50$ ns, and more than 80% of the radiation energy was contained within the diffraction angle $\theta_d = 2.44\lambda/D$ where D is the beam diameter. In the injection locking regime, the output beam energy was $E = 100$ mJ, $\Delta\nu = 0.01$ cm⁻¹, and $t = 100$ ns, and more than 50% of the radiation energy is contained within θ_d [5]; in the two-pass amplification regime with phase conjugation the parameters were $E = 50$ mJ, $\Delta\nu = 0.01$ - 0.4 cm⁻¹, $t = 30$ ns, and the divergence θ was near θ_d

[6]; in the radiation pulse compression regime with stimulated Brillouin scattering, the pulse duration was 1 - 2 ns, $E = 10$ mJ, $\Delta\nu = 0.01$ cm⁻¹, and $\theta \sim \theta_d$ [7].

The preamplifier consists of an electric-discharge laser in which the active volume dimensions is 6 cm x 11 cm x 80 cm [8]. Its external appearance is illustrated in Fig.2. The design of the laser comprises an external metal casing containing a dielectric laser chamber, capacitors connected directly to the electrodes and having an overall capacitance of 368 nF, and a source of x-ray radiation. Outside, there is a discharge gap and a 0.4 nF storage capacitor. An Ne: Xe: HCl = 100:10:1 mixture is excited at a pressure of 2-4 bar in the phototriggering regime [9]. After connecting the storage capacitor to the discharge gap, a x-ray source is switched on for this purpose 300 ns before the attainment of the maximum voltage on the electrode and its radiation initiates the onset of the discharge. The injection of x-rays were realized through a stainless steel net with a 50% geometrical transparency. The radiation dose in the laser chamber was not less than 25 mR. The maximum laser energy reached 10 J for a pulse duration (FWHM) of 80 ns.

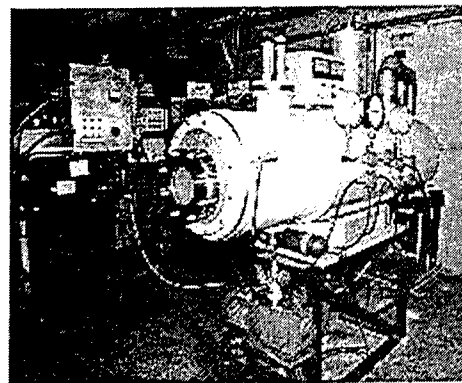


Fig.2 Pre-amplifier.

The main amplifier had a 25 cm x 25 cm x 100 cm active volume excited by two electron beams [10]. A photograph of the amplifier is shown in Fig. 3. The electron accelerators are placed above and below a laser chamber with an internal volume of 360 liters. In each accelerator, a vacuum diode and a voltage pulse generator supplying it share a metal casing. The voltage pulse generator is insulated from the casing by the vacuum between them. For a plane-plane cavity, the laser energy was 200 J with a pulse duration 250 ns. In the amplification regime, the windows of the laser chamber were tilted relative to the optical axis by 10°.

The high voltage pulse generator was used to switch and synchronize of an master oscillator with the amplifiers. The instant when the master oscillator and the amplifiers are switched on was regulated with the aid of cable and artificial delay lines. In the amplification regime the input pulse intensity maximum coincided with the pump power maximum for each amplifier.

In order to determine distortions of the wave front at the amplified beam by the optical components, we carried out a calculation taking account of the disposition of the components and the

quality of the treatment of their surfaces. The results indicated that the deviation from the specified surface of the optical components used in the system up to 100 mm in diameter did not exceed $\lambda/2$ whereas for diameters in excess of 100 mm it amounted to λ .

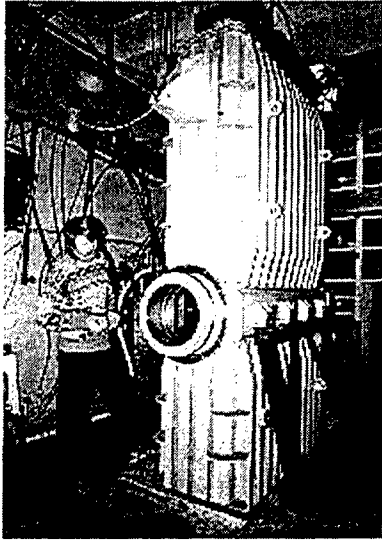


Fig.3 Output amplifier.

The radiation energy in the experiments was measured with the aid of IKT-IN and TPI-7 calorimeters. The spectral characteristics of the radiation were measured with the aid of a IT28-30 interferometer and a STE-1 spectrograph, while the time characteristics were measured with the aid of FEK22-SPU photodiodes. The electrical pulses were recorded with the aid of a 6LOR-04 oscilloscope. The divergence of the master-oscillator and the electric-discharge amplifier beams was determined by the method of calibrated apertures with the aid of a lens having the focal length $F = 10$ m. For the main amplifier, the divergence was found from the radiation intensity distribution in the focal spots obtained with the aid of a mirror-attenuator [II].

Apart from the experiments, numerical simulation of the amplifiers was also carried out. In our calculations, a one-dimensional model

consisting of a system of time-dependent equations for the concentration of excimer molecules and photon fluxes was used:

$$\frac{\partial F^{\pm}(x,t)}{\partial x} \pm (1/C) \cdot \frac{\partial F^{\pm}(x,t)}{\partial t} = F^{\pm}(x,t) \cdot \{ \sigma \cdot N(x,t) - \alpha + \Omega_F(x) \cdot N(x,t) / \tau_s \} \quad (1)$$

$$\frac{\partial S^{\pm}(x,t)}{\partial x} \pm (1/C) \cdot \frac{\partial S^{\pm}(x,t)}{\partial t} = S^{\pm}(x,t) \cdot \{ \sigma \cdot N(x,t) - \alpha \} + \Omega_S(x) \cdot N(x,t) / \tau_s \quad (2)$$

$$\frac{\partial P_{1,2,3,4}(x,t)}{\partial x} \pm (1/C) \cdot \frac{\partial P_{1,2,3,4}(x,t)}{\partial t} = P_{1,2,3,4}(x,t) \cdot \{ \sigma \cdot N(x,t) - \alpha \} + \Omega_P(x) \cdot N(x,t) / \tau_s \quad (3)$$

$$\frac{\partial N(x,t)}{\partial t} = \Psi - \{ F^{\pm}(x,t) + S^{\pm}(x,t) + P_{1,2,3,4}(x,t) \} \cdot \sigma \cdot N(x,t) - N(x,t) / \tau_{\phi} \quad (4)$$

where F is the flux of the amplified signal photons (the plus and minus signs denote photon fluxes moving in opposite directions); S is the amplified spontaneous emission (ASE) photon flux, which propagates in the direction of the optical axis within a solid angle determined by the geometry of the active medium; P_{1-4} are the photon fluxes moving across the optical axis in mutually opposed directions between opposite lateral faces of a tetragonal parallelepiped, which models the active medium of the amplifier; σ - is the stimulated emission cross section; τ_s and τ_{eff} are, respectively, the spontaneous and effective lifetimes of the excimer molecules; $N(x,t)$ is the concentration of the $XeCl^*$ excimer molecules; Ψ is the rate of formation of the excimer molecules; α is the absorption coefficient; c is the velocity of light; $\Omega_{S,P,F}(x)$ is the fraction of the spontaneous radiation photons, the direction of which coincides with that of the corresponding flux.

In the calculations, account was also taken of the narrowing of the spectral line during amplification [12]. The quantities σ , τ_s and τ_{eff} were taken from Ref. [14]. The time dependence of Ψ was specified in the form of a trapezium of height

$$\Psi_0 = g_0 / (\tau_{eff} \sigma), \quad (5)$$

where g_0 is the small signal gain. The system of equations (1) - (4) was solved by standard methods.

3. Results of the calculations

The short spontaneous lifetime of the upper active level of the excimer molecules (10 -14 ns) and the high gain g_0 of the spontaneous signal ($0.05-0.1 \text{ cm}^{-1}$) lead to a high intensity of the ASE. The aim of

the calculations was to predict the output parameters to the laser system taking into account the influence of the ASE in a particular optical system. It has been shown [13] that the most accurate calculation of ASE intensity is possible only on the basis of a three-dimensional model. Nevertheless, as the ratio D/L decreases (L is the length of the active medium and D is its transverse dimension), the results of the calculations in the three-dimensional and one-dimensional problems approach one another. Under our conditions, D/L did not exceed 0.25 and we therefore used only the one-dimensional model.

The output characteristics were calculated for the preamplifier and the main amplifier in which the influence of ASE was maximal. Fig. 4 presents the distribution of the radiation intensity along the length of the active region of the preamplifier for different intensities of the input signal. The following parameters of the active medium were adopted as the initial data: $g_0 = 0.08 \text{ cm}^{-1}$, $\alpha = 0.015 \text{ cm}^{-1}$, $\tau_{\text{eff}} = 2.5 \text{ ns}$, $\sigma = 4 \times 10^{-16} \text{ cm}^2$, and the spontaneous lifetime of the XeCl^* molecules was taken to be $\tau_s = 14 \text{ ns}$. This set of parameters was based on the results of our measurements of the gain in electric discharge media and also on the analysis of the published data. The results of the calculations and the duration of the input signal pulse permit us to conclude that an input energy of the order of 10 mJ should be sufficient to saturate this amplifier after two passes. The amplified signal intensity is then approximately $2I_s$ (I_s is the saturation intensity). For large input signals (with an intensity of 100 kW cm^{-2} and above), it is useful to employ single-pass amplification. In general, for the given parameters of the active medium and its dimensions, the influence of ASE is small when the input signals are 2 kW cm^{-2} and above.

Apart from the gain, calculations were performed also for other cases under conditions when the cross section of the active medium is filled completely by the input flux. Since in our laser system the rectangular (5 cm x 10 cm) preamplifier aperture had to be matched to the square aperture of the main amplifier in the system, it was necessary to estimate the energy losses incurred on amplification of a beam with a square cross section in the preamplifier. According to the calculations, for input radiation with an energy of 30 mJ filling completely the preamplifier aperture, the output energy amounts to 3.56 J after two passes, whereas in the case of a beam with a square cross section (5 cm x 5 cm) and under conditions such that fluxes propagating in opposite directions did not intersect, the output energy falls to 2.67 J.

In the case of the main amplifier, excited by a lower pump power, the following parameters of the active medium were adopted: $g_0 = 0.065 \text{ cm}^{-1}$, $\alpha = 0.0145 \text{ cm}^{-1}$, $\tau_{\text{eff}} = 3 \text{ ns}$, $\sigma = 4 \times 10^{-16} \text{ cm}^2$, $\tau_s = 14 \text{ ns}$. We found the gain g_0 and α the coefficient a earlier from the experimental results and from the results of calculations based on a program involving calculation of the energy input and the overall kinetics [10].

Fig. 4 presents the distributions of the amplified signal and ASE intensities in one- and two-pass systems. As can be seen from Fig. 4, the influence of the ASE in the main amplifier is significantly higher compared with that in the preamplifier, despite the comparable values of the product g_0L . For example, for a kilowatt power of the input radiation, the ASE intensity at the output from the main amplifier approaches that of the amplified radiation preventing the latter from depleting effectively the inverse population. On the other hand, if one takes into account the fact that the one-dimensional model gives rise to a signal/noise ratio which is somewhat too

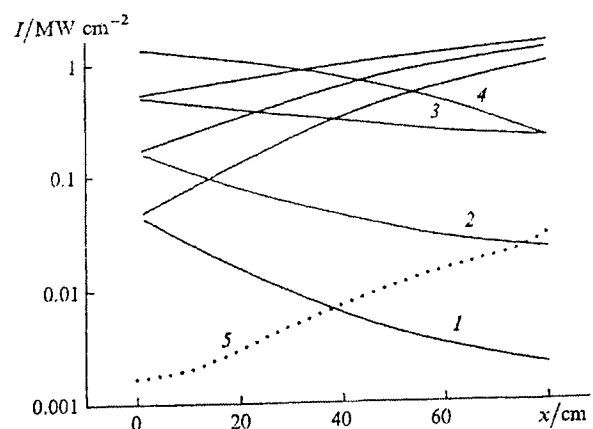


Fig. 4. Distribution of the amplified radiation intensity (1-4) and the overall ASE (5) fluxes for double (1-3, 5) and single (4) passes through the active medium of the preamplifier.

high (particularly for the two-pass amplification), then the influence of the ASE should be even greater in practice. Thus, the minimum input radiation intensity for the main amplifier should be of the order of

10 kW cm^{-2} , which corresponds to an energy density of $\sim 1 \text{ mJ cm}^{-2}$ for a pulse duration at 80 ns. From the standpoint of the amplified radiation energy, under these conditions it is preferable to employ a two-pass system.

Since a time-dependent model was used in the calculations, we were able to follow the useful radiation and ASE profiles. It was found that the pulses at the input to the output from the active medium may differ greatly; the difference depends on the difference between the radiation and pump pulse profiles, and on the rate of growth of the pulses and of the length of the active medium. All the intensity distributions presented previously refer to the case of radiation and pump power which does not vary with time.

4. Experimental results

The experiments on the amplification of radiation in the laser system were performed for pulses of 80 ns duration. Their aim was to determine the energy characteristics of each amplifier and the distortions of the beam wave front in the optical channel. In these experiments a front end consisted of a master oscillator and double pass amplifier. Laser beam of a front end was amplified in preamplifier (double pass) and then in output amplifier (single pass). In order to match the beams size a telescope in optics scheme was used.

The results of our measurements of the energy and divergence of the radiation after each amplifier are presented in Table. The difference between the output and input energies in the different stages was the consequence of the losses on the turn mirrors and

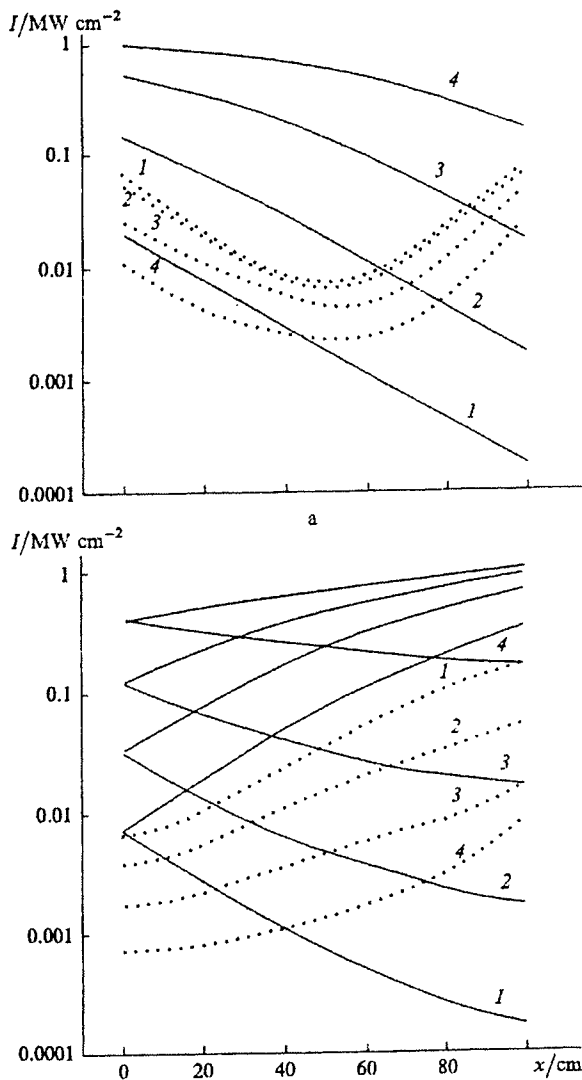


Fig.5. Distribution of the amplified radiation fluxes intensity (solid lines, 1-4) and of the corresponding overall ASE fluxes (dashed lines, 1-4) for single (a) and double (b) passes in the output amplifier.

the losses incurred in matching the apertures.

As can be seen from Table, the divergence of the radiation at the output from the master oscillator was near to the diffraction limit θ_d . Nevertheless, the fraction of the energy in the angle θ_d fell to 50% and below when the homogeneity of the discharge was deteriorated or the diameter of the laser beam was decreased. The use of single-pass amplification in the unutilized part of the active medium of the master oscillator made it possible to increase its output energy by a factor of approximately 20.

Table

Parameters	Master oscillator	Amplifier	Preamplifier		Output amplifier	
			4 x 5	5 x 6	10 x 12	21x25
A, cm	$\varnothing = 0.6$	1.2 x 1.8	4 x 5	5 x 6	10 x 12	21x25
E_{in} , J	-	0.003	0.03	0.03	0.8	1.2
E_{out} , J	0.005	0.08	1.0	1.5	10	25
E_d/E_{out}	0.82	0.77	0.6	0.5	~0.1	-

Note: A is beam size at the output from the amplifier; E_{in} and E_{out} - the input and output energies; E_d is the energy contained in the diffraction limited angle θ_d .

An input energy of 3 mJ in the amplifier was sufficient to saturate its active medium in two passes. The increase in the divergence of the radiation after the amplifier compared with the master oscillator, was due to the presence of proportion of ASE in the beam.

It follows from Table that the output energy in the preamplifier was less than the calculated value, which (in our view) was associated with a reduction of the gain in the region of the beam intersection which occurred in the experiments. Here, the active medium did not contribute to the observed increase of the radiation divergence. It was induced by the distortions in the remaining optical channel (air plus optical components).

Calculation of the output energy in the main amplifier for the beam size and pulse duration corresponding to the experimental conditions demonstrated a satisfactory agreement between the measured and calculated quantities. For the 10 cm x 12 cm and 20 cm x 25 cm beam cross sections, the calculated output energies were respectively 11 and 26 J. Measurements of the divergence of the beams of this size were complicated by atmospheric turbulence. When the radiation from the master oscillator passed the entire optical path without amplification, the position of the focal spot in the structure was unstable. The instability depended significantly on the presence of any kind of heat sources near the optical path and also on the time elapsed after the operation of the amplifiers.

For this reason, the value of E_d/E_{out} for the 10 cm x 12 cm beam was shown only approximately. One can only state with greater precision that about 50% of the energy was contained in the 5×10^{-5} rad angle. This also agrees with the results of other measurements in which the output radiation was focused by a lens with $F = 1.5$ m on a titanium foil 50 μm thick, which had an hole approximately 100 μm in diameter, corresponding to a divergence of $\sim 6.5 \times 10^{-5}$ rad. The active medium (pump inhomogeneity) of the main amplifier did not influence on the wave front of the radiation transmitted through it.

5. Conclusions

A laser system MELS-4k was developed for obtaining UV radiation with a high brightness. The amplification of diffraction-limited laser beams with a large cross section in this system was investigated. It was shown that the divergence of the amplified radiation remains close to the diffraction limit for beam sizes up to 5 cm x 5 cm. For a beam size of 10 cm x 12 cm, the divergence exceeds significantly the diffraction limit. This is the effect primarily of distortions of the wave front by the turbulent streams in the laser mixture and in air. The simulation of the amplification of radiation, taking into account the influence of ASE, demonstrated a satisfactory agreement between the calculated and experimental data. In the main amplifier, the influence of the ASE becomes insignificant starting with

an input radiation intensity of the order of 0.05 saturation intensity.

References

1. Owadano Y, Okuda I, Matsumoto Y et al., *M Jr Laser Part. Beams*, Vol.7, 383, 1989.
2. Edwards C B, O'Neill F, Shaw M J et al., *Excimer Lasers 1983* (Proceedings of the OSA Conference on Excimer Lasers, Lake Tahoe, NV, 1983; Eds C K Rhodes, H Egger, H Pummer), in *AIP Conf. Proc.* (100) 59 (1983); E.J.Divall, C.B.Kidd, J.M.Lister et al., *J. Modern Optics*, Vol.43, №5, 1025-1033, 1996.
3. S.P.Obenschain, S.E.Bodner, D.Colombent et al., *Phys. Plasmas*, Vol.3, 2098-2107, 1996.
4. Basov N G, Bogdanovskii A V, Zvorykin V D et al, *Sb. Tezisev. Konf. Optika Lazerov-93, Leningrad, W3* (Abstracts of Papers presented at the Laser Optics Conference, Leningrad, 1993) Vol. 1, P.186.
5. Ivanov N G, Kovalenko S E, Losev V F, Panchenko Yu N, *Opt. Atmos. Okeana*, №8, P.1590, 1995.
6. Bychkov Yu. I, Losev V F, Panchenko Yu N., *Kvantovaya Elektron. (Moscow)*, **19**, P.688, 1992, [*Sov. J. Quantum Electron.* **22**, P.638, 1992].
7. Losev V F, Panchenko Yu N, **21**, 55, 1994 [*Sov. J. Quantum Electron.* **24**, P.52, 1994].
8. Ivanov N G, Losev V F, Panchenko Yu. N, Yastremsky A G, *Kvantovaya Elektron. (Moscow)*, **29**, P.14, 1999.
9. Lacour B, Vannier C *J. Appl. Phys.*, **62**, P.754, 1987.
10. Ivanov N G, Losev V F, et al., *Kvantovaya Elektron. (Moscow)*, **24**, P.688, 1997 [*Sov. J. Quantum Electron.*, **27**, P.670, 1997].
11. Ivanov N G, Losev V F *Kvantovaya. Elektron., (Moscow)* **23**, P.811, 1996 [*Sov. J. Quantum Electron.*, **26**, P.790, 1996].
12. Hunter A. M., Hunter R. O., *IEEE J. Quantum Electron.* **17**, P.1879, 1981.
13. Sasaki A, Ueda K.I., Takuma H, Kasuya K., *J. Appl. Phys.*, **65**, P.231, 1989.
14. Kannari F, Suda A, Obara M, Fujioka T., *IEEE J. Quantum Electron.* **QE-19**, P.1587, 1983.

Electron beam transport and foil stability in high-energy e-beam-pumped KrF lasers.

Vladimir D. Zvorykin*, S.V. Arlantsev, V.G. Bakaev, O.V. Rantsev, G.V. Sychugov,
A.Yu.Tserkovnikov

P. N. Lebedev Physical Institute, Russian Academy of Sciences,
Leninsky Prospect 53, 117924 Moscow, Russia

ABSTRACT

There are several key engineering and physical issues for the development of Krypton Fluoride driver for Inertial Fusion Energy Program. In the frame of this Program we have performed experiments with e-beam-pumped KrF laser installation GARPUN on the transportation of relativistic e-beams through Aluminum-Beryllium and Titanium foils and compared them with Monte Carlo numerical calculations. It was shown that 50- μm thickness Al-Be and 20- μm Ti foils had equal transmittance of 75% for ~ 300 keV, 50 kA/cm², 100 ns e-beams, being lower than calculated one. In contrast to Ti foil, which surface was strongly etched by fluorine, no surface modification and no fatal damages were observed for Al-Be foils after ~ 1000 laser shots and protracted fluorine exposure. It was shown that applied magnetic field of ~ 1 kGs significantly reduced electron scattering both across and along laser cell at typical pumping conditions with 1.5-atm pressure working gas. The energy fluence of scattered electrons fell down from ~ 100 mJ/cm² to ~ 1 mJ/cm² per pulse at 8.5-cm distance from the boundary of injected e-beams. Without magnetic field the scattered electrons were spread up to 20 cm, thus strongly irradiating optical windows and being a cause of additional induced absorption of laser radiation.

Keywords: e-beam-pumped high-power KrF laser, Aluminum-Beryllium foil transmittance and stability, e-beam scattering.

1. INTRODUCTION

Several physical and engineering problems should be developed for high-energy large-scale e-beam-pumped KrF lasers in order they could operate with a few Hz in Inertial Confinement Fusion Energy Reactors¹⁻³. As high as 10^8 laser shots between the major maintenance are required for the IFE plant. In KrF modules high-current relativistic e-beams of a large cross section are passed throughout vacuum-tight foil windows from vacuum diodes into a laser cell to pump a fluorine-containing working gas. This foil window, being arranged together with a foil-support structure (usually called as "hibachi") should have a transmittance of about 90%, high mechanical strength to withstand to a steady pressure difference and its sudden rise during e-beam energy release in a gas. Additional factors, such as foil stability with temperature rise, possibility of foil cooling to conduct a heat of absorbed electrons, and chemical foil resistance to fluorine should be taken into account for a durable repetition-rate operation of KrF driver. Titanium foils or Kapton (polyimide) films typically used in single-pulse large KrF installations⁴⁻⁸ have a limited lifetime from several tens to hundreds shots. They are not suitable for a repetition-rate machine because of low heat conductivity and tend to allotropic transformation at elevated temperatures. By today only the HOVAR foil was chosen for tests at repetition-rate KrF laser facility⁹. To our mind Aluminum-Beryllium (Al-Be) compounds might be the best choice for the foil window due to a high strength compared with Ti one, excellent heat conductivity, and very small density of Al-Be alloys¹⁰, which determines in the main an absorption of e-beam. Another problem to be solved for IFE KrF laser driver is a protection of output optical windows against scattered fast electrons that could induce additional transient¹¹⁻¹⁴ and residual absorption of laser radiation¹⁵, thus decreasing total efficiency and durability of KrF laser driver operation.

This paper presents the first comprehensive investigation of Al-Be foil carried out with e-beam-pumped large-aperture amplifier and preamplifier modules of GARPUN KrF laser installation^{16,17}. Direct comparison of transparency of 50- μm thickness Al-Be foil manufactured by Russian industry and convenient 20- μm Ti foil has been done using Faraday cup technique. Durability of both foils was determined in a prolonged run of single-pulse experiments lasting up to 1000 shots. Statistics and morphology of typical damages of the foil and its resistance to fluorine etching were investigated. The

* Correspondence: zvorykin@sci.lebedev.ru

distribution of energy fluence of e-beams and scattered electrons have been measured at various pumping conditions with a set of calorimeters placed in the middle of the laser chamber and apart of injected e-beams region at various distances along laser cell axis. The influence of applied magnetic field of $\sim 1\text{kGs}$ on e-beam scattering was investigated. Monte Carlo numerical code has been developed to calculate e-beam transport through different foil materials and distribution of scattered electrons inside the laser cell. Being verified in present experiments with the GARPUN laser of $16 \times 18 \times 100\text{ cm}$ active volume, then it was applied to calculate e-beam scattering and electron escape onto optical windows in the $30 \times 30 \times 100\text{ cm}$ repetition-rate prototype of KrF IFE driver, which is under development at the Naval Research Laboratory (NRL)^{2,3}.

2. LASER FACILITIES AND EXPERIMENTAL PROCEDURE

The experiments with two laser modules of GARPUN installation have been performed to investigate e-beam transportation throughout Al-Be foil and to determine its stability in comparison with convenient Ti foil of $20\text{-}\mu\text{m}$ thickness. The Al-Be foil was manufactured by means of multi-stage hot rolling and following annealing of the samples of heterogeneous alloy. Consisting of 50% weight amount of aluminum and 50% of beryllium it had an average density of 2.2 g/cm^3 . For safe to handle $2\text{-}\mu\text{m}$ aluminum layer laminated its both sides. The total thickness of Al-Be foil was $50\text{ }\mu\text{m}$.

The preamplifier laser module "Berdysh" of $10 \times 10 \times 100\text{ cm}$ active volume was adjusted for transmittance measurements of different foils. It was pumped with a single-side e-beam of 900 J total energy and $\sim 100\text{ ns}$ pulse duration. High-voltage power supply of the electron accelerator consists of a 7-stage Marx generator with 3.0 kJ energy storage at 400 kV pulsed voltage and water-filled Blumlein forming line of $7.6\text{ }\Omega$ wave impedance, which produced pulses of $\sim 350\text{ kV}$ voltage. The layout of laser chamber (1) and vacuum diode (2) equipped for e-beam transport experiments is shown schematically in Fig.1.

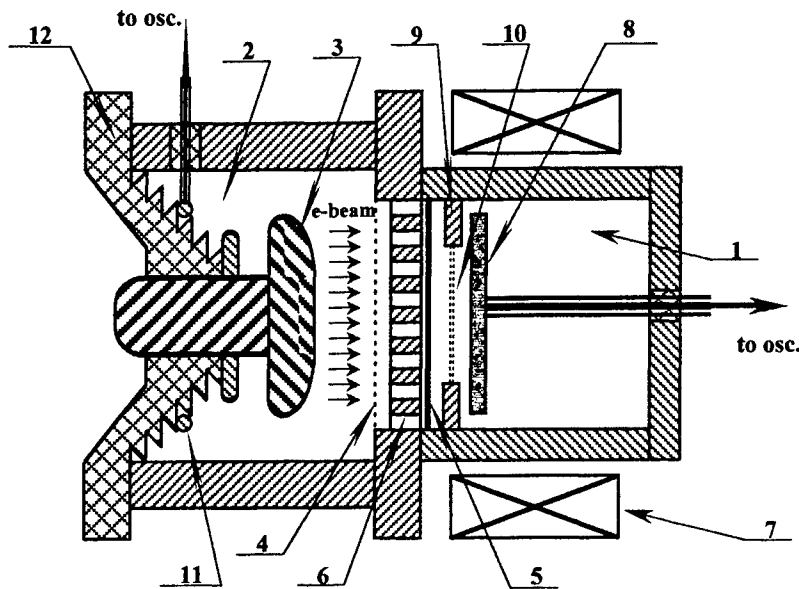


Fig.1. Cross section of "Berdysh" laser module arranged for e-beam transport measurements: 1-laser chamber; 2-vacuum diode; 3-cathode; 4-anode grid; 5-foil; 6-hibachi; 7-solenoid; 8- Faraday cup; 9- stops; 10- additional foil; 11- Rogowski coil; 12- bushing.

The cathode (3) of 100-cm length and 8-cm width had a convex-shaped emitting surface formed by a graphite fabric to prevent a "halo" effect and to insure uniform electron emission. It was placed at 3-cm distance from the anode grid (4). The foil (5) was set 3 cm behind the grid and was supported by the hibachi structure (6). Hibachi's ribs having 3-mm width and 6-mm thickness separated the free gaps of 27-mm width and 100-mm height. This would correspond to a geometric transparency of 90% , if one suppose that electrons have no any velocity component transverse to the accelerating electric field. But due to the intrinsic azimuthal magnetic field of e-beam electrons obtained a transverse component that should reduce this value. In order to prevent e-beam pinching and to diminish the losses of electrons in a vacuum diode and scattered in a foil external pulsed magnetic field was applied collinearly to the electric field. It was produced by a solenoid

(7) and reached maximum inductance of 650 Gs at 40 ms. Magnetic field was altered in experiments by varying the voltage at the capacity bank of solenoid's power supply. E-beam current transmitted through the foil and foil support structure has been measured by means of Faraday cup (8) set 1.7-cm behind the foil inside laser chamber, which was evacuated up to 10^{-2} Torr. The graphite receiving plate of Faraday cup dimensioned 9.3*23 cm was slightly less than the height of the chamber. The stop (9) with variable gap was used to measure E-beam distribution in the vertical (perpendicular to the cathode axis) direction. Preliminary the Faraday cup was placed in different positions along the cathode demonstrating uniform distribution of e-beam current in that direction. Additional Ti foils (10) were tightened between the stop's gap to measure attenuated e-beam current and to determine the energy distribution of electrons. Rogowski coil (11), which enveloped a high-voltage bushing (12) with a conductor to the cathode, controlled the total current in vacuum diode during all measurements.

The main "GARPUN" module was arranged to measure the distribution of scattered electrons in conditions typical for large-aperture e-beam-pumped KrF laser installations. The stability of Al-Be foil has been determined simultaneously. The layout of these experiments is shown schematically in Fig.2. The "GARPUN" module^{18, 19} has a laser chamber (1) with dimensions $19 \times 22 \times 140$ cm and output aperture 16×18 cm. Two counter-propagating e-beams of the area 12×100 cm and with

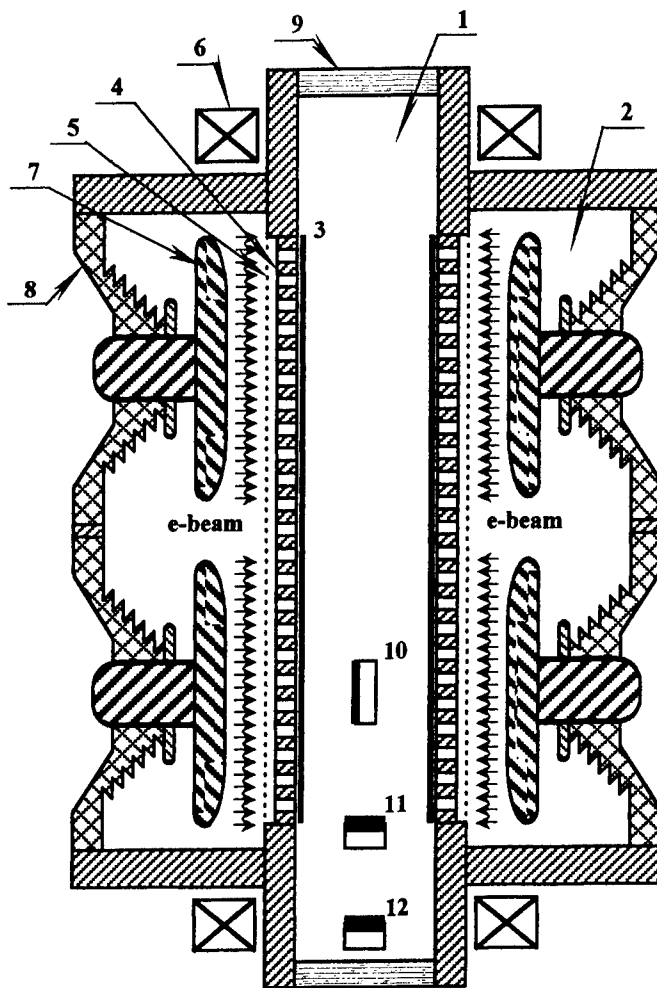


Fig.2. Cross section of "GARPUN" laser module arranged for e-beam scattering measurements: 1- laser chamber; 2- vacuum diode; 3- foil; 4- hibachi; 5- anode grid; 6- solenoid; 7- cathode; 8- bushing; 9- output window; 10, 11, 12- calorimeters.

current density 50 A/cm^2 were coupled into the chamber from opposite sides throughout vacuum-tight $20\text{-}\mu\text{m}$ thickness Ti or $50\text{-}\mu\text{m}$ Al-Be foils, which separated the working gas in a chamber from the vacuum diodes (2). The foils (3) were supported by the hibachi structure (4) having the ribs of 2-mm width, 10-mm thickness and 8-mm inter-rib gaps. The e-

beams were stabilized usually by a pulsed magnetic field of inductance $B \sim 1$ kGs, generated by a pair of solenoids (6) in a direction along the beams. The experiments have been also performed without magnetic field in order to understand its influence on e-beam scattering. The pulses of 350 kV accelerating voltage and 120 ns duration were delivered to a pair of cathodes (7) in each vacuum diode by four water-filled Blumlein forming lines with 7.6Ω wave impedance. A 7-stage Marx generator with 14 kJ storage energy charged them.

3. MONTE CARLO NUMERICAL MODELLING

The most accurate and universal description of the processes of electron transport in a medium is provided by the Monte Carlo method, which has been used earlier in calculations of the electron-beam pumping of GARPUN laser¹⁹. Its main advantage is that the real geometry and the structural features of the apparatus can be allowed for by modeling the real process of the passage of electrons through matter. We used the "single-particle" approximation, ignoring the interaction of the beam electrons with one another. This neglect of the collective effects was justified by the weakness of the intrinsic magnetic field compared with the external magnetic field¹⁸. The second requirement, suppression of the plasma instabilities, was also satisfied since at typical gas densities the frequency of collisions of the plasma electrons with neutral particles was higher than the instability growth increment. Under these conditions the main interactions between the electron beam and the medium were pair collisions of electrons with foil and gas atoms, which resulted in the excitation or ionization of these atoms or in the elastic scattering of electrons by the atoms. Radiative energy losses in elastic collisions could be ignored at the electron energies under consideration.

The algorithm used to solve the problem has been described earlier¹⁹. It included a calculation of the paths of individual electrons in the beam in the intervals between successive collisions and modeling of the energy loss and scattering processes in collisions between electrons and atoms. We also studied the deceleration of high-energy secondary electrons, which were created by the ionization of atoms and were capable in turn of generating an avalanche of secondary electrons. The modeling began with selection of the initial energy of an electron, its coordinates, and direction of injection into the investigated region. Then the coordinates of the point of interaction of an electron with an atom were found by solving the equations of motion:

$$\frac{d\mathbf{P}}{dt} = e[\mathbf{v} \times \mathbf{B}], \quad \mathbf{P} = \frac{m_e \mathbf{v}}{\sqrt{1 - v^2/c^2}}, \quad \frac{dS}{dt} = v, \quad (1)$$

where the path S traveled by an electron was calculated by solving the equation:

$$\int_0^S ds' Q(s') \exp\left[-\int_0^{s'} Q(s'') ds''\right] = \xi. \quad (2)$$

Here, $Q = N\sigma_t$ is a product of the density of the scattering particles and the total collision cross section; ξ is a random number distributed uniformly in the interval (0, 1). For a homogeneous medium Q is a constant and Eqn. (2) can be transformed to the simple expression:

$$S = -Q^{-1} \ln(1 - \xi) \quad (3)$$

The equations of motion (1) were solved numerically. When the point of collision was inside the selected region, the type of the collision was picked at random and then the energy loss and the scattering angle were found. The new collision point was then determined and so on, until the particle left the investigated region or until its energy became less than a certain value below which it could be regarded as having come to rest. The angle and energy of the electrons escaping outside the selected region, as well as their total number were determined.

Inelastic collisions of the beam electrons with atoms were considered on the assumption that the interaction could be treated in the same way as that of free electrons. In the relativistic case the differential inelastic scattering cross section was described by the Moliere expression²⁰:

$$\frac{d\sigma_n}{d\varepsilon} = 2\pi r_e^2 \frac{Z}{\beta^2 T} \left[\frac{1}{\varepsilon^2} - \frac{1}{\varepsilon(1-\varepsilon)} \frac{2T+1}{(T+1)^2} + \frac{1}{(1-\varepsilon)^2} + \frac{T^2}{(T+1)^2} \right], \quad (4)$$

where ε is the fraction of the energy lost by a primary electron in a collision; r_e is the classical radius of an electron; $\beta = v/c$; T is the electron energy in units of $m_e c^2$; Z is the nuclear charge of an atom.

Elastic collisions of electrons with atoms were considered as the scattering of electrons in the field of a nucleus screened by the atomic electrons. The differential cross section of such scattering was described by the Rutherford expression with a correction for the screening²¹:

$$\frac{d\sigma_y}{d\Omega} = Z^2 \frac{r_e^2}{\beta^2 p_e^2 (1 + 2\eta - \cos\theta)^2}, \quad (5)$$

where $d\Omega$ is a solid-angle element; p_e is the relativistic momentum of an electron in units of $m_e c$; η is the screening parameter; θ is the scattering angle. In the Thomas—Fermi model of an atom the screening parameter is^{20,21}:

$$\eta = \left(\frac{Z^{1/3}}{137 \times 0.885} \right)^2 \frac{1.1 + 3.76(Z/137)^2 (T+1)^2 / T(T+2)}{4T(T+2)}. \quad (6)$$

The following relationships were used in the above expression:

$$p_e^2 = T(T+2), \quad \beta^2 = (v/c)^2 = T(T+2)/(T+1)^2.$$

The total energy losses were normalized in accordance with the Bethe-Bloch equation:

$$\frac{dT}{dS} = 0.3056 \frac{\rho Z}{A\beta^2} \left\{ \ln \left[\frac{T^2(T+2)}{2I^2} \right] + \frac{\frac{1}{8}T^2 + 1 - (2T+1)\ln 2}{(T+1)^2} \right\}, \quad (7)$$

where A and ρ are the atomic weight and the density of the gas; I is the average bond ionization potential, representing the average energy of an electron in an atom; its values, expressed in units of $m_e c^2$, were found from tabulated data or were calculated from the semiempirical Sternheimer expression:

$$I = \frac{Z(9.76 + 58.6Z^{-1.10})}{0.511 \times 10^6}. \quad (8)$$

The described Monte Carlo algorithm was applied for the modeling of e-beam transportation from vacuum diodes into laser chamber throughout Al-Be and Ti foils. Fig.3 illustrates this process for the GARPUN laser by visualizing the trajectories of 100 individual electrons in a working gas at 1.5-atm pressure when the external magnetic field with 650 Gs inductance was

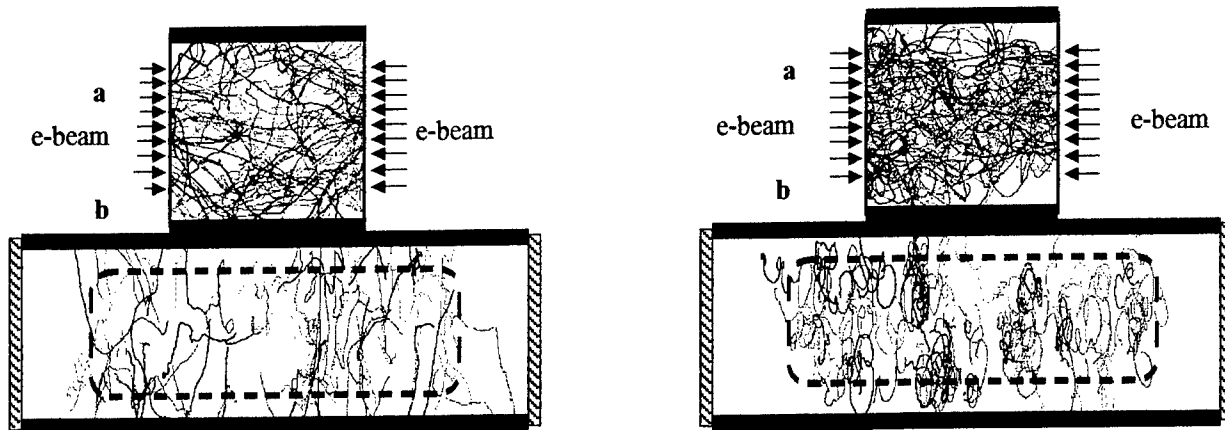


Fig.3. Trajectories of individual electrons in GARPUN laser chamber filled by 1.5-atm argon gas without (left) and with external magnetic field of 650 Gs (right): a- view along laser axis; b- view along e-beams (their initial cross section is shown by dotted line). The scale in longitudinal direction is reduced in 3.8 times.

switched off and on. The scale of the pictures in longitudinal direction is reduced in 3.8 times in order to adjust them to paper sheets. Taking into account this distortion one could see clearly how magnetic field causes the electrons to rotate around the strength lines when they are scattered during their passage the foils and the gas. The Larmor radius for the electrons with an average energy $\epsilon_e=300$ keV is equal to $r_L=3.3$ cm. This spiral rotation increases significantly a density of electrons, and hence a specific pumping power in the central region of the laser chamber that corresponds approximately to an initial cross section of injected e-beams. At the same time a total amount of particles reaching top and bottom walls is

reduced together with their escape towards the laser windows. It means that the applied magnetic field controls not only energy losses due to scattered electrons and hence the pumping efficiency, but prevents the laser windows of an illumination by energetic electrons.

4. E-BEAM TRANSPORT THROUGH Al-Be FOIL

This section presents the main results obtained in comparative studies of 50- μm thickness Al-Be and 20- μm Ti foils. Fig.4 demonstrates typical oscillograms of the current in the vacuum diode measured by the Rogowski coil (upper trace) and e-beam current measured by the Faraday cup (lower trace) behind Al-Be foil. Both signals are similar one to another thus demonstrating that no distortions of the pulse-form were introduced by measuring technique. Their duration at FMHM was about 100 ns, the maximum current being reached at ~ 80 ns. For fully opened stops e-beam current attained $I_e=10$ kA corresponding to an average value of current density $I_e/S_c \approx 50$ A/cm², where $S_c=210$ cm² is a full area of receiving plate of the Faraday cup. E-beam absorption by the graphite was calculated with the Monte Carlo method to be 94-96% for electron energies in the range $\epsilon_e=200$ -600 keV.

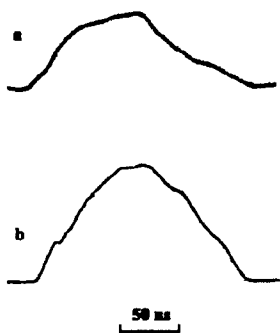


Fig.4. Typical oscillograms of the current in vacuum diode (a) and e-beam current behind the foil (b).

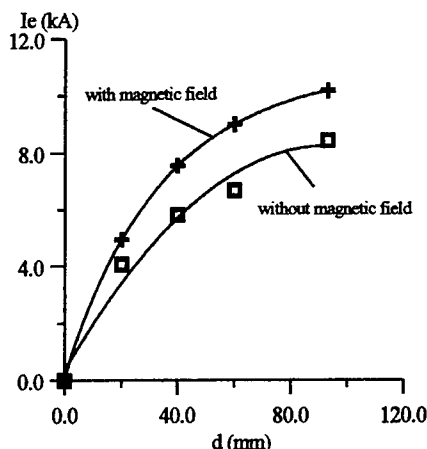


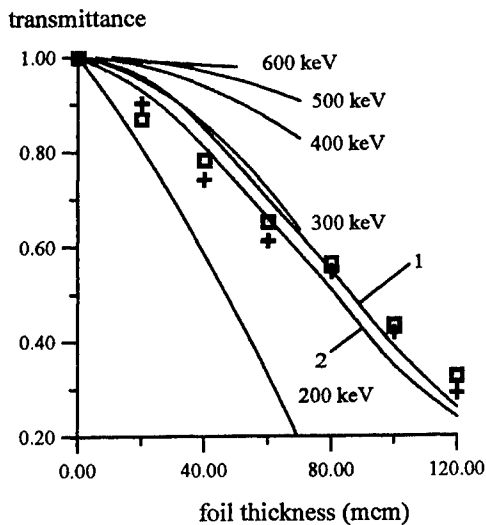
Fig.5. E-beam currents versus opened gap width.

The dependence of e-beam current on the opened gap width of the stop (Fig.5) permits one to derive the distribution of current density across the width of the cathode. The maximum value in the center is twice as high as the average value. This might be originating of geometry of the vacuum diode. It is also seen in Fig.5 that the external magnetic field did not influence significantly upon e-beam current. This might be explained by the fact that the Faraday cup was set not far from the foil if compared with mean scattering angles of 20-30 degrees calculated for the expected electron energies $\epsilon_e=300$ -500 keV.

The transparency of the hibachi structure was determined immediately in comparison of e-beam current through anode grid only (without neither hibachi nor any foil) with another one measured through the anode grid and hibachi (without any foil). It was 83% if compared with 90% of geometric transparency. The difference was apparently due to the transverse component of electron velocity.

The comparison of Al-Be and Ti foils has been done in our experiments. The transport of the initial e-beam generated in vacuum diode throughout Al-Be foil (or the same through Ti foil) was examined in direct measurements of e-beam current behind full-arranged foil unit (with anode grid and hibachi) and another one without foil (anode grid and hibachi only). Within a measurement accuracy of 5% both Al-Be and Ti foils demonstrated equal transmittance 75%. This measured value revealed significant difference with the calculated transmittance. The last decreased rapidly from 100 to 91% when electron energy was varied from 400 down to 200 keV. We suppose that the discrepancy might be originating from a wide energy distribution of electrons in initial e-beam generated in vacuum diode. The low-energy electrons would be absorbed predominantly in the foil and this might cause its overheating in repetition-rate laser facility.

The experiments have been performed to measure energy distribution of the electrons at the entrance into laser chamber after e-beam pass throughout Al-Be (or Ti) foil. For this purpose e-beam current was measured in dependence on the total thickness of additional Ti foils set between the main foil and the Faraday cup. These results are shown in Fig.6 together with the calculated ones. They demonstrate that approximately linear decrease in the transmitted current with foil thickness could not be explained by any calculated dependence for monoenergetic electrons, which energies were varied from $\epsilon_e=200$ keV



to $\epsilon_e=600$ keV. The coincidence has been achieved in the assumption that electron energies were distributed uniformly in the range $\epsilon_e=250-350$ keV ($\Delta\epsilon_e=100$ keV), having a mean value $\langle\epsilon_e\rangle=300$ keV. Different angular distributions $\Delta\alpha=0^\circ$ (1) and $\Delta\alpha=45^\circ$ (2) of initial electron velocities in e-beam before the foil have been compared and demonstrated small influence on the transmittance.

Fig.6. Experimental transmittance in dependence on thickness of Ti foils and numerical calculations for monoenergetic electrons with $\epsilon_e=200\dots600$ keV, e-beams with uniform energy distribution in $\epsilon_e=250-350$ keV range and input e-beam divergence $\Delta\alpha=0^\circ$ (1) or $\Delta\alpha=45^\circ$ (2).

5. STATISTICS AND MORPHOLOGY OF Al-Be FOIL DAMAGE

We didn't achieve the fatal damage of Al-Be foils neither at preamplifier nor at amplifier modules in correspondingly 550 and 580 e-beam pulses. It is significantly higher than mean lifetime of usual Ti foils. After these series both foils have been examined visually and with the help of an optical microscope. In contrast to Ti foil, which surface was strongly modified by fluorine etching, no noticeable changes were observed with Al-Be foil surface after a protracted fluorine action, even if the foil sample was then taken into atmosphere air. This evidenced that AlF_3 substance the most likely appeared in chemistry of laminating Al layer with fluorine-containing working gas mixture of KrF laser was stable enough to consequent fluorine action. This is clearly seen in the microscope pictures of Al-Be foil presented in Fig.7 a, b. Its both sides turned to vacuum diode and to laser cell seem identical.

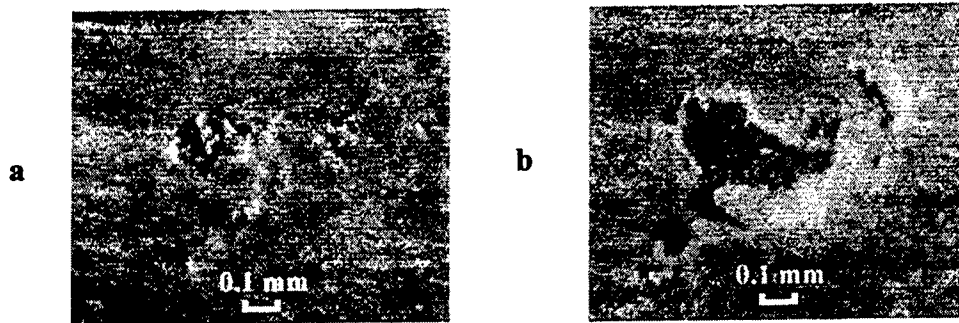


Fig.7. Microscopic pictures of Al-Be foil after multiple e-beam irradiation in fluorine- containing working gas mixture of KrF laser: a- foil surface from a side of vacuum diode; b- the same area from a side of laser cell (mirror-converged image).

The only visible defects at Al-Be foil surface were spread with an average density of 1-2 per 100 cm^2 and looked from a side of vacuum diode (Fig.7 a) like micro-craters with non-through hole in a center surrounded by a rim of ejected material. They were also accompanied by a halo of thermal burn. These non-fatal defects might be originated from the impacts of charged micro-particles of the cathode material accelerated by an electric field or micro-pinch discharges inside vacuum diode. It should be noted that cathodes after prolonged exploitation also demonstrated thermal burn spots spread casually across their surfaces. But they had rather bigger diameter of about centimeter. The micro-picture of backside of the same Al-Be foil sample is shown in Fig.7b. Using computer processing a mirror-converging procedure has been done for this image. It allows one to make more precise comparison of both sides of the foil. For example, it is clearly seen that laminating Al layer of 2- μm thickness was spalled exactly opposite micro-craters. The spallation effect was apparently caused by a shock wave that was generated in a foil by the micro-particle impacts or local energy release in the micro-pinch. Therefore initial layered structure of Al-Be foil seems to be more reliable in regard of short-pulse mechanical breakdown than monolayer foil.

In the case of Ti foil being in contact with KrF working gas mixture a modified layer of some friable material of dark-red violet, or white color usually covered its surface. TiF_3 and TiF_4 substances being the most probable in chemistry of Ti and F are not stable with the temperature and couldn't protect the rest foil consequently. In addition, they would absorb water vapor from the air. As a result a large amount of through holes arose in Ti foil some time later its even short existence in the air. Apparently, it was due to a strong action of HF acid that might be formed between absorbed H_2O and F. These outcomes for Ti foil are illustrated by Fig.8, where serious degradation of the foil surface and a formation of typical through hole are clearly observed after foil exploitation.

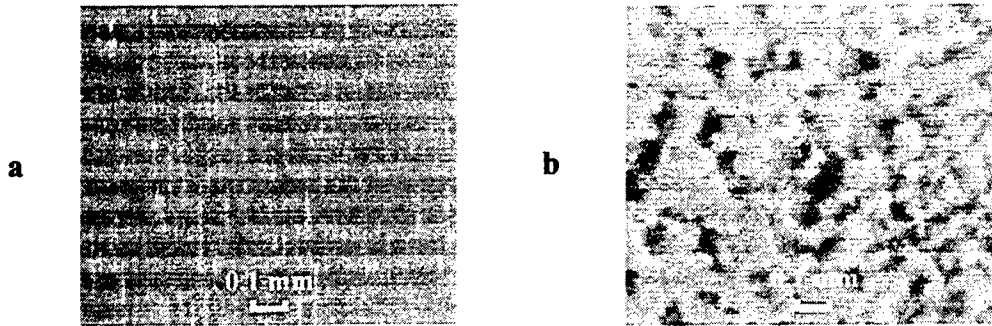


Fig.8. Microscopic pictures of Ti foils before (a) and after multiple e-beam irradiation in fluorine-containing working gas mixture of KrF laser (b): view from a side of laser cell.

6. DISTRIBUTION OF SCATTERED ELECTRONS IN LASER CHAMBER

The distribution of energy fluence of e-beams and of scattered electrons has been measured by means of calorimeters, which of were set inside the "GARPUN" laser chamber (see Fig.2). One of them (10) having an open graphite receiving plate of 5-cm diameter measured immediately the energy of the incoming e-beam. Another sensitive calorimeter of 2.7-cm diameter was displaced at different positions (11, 12) along the chamber axis outside the region straightly irradiated by e-beams. To diminish heat and radiation fluxes acting on the calorimeter because of the temperature rise and argon fluorescence during e-beam deposition it was screened by a 20- μ m thickness aluminized polymer film. Being directed perpendicular to the axis towards the chamber it measured the energy of scattered electrons and apparently a small amount of soft X-rays that might be absorbed by its ~ 200 - μ m thickness copper receiving plate. The heat transfer from a gas was taken into account by subtracting the successive value obtained when the calorimeter was turned in opposite direction. The indicated energies were then multiplied by the coefficient 2.2, which accounted for the full aperture angle of the calorimeter of 84° in assumption that scattered electrons were uniformly distributed in a solid angle of 2π sr. Numerical calculations using Monte Carlo code confirmed this correction procedure.

Fig.9 gives the energy fluence delivered by each of two e-beams to the middle point of laser chamber in dependence on buffer argon gas pressure and guiding magnetic field. It is seen that magnetic field strongly influenced on e-beam transport from vacuum diodes into laser chamber. In our previous experiments e-beam pinching took place without magnetic field. This effect would introduce additional losses and scattering of electrons^{18, 19}. This effect is clearly demonstrated in Fig.10, where the energy fluence of scattered electrons at 8.5-cm distance from e-beam boundary was much higher without magnetic field than in opposite case. At a double 17-cm distance the energy fluence fell down especially at higher gas pressure. As a result we could not detect the scattered electrons in the presence of magnetic field at all.

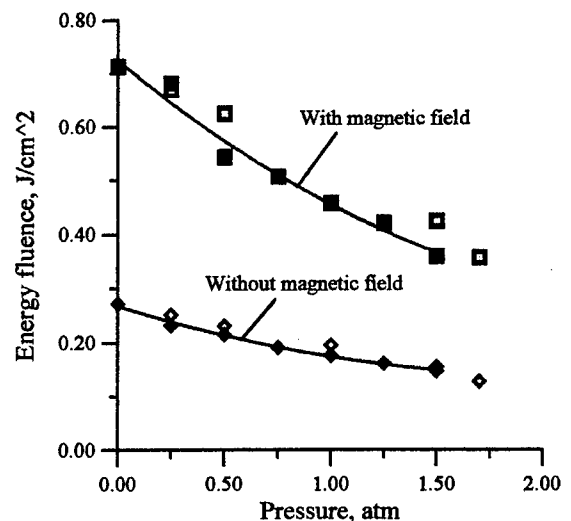


Fig.9. Dependence of energy fluence for one e-beam in the middle of laser chamber on argon pressure with and without magnetic field: solid dots- experiments, outlined dots-calculations.

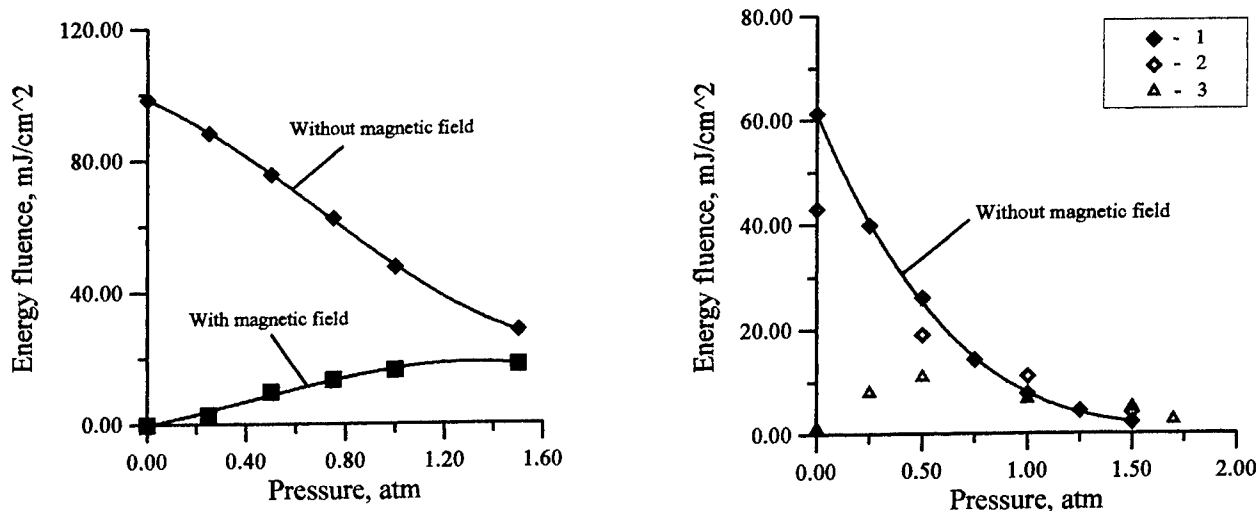


Fig.10. Energy fluence of scattered electrons in dependence on argon pressure at 8.5-cm distance (left) and at 17-cm distance from e-beam edge (right): 1-experiments; 2,3- calculations.

A comparison of the experimental results on e-beam scattering (1) with the numerical modeling (2) in Fig.10 reveals a great discrepancy at low argon pressures, if only e-beam scattering in the foils and in the gas was assumed. Although a low-pressure range is untypical for KrF laser pumping conditions, it stimulated us to look for some additional effects. Multiple passage of electrons from one vacuum diode into the laser chamber, then into another vacuum diode, and then once again in opposite direction was considered. Such regime might take place not only at low gas pressures, but if one makes electron energy too high in order to uniform a specific pumping power across laser chamber. In this multi-passage case a mean scattering angle would increase and additional significant heat loading of the foils would appear due to absorption of decelerated electrons. It should be noted also, that the most of scattering in experiments might be caused by e-beam interaction with the hibachi structure particularly without magnetic field guiding. Both these effects were taken into account (the latter by introducing angular distribution of initial e-beams with $\Delta\alpha=45^\circ$) in the next run of calculations (3) that demonstrates good qualitative agreement with experimental results (1) in Fig.10.

The same assumptions have been done to calculate the distribution of scattered electrons along the axis of laser chamber at typical argon pressure of 1.5 atm (Fig.11). The distance in this graph is measured from the boundary of initial e-beams (cathode edge). Two experimental points coincide well with calculated ones. The main conclusion should be drawn from these investigations that external magnetic field besides increasing pumping efficiency and uniformity strongly reduces electrons escape towards laser windows.

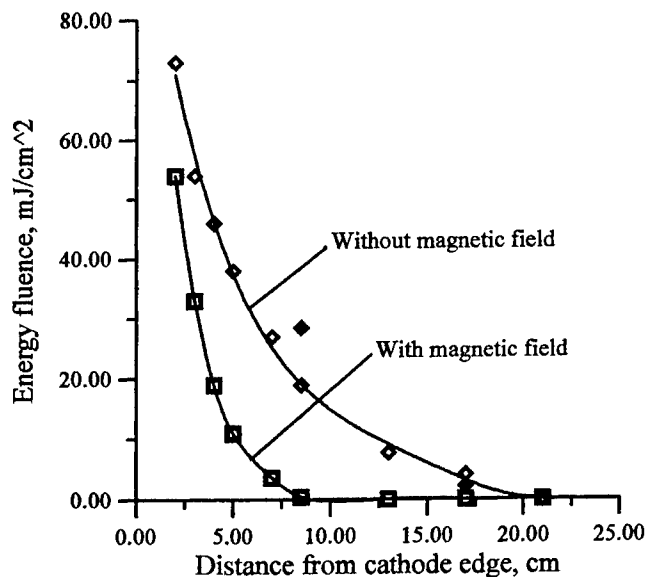
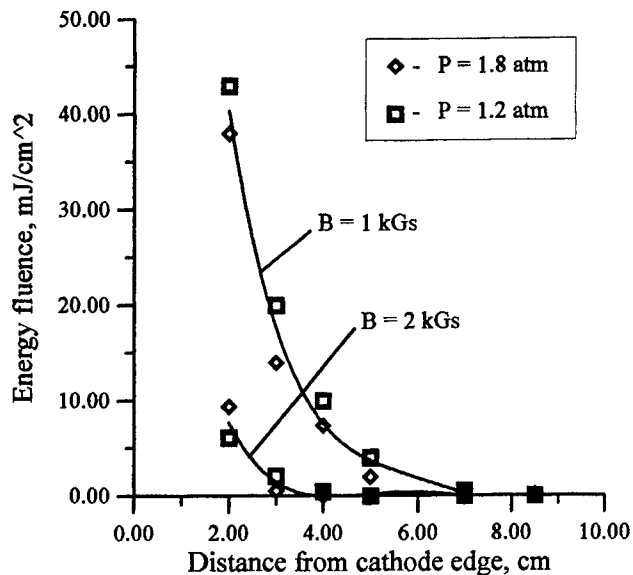


Fig.11. Distribution of scattered electrons along the axis of laser chamber at argon pressure 1.5 atm: solid dots- experiments; outlined dots- calculations.



Monte Carlo code, being tested by the experimental results obtained with the "GARPUN" laser, have been applied then to simulate analogous distributions for the NRL repetition-rate laser, which has an active volume 30*30*100 cm pumped by two opposite-side 500 keV, 112 kA, 100-ns e-beams stabilized by the magnetic field^{2,3}. The calculated distributions of scattered electrons along the axis of the laser are shown in Fig.12 for various working gas pressures and magnetic field values. It is clearly seen that the amount of scattered electrons falls down rapidly with increasing magnetic field. Gas pressure being varied in the optimal pumping range doesn't effect significantly on the electron scattering.

Fig.12. Distribution of scattered electrons along the axis of laser chamber for repetition-rate NRL KrF laser conditions.

7. CONCLUSIONS

The experiments have been performed with single-pulse large-aperture e-beam-pumped GARPUN KrF laser installation to investigate Aluminum-Beryllium foil transmittance and stability to multiple high-current e-beam irradiation, as well as to protracted fluorine action. E-beam scattering in the laser chamber in typical pumping conditions with and without guiding magnetic field was also investigated. Both problems are related to the development of the repetition-rate prototype of KrF laser driver for the Inertial Fusion Energy scheme. Such prototype, being constructed at the Naval Research Laboratory aimed at the research and development of key technologies, which would allow e-beam-pumped KrF laser to operate with output energy of tens kJ at 5-Hz repetition rate. The new technologies, when being developed should allow obtaining 10⁸ shots without any laser repair.

The main results obtained during the present investigation are as follows.

1. A large-aperture GARPUN module with 16*18*100 cm active volume pumped by two-side counter-propagating e-beams and middle-aperture "Berdych" module with a single-side-pumped active volume of 10*10*100 cm were adjusted for e-beam transport and Al-Be foil lifetime investigations. Both modules were arranged by the magnetic field to guide e-beams with average electron energy of ~300 keV and current density ~50 A/cm² from vacuum diodes into laser chamber.
2. Monte Carlo numerical code has been developed to calculate e-beam transport through different foil materials and distribution of scattered electrons inside the laser chamber.
3. Transparency of 50- μ m thickness Al-Be foil and 20- μ m Ti foil has been compared for 300 keV e-beams using Faraday cup technique. Both foils demonstrated equal transmittance of 75% that was lower than calculated one apparently due to the presence of low-energy electrons in initial e-beam.
4. No fatal damages and no surface modification due to fluorine etching were observed for Al-Be foils at GARPUN and "Berdych" modules after 1000 and 550 e-beam shots. It is significantly higher than mean lifetime of Ti foil in such conditions.
5. Distribution of scattered electrons have been measured for the GARPUN laser by means of calorimeters. It was shown that applied magnetic field of ~1kGs reduced the energy fluence of scattered electrons in 100 times at 8.5-cm distance from the boundary of injected e-beams. It means that e-beam-induced absorption of laser radiation in optical windows might be fully eliminated in such pumping scheme.
6. Monte Carlo code, being tested with GARPUN laser has been applied to simulate e-beam scattering in the repetition-rate NRL laser.

ACKNOWLEDGEMENTS

The authors are grateful to Dr. J.D. Sethian and Dr. S.P. Obenschain for the helpful discussions, and also to E.V. Polyakov for the assistance in experiments. This work was supported by Russian Foundation of Basic Research under Project No. 98-02-16993 and by the Naval Research Laboratory under Contract No. N68171-99-M-6338.

REFERENCES

1. I.N. Svyatoslavsky, M. E. Sawan, R. R. Peterson, et al. "A KrF laser driven inertial fusion reactor "Sombbrero", *Fusion Technology*, **21**, p. 1470, 1992.
2. J.D. Sethian, S.P. Obenschain, R.H. Lehmberg, M.W. McGeoch "KrF Lasers for Inertial Fusion Energy" in *Proceedings of 17th IEEE/NPSS Symposium on Fusion Engineering, San Diego, CA, October 1997*, p. 593, IEEE, Piscataway, NJ, 1998.
3. J.D. Sethian, S.P. Obenschain, R.H. Lehmberg, M.W. McGeoch "A Rep-Rate KrF System to Address the Issues Relevant to Inertial Fusion", *Fusion Engineering and Design*, **44**, p. 371, 1999.
4. L.A. Rosocha, K.B. Riepe "Electron-Beam Sources for Pumping Large Aperture KrF Lasers", *Fusion Technology*, **11**, p. 576, 1987.
5. Y. Owadano, et al. in *Plasma Physics and Controlled Nuclear Fusion Research 1994*, vol. **3**, p. 121, International Atomic Energy Agency, Vienna, 1996.
6. E.J. Divall, C.B. Edwards, G.J. Hirst, et al. "Titania- a 10^{20} Wcm⁻² ultraviolet laser", *J. Mod. Opt.* **43**, p. 1025, 1996.
7. J.D. Sethian, S.P. Obenschain, K.A. Gerber, et al. "Large area electron beam pumped krypton fluoride laser amplifier", *Rev. Sci. Instrum.* **68**, p. 2357, 1997.
8. J.D. Sethian, C.J. Powley, S.P. Obenschain, et al. "The Nike Electron-Beam-Pumped KrF Laser Amplifiers", *IEEE Transactions on Plasma Science*, **25**, p. 231, 1997.
9. E. Takahashi, I. Okuda, Y. Matsumoto, et al. "Electron-beam Pumped High-Repetition Rate KrF Laser System", in *Book of Abstracts of International Forum on Advanced High-Power Lasers and applications AHPLA' 99*, paper 3886-49, p. 71.
10. *Beryllium science and Technology*, Plenum Press, New York, 1979.
11. V.S. Barabanov, N.V. Morozov, P.B. Sergeev "Ionizing radiation induced absorption in KrF-laser windows", *J. of Non-crystalline Solids*, **149**, p. 102, 1992.
12. A.V. Amosov, V.S. Barabanov, et al. "Electron-beam-induced absorption of laser radiation in a quartz glass at wavelengths of 193, 248, and 353 nm", *Quant. Electron.* **23**, p. 939, 1993.
13. V.S. Barabanov, P.B. Sergeev, "Electron-beam-induced absorption of ArF, KrF, and XeF laser radiation in optical materials", *Quant. Electron.* **25**, p. 717, 1995.
14. E.N. Eliseev, E.I. Fadeeva, V.D. Zvorykin, et al. "Laser damage resistance of optical materials and coatings for excimer ArF- and KrF-lasers", *J. of Optical Technology*, No.2, p. 40, 1996.
15. E.J. Divall, G.J. Hirst. "Radiation damage to Goblin windows", in *Rutherford Appleton Laboratory Report RAL-93-031*, p. 143, 1993.
16. N.G. Basov, V.G. Bakaev, et al. "E-beam pumped GARPUN broadband KrF laser with ~1GW pulsed lasing power", *J. Sov. Laser Res.*, **14**, p. 326, 1993.
17. V.D. Zvorykin and I.G. Lebo "Laser and target experiments on KrF GARPUN laser installation at FIAN", *Laser and Particle Beams*, **17**, p. 69, 1999.
18. V.G. Bakaev, A.D. Vadkovskii, E.O. Danilov, et al. "Generation of electron beams for pumping of the GARPUN wide-aperture excimer laser", *Quant. Electron.* **24**, p. 5, 1994.
19. S.V. Arlantsev, E.A. Grigor'yants, A.D. Vadkovskii, et al. "Pumping of the GARPUN wide-aperture excimer laser by counterpropagating electron beams", *Quant. Electron.* **24**, p. 223, 1994.
20. C.D. Zerby and F.L. Keller *Nuclear Science Engineering*, **27**, p. 190, 1967.
21. H.A. Bethe "Moliere's theory of multiple scattering", *Phys. Rev.* **89**, p. 1256, 1953.

KINETIC RESEARCH OF ACTIVE MIXTURES OF THE XeF EXIMER LASER WITH OPTICAL PUMPING

V.P.Fokanov, A.B.Pavlov

197198, S.-Petersburg, Dobrolubova str.14, RSC "APPLIED CHEMISTRY".

tel.(812) 2399843, fax (812) 2389251, e-mail: fokanov@mail.rcom.ru

The results measurements integral intensity luminescence laser transitions B→X (353 nm) and C→A (480 nm) eximer XeF depending on pressure buffer gases are present. The constants quenching K_B , K_C and transfer K_{BC} for thirteen connections are measured. Twenty two constants are obtained for the first time. The simplified model an vibrational relaxation in the state B, obtained ratio $T_{vib}^{-1} = a + b \cdot \ln p$ is confirmed experimentally

1. Experimental installation for a record of a spectrum of luminescence.

The inverse population in XeF laser with optical pumping is the result of photolysis of gaseous XeF_2 / 2-5 /. The inverse population on transition B←X ($\lambda \approx 353$ nm) is the result of optical pumping by the most absorption band (145÷175 nm) with formation XeF(B). The possibility of obtaining of laser generation on transition C→A ($\lambda \approx 480$ nm) is stipulated by a population XeF (C), that is the result of exchange by energy $XeF(B) + M = XeF(C) + M$, here M - particles of buffer gas / 6,7 /. The balance of this reaction at room temperature is essentially shifted in the side XeF(C), so as the state C is lower on ~ 700 cm^{-1} , than a state B / 8,9 /.

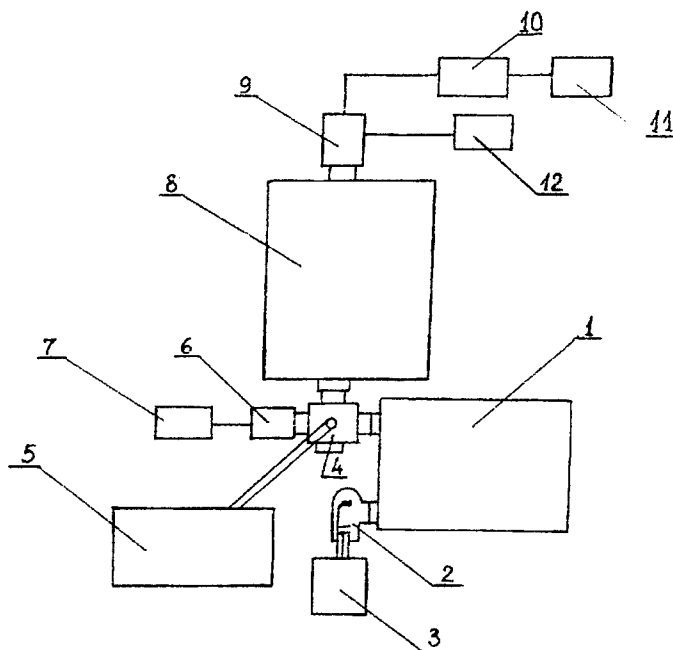


Fig 1 The scheme of the experimental installation

1 – a vacuum monochromator BMP-2, 2 – a lamp ДНУ-170, 3 – a system of the lamp power supply, 4 – a volume, 5 – a system of the volume filling, 6, 9 – photomultipliers ФЭУ-100, 7, 10 – counters of photons ИФП-2, 11 – a recorder КСП-4, 12 – a system of the power supply of photomultipliers

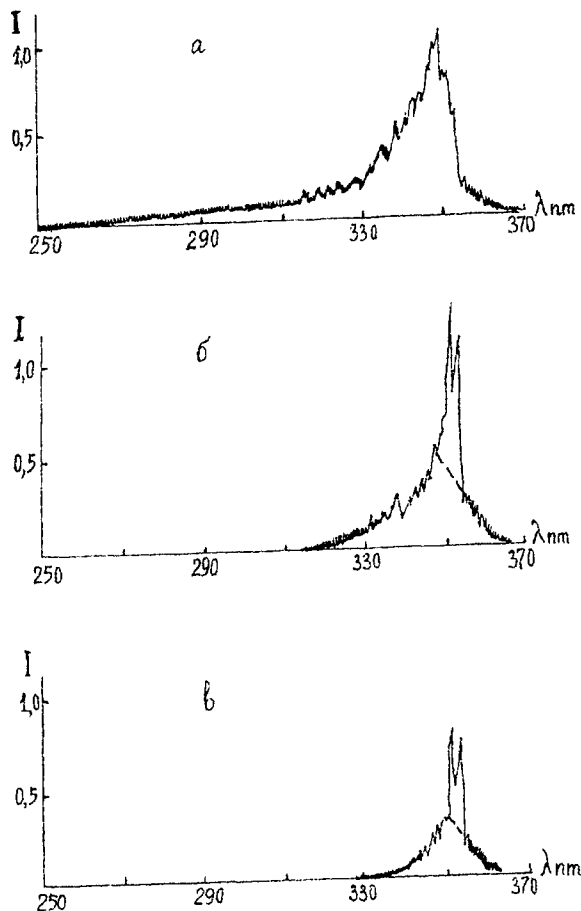


Fig.2 The spectra of luminescence XeF
 a-XeF₂(0.4mm Hg); б-with CF₄(48mm Hg);
 в-with CF₄(250mm Hg)

the help of calibrated deytro-neon lamp, and for the interval of waves lengths, bigger than 370nm – with the help of of standard band lamp. At the analysis of experimental results were used integral of intensity spectra of luminescence on transitions XeF (B→X) and XeF (B→A).

The pressure XeF₂ in volume was 0.4 mm Hg. The pressure of researched gases varied from 0 up to 730 mm Hg. The pressure C₂F₆ did not exceed 300 mm Hg, and n-C₅F₁₂ — 80 mm Hg, that was stipulated by an absorption of that gases on a wavelength of excitation. The pressure of gases CO₂, CO, O₂, HF, N₂O varied in limits 0-10mmHg due to high effectiveness of quenching by these gases of laser levels eximer XeF.

Constants of speeds of exchange XeF (B↔C) and quenching of states B and C it is possible to define from the relations of the integral intensities luminescence XeF (B→X, A) and XeF (C→ A, X).

In the present report the research of two types of molecules is conducted: molecules, which have small effectiveness of quenching of states XeF (B), XeF (C) – Ar, Kr, N₂, SF₆, CF₄, C₂F₆, C₃F₈, n-C₅F₁₂, and molecules have high effectiveness of quenching of these states - CO₂, CO, O₂, HF, N₂O. The first group of substenses is of interest for selection of optimum lasing on transition XeF (C→A, X), 480 нм. The second group determines probable impurity

The scheme of the experimental installation is shown on fig.1. The deytro-neon lamp with a window from MgF₂ was used as a light source. The spectral interval of pumping radiation (157÷163 nm) was set by vacuum monochromator. Photolyse XeF₂ was in volume, made from a stainless steel with MgF₂ windows . Volume was ~ 50m³, its length - 4cm. The volume passivated F₂, and then XeF₂. The degree of destruction XeF₂ on volume walls and by operation of exciting radiation was controlled by change of a radiation absorption passing through volume and did not exceed 10% during a record of a luminescence spectrum.

The radiation on transitions B→X and C→A molecule XeF₂ was observed under a right angle to an exciting light flow and was registered with the help of double monochromator and photomultiplier as the account of photons. The reverse dispersion monochromator has made linear of 0.8 nm/mm width of input and output splits was selected equal 1.0 mm at registration of luminescence XeF(B) and 2.5mm at XeF(C). The spectra examples show on fig.2.

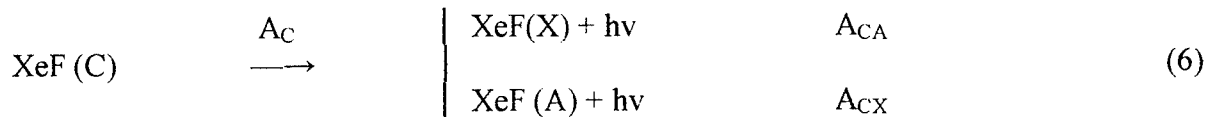
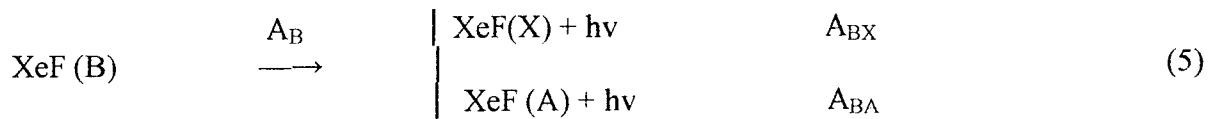
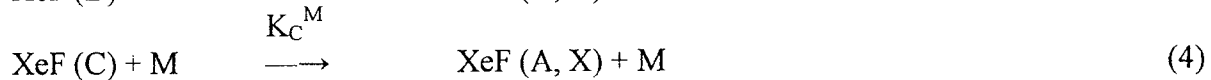
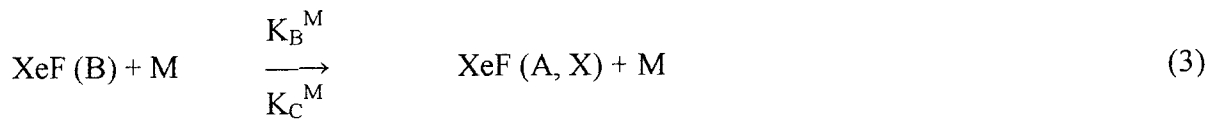
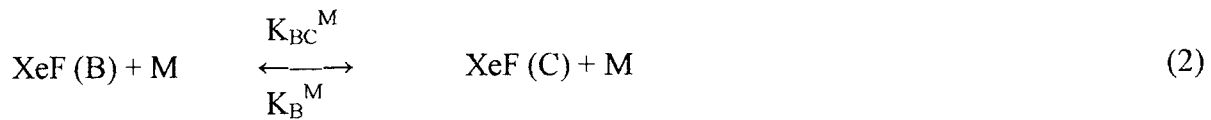
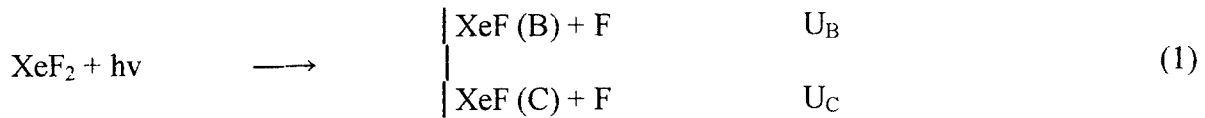
The spectra of luminescence were corrected out of the wavelength sensitivity of recording system. It was determined in the interval of waves lengths 250÷370 nm with

formed at synthesis and storage of the initial XeF₂.

At research of gases with high effectiveness of quenching of states B and C the molecule XeF it is difficult to define change of luminescence intensity from a level C. Therefore luminescence spectra of such gases at different pressure were registered after adding in volume of fixed quantity of additional gas Kr. Kr was selected due to of enough high effectiveness of transmission of energy B→C and small effectiveness of quenching of states B and C.

2. Development of a kinetic model for the eximer XeF

Kinetic model for analysis and the processing of experimental results took into consideration the following processes:



The processes happening at collision of three and more particles, were not considered, as these processes do not play a determining role / 8 / at pressure of researched gases less than 1 atm. The transitions from a state XeF (D) nor were taken into account, as the quantum exit XeF (D) at a dissociation XeF₂ in the wavelength 160 nm is less than 1.5% / 6 /.

The solution of equation systems for concentration XeF (B) and XeF (C) under condition of fixed pumping results in formulars:

$$\frac{I_B}{I_C} = \frac{(R_C + \Theta S_{BX}) A_{BX} + (\Theta R_B + S_{BC}) A_{CX}}{(R_C + \Theta S_{BX}) A_{BA} + (\Theta R_B + S_{BC}) A_{CA}} \quad (7)$$

$$\frac{I_B^0}{I_B} = \frac{R_C^0 A_{BX} + \Theta R_B^0 A_{CX}}{(R_C + \Theta S_{CB}) A_{BX} + (\Theta R_B + S_{BC}) A_{CX}} \cdot \frac{(R_B R_C - S_{BC} S_{CB})}{R_B^0 R_C^0} \quad (8)$$

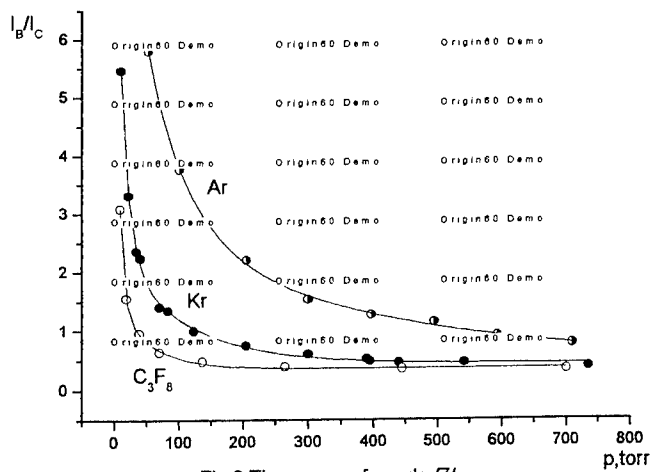


Fig.3 The curves - formula 7/.

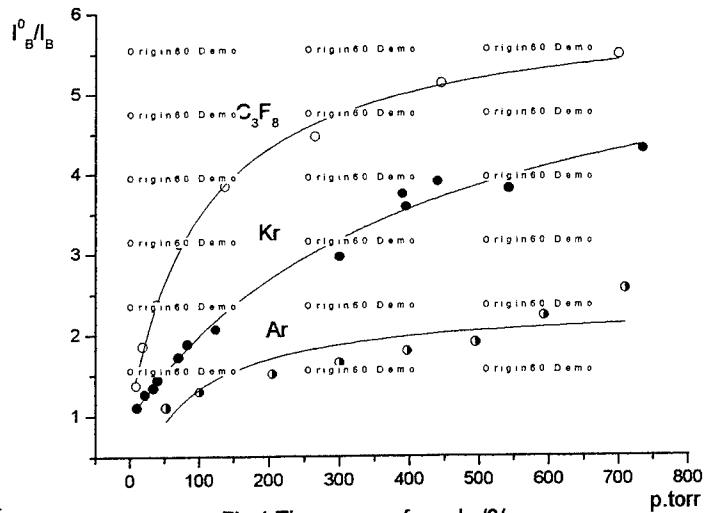


Fig.4 The curves - formula 8/.

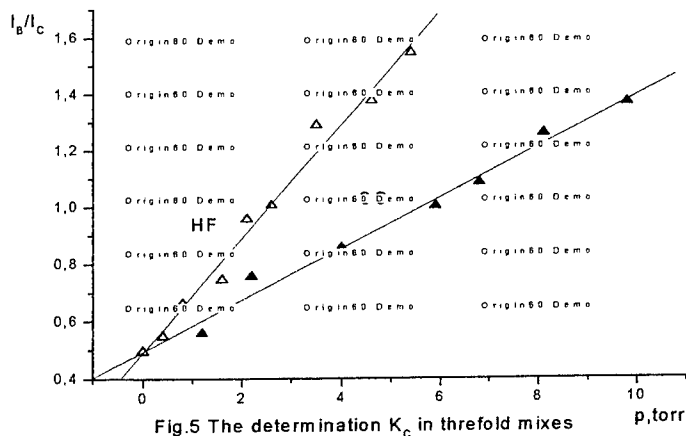


Fig.5 The determination K_C in threfold mixes

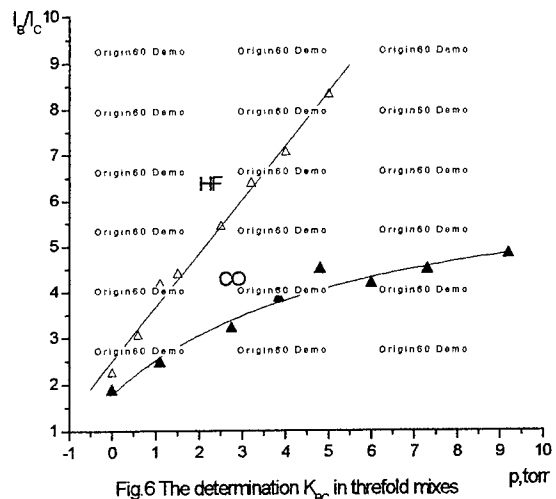


Fig.6 The determination K_{BC} in threfold mixes

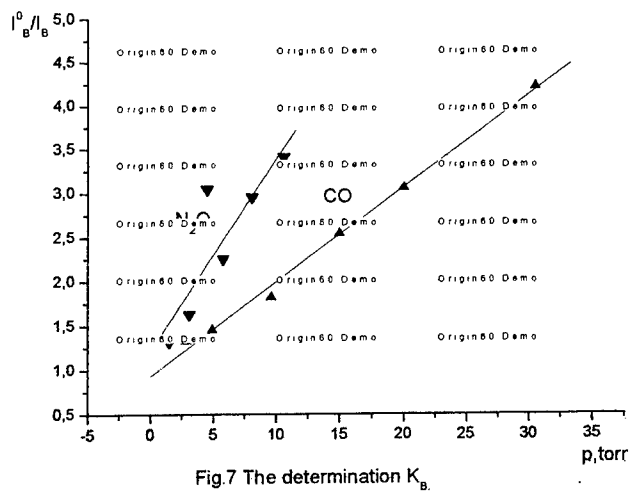


Fig.7 The determination K_B

$$\begin{aligned} \text{here } R_C &= A_C + k_C^{\text{XeF}_2} \cdot N_{\text{XeF}_2} + k_C^M \cdot N_M + k_{CB}^M N_M; \\ R_B &= A_B + k_B^{\text{XeF}_2} \cdot N_{\text{XeF}_2} + k_C^M \cdot N_M + k_{CB}^M \cdot N_M; \\ S_{BC} &= k_{BC}^M \cdot N_M; \quad S_{CB} = k_{CB}^M \cdot N_M; \\ R_B^0 &= A_B + k_B^{\text{XeF}_2} \cdot N_{\text{XeF}_2}; \\ R_C^0 &= A_C + k_C^{\text{XeF}_2} \cdot N_{\text{XeF}_2}; \end{aligned}$$

$$\Theta = \varphi_C / \varphi_B;$$

N_M — concentration of M-gas,

I_B — integral intensity of luminescence on transitions $B \rightarrow X$ and $C \rightarrow X$ ($\lambda = 250 \div 370 \text{ nm}$);

I_C — integral intensity of luminescence on transitions $B \rightarrow A$ and $C \rightarrow A$ ($\lambda = 370 \div 600 \text{ nm}$);

I_B — integral intensity of luminescence on transitions $B \rightarrow X$ and $C \rightarrow X$ $N_M = 0$

The technology for definition of constants of speeds of processes (2) - (4) /8/ was the same, however in / 8 / the radiant transitions XeF ($B \rightarrow X$) and XeF ($B \rightarrow A$) were not taken into account, although their intensity is 3.5% and 10% of intensity of transitions XeF ($B \rightarrow X$) and XeF ($B \rightarrow A$), accordingly, / 9 /. The constants of speeds were determined from formular (7) and (8) by computer.

The values of Einstein coefficients from / 9 / were used:

$$A_{BX} = 6.75 \cdot 10^7 \text{ sec}^{-1}$$

$$A_{BA} = 2.4 \cdot 10^6 \text{ sec}^{-1}$$

$$A_{CA} = 1 \cdot 10^6 \text{ sec}^{-1}$$

$$A_{CX} = 9.96 \cdot 10^6 \text{ sec}^{-1}.$$

The altitude $k_{BC}^M / k_{CB}^M = 42$, proceeding from a difference between levels XeF (B) and XeF (C) 775 cm^{-1} undertook from / 8 /. The attitude $\Theta = \varphi_C / \varphi_B$ was determined by experiment, proceeding from the relation of integral intensities I_B^0 and I_C^0 in absence of buffer gas.

$$\Theta = \frac{A_{BX} - A_{BA} (I_B^0 / I_C^0) \quad A_C + k_C^{\text{XeF}_2} \cdot N_{\text{XeF}_2}}{A_{CA} (I_B^0 / I_C^0) - A_{CX} \quad A_B + k_B^{\text{XeF}_2} / N_{\text{XeF}_2}}$$

The size $k_C^{\text{XeF}_2} = k_B^{\text{XeF}_2} = 2 \cdot 10^{-10} \text{ cm}^3 \cdot \text{s}^{-1}$ is taken from / 8 /.

The result of calculation is $\Theta = 0.048 \pm 0.004$.

In case of a triple mix, with adding Kr (section 1), the formular (7) has a kind:

$$R_C = A_C + k_C^{\text{XeF}_2} \cdot N_{\text{XeF}_2} + k_C^M \cdot N_M + k_{CB}^M \cdot N_M + k_C^{\text{Kr}} \cdot N_{\text{Kr}} + K_{CB}^{\text{Kr}} N_{\text{Kr}};$$

$$R_B = A_B + k_B^{\text{XeF}_2} \cdot N_{\text{XeF}_2} + k_B^M \cdot N_M + k_{BC}^M N_M + k_B^{\text{Kr}} \cdot N_{\text{Kr}} + k_{BC}^{\text{Kr}} \cdot N_{\text{Kr}};$$

$$S_{BC} = k_{BC}^M \cdot N_M + k_{BC}^{\text{Kr}} \cdot N_{\text{Kr}};$$

$$S_{CB} = k_{CB}^M \cdot N_M + k_{CB}^{\text{Kr}} \cdot N_{\text{Kr}}.$$

At use of gases with high effectiveness of quenting of laser levels eximer XeF the dependense I_B / I_C from pressure of gas were determined at two fixed pressure Kr: 400-410 mm Hg and 40-50 mm Hg. At high pressure Kr altitude of $K_{BC}^{\text{Kr}} \cdot N_{\text{Kr}} \gg K_{BC}^M \cdot N_M$ and determining role depending on N_M has the constant of speed K_C^M . At small pressure of Kr the altitude $K_{BC}^{\text{Kr}} \cdot N_{\text{Kr}}$ and

$k_{BC}^M \cdot N_M$ (at used pressure N_M) are comparable also relation I_B / I_C from N_M determine both

Tabl. 1(Data of this report)

Subject	$k_{BC} \cdot 10^{11}, \text{cm}^3 \text{s}^{-1}$	$k_B \cdot 10^{11}, \text{cm}^3 \text{s}^{-1}$	$k_C \cdot 10^{11}, \text{cm}^3 \text{s}^{-1}$
Ar	0.66 ± 0.09	$(6 \pm 4) \cdot 10^{-3}$	$(6 \pm 4) \cdot 10^{-3}$
N ₂	3.0 ± 0.5	$(1.5 \pm 0.5) \cdot 10^{-2}$	$(1.0 \pm 0.5) \cdot 10^{-2}$
Kr	3.5 ± 0.6	$(1.0 \pm 0.5) \cdot 10^{-2}$	$(1.0 \pm 0.5) \cdot 10^{-2}$
SF ₆	5.2 ± 0.7	$(1.0 \pm 0.7) \cdot 10^{-2}$	$(0.9 \pm 0.7) \cdot 10^{-2}$
CF ₄	2.8 ± 0.2	$(2.0 \pm 1.0) \cdot 10^{-2}$	$(1.5 \pm 1.0) \cdot 10^{-2}$
C ₂ F ₆	6.3 ± 0.3	$(6 \pm 3) \cdot 10^{-2}$	$(5.5 \pm 2.5) \cdot 10^{-2}$
C ₃ F ₈	9.5 ± 1.0	$(2.5 \pm 1.5) \cdot 10^{-2}$	$(2.5 \pm 1.5) \cdot 10^{-2}$
n-C ₅ F ₁₂	18 ± 3	0.45 ± 0.25	0.45 ± 0.25
CO ₂	7 ± 3	47 ± 11	34 ± 4
CO	11 ± 3	12 ± 4	17 ± 3
O ₂	3 ± 2	10 ± 2	8 ± 1
HF	8.5 ± 2.5	45 ± 9	40 ± 5
N ₂ O	6 ± 2	44 ± 6	18 ± 2

Tabl. 2 (Data /8/)

Subject	$k_{BC} \cdot 10^{12}, \text{cm}^3 \text{s}^{-1}$	$k_B \cdot 10^{12}, \text{cm}^3 \text{s}^{-1}$	$k_C \cdot 10^{12}, \text{cm}^3 \text{s}^{-1}$
Ar	8.6 ± 1.1	0.05 ± 0.02	0.05 ± 0.02
Kr	34 ± 3	0.1 ± 0.03	0.1 ± 0.03
N ₂	44 ± 6	0.1 ± 0.03	0.1 ± 0.03
SF ₆	60 ± 12	0.2 ± 0.05	0.2 ± 0.05
CF ₄	41 ± 4	0.53 ± 0.11	0.53 ± 0.11
HF		$300 - 500$ *)	
CO ₂		$300 - 500$ *)	

*) Here are measured the sum of constants of speeds $k_B^M + k_{BC}^M$

constants of speed K_C^M and K_{BC}^M . The constant of speed K_B^M together with a constant K_{BC}^M determines declination of relation I_B^0/I_B from N_M without Kr at small N_M .

The comparison of obtained experimental results (point) and theoretical curve, designed on the developed kinetic model is shown on fig.3-7. The error of definition of constants was calculated as a dispersion of experimental points near computational curve.

The results of speed constants are adduced in table 1. In table 2 the values of speed constants measured in / 8 /. At absence of buffer gases maximum intensity of the luminescence XeF (B→X) was observed on transition B ($v' = 2$) → X ($v'' = 5$) ($\lambda = 348.8$ nm)

3. Model of an vibrational relaxation of a laser condition XeF (B).

The shape of a luminescence spectrum varied at introduction of buffer gases: the maximum displaced in the long-wave regime and at rather large pressure of the buffer gas appeared in the field of transitions $v' = 0 \rightarrow v'' = 2$ ($\lambda = 351.1$ nm) and $v' = 0 \rightarrow v'' = 3$ ($\lambda = 353.3$ nm). Such change of a spectrum of luminescence is stipulated by an oscillatory relaxation XeF (B) in collisions with molecules of buffer gas. the shape of a luminescence spectrum varied Most effective relaxants are perftoralkans (CF_4 , C_2F_6 , C_3F_8 , $n-C_5F_{12}$). The spectra of luminescence XeF (B→X) in pure vapours XeF_2 are shown on fig.2 and at introduction CF_4 (48 and 250 mm P Hg. The some electronic - vibrationally transitions, which were allowed at used in the data experiments to spectral width of a slot monochromator(0.8 nm) are indicated on this figure too.

The potential curves of the electronic states eximer XeF are showed in a fig. 8. The maximum of vibrationally excitation by formed eximer XeF (B), at a photodissociation XeF_2 in the field of 160 nm, is located close of 4- 5 oscillatory levels of the state B / 8,10 /. The significant contribution to intensity of luminescence introduce also higher (up to 20-th and above) vibrationally levels. Thus, the energy of electron excitation "is spreaded" on a large spectral interval in the initial act of photoexcitation. The laser generation on a wavelength 351 nm from the state XeF (B) result from $v'_B = 0$. The interception potential curve B and C and, therefore, most effective transitions B→C, as showed from fig.8, are located close $v'_B=0$. Thus, the vibrotionally relaxation in the state B eximer XeF is process essential influenced on an overall performance of the laser on both lengths of waves, 351 and 480 nm. The data, obtained in the report, allow, basically, to select in spektra of luminescence the transitions with $v'_B = 0$, as it is showed from the fig. 2,. The practical way of such selection is illustrated on fig.2 by dashed lines. The way, developed by us, a classification of buffer gases on their efficiency during vibrationally relaxation of the electron state XeF (B) is submitted below. The experimental value - the altitude of the area of spectra luminisence - is used as criterion of an vibrationally relaxation

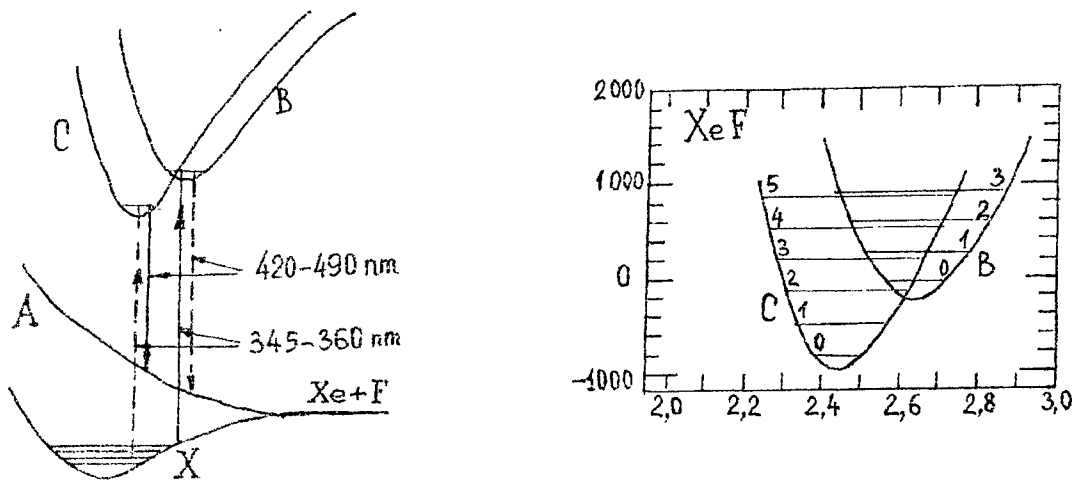


Fig.8 The potential curves of the electronic states eximer XeF /9/.

The following assumption are set up:

1. The state of equilibrium between of an vibrationaly relaxation, on the one hand, and an introduce of energy in the primary process of a photodissociation: $XeF_2 \rightarrow XeF (B, v') + F$ is installed at each value pressure of buffer gas.
2. The condition of equilibrium is characterized certain, distinct from room, temperature of a system of vibrationaly levels of the electron state B.
3. The system of vibrationaly levels XeF (B) is divided into two parts: $v' = 0$, on the one hand, and remaining vibrationaly levels. Vibrationaly temperature, entered in item 2, determines a condition of equilibrium of these parts.
4. The condition of equilibrium inside vibrationaly levels XeF (B) is installed independently of processes of an electron relaxation.
5. All of Franc - Kondon factors for v_B' are identical.

obtainedThe data for substances Ar and Kr are shown in a fig. 9. Value T on figures is understood as temperature of the vibrationaly subsystem XeF (B). The dependences present in fig. 9 have expressed linear character. Especially it is visible for inert gases Ar and Kr. The processes including just of these gases to the greatest degree approach for selected model. In these cases take place simple V-T process. Vibrationaly quantum of the state B is equal 308 cm^{-1} , that is not too hardly exceeds kT . It is one more argument for a hypothesis of the equilibrium in subsystem v'_B . Value T caculate take into assumptions 1 -5.

The equilibrium condition subsystem v'_B is:

$$\frac{dn_{v'_B}}{dt} = k_+ \cdot M \cdot n_{v'} - k \cdot M \cdot n_{v'0} = 0 \quad (9)$$

Where $n_{v'0}$, $n_{v'}$ - concentrations XeF (B) on zero and remaining vibrationaly levels, accordingly,

M - concentration of a buffer gas,

k_+ - constant of an vibrationaly relaxation on level $v'0$,

k. - constant of an vibrationaly relaxation with v' .

From (9) follows:

$$\frac{n_{v'}}{n_{v'0}} = \frac{k_-}{K_+} = K_R, \text{ here } K_R - \text{ the constant equilibrium subsystem } v'_B.$$

The constant equilibrium is determined by energy of activation of equilibrium process and relation statistical wights of participating particles (see, for example, / 12 /). The energy of

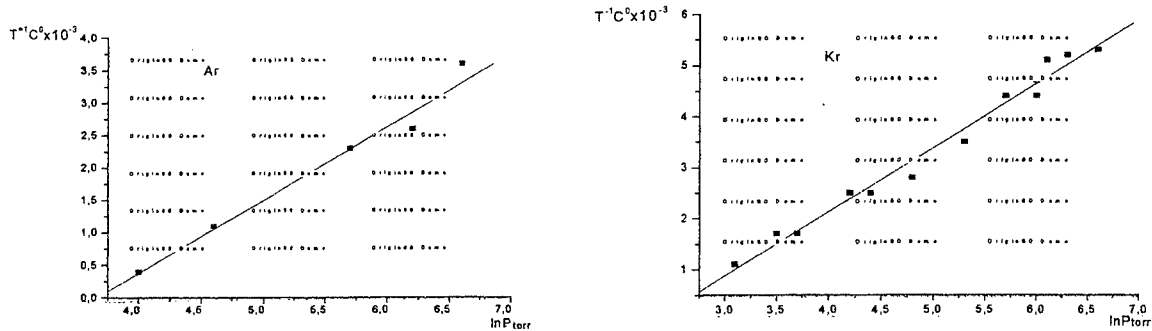


Fig.9 The Illustrations to vibrational relaxation model of the electronic state B eximer XeF

the activation, $E_{v'_B}$, is the energy of transition with v'_0 on v'_1 , that is is equal 308cm^{-1} . The statistical sums of translational, rotary and electron degree of freedoms are identical and are reduced. Thus:

$$K_R = V'_B \cdot \exp(- E_{v'_B} / kT)$$

Where V'_B - statistical sum of the vibrationally levels state B,
 T - temperature of an vibrationally system XeF (B).

Tabl. 3. The coefficients linear regression formular $1/T = a + b \cdot \ln p$

Substans	a	b · 10 ³
KR	- 2.87 ± 0.27	1.25 ± 0.05
AR	- 4.06 ± 0.41	1.11 ± 0.07
C ₂ F ₆	- 1.41 ± 0.70	1.20 ± 0.15
C ₃ F ₈	- 0.90 ± 0.38	1.04 ± 0.08
C ₅ F ₁₂	- 1.43 ± 0.30	1.31 ± 0.09
CF ₄	- 1.18 ± 0.66	0.96 ± 0.14
N ₂	0.19 ± 0.35	0.75 ± 0.07
SF ₆	- 2.43 ± 0.84	1.11 ± 0.07

The value $V'_B = 8$ well agree the results for Ar at the greatest pressure by room temperature. This value is taken for the calculation T. At an extrapolation $T \rightarrow \infty$ within the framework of the given model we should obtain the vibrationally sum state B. More exactly model /10/, with allowance for of factors of Frank - Condon, give as the primary deposit in luminescence ~ 10 vibrationally levels of the state B.

Литература.

1. Borovich B.A., Grigorjev P.G., Zuev V.S. and others. Transactions of FIAN, v.76, p.3 - 35 (1974).
2. 4. Basov N.G., Zuev V.S., Miheev L.D., Stavrovsky D.B., Qwantum electronic, v.4, 11, p. 2453 (1977).
3. Eden J.G. Opt. Lett, v.3, 7, p. 94 - 96 (1978).
4. Basov N.G., Zuev V.S., Kapaev A.V., Miheev L.D., Stavrovsky D.B., Qwantum electronic, v.6, 5, p.1074 (1979).
5. Bishel W.K., Nakano H.H., Eckstrem D.J., Hill R.M., Huestis D.L., Lorents D.C. Appl. Phis. Lett., v.34, N9, p.565 - 567 (1979).
6. Bibinov N.K., Vinogradov I.P., Miheev L.D., Stavrovsky D.B., Qwantum electronic, v.8, 9, p.1945 - 1951 (1981).
7. Black G., Sharpless R.L., Lorents D.C., Huestis D.L., Gutcheck R.A., Bonifield T.D., Helm D.A., Walters G.K. J.Chem.Phis., v.75, 10, p. 4840 - 4846 (1981).
8. Brashears H.C., Setser D.W. J.Chem.Phis., v.76, 10, p. 4932 - 4946 (1982).
9. Helm H., Huestis D.L., Dyer M.J., Lourents D.C. J.Chem.Phis., v.79, 7, p. 3220 - 3226 (1983).
10. Koch D.B., Dissertation, St.Petersburg State University, (1994).
11. K.-P.Hjuber, Gerberg G., "Constants of diatomic molecules" p.2, M., "Mir", 1984
12. Kondratjev V.N., Nikitin V.E., "Kinetic and mechanism gase reactions", M., "Nauka", 1974.

Nonlinear reflection of laser radiation in Xe-containing dense gas mixtures and cryogenic solutions.

A.P.Burtsev, V.V.Bertsev, V.N.Bocharov

Department of Molecular Spectroscopy, Institute of Physics, St.Petersburg State University
Peterhof, St.Petersburg, 198904 Russia e-mail burcev@molsp.phys.spbu.ru

ABSTRACT

Nonlinear reflection of focused laser radiation (222-413 nm, H₂-SRS-converted depolarized XeCl-excimer laser output) in Xe-containing binary gas mixtures and cryogenic solutions was studied. The effect of strong enhancement of unsaturated reflectivity, especially pronounced and frequency selective for admixture of Cl, Br-substituted hydro-carbons (CF₂Cl₂, CF₃Cl, CF₃Br) was observed, whereas no effect was found when fluorides (CF₃H, NF₃) or oxygen were added. For linearly polarized $\lambda=308$ nm radiation reflectivities increased twofold up to ~ 0.8 at the intensity $\sim 5 \cdot 10^{10}$ wt·cm⁻². Nonlinear reflection at $\lambda=308$ nm in low-temperature solutions of Xe (20% mol) in LAr (at 140K) and LKr (at 170K) was observed and analyzed. Close to second order pump intensity dependences of reflection, photo-acoustic signals and secondary emission were found.

1. INTRODUCTION

The quest for the new optical mediums with high nonlinear frequency selective reflectivities R in IR or UV regions and studies of their characteristics are of considerable importance for the fields of optical communication and laser beam parameters control.

Earlier the effect of strong nonlinear reflection of 10.6 mkm TEA-CO₂ laser radiation in liquefied molecular gas SF₆ was observed and utilized for IR-laser pulses reshaping [1]. In UV region nonlinear backward stimulated scattering (bss) of XeCl and KrF excimer lasers radiation was observed in compressed and liquid Xe and dense CF₃Cl [2,3] at broadband pump conditions. On the basis of experimental data the stimulated Brillouin scattering nature of this effect was stated [3]. Data on nonlinear properties of gaseous and liquid mixtures are practically absent.

2. EXPERIMENT

Home-made electric-discharge excimer XeCl-laser with unstable resonator was used as the primary light source. It delivers unpolarized broadband light pulses (at repetition rate 1÷10 Hz) with typical energy $\approx 5 \cdot 10^{-3}$ J, duration (FWHM) ≈ 5 ns and effective coherence length ≈ 0.3 cm.

To study spectral selectivity of nonlinear effects, pump radiation I_{pump} in the 222÷413 nm spectral region was produced by SRS-conversion of focused (intensity $I \approx 10^9$ wt·cm⁻²) laser output in compressed H₂ ($p=30\div 80$ atm). Chosen SRS-components were additionally focused into high-pressure stainless steel photo-acoustic cell with crossed BaF₂ windows to monitor IR-UV spectral absorption of impurities, possible stable photoproducts and to record UV-VIS secondary emission from the caustic zone. In some experiments low-temperature cryostats were used as an optical cell. For discrete reduction of pump intensity I_{pump} calibrated linear glass filters were used. High-speed and "sun-battery" type Si-detectors were used for measurements of pulse duration and energy respectively.

The rare gases used were of guaranteed purity better than 99.99%. Freons CF₂Cl₂, CF₃Cl, CF₃Br, CF₃H and NF₃ were chosen due to relatively high density of their saturated vapours at room temperature (295K), different types of halogen-atoms and essentially different values of R-Hal break-bond energy. Their purity varied in (99.9÷99.5)% limits.

3. RESULTS AND DISCUSSION

The most extensive studies at $\lambda=308$ nm have been done. To study consistently the influence of buffer components on the nonlinear reflection in Xe-containing binary compositions first of all simplest compounds (Ar, Kr, O₂) were chosen (Fig. 1). Keeping in mind that at similar pump conditions threshold density of Xe is close to 50 Amagat, substantial enhancement of the effect is seen for the rare gases admixture, whereas oxygen definitely destroys the reflection. It is slightly remarkably, keeping in mind obvious resemblance of basic physical properties of argon and oxygen. It should be mentioned, that such parameter as electronegativity is sufficiently different for these substances, this fact may be useful in understanding of physical nature of bss effect.

Under fixed pump conditions ($I_{\text{pump}} \approx 4 \cdot 10^{10} \text{ wt} \cdot \text{cm}^{-2}$) the nonlinear dependences, including in the threshold region, of bss pulse energy on the density and composition of the sample were studied (Fig. 2). Strong enhancement of unsaturated reflectivity, especially pronounced for admixtures of Cl-containing freons is seen, whereas the effect is absent when fluorides CF₃H (NF₃) are added. The enhancement is more pronounced when freon with lower R-Halogen breakbond energy is used as a buffer gas ($E_{\text{br.b. CF}_3\text{Cl}} > E_{\text{br.b. CF}_2\text{Cl}_2}$). The dependence of such kind is naturally valid only for doping substances with the same type of halogen-atom.

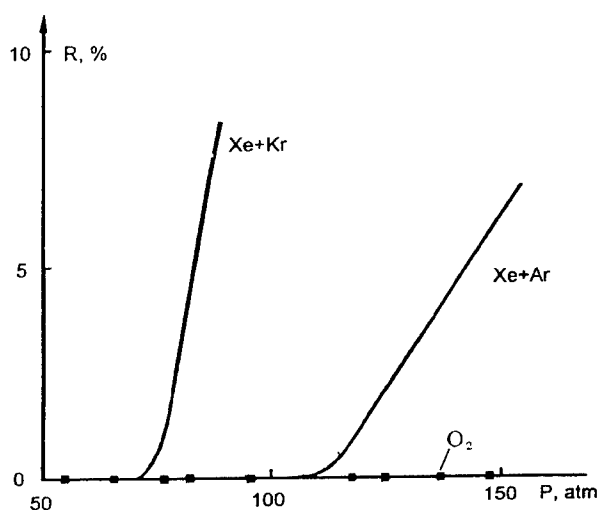


Figure 1. The influence of buffer gases on the reflectivity R, mixture (Xe+M), 20% Xe (vol.), T=295K, $I_{\text{pump}} \approx 4 \cdot 10^{10} \text{ wt} \cdot \text{cm}^{-2}$

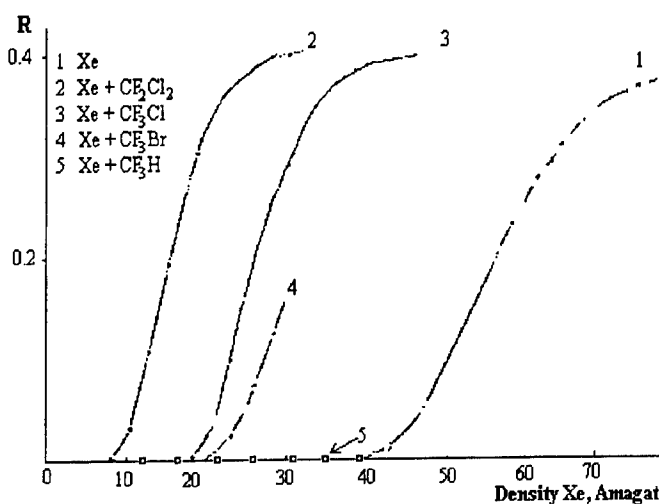


Figure 2. The influence of different freons admixture on the reflectivity R. Freons density is 3 Amagat for all curves ($I_{\text{pump}} \approx 4 \cdot 10^{10} \text{ wt} \cdot \text{cm}^{-2}$)

Analysis of the data obtained for various admixtures and mixture compositions in the threshold (Fig. 3, Table 1) and in the quasi-linear on density regions (Fig. 4) unambiguously suggested the cooperative (binary) mechanism of bss. Strong spectral selectivity (lowering to zero for $\lambda_{\text{pump}} > 308 \text{ nm}$) of nonlinear reflection was observed in Xe+CF₂Cl₂ mixture, for pure Xe selectivity was not found.

Table 1. Bss threshold binary density conditions for (Xe+M) gas mixtures, $I_{\text{pump}} \approx 4 \cdot 10^{10} \text{ wt} \cdot \text{cm}^{-2}$.

M	$(\rho_{\text{Xe}} \cdot \rho_{\text{M}})_{\text{th}}, \text{ Amagat}^2$
Ar	2300
O ₂	>3600
Kr	1200
CF ₂ Cl ₂	20
CF ₃ Cl	60
CF ₃ Br	66
CF ₃ H	>120
NF ₃	>100

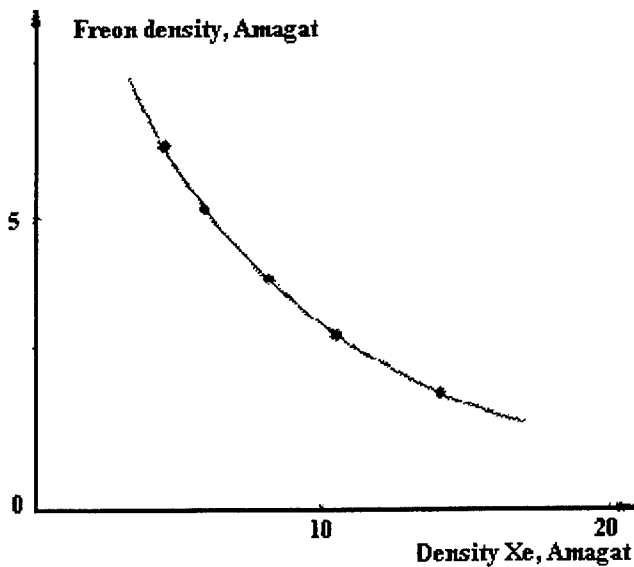


Figure 3. Bss threshold density conditions for Xe:CF₂Cl₂ mixture ($I_{\text{pump}} \approx 4 \cdot 10^{10} \text{ wt}\cdot\text{cm}^{-2}$)

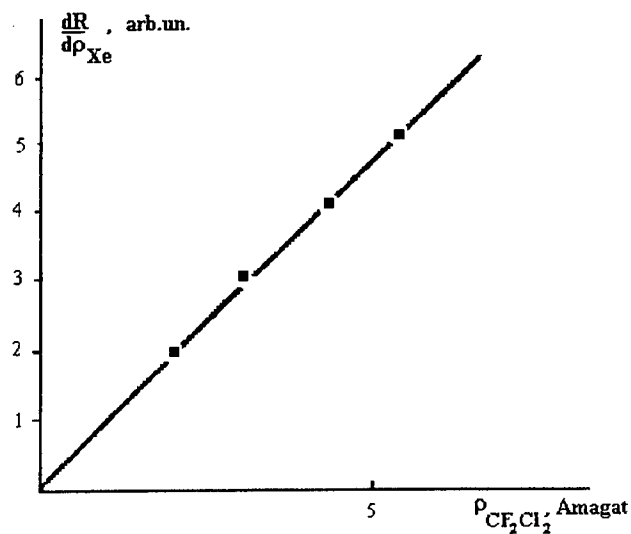


Figure 4. The effect of CF₂Cl₂ concentration on the slope of quasi-linear region of $R(\rho_{\text{Xe}})$ dependence (See Fig. 2), $I_{\text{pump}} \approx 4 \cdot 10^{10} \text{ wt}\cdot\text{cm}^{-2}$.

The data on the pump intensity dependences of nonlinear reflection and photo-acoustic signal are presented in Fig. 5. Very close to the second order dependence of S_{pa} is seen, for E_{bss} some deviation, more pronounced for lower gas density demonstrate the threshold effect. It should be mentioned, that when pure Kr ($\rho \sim 80$ Amagat) was studied under the same pump conditions, ~ 6 times lower, but also quadratic in intensity photo-acoustic signals were detected.

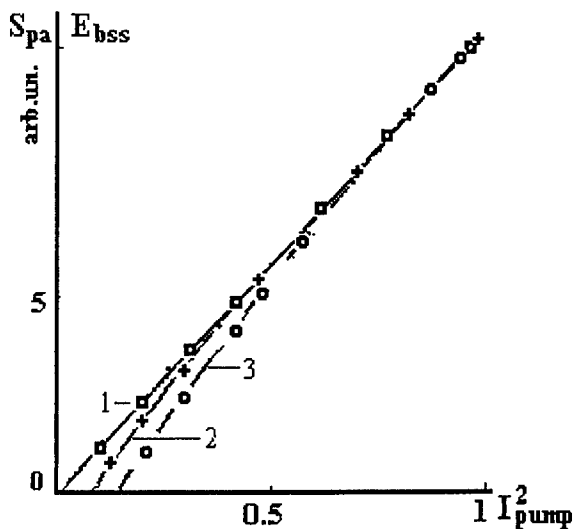


Figure 5. The dependence of the amplitude of photoacoustic signal S_{pa} (1) and reflected pulse energy E_{bss} (2,3) on pump conditions, $I_{\text{pump}}^{\text{max}} \approx 4 \cdot 10^{10} \text{ wt}\cdot\text{cm}^{-2}$, $\lambda = 308 \text{ nm}$. 1,2 - $\rho_{\text{Xe}} = 50$ Amagat, 3 - $\rho_{\text{Xe}} = 45$ Amagat.

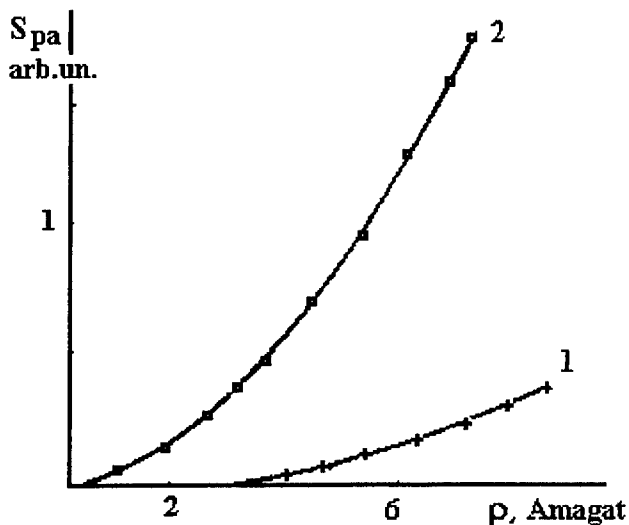


Figure 6. The influence of the freon-12 admixture on the amplitude of the photoacoustic signal S_{pa} . 1 - Xe, 2 - Xe+CF₂Cl₂ mixture, 7:1 vol., $I_{\text{pump}} \approx 4 \cdot 10^{10} \text{ wt}\cdot\text{cm}^{-2}$, $\lambda = 308 \text{ nm}$.

On the basis of observations of close to second order pump intensity dependences of studied nonlinear effects it was believed initially that two-photon laser-assisted reactions [4] were induced under our experimental conditions, and strong

optical nonlinearity of mediums was created by produced excimer molecules. One more possible channel of their formation is ions recombination [5], but, to the best of our knowledge, it was observed either at discharge conditions or at two-photon optical excitation of rare gas atoms by frequency tunable laser source [4]. To realize properly what channel is valid spectral study of strong secondary emission from the caustic zone in 250÷500 nm region has been done using OMA. Emission spectra for pure Xe and (Xe+CF₂Cl₂) mixture were obtained at different pump conditions (Fig. 7). Strong broad emission bands $\lambda_1 \approx 460$ nm and $\lambda_2 \approx 230$ nm (the second band is not seen in Fig. 7 due to high-frequency cut-off filter used in this experiment to decrease the level of scattered pump radiation) observed in pure Xe may be firmly attributed to density broadened lines of ionized xenon [6]. It should be mentioned, that free electrons can obtain energy ≥ 10 eV in dense rare gases under the influence of focused laser radiation [7], in addition their concentration at the same conditions may increase with multiplication factor $\sim 10^5$ [8]. Thus, the second channel of excimer molecules formation may be realized in our experimental conditions. Indeed, in emission spectra of mixture strong additional band ($\lambda=345$ nm) is clearly seen, it has to be attributed to XeCl (C-A, B-A) transitions [5]. The pump intensity dependence of this emission band is close to the second order.

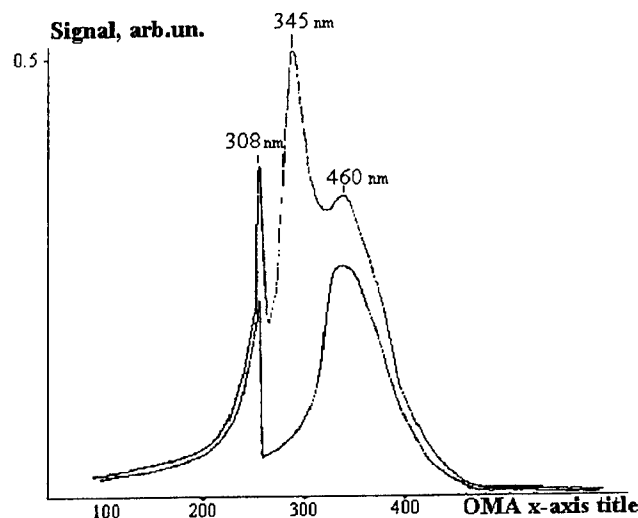


Figure 7. Nonlinear right angle emission, 1- Xe, 50 Amagat, 2- Xe+CF₂Cl₂ mixture, 1:4 vol , density 16 Amagat, $I_{\text{pump}} \approx 2 \cdot 10^{10} \text{ wt} \cdot \text{cm}^{-2}$, $\lambda = 308 \text{ nm}$.

4. CONCLUSIONS

Strong frequency selective nonlinear reflection of laser radiation in Xe-containing gas mediums was observed, when Cl, Br-containing freons were added. For linearly polarized laser radiation ($\lambda=308$ nm) reflectivity up to $\sim 80\%$ at the intensity $\sim 10^{11} \text{ wt} \cdot \text{cm}^{-2}$ was achieved. Emission of XeCl excimer molecules was detected in mixtures with CF₂Cl₂. These results may be useful in creating of new high pressure gas lasers and reflective laser optics.

REFERENCES

1. A.P.Burtsev, *Nonlinear laser mirror on the basis of liquefied molecular gas SF₆*, Abstracts of International conference Applied Optics-96, p.247 (in Russ.), St.-Petersburg, September 1996.
2. V.V.Bertsev, M.O.Bulanin, A.A.Pastor, *Stimulated scattering of XeCl and KrF excimer laser radiation by inert gas fluids*, Opt.Comm., vol.77, p.71-74, 1990.
3. M.A.O'Key and M.R.Osborne, *Broadband stimulated Brillouin scattering*, Opt.Comm., vol.89, pp.269-275, 1992.
4. J.K.Ku, G.Inoue, D.W.Setser, *Two-Photon Laser-Assisted Reaction with Xe/Cl₂ To Form XeCl* and with Xe/Icl To Form XeCl* and Xel**, J. of Phys. Chem., vol.87,N16, pp.2989-2993, 1983.
5. A.Schwabedissen et al., *Experimental verification of a zero-dimensional model of the kinetics of XeCl* discharges by XeCl*(B)-, XeCl*(C)-, and Xe₂Cl*-density measurements*, Applied Physics B, B61, pp.175-186, 1995.

6. A.K.Shuaibov, *Production Conditions and Optical Properties of a Streamer Corona in Working Media of Electric-Discharge XeCl* and KrCl* lasers*, (In Russ.) Opt. Spectrosc., 88, N5, pp.875-879, 2000.
7. N.B.Delone, V.P.Krainov, *Atom in strong light field* (in Russ.), Moscow, 1978.
8. Mayer Guy, *Laser induced multiplication and visualization of free electrons in dense monoatomic gases*, Nucl. Instrum. and Meth. Phys. Res., A254, N1, pp .100-110 , 1987.

Nonlinear absorption and laser-induced damage of BaF₂, CaF₂ and Al₂O₃ at 248 nm

N.V.Morozov, P.B.Sergeev

P.N. Lebedev Physical Institute,
Leninsky Prospect, 53, Moscow, 117924, Russia

ABSTRACT

Transmission dependencies of optical materials samples BaF₂, Al₂O₃ and CaF₂ (the infrared range sample) from KrF-laser radiation intensity with pulse duration of 85 ns are experimentally received. From these dependencies, two-photon absorption coefficients at laser wavelength 248 nm are found which for the appropriate materials are equal to 0.5 ± 0.2 , 2 ± 1 and 30 cm/GW. Laser damage thresholds of the surface and volume of the investigated samples at 248 nm are also determined.

Keywords: optical materials, laser damage, two-photon absorption

1. INTRODUCTION

For manufacturing optical elements of excimer KrF-lasers the crystals MgF₂, CaF₂, and also fused silica are widely used. On behavior of these optical materials (OM) under action of intensive laser radiation (LR) with quantum in 5 eV an extensive file of the experimental information has been accumulated. For specification of a physical picture of the interaction of the UV range LR with the crystals of the alkaline earth metal fluorides and oxides it is typically to expansion of a circle of tested materials. With this purpose the given work on study of behavior of the crystals BaF₂, CaF₂ and sapphire (Al₂O₃) under LR action with the wavelength 248 nm was put. The received transmission dependencies of these materials from LR intensity (I) in the range ~ 10 - 500 MW/cm² allowed to determine the nonlinear absorption coefficient factor (β). Laser damage thresholds are also determined. These data naturally supplement the results on behavior of crystals LiF, MgF₂, CaF₂ and line of grades of fused silica at similar irradiation conditions [1-3]. And together with results on absorption induced by an electron-beam of the UV-range LR in listed crystals at the same duration 80 ns [4] we receive an extensive complex of experimental data.

2. EXPERIMENTAL DESCRIPTION

The work was carried out on electron-beam laser installation ELA [5]. The KrF-laser in the experiments provided energy at a level 3J for pulse duration 85 ns. From the whole laser beam by diaphragm with the diameter 2 cm is cut out a part with energy ~ 0.8 J. This radiation was focused by a lens with focal length 1 m. The distribution of the energy on caustic of a lens was carried out by direct measurements of LR energy, run through diaphragms of the known size, having been located in focus of a lens [2].

The LR divergence had large asymmetry on two perpendicular directions: $\theta_1=0.7$ and $\theta_2=1.6$ mrad. At such parameters of radiation and lens the caustic length exceeded 30 mm. The thickness of the tested samples was no large than 18 mm. Average on the cross-section of lens caustic the LR intensity was determined under the formula $I_x = E_x / S \cdot \tau$, where E_x - energy of laser radiation with a pulse duration $\tau=85$ ns, $S=(\theta_1\theta_2) \cdot f^2$ - area of caustic cross-section in which is contained $0.65 E_x$.

Falling and passing through samples the LR energy was measured in calorimeters. The form of the laser power pulses was supervised with the help of photocells. The typical oscillogrames are shown on fig. 1. The required change of laser intensity was carried out by introduction in a path of a laser beam weakening light filters with transmission up to 5%.

Integrated for a pulse the transmission of samples (T) was defined from the expression $T=O_1/O_0$, where O_1 and O_0 are the indications of calorimeters measured passing and falling energy of LR in a pulse at presence of a sample in focus of a lens (1) and without it (0). The meanings of points $T(I)$, submitted on the diagrams, for a specific sample were obtained by averaging values of T in not less than 5 measurements. The values $T(0)$ were taken from spectrograms.

The laser damage thresholds of samples were determined on a standard technique. The laser beam was limited in this case by the diaphragm with a hole diameter 1 cm. For focusing of this radiation in samples a lens with $f=10$ cm was used.

As the laser damage threshold (E_d) was accepted the maximum density of LR energy in the area of lens caustic, run through a crystal without its destruction. The laser damage intensity was found from expression $I_d=E_d/t$. The presence of the damage in a pulse was registered on a complex of attributes: on visually observable powerful luminescence from irradiated area of the sample; on residual destruction, well visible in light of the He-Ne-laser; on sharp jump in value O_1 in comparison with predamage value. In all experiments, as on study of dependence $T(I)$, and at determination of the laser damage thresholds, each impulse of the laser was carried out on new, not irradiated earlier, site of a sample.

3. EXPERIMENTAL RESULTS ON BaF_2 and CaF_2

The experimental transmission dependencies of the four different samples BaF_2 from radiation intensity of the KrF-laser are submitted on fig. 2. In area $I < 100$ MW/cm² the each sample has individual dependence $T(I)$. At higher I the values T at different samples are closed at inclined direct, describing behavior $T(I)$ of the best samples of the mark FBU in the whole range I . On an inclination of dependence $1/T$ it is possible determine nonlinear absorption of LR in OM[6,7]. Our accounts on the given technique have shown, that at samples of the mark FBU the values of two-photon absorption coefficient are $\beta=0,5\pm 0,2$ cm/GW. The similar result for BaF_2 , but for pulses with duration 25 ns was received in [8].

The range, submitted on fig. 2, of the LR intensities was from above limited by the surface damage of crystals. At the most transparent samples of BaF_2 (O1 and O4) damage was observed at $260\div 270$ MW/cm². We shall note, that it in the case, when the area of the caustic cross-section (on a level $0,65\cdot E_L$) is equal 2 mm² and pulse duration is 85 ns. The quality of polishing of the crystal surfaces corresponded to 3 class of cleanliness. The surface damage was accompanied and volume damages as the black dot clots lengthways the caustic. Therefore at the area irradiation ~ 1 mm² the thresholds of the volume damage and surface damage for best samples of BaF_2 at 248 nm in limits of accuracy of measurement coincide and are equal 250 ± 50 MW/cm².

At research of the volume damage with use of the short-focus lens with $f=10$ cm, when the area of caustic cross-section was equaled $0,02$ mm², maximum of the damage threshold for tested samples of the mark FBU has made 800 MW/cm². This estimated value I_d is received that the transmission of the samples BaF_2 with thickness 18 mm in the predamage mode was equaled $0,35 \div 0,40$. The value of the LR energy in area of the caustic bottleneck at the laser damage was taken as average between input and output energy of the laser radiation. Absence of change of distribution of the LR intensity on caustic cross-section of a lens was also supposed at propagation of light on a crystal. If the value I_d were determined on input energy, it would be $1,2$ GW/cm².

For the samples BaF_2 of the marks FBI at the given focusing mode with the of cross-section area $0,02$ mm² the values I_d were almost the same, as well as on a large spot: $250 \div 300$ MW/cm². The transmission of these samples at damage threshold was 0,8.

A series of experiments on the influence of radiation of the ArF-laser with the pulse duration 70 ns on samples BaF_2 of the best quality (O1, O4) was also carried out. The surface damage at irradiation spot 6 mm² at 193 nm was observed at laser intensities about 20 MW/cm². At these intensity the transmission of our samples in limits of an error of measurement (1,5 %) did not differ from initial (72 %), that has not allowed to establish value of nonlinear absorption.

On Fig. 3 the dependence $T(I)$ for a crystal CaF_2 of the mark FKI (calcium fluoride for IR area) with the initial transmission 0,72 at 248 nm is submitted. On high quality samples CaF_2 (calcium fluoride for UV area) the results of our measurements are submitted in [1]. At them the values β do not exceed $0,1$ cm/GW, and laser damage in a spot with a diameter of $\sim 0,1$ mm is observed at intensities ~ 1 GW/cm². For investigated of a sample FKI the value β is equal 30 cm/GW, and laser damage (simultaneously both surface, and volume) was observed already at the laser intensities ~ 50 MW/cm². This example shows strong difference in behavior of the samples CaF_2 and BaF_2 of the mark FKI under action of the KrF-laser radiation.

4. EXPERIMENTAL RESULTS ON Al_2O_3

In the given experiments two samples Al_2O_3 were investigated. They had the form of disks with diameter of 60 mm and thickness 11 mm. Their surfaces were polished on 4 class of cleanliness. In end faces of disks two small flat platforms parallel each other were polished. They were used for introduction of LR in volume of a material in experiments on laser strength. Based on transmittance, the material of disks has extreme high cleanliness [9]. For the first the transmittance at 248 nm was 71 %, for the second - 67 %.

The received dependencies $T(I)$ for two samples of Al_2O_3 are submitted on Fig.4. At the first sample the behavior of the transmission in the field of low intensities has sharp nonlinearity. At the second sample T almost is constant at low intensities ($I < 50 \text{ MW/cm}^2$), and at $I > 50 \text{ MW/cm}^2$ T practically coincides with the transmission of the first sample. On an average inclination of dependencies $1/T(I)$ the coefficient of nonlinear absorption in Al_2O_3 at 248 nm was found: $\beta = 2 \pm 1 \text{ cm/GW}$.

The top limit of a range of intensity, as well as in a case with BaF_2 , was limited by damage of the input surface. At tested in the given experiments samples Al_2O_3 the damage of the output surface was observed already on 250 MW/cm^2 . Earlier on other samples of sapphire with better quality of processing of a surface we observed higher surface damage thresholds at a level 800 MW/cm^2 [1].

The laser strength of the samples Al_2O_3 was investigated at focusing of radiation in the material volume through their end face. The sapphire thickness in this direction was 57 mm. In the given experience the limiting power density of radiation in focus reached 20 GW/cm^2 . At such parameters of the output radiation, the energy, run through samples, was 20 % from the input energy. In spite of the strong luminescence of a material the mechanical damages in it was not observed. Assuming, what no less than half the energy of radiation was absorbed at the approach to focus, it is possible to consider, that the damage threshold of Al_2O_3 at 248 nm with pulse duration 85 ns is not lower 10 GW/cm^2 .

5. DISCUSSION OF RESULTS AND CONCLUSIONS.

The values of coefficients of the two-photon absorption at 248 nm with the pulse duration of the laser radiation 85 ns as at BaF_2 , and at Al_2O_3 exceed the β , measured at the ps pulse duration [6,10] in 5-10 times. To explain it is possible so [11].

Under irradiation of crystals by intensive UV LR due to two-photon ionization (β have magnitudes, determined from experiments with the ps pulses) in them will be formed electron-hole pairs. In case of a long (~100 ns) pulse the relaxation of the electron-hole pairs results in formation of various defects, which during the life have time to absorb and to convert to a heat yet on a few quanta of LR, as explains increase of nonlinear absorption in the given mode.

Important parameter of process of LR absorption in a mode of a long pulse is life time of the absorbing component [2,4,11]. The absence observed in the conducted experiments of appreciable change of the pulse shape of LR, run through samples, at wide change of values of the laser intensity indicates that the life time of the basic absorbing centers as in BaF_2 , and in Al_2O_3 , doesn't exceed 10^{-9} s. Such times of relaxation have autolocated excitons and weakly separated pairs of Frenkel defects [12]. Consequently the analysis of any process, connected to absorption of the intensive UV laser radiation with the long pulse in crystals, demands the account of kinetics of the given complexes.

In more details questions of modeling of UV LR interaction with ionic crystals are considered in work by S.V.Kurbasov, P.B.Sergeev "SIMULATION OF MECHANISMS CAUSING A NONLINEAR ABSORPTION OF UV LASER RADIATION IN IONIC CRYSTALS", which is represented at the given conference

The submitted results on BaF_2 and Al_2O_3 together with the similar data on MgF_2 , CaF_2 and SiO_2 create an extensive base of experimental data on which it is possible to debug theoretical models of interaction of the intensive radiation of the UV lasers with optical materials.

The work is carried out at the support of the Russian Fund for Fundamental Research, grant N98-02-16562.

REFERENCES

1. V.S.Barabanov, N.V.Morozov, S.I.Sagitov, P.B.Sergeev, "Optical Materials and Coatings for Excimer Lasers", *Journal of Soviet Laser Research*, **14**, 294 (1993).
2. A.V.Amosov, V.S.Barabanov, S.Yu.Gerasimov, N.V.Morozov, P.B.Sergeev and V.N.Stepanchuk, "Optical breakdown of quartz glass by XeF laser radiation", *Quant.Electr.*, **24**, 307 (1994).
3. A.V.Amosov, V.S.Barabanov, S.Yu.Gerasimov, N.V.Morozov, P.B.Sergeev and V.N.Stepanchuk, "Optical breakdown and nonlinear absorption of a quartz glass at 353, 248 and 193 nm", *Izvestiya RAN. Seriya physycheskya (Moscow)*, **58**, 102 (1994).
4. V.S.Barabanov, P.B.Sergeev, "Electron-Beam-Induced absorption of ArF, KrF, and XeF laser radiation in optical materials", *Quantum Electronics*, **25**, 717 (1995).
5. P.B.Sergeev "Electron-Beam Noble-Gas Halide Lasers with High Excitation Level", *J.of Soviet Laser Research*, **14**, 237 (1993).
6. V.Nathan, A.N.Guenter, S.S.Mitra, "Review of multiphoton absorption in crystalline solids", *J.of the Optical Society of America*, **B2**, 294 (1985).
7. A.F.Gibson, C.B.Hatch, P.N.D.Maggs, D.R.Tilley and A.C.Walker, "Two-photon absorption in indium antimonide and germanium", *J.Phys.C: Solid St.Phys.*, **9**, 3259 (1976).
8. K.Mann, E.Eva, B.Granitza, "Characterization of absorption and degradation on optical components for high power excimer lasers", *Proc.SPIE* **2714**, 2 (1995).
9. M.I.Musatov, E.A.Sidorova, B.G.Ivanov, "Optical transparency of large sapphire crystals", *Sov. J. Opt.Technol.* **44**, 96 (1977).
10. A.J.Taylor, R.B.Gibson, J.P.Roberts, "Two-photon absorption at 248 nm in ultraviolet window materials", *Optics Lett.*, **13**, 814 (1988).
11. P.B.Sergeev, "Avalanche-type mechanisms of ionic crystals destruction at UV and VUV laser radiation influence", *Bulletin of the Lebedev Phys.Inst.* №5, 39 (1999).
12. Ch.B.Lushchik, A.Ch.Lushchik, "Decay of Electronic Excitations with Defect Formation in Solids", (in Russian), Moscow, Nauka, 1989.

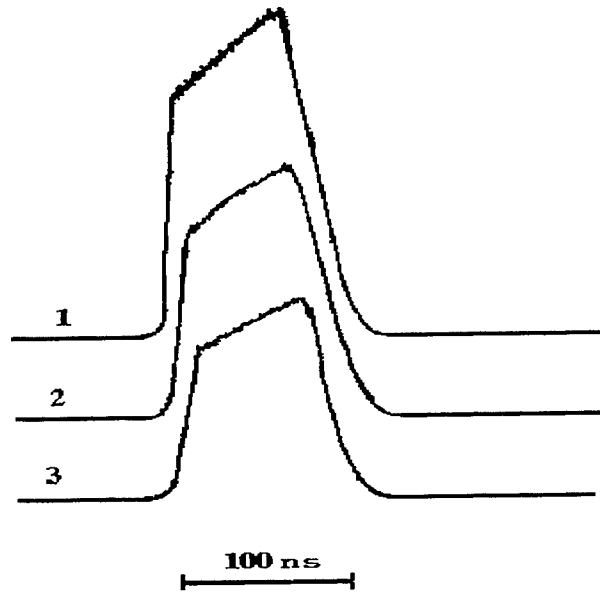


Fig. 1. The typical oscillogrames of the power pulses of KrF-laser radiation falling on samples (1) and run through samples BaF₂ (2) and Al₂O₃ (3).

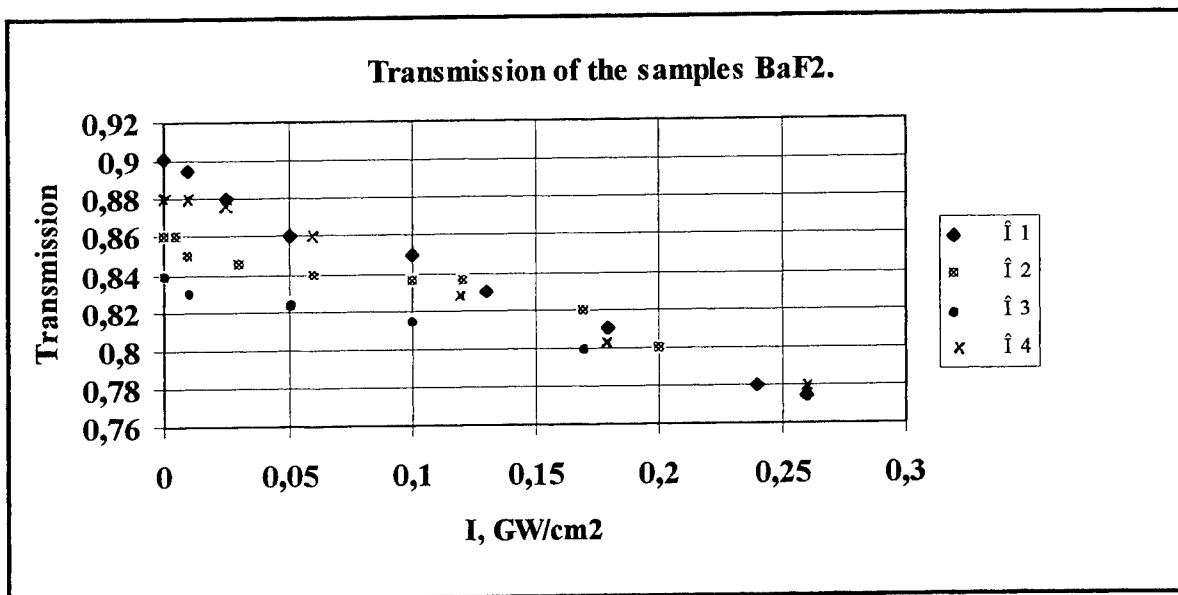


Fig. 2. The Transmission of the samples BaF₂ with thickness 18 mm at various intensities of the KrF-laser radiation.

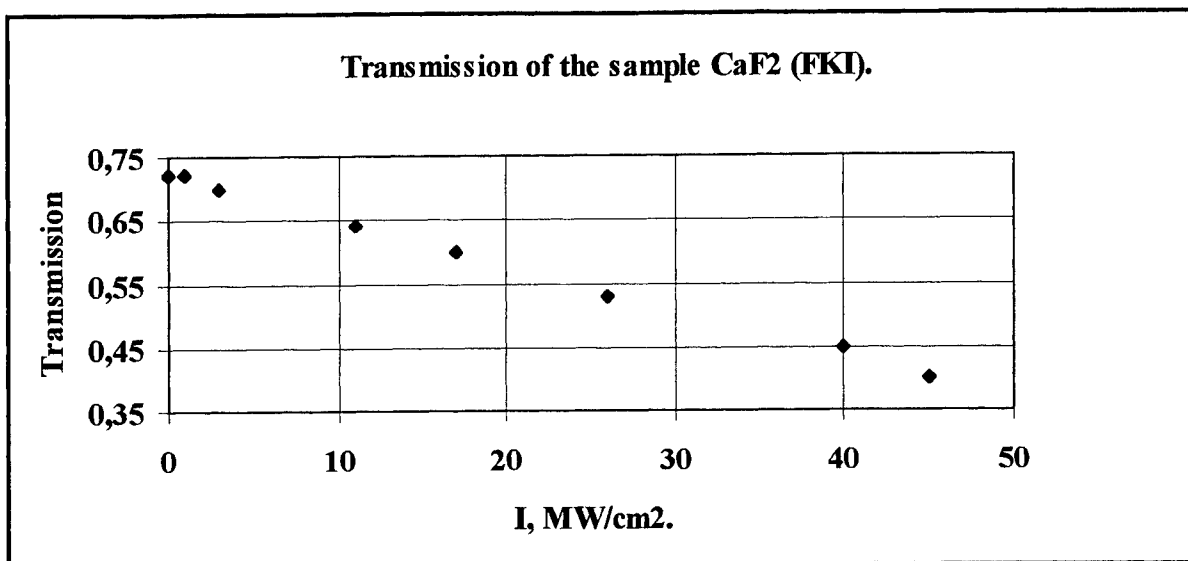


Fig.3. The transmission of the sample CaF₂ with thickness 11 mm at various intensities of the KrF-laser radiation.

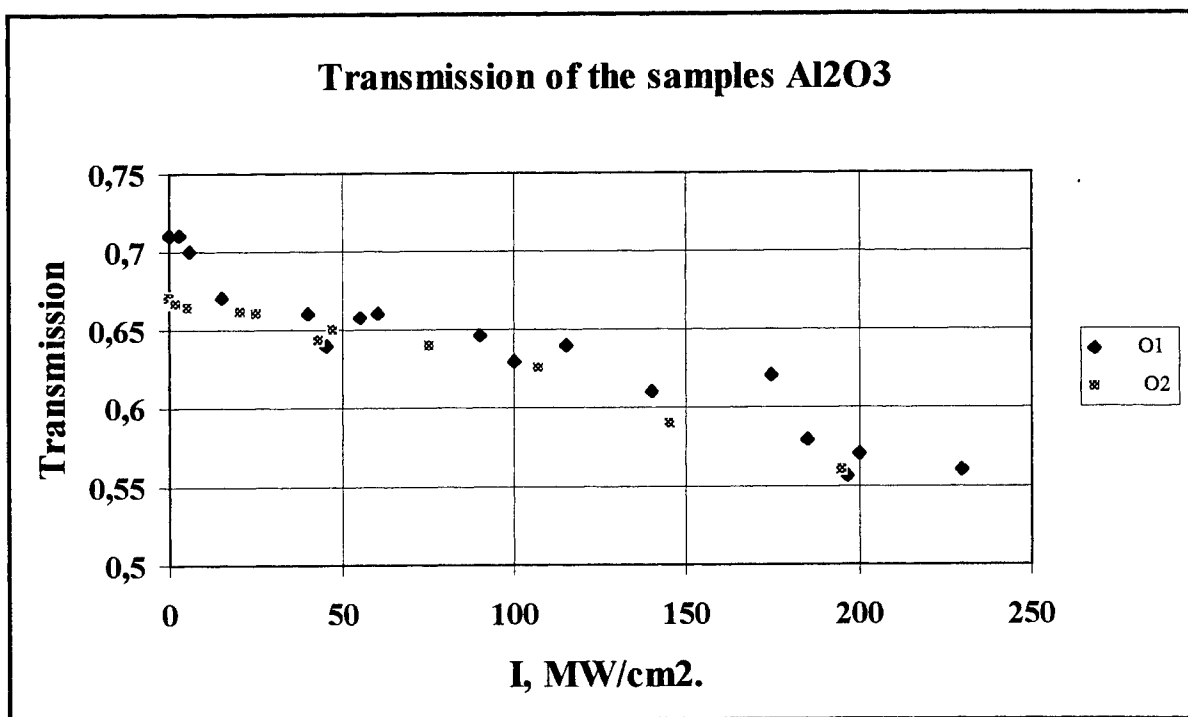


Fig.4. The transmission of the samples Al₂O₃ with thickness 11 mm at various intensities of the KrF-laser radiation.

SIMULATION OF MECHANISMS CAUSING A NONLINEAR ABSORPTION OF UV LASER RADIATION IN IONIC CRYSTALS

Sergey V. Kurbasov, Paul B. Sergeev

P.N. Lebedev Physical Institute,
Leninsky Prospect, 53, Moscow, 117924, Russia.

ABSTRACT

In the work two models describing interaction of UV laser radiation (LR) with ionic crystals are considered. In the first version the wavelength of LR lies in absorption region of F centers, in the second - it is in a short-wave area of H centers absorption wing. It is shown, that the photodissociation in crystals of F_2^- complexes on two holes is the effective mechanism of defects formation in a crystalline structure. The account of these and other electronic excitation relaxation processes in models allows to explain many experimental results of LR action on ionic crystals.

Keywords: nonlinear absorption, ionic crystals, colour centers.

INTRODUCTION

The crystals of MgF_2 and CaF_2 are transparent for radiation with the energy of photons up to 11 and 10 eV correspondingly. They are widely used for manufacturing of many optical elements for excimer, and other UV lasers. In VUV range MgF_2 practically remains the only rather reliable material for laser output windows. However, as well as with other optical materials (OM), the transparency of these crystals falls at operation in an intense short-wavelength laser radiation (LR) [1-2]. The basic reason is the creation of point defects during a relaxation of electronic excitations (EE), originating in an outcome of a nonlinear absorption of LR [3-5].

In alkaline earth fluoride crystals the action of ionizer is exhibited basically on an anions sublattice. Free electrons and holes arise here. The relaxation of a potential energy of this electron-hole pair flows past on levels of excitons and two pairs Frenkel's defects. These are α , I and also H and F centres. Each of these defects has an own structure of absorption spectrum and, except for basic, series of intermediate electronic levels with own lifetime [3-5].

It is obvious, that for description of a behaviour of the induced absorption of these crystals at different conditions of ionizing and LR action, it is necessary to take into account a great number of interconnected processes. That results in necessity of use of the numerical methods of simulation.

The purpose of the given work is determination of the principal parameters of EE relaxation processes in these crystals at an action of ultraviolet LR on the base of numerical simulation. Two variants of numerical models are represented here. In the first case LR photons energy corresponds to band of F-centers, in the second it is at an absorption band of H-centers.

ABSORPTION OF LASER RADIATION BY F CENTERS

At an exposure of MgF_2 , CaF_2 and BaF_2 crystals by e-beam strong bands of absorption with centers at 275, 400 and 600 nm and half-width of ~ 100 nm arise in them. This absorption is assigned to F-centers [3-6]. However an attempt to describe it by two-level approximation fails. The matter is that for this absorption band the whole hierarchy of lifetimes with magnitudes from $\sim 10^{-9}$ s up to ~ 1 s is observed.

It is explained by the fact that during formation of Frenkel's defects the important stage of an electron-hole pair relaxation are self-trapped excitons (STE), formed by capture of electron by a V_k -center. They have two ground states: singlet (S_1) and triplet (S_3). The absorption both at S_1 and at S_3 (σ_5 and σ_6) practically coincide with an absorption cross-section of stable F-centers (σ_9). Thus it is possible to present STE as a pair of F- and V_k -centers with very low spatial separation and exhibiting their own structure of absorption spectrums which are close to the absorption of stable defects.

At an absorption of quantum a F-center and also electronic component STE pass in one of excited states (F^* and S^*) laying close to an ionization threshold. These states, having large sizes, have also large possibility to grasp in an orb of the action a conjugate center and to relax with him.

The submitted above experimental facts and their interpretation have defined the list from 11 electronic states

requiring the account at the analysis of processes of ionizing and LR action on crystals. In gas-kinetic approximation these states can be considered as a particle, and their interaction with each other and with LR can be described by a system of the linear differential equations for concentration of components. For a case, when LR hits in a band of F-centers absorption, from many checked most acceptable there was a following system of the kinetic equations.

1. $dn/dt = W_1 + (K_{811}F^* + K_{911}F)I + (\sigma_4 S^* + \sigma_8 F^*)J - (K_{13}V_k + K_{17}H + K_{110}\alpha)n$;
2. $dp/dt = W_1 + \sigma_{10}\alpha J - p/\tau_2$;
3. $dV_k/dt = p/\tau_2 + \sigma_4 S^* J - (1/\tau_3 + K_{13}n)V_k$;
4. $dS^*/dt = \beta J^2 + K_{13}nV_k + (\sigma_5 S_1 + \sigma_6 S_3)J - 1/\tau_4 + K_4 n + \sigma_4 J S^*$;
5. $dS_1/dt = X_{45}(1/\tau_4 + K_4 n)S^* - (1/\tau_5 + 1/\tau_{57} + K_5 n + \sigma_5 J)S_1 - K_{56}n(S_1 - S_3)$;
6. $dS_3/dt = X_{46}(1/\tau_4 + K_4 n)S^* - (1/\tau_6 + 1/\tau_{67} + K_6 n + \sigma_6 J)S_3 - K_{65}n(S_3 - S_1)$;
7. $dH/dt = V_k/\tau_3 + X_{47}S^*/\tau_4 + S_1/\tau_{57} + S_3/\tau_{67} - (K_{17}n + K_{78}F^* + K_{79}F)H$;
8. $dF^*/dt = K_{110}\alpha n + \sigma_9 F J - (1/\tau_8 + K_8 n + K_{78}H + K_{811}I + \sigma_8 J)F^*$;
9. $dF/dt = X_{47}S^*/\tau_4 + S_1/\tau_{57} + S_3/\tau_{67} + (1/\tau_8 + K_8 n)F^* + \sigma_{10}\alpha J - (K_{79}H + K_{911}I + \sigma_9 J)F$;
10. $d\alpha/dt = V_k/\tau_3 + \sigma_8 F^* J - (K_{110}n + K_{1011}I + \sigma_{10}J)\alpha$;
11. $dI/dt = K_{17}nH - (K_{811}F^* + K_{911}F + K_{1011}\alpha)I$.

The following labels here are used: n and p - concentration of free electrons and holes, W_1 - velocity of ionization, σ_i - the crosssection of absorption by i -that component on wavelength of LR, J - intensity of LR, K_{ij} - a reaction velocity constants between components i and j , τ_i - lifetimes of a components, X_{ij} - exit factors of the appropriate reactions, β - two-photon absorption coefficient.

The radiation of KrF- and ArF-lasers with quanta 5.0 and 6.3 eV gets on different sites of the absorption band of F-centers in MgF₂. Therefore debugging of the model was carried out on the base of comparisons of its predictions with outcomes of a series of experiments first of all on this crystal [7-10].

Major of such outcomes has become preservation of the form of the LR power impulses, past through MgF₂ samples at the moment of their irradiation by e-beam, and also magnitude of the absorption [9]. The preservation of the form of transparent LR impulse testifies to two important moment.

1. The relaxation time of basic absorbed components does not exceed several ns. And it signifies, that the quasi-stationary e-beam induced absorption in a band of F-centers at MgF₂ is stipulated in basic by STE.
2. The stable F and H centers yield does not exceed 5% from full number of STE. Otherwise to an extremity of 80 ns pulse the noticeable raise of an absorption would be observed.

The debugging of the kinetic equations system was carried out on the base of comparisons of its outcomes with experiments on e-beam induced absorption in view of the measured distribution of a specific absorbed doze $D(x)$ about a thickness of a sample [8], which has a view $W_1(x) = D(x)/3TE_g$. Here x - coordinate along a thickness of a sample, T - duration of impulse, E_g - the bandgap of crystal ($3E_g$ - average formation energy of electron-hole pairs). As the intensity of LR in these experiments was ~ 1 MW/cm², the magnitude βJ^2 practically is equal to zero, so a source of EE in crystal is only e-beam.

The optical density was calculated by integration on sample thickness of the induced absorption, received from the equations, $(K_\Sigma = \sigma_4 S^* + \sigma_5 S_1 + \sigma_6 S_3 + \sigma_8 F^* + \sigma_9 F + \sigma_{10}\alpha + \beta J)$ and was compared to experimental meaning. The basic absorption here occurs on S_1 , S_3 and F-centres. To vary the specified parameters of model, receiving agreed with experiment value of optical density and the form of LR impulse (fig. 1), was possible within 20%. The chosen thus values of the included in equation coefficients are reduced below.

$K_{13} = 5 \cdot 10^{-8}$; $K_{17} = 2 \cdot 10^{-8}$; $K_{110} = 3 \cdot 10^{-8}$; $K_4 = 1 \cdot 10^{-7}$; $K_5 = 1 \cdot 10^{-8}$; $K_{56} = K_{65} = 5 \cdot 10^{-8}$; $K_6 = 1 \cdot 10^{-8}$; $K_{78} = 1 \cdot 10^{-10}$; $K_{79} = 1 \cdot 10^{-11}$; $K_8 = 1 \cdot 10^{-7}$; $K_{811} = 1 \cdot 10^{-10}$; $K_{911} = 1 \cdot 10^{-11}$; $K_{1011} = 1 \cdot 10^{-10}$ [cm³s⁻¹].

$\tau_2 = 1 \cdot 10^{-11}$; $\tau_3 = 1 \cdot 10^{-5}$; $\tau_4 = 1 \cdot 10^{-10}$; $\tau_5 = 1 \cdot 10^{-8}$; $\tau_{57} = 6 \cdot 10^{-7}$; $\tau_6 = 1 \cdot 10^{-4}$; $\tau_{67} = 6 \cdot 10^{-7}$; $\tau_8 = 5 \cdot 10^{-10}$ [s].

$\sigma_4 = 2 \cdot 10^{-18}$; $\sigma_5 = \sigma_6 = \sigma_9 = 7 \cdot 10^{-17}$; $\sigma_8 = 2 \cdot 10^{-18}$; $\sigma_{10} = 1 \cdot 10^{-20}$ [cm²].

The data of a value σ_i are taken on $\lambda = 248$ nm.

$X_{45} = X_{46} = 0,45$; $X_{47} = 0,03$.

The behaviour in time of concentration of taken into account components for two modes of an irradiation of samples MgF₂ by e-beam and LR is shown in a fig. 2 and 3.

The check of a model with the submitted coefficients was carried out by a comparison of its predictions with experimental outcomes on a nonlinear absorption of the KrF-laser radiation in MgF₂ [10] at pulse duration of 80 ns. In

this case $W_1=0$, and the magnitude β equals 0,003 cm/GW. This value was obtained at ~ 1 ps pulses [11]. The results of accounts are shown in a fig. 4 and 5.

Thus becomes clear and reason of a raise of a nonlinear absorption at measurements in a condition of 80 ns pulses. Two-photon laser-induced STE and the F centers at long pulse have time to absorb still on some quantum, as explains a raise of a nonlinear absorption in the given condition. Thus "long" it is possible to consider pulses with duration greater, than formation times of basic absorbing centers, in this case STE. On many data these times do not exceed 10^{-10} s.

The similar situation was observed with semiconductors and radiation of infrared lasers [12]. An additional absorption here ensured free electrons. In wide bandgap crystals for UV and, especially, for VUV LR the contribution of free electrons in an absorption sharply falls. The principal role here is played by others quasiparticles, the own electronic transition frequencies of which are close to LR frequency.

The model well describes also experimental results on laser damage of MgF_2 on $\lambda=248$ nm and duration of pulses 80 ns [10]. The account shows, that the crystal at threshold intensities of LR taken from experiment is heated up to melting temperature, that is a criterion of approach of laser damage [3]. Let's mark, that included in the base system of equations the coefficients thus are considered as constants in all range of crystal temperature variation from 300 up to ~ 1600 K. Obviously, that the given assumption requires detailed examine, before the model can be used for quantitative description of a behaviour of investigated crystals in limiting extreme conditions of a LR exposure.

In an inference of the section we shall mark the following prediction of a model. The saturation intensity of LR for the e-beam induced absorption in MgF_2 in a quasistationary condition works out about 8 MW/cm². The experienced check of the given statement can become resolving experiment for a model.

ABSORPTION OF LR BY F_2^- COMPLEXES

With promoting in UV area of a spectrum at crystals behind a band of F-centers absorption the wide bands of V_k and H centers absorption place. These defects represent a molecule F_2^- , localized on two or one of anion lattice nodes and insignificantly differ only by distances between the atoms. And basic, the most strong bands of their absorption were in UV range, practically merge [3-6]. The capture of quantum in this band leads to dissociation of a molecule F_2^- on F^- and free hole [5, p.73], which fast again is localized.

To describe this variant it is possible on the base of above mentioned set of equations after its small modification. It is necessary to take into account, that the absorption crosssection of F centers with increase of quantum energy decreases. A final state of electrons here varies also. This is a conductive zone. Is added, as it was marked, also an absorption on V_k and H centers, and also on a hole component of STE. After absorption of the quantum, in time of a relaxation ~ 100 ps, the centers are restored and absorption process repeats.

With shortening of LR wavelength the kinetics of EE relaxation in crystals keeps marked above singularities so long as energy of quantum will not become enough for translation binding electrons of V_k or H centers on exciton levels, or in conductive zone. In the latter case energy of quantum should be close to E_g . The threshold for transition on exciton levels less and approximately is equal to a difference between E_g and Rydberg energy for the appropriate crystal. At MgF_2 and CaF_2 this energy equals 5-6 eV, and at BaF_2 it is close to 7 eV. We have not while exact information about such transition, though the mentions of them meet [5, p.113].

Formed from F_2^- after electron transition on rather long-lived exciton levels "molecule" F_2 in crystal is unstable. During 10^{-12} s included in it holes scatter, lose the energy and are localized, turning in new V_k , H centers or STE. Here absorption of one rigid quantum reduces in birth of two new absorbing centers. The base system of the kinetic equations in this case can be presented in the following aspect.

1. $dn/dt = W_1 + \beta J^2 + (K_{811}F^* + K_{911}F)I + (\sigma_{41}S^* + \sigma_{51}S_1 + \sigma_{61}S_3 + \sigma_8H + \sigma_9F)J - (K_{13}V_k + K_{17}H + K_{110}\alpha)n.$
2. $dp/dt = W_1 + \beta J^2 + (\sigma_3V_k + \sigma_{10}\alpha)J^2 - p/\tau_2.$
3. $dV_k/dt = p/\tau_2 + (\sigma_{41}S^* + \sigma_{51}S_1 + \sigma_{61}S_3)J - (1/\tau_3 + K_{13}n + \sigma_3J)V_k.$
4. $dS^*/dt = X_{34}K_{13}nV_k + (\sigma_3V_k + \sigma_{52}S_1 + \sigma_{62}S_3 + \sigma_7H)J - [1/\tau_4 + K_{4n} + (\sigma_{41} + \sigma_{42})J]S^*.$
5. $dS_1/dt = X_{45}(1/\tau_4 + K_{4n})S^* + X_5\sigma_{42}S^*J - (1/\tau_{50} + 1/\tau_{57} + K_5n + \sigma_{51}J + \sigma_{52}J)S_1 - K_{56}(S_1 - S_3)n.$
6. $dS_3/dt = X_{46}(1/\tau_4 + K_{4n})S^* + X_5\sigma_{42}S^*J - (1/\tau_{60} + 1/\tau_{68} + K_6n + \sigma_{61}J + \sigma_{62}J)S_3 - K_{65}(S_3 - S_1)n.$
7. $dH/dt = V_k/\tau_3 + X_{47}S^*/\tau_4 + S_1/\tau_{57} + S_3/\tau_{67} + H^*/\tau_{12} + (\sigma_{42}S^* + \sigma_{52}S_1 + \sigma_{62}S_3)J - (K_{17}n + K_{78}F^* + K_{79}F + \sigma_7J)H.$
8. $dF^*/dt = K_{110}\alpha n + (\sigma_{42}S^* + \sigma_{10}\alpha)J - (1/\tau_8 + K_{89}n + K_{78}H + K_{811}I + \sigma_8J)F^*.$
9. $dF/dt = X_{47}S^*/\tau_4 + S_1/\tau_{57} + S_3/\tau_{67} + (1/\tau_8 + K_{89}n)F^* + (\sigma_{52}S_1 + \sigma_{62}S_3)J - (K_{79}H + K_{911}I + \sigma_9J)F.$

$$10. \frac{d\alpha}{dt} = V_k/\tau_3 + (\sigma_8 F^* + \sigma_9 F)J - (K_{110}n + K_{810}H + K_{1011}I + \sigma_{10}J)\alpha.$$

$$11. \frac{dI}{dt} = K_{17}nH - (K_{811}F^* + K_{911}F + K_{1011}\alpha)I.$$

$$12. \frac{dH^*}{dt} = \sigma_7 H - H^*/\tau_{12}.$$

The equation for H^* (atom F with a large kinetic energy and were between nodes of a lattice) here is added.

The total absorption in this variant is defined as follows:

$$K_{\Sigma} = (\sigma_3 V_k + \sigma_{42} S^* + \sigma_{52} S_1 + \sigma_{62} S_3 + \sigma_7 H) + \sigma_{41} S^* + \sigma_{51} S_1 + \sigma_{61} S_3 + \sigma_8 F^* + \sigma_9 F + \sigma_{10} \alpha + \beta J = \\ = \sigma_3 (V_k + S^* + S_1 + S_3 + H) + \sigma_8 (S^* + F^*) + \sigma_9 (S_1 + S_3 + F) + \sigma_{10} \alpha + \beta J.$$

Here is taken into account, that $(\sigma_3 = \sigma_{32} = \sigma_{52} = \sigma_{62} = \sigma_7)$, $(\sigma_8 = \sigma_{41})$ and $(\sigma_{51} = \sigma_{61} = \sigma_9)$.

The debugging of the given model was carried out by results for CaF_2 and both KrF - and ArF -laser radiation [6-9]. The calculation show, that at intensity of LR more than $0,1 \text{ GW/cm}^2$ a multiple absorption of quanta by each center during long pulse provides the much greater input of an energy into the lattice, than at two-photon absorption.

For demonstration of basic distinctions in behaviour of crystals under action of LR in the first and second model we shall consider the equations for total concentration of quasi-particles (N) except for concentration of free electrons. For this purpose we shall combine the equations of the appropriate systems from second up to last and receive:

$$\frac{dN}{dt} = \beta J^2 - [S_1/\tau_5 + S_3/\tau_6 + 2(K_{78}F^* + K_{79}F)H + 2(K_{811}F^* + K_{911}F)I + 2K_{1011}I\alpha] = \beta J^2 - R \cong \beta J^2 - \mu N^2, \quad (1)$$

$$\frac{dN}{dt} = \beta J^2 + (\sigma_3 V_k + 2\sigma_{42} S^* + 2\sigma_{52} S_1 + 2\sigma_{62} S_3 + \sigma_7 H)J - R \cong \beta J^2 + \sigma_{e2} N J - \mu N^2. \quad (2)$$

Last expressions are received so. The concentration of a components are presented as $k_i N$, where k_i - a part of given component in N . After that we bear from brackets N and N_2 , and the combination, which have stayed in brackets, we shall designate as μ and σ_{e2} .

From (1) is visible, that for the first model in a quasistationary regime $N = (\beta J^2 / \mu)^{1/2}$. In this regime the expression for absorption factor K_{Σ} accepts a kind:

$$K_{\Sigma} = \beta J + \sigma_{e1} N = [\beta + \sigma_{e1} (\beta / \mu)^{1/2}] J = [1 + \sigma_{e1} (\beta / \mu)^{1/2}] \beta J, \quad (3)$$

where σ_{e1} - effective crosssection of absorption on all defects. It is obvious, that the expression in square brackets is a factor showing as far as nonlinear absorption coefficient in a regime of long impulse more appropriate two-photon absorption in a regime of short impulse.

For the second model in a quasistationary regime is received: $N = (\sigma_{e2} / \mu) J$. Then the expression for effective nonlinear absorption accepts a kind:

$$K_{\Sigma} = [\beta + (\sigma_{e2} / \mu) J] J = [1 + (\sigma_{e2} / (\mu \beta))] \beta J. \quad (4)$$

Is obvious, that and here nonlinear absorption for long impulses is much more of two-photon absorption in a regime of short ps impulses. It can explain the large nonlinear absorption at 248 nm in CaF_2 with impurity measured at 80 ns impulses [13].

For each model the own regime of exit of N on stationary meaning is realized at submission of LR impulse of a rectangular form. In the first model on the initial stage N grows linearly. In the second model is observed exponential growth of number of particles, that specifies avalanche-type character of development of LR absorption [14]. But in both cases on a quasistationary sites N linearly depends on LR intensity.

CONCLUSION

Thus in work is shown, that at the description of interaction of an intense short-wavelength laser radiation at impulse more than $\sim 10 \text{ ns}$ with crystals the account of intermediate electronic states arising in crystals at electron-hole recombination is necessary. It is caused by that on such states much more energy is absorbed with what in classical two-photon absorption.

The base of the models, offered in work, is served by the representations, which have usually for today, about processes of formation and relaxation of defects in anion sublattice of crystals. These processes are very similar not only in the considered group of crystals MgF_2 , CaF_2 and BaF_2 , but also in others ionic crystals. In this connection the submitted systems of the kinetic equations after a choice of the appropriate coefficients can be used and for the analysis of experiments on influence of ionizing and laser radiation and on this extensive circle of optical materials.

ACKNOWLEDGEMENTS

The work was supported by the Russian Foundation for Basic Research (grant No.98-02-16562).

REFERENCES

1. T.S. Fahlen, "200-W KrF-gas-transport laser", *IEEE J.QE*, **QE-8**, 1260 (1980).
2. M.Rothschild, D.J.Ehrlich, D.C.Shaver, "Effects of excimer laser irradiation on the transmission, index of reflection, and density of ultraviolet grade fused silica", *Appl.Phys.Lett.* **55**, 325(1989).
3. S.C.Jones, P.Braunlich, R.T.Casper, X.Shen, P.Kelly "Recent progress on laser-induced modifications and intrinsic bulk damage of wide-gap optical materials". *Optical Engin.* **28**, 1039(1989).
4. Williams R.T. "Optically generated lattice defects in halide crystals" *Opt.Engineering.* **28**, 1024(1989).
5. Ch.B.Lushchik, A.Ch.Lushchik, "Decay of Electronic Excitations with Defect Formation in Solids" (in Russian), Moscow, Nauka, 1989.
6. A.M.Stoneham. "Theory of defects in solids".(in Russian) Moscow. Mir, V.2, p.16, 1978.
7. V.S.Barabanov, N.V.Morozov, P.B.Sergeev, "Absorption induced by ionizing radiation in windows of a KrF-laser", *Kvantovaya Elektron.* (Moscow), **18**, 1364(1991).
8. V.S.Barabanov, N.V.Morozov, P.B.Sergeev "Ionizing radiation induced absorption in KrF-laser windows". *Journal of Non-Crystalline Solids*, **149**, 102(1992).
9. V.S.Barabanov, P.B.Sergeev, "Electron-Beam-Induced absorption of ArF, KrF, and XeF laser radiation in optical materials". *Quantum Electronics.* **25**, 717(1995).
10. V.S.Barabanov, N.V.Morozov, S.I.Sagitov, P.B.Sergeev, "Optical Materials and Coatings for Excimer Lasers". *Journal of Soviet Laser Research.* **14**, 294(1993).
11. A.J.Taylor, R.B.Gibson, J.P.Roberts, "Two-photon absorption at 248 nm in ultraviolet window materials", *Optics Lett.*, **13**, 814(1988).
12. A.F.Gibson, C.B.Hatch, P.N.D.Maggs, D.R.Tilley and A.C.Walker "Two-photon absorption in indium antimonide and germanium". *J.Phys.C: Solid St.Phys.* **9**, 3259(1976).
13. N.V.Morozov, V.M.Reiterov, P.B.Sergeev, "Nonlinear absorption and optical strength of BaF₂ and Al₂O₃ at the wavelength of 248 nm". *Quant.Electr.* **29**, 979(1999).
14. N.N.Semenov, Chain reactions. (in Russian) Moscow, Nauka, p.68, 1986.

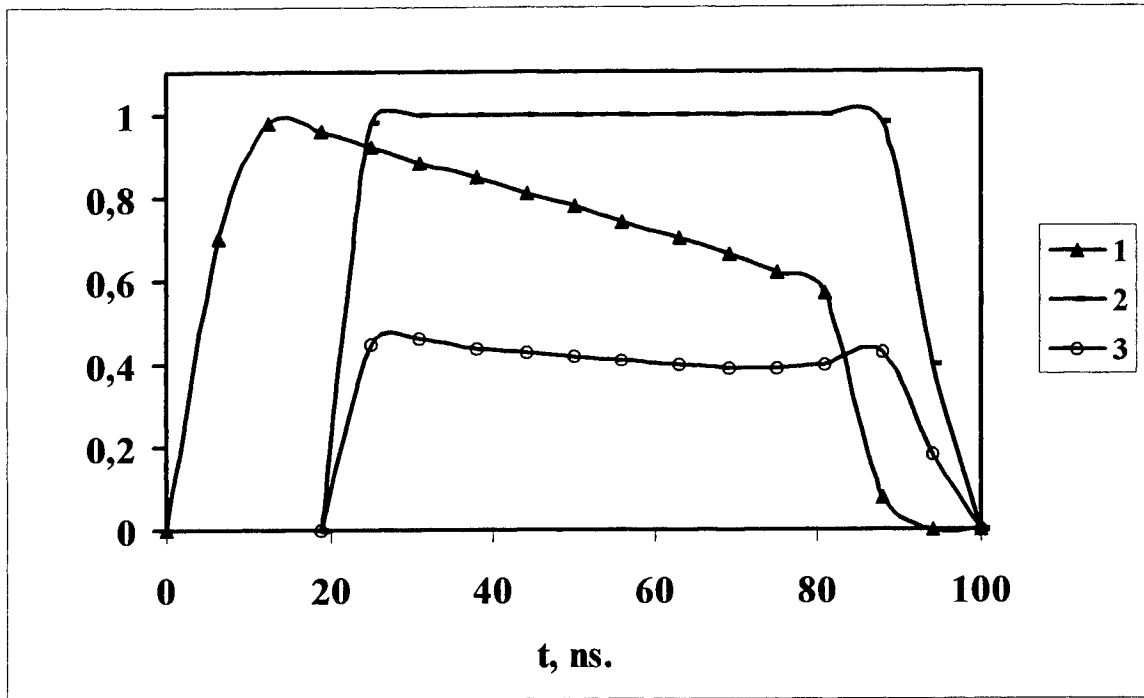


Fig.1. Impulse shape of e-beam power (1), input power of LR (2), output power of LR (3).

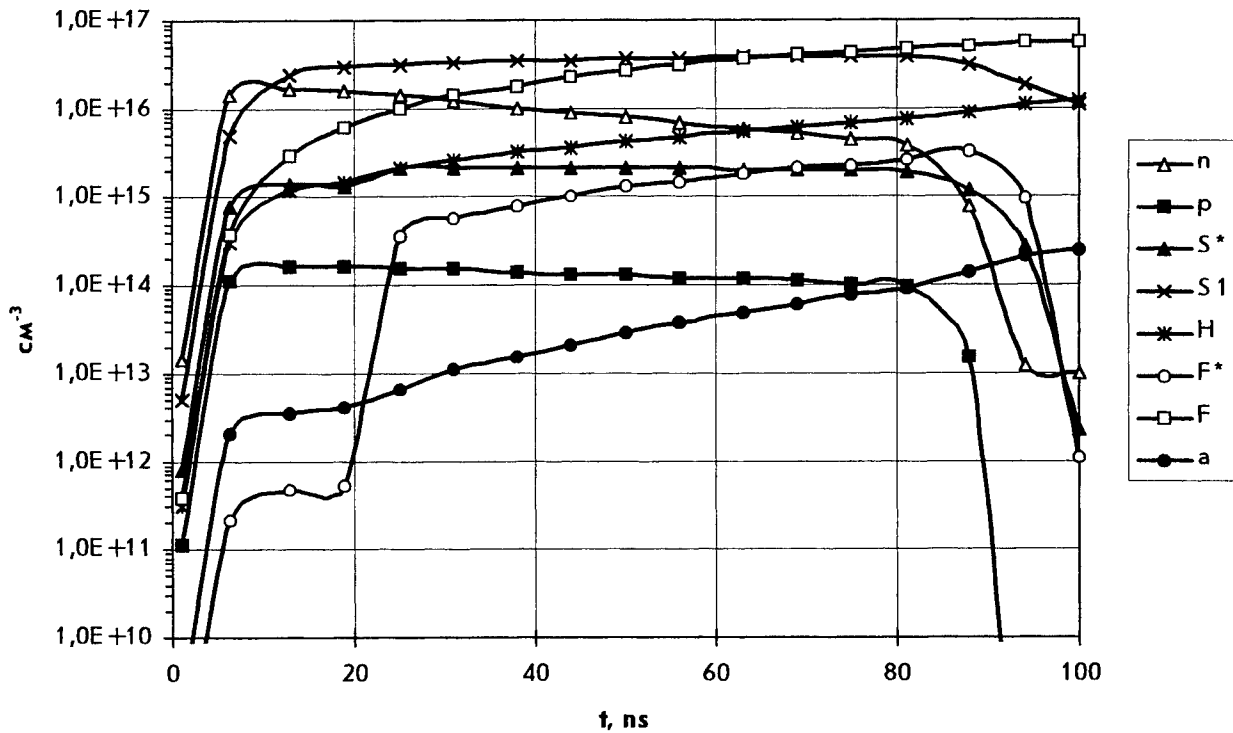


Fig.2. The behaviour of components in MgF_2 at action of e-beam.

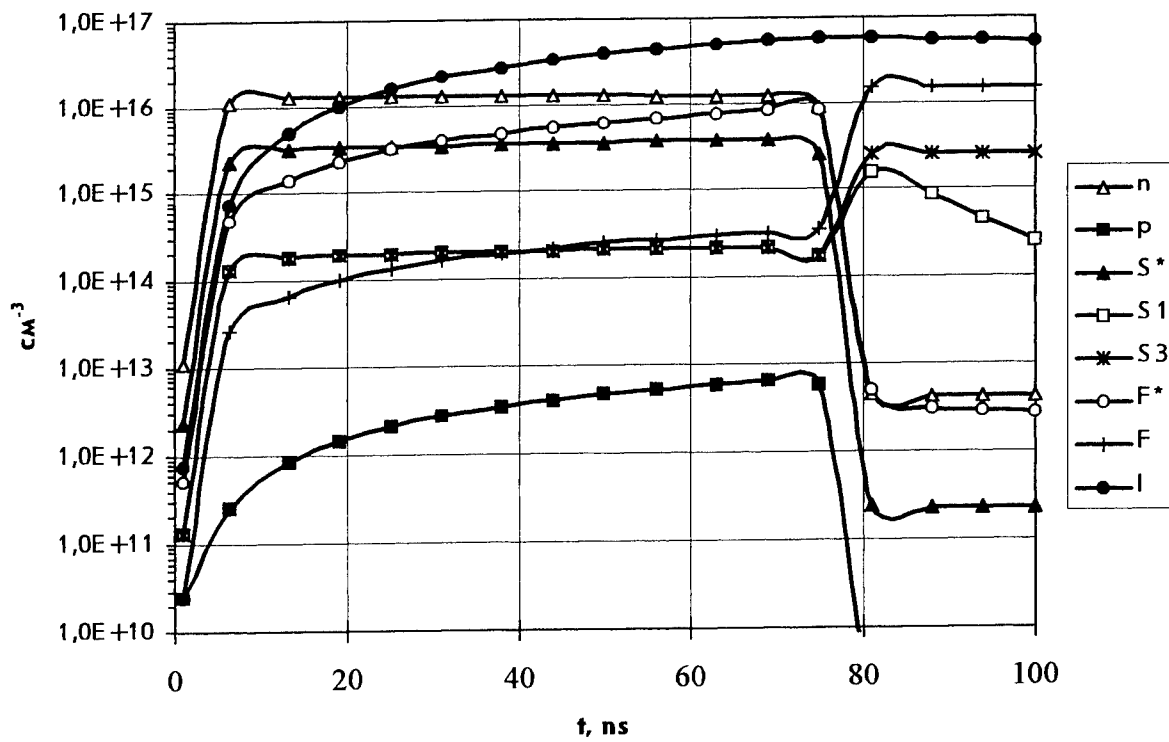


Fig.3. The behaviour of the appropriate components at action on MgF_2 of LR with intensity 1 GW/cm^2 .

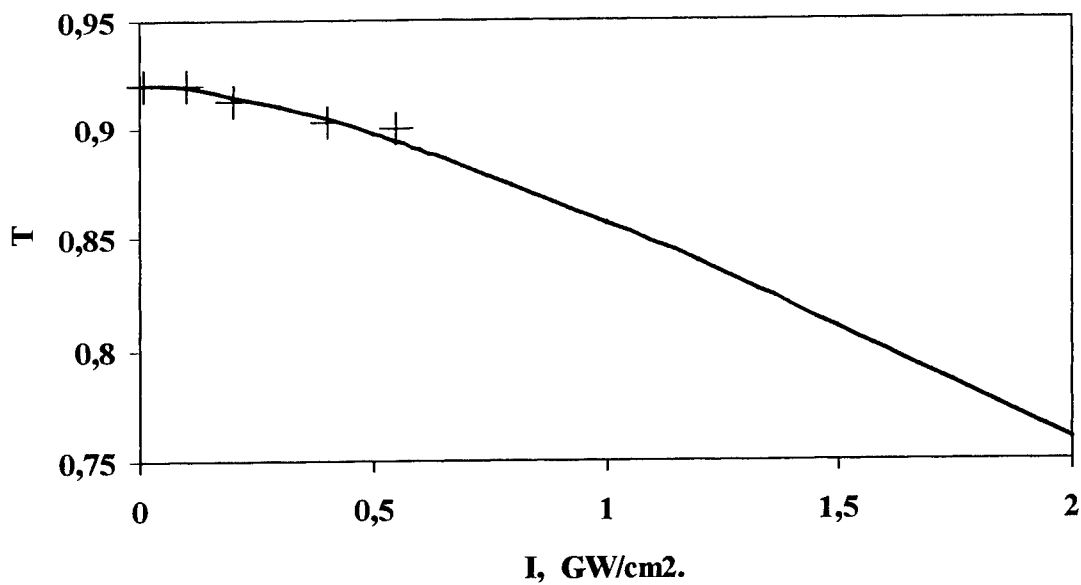


Fig.4. Transmission (T) of MgF_2 sample at 248 nm laser radiation. (\dagger) - experimental results [10].

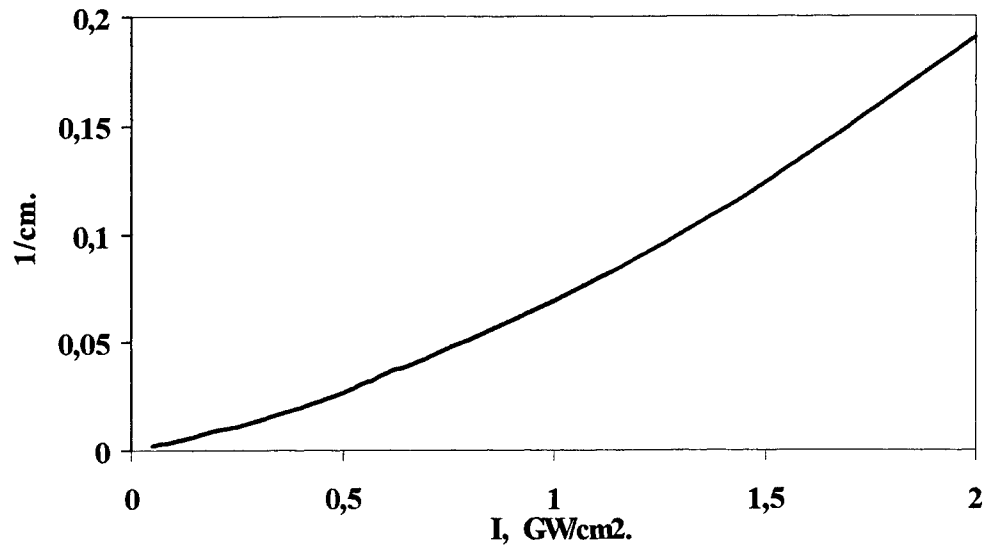


Fig.5. Calculated dependence of a behaviour of an absorption (K_2) in MgF_2 from laser radiation intensity at 248 nm.

Detuning characteristics of ionic anti-Stokes Raman laser

S. A. Babin, S. I. Kablukov, S. V. Khorev, E. V. Podivilov,
V. V. Potapov, D. A. Shapiro, M. G. Stepanov
Institute of Automation and Electrometry,
Siberian Branch, Russian Academy of Sciences,
Novosibirsk 630090, Russia

ABSTRACT

Continuous-wave generation is demonstrated of the anti-Stokes Raman laser in new Λ scheme $\text{ArII } 3d'^2G_{9/2} \rightarrow 4p'^2F_{7/2} \rightarrow 4s'^2D_{5/2}$ with long-lived start and final levels. Red pump radiation with wavelength $\lambda_p = 611$ nm from a dye laser that excites transition $3d'^2G_{9/2} \rightarrow 4p'^2F_{7/2}$ is converted into the blue radiation at $\lambda = 461$ nm ($4p'^2F_{7/2} \rightarrow 4s'^2D_{5/2}$) with efficiency of about 30%. The tunability range spans more than ± 10 GHz around exact resonance, which is five times as wide as the Doppler contour. The output frequency ω is found to depend linearly on the frequency ω_p of the pump field: $\omega \simeq \omega_p \lambda_p / \lambda$. A sharp peak of output power is observed in the detuning curve at the exact resonance instead of well-known two-photon dip. The model is proposed that includes ionic scattering in plasma and interaction of the running pump and standing output waves. The derived formula offers an interpretation of the observed peak.

1. INTRODUCTION

Many interesting optical effects have attracted particular interest to Raman lasing. Recent examples are nonlinear dynamics, including longitudinal mode competition and bistability,¹ inversionless gain,² amplification of ultra-short pulses,³ suppression of quantum noise,⁴ intracavity electromagnetically induced transparency,⁵ creation of the population inversion on transitions involving the ground state.⁶ Meanwhile, one of major purposes of these efforts is to achieve short-wavelength amplification and generation (for reference list see⁷⁻⁹).

Up-conversion methods are based in general on 3- and 4-level systems. Most progress has been made toward that goal in four-wave mixing schemes.¹⁰⁻¹² However, in the mixing experiments the efficiency was low,¹⁰ or the frequency shift was small,¹¹ or the output radiation was not continuous.¹² Proposed "inversionless" gain schemes with large shifts¹³ have not been experimentally confirmed yet. Thus, in spite of obvious achievements in principle demonstrations, realization of the continuous powerful up-conversion with large frequency shift remains an unsolved problem.

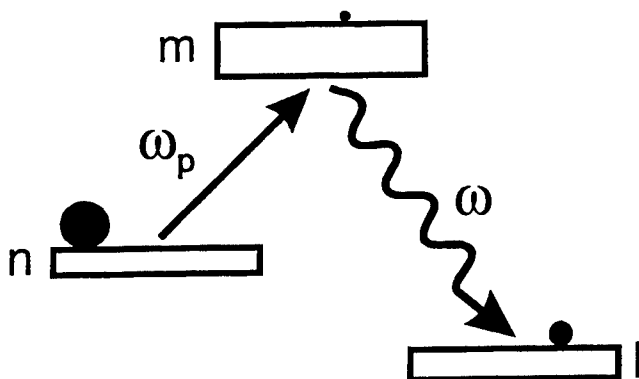


Figure 1. Raman Λ -configuration with Bohr frequencies $\omega_{mn} = (E_m - E_n)/\hbar$ and $\omega_{ml} = (E_m - E_l)/\hbar$, E_j are the levels of energy. The widths of levels are shown schematically by the boxes. Circles denote relative populations.

In this view, the Raman Λ -scheme, Fig.1, is still of interest, especially its capability of short-wave generation. The largest frequency shift in continuous mode, from the red to blue spectrum, has been obtained in argon plasma.^{14,15} In the experimental configurations, $3d$ -metastable levels were used as starting ones (n), while short-lived $4s^2P_{1/2,3/2}$ served as final levels (l). This group of states is thoroughly studied, since they are utilized as lower levels in argon-ion laser transitions. This combination of lifetimes provides the maximum population inversion on the Raman transition nl , as a result the conversion efficiency can be high enough, up to 60%. Meanwhile, the tunability range for that scheme is limited by the Doppler width, since the stepwise process is the main lasing channel. Pump photon is absorbed on the transition nm from initial to intermediate state m , after that the output photon is emitted on the adjacent transition ml .

Schemes with long-lived final level realized in atomic gases, e.g., NeI,¹⁶ have lower conversion coefficient (less than 10%), whenever their tunability range exceeds 100 Doppler widths. The physical reason is the two-photon process, predominant in these schemes. Simultaneous absorption of the pump photon and emission of the output photon occur. A narrow dip has been predicted in the output spectrum having the width of forbidden transition (see, e.g.,^{17,18}). This two-photon dip was observed in neon Λ -scheme $2p_1 \rightarrow 2s_2 \rightarrow 2p_4$ with wavelengths $\lambda_p = 1.5 \mu\text{m}$, $\lambda = 1.15 \mu\text{m}$.¹⁹ The detuning curve displayed a dip with the width of forbidden transition between the start and the final levels.

In the present paper, the scheme of up-conversion is proposed for ArII transitions $3d^2G_{9/2} \rightarrow 4p'^2F_{7/2} \rightarrow 4s'^2D_{5/2}$ with relatively long-lived final state. Level lifetimes in this scheme are close to that in NeI, while the wavelength shift is much greater. Our measurement does not reveal the expected two-photon dip. A sharp peak is observed in the center of detuning curve instead.

In contrast to other gas lasers, an additional broadening of nonlinear resonances occurs in ion lasers, in particular the two-photon resonance gets broadened. Analysis of the Coulomb broadening due to ion scattering in plasma is based on Fokker-Plank type kinetic equation (see²⁰ and citation therein). The small-angle scattering leads to diffusion in the velocity space. This theory was limited by the domain of weak saturation, whereas the strong-field effects are important to explain the intracavity photon-ion interaction in the Raman laser.

Now the theory is extended for strong field in a standing-wave mode. It occurs that either two-photon, or other optical coherence effects are suppressed by the diffusion of phase and turn to be negligible under a strong field. The only essential broadening is that of population distribution over velocity. The derived expression is appropriate to interpret the peak in the detuning curve, i.e., the output power as a function of the pump frequency.

In Sec. 2, we describe the experimental setup. The frequency curve, i.e., the dependence of output frequency on the input one, is shown to be a linear function. The detuning curve with the sharp peak in the center is presented. In Sec. 3, the equations for the density matrix are solved for three-level Λ -system with Coulomb scattering. A simple formula for the output power as a function of input detuning is derived. Sec. 4 is devoted to comparison between theory and experiment. The least-square fitting with reasonable parameters is performed. Validity domains of the theoretical model are discussed. Sec. 5 summarizes the results.

2. DETUNING CHARACTERISTICS

The three-level Λ -scheme is shown in Fig. 1. The input pumping field resonant to transition mn with frequency ω_p is converted into output field with frequency ω , resonant to transition ml . The wavelengths for ArII $\lambda_p = 611 \text{ nm}$, $\lambda = 461 \text{ nm}$ correspond to up-conversion. Starting level n ($3d^2G_{9/2}$) is metastable, its radiative decay into the ground state $3p^5^2P_{3/2}$ is forbidden by $\Delta J = 0, 1$ selection rule. However, in gas-discharge plasma the lifetime of level n is limited by inelastic collisions with electrons and amounts to $\Gamma_n^{-1} \approx 40 \text{ ns}$.^{15,21} For final level l ($4s'^2D_{5/2}$) the dipole transition into ground state is also forbidden, since the parent ArIII configuration changes. Nevertheless, this rule is not strict for ArII, hence the characteristic radiative lifetime is in the interval $\Gamma_l^{-1} \approx 10 \div 27 \text{ ns}$ according to calculations by different authors.^{22,23} The intermediate level m ($4p'^2F_{7/2}$) is similar to the laser level $4p'^2F_{5/2}$. The latter is used as the upper level of laser line 501.7 nm, and is well studied. Its radiative lifetime is 8.5 ns. The electron deactivation decreases this value to $\Gamma_m^{-1} \approx 6 \text{ ns}$, see.²⁰ Thus, the inequality $\Gamma_n, \Gamma_l \ll \Gamma_m$ is roughly valid.

The off-diagonal relaxation constant Γ_{nl} of forbidden transition is much less than those of allowed transitions Γ_{mn}, Γ_{ml} . In this case, the effects of optical coherence should prevail in three-level system considered. The ratio of relaxation constants and their absolute values are close to that of the Raman laser in atomic neon $2p_1 \rightarrow 2s_2 \rightarrow 2p_4$. In neon, the coherence effects led to a narrow dip that appeared in the center of detuning curve. The width of the dip is given by the constant Γ_{nl} of the forbidden transition.

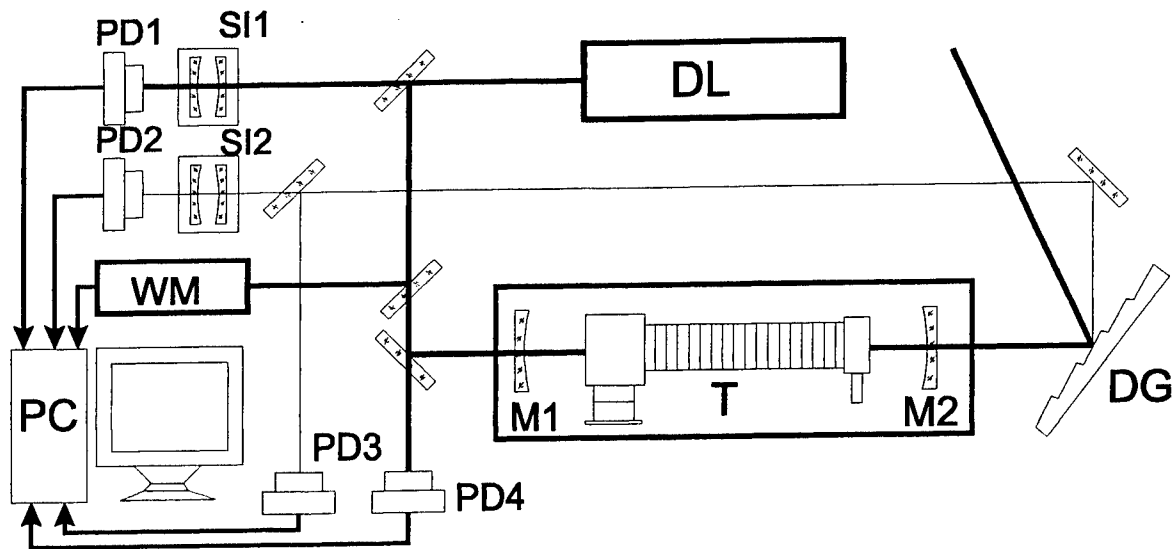


Figure 2. Experimental setup.

Level populations in argon-laser plasma are governed by the balance between radiation and collision processes. In the scheme under consideration they are $N_n \approx 10^{11} \text{ cm}^{-3} \gg N_l \sim N_m \approx 10^{10} \text{ cm}^{-3}$.²¹ The starting level is much more populated than other levels. Population inversion on transition ml in conventional discharge is absent, correspondingly the continuous generation was never observed at this line, see.^{24,25}

A sketch of the experimental setup is shown in Fig. 2. Active medium of the Raman laser was created by means of the low-pressure discharge at current $I \approx 100 \text{ A}$ in 7 mm-bored tube T. The length of active part was $L = 50 \text{ cm}$. Homogeneous pressure distribution along the tube axis was kept with the help of a slow longitudinal flow of gas.²⁶ The continuous-wave dye laser (DL) with R6G was used for pumping. Its power was up to 100 mW in single-frequency mode at the wavelength 611 nm. The pump radiation was directed by mirrors into the tube T. Internal mirrors M1, M2 were attached to tube ends by means of vacuum bellows. The reflection coefficient of the mirrors was high at 461 nm and low at 611 nm. The output transmission at 461 nm in first experiment was about $T \approx 0.3\%$. An absorption of the weak signal was also measured, in this measurement the power of the dye laser was lowered. The red and blue lines were separated with diffraction grating DG. The spectra of the dye and Raman lasers were registered by scanning interferometers SI1, SI2, photodiodes PD1, PD2 and λ -meter WM "Angstrom" with a sensitivity of 8 digits (down to 10 MHz in frequency units). The power was measured with photodiodes PD3, PD4.

During the scanning of pump frequency the data were synchronously written by a PC. Recorded data gave two experimental curves: the generated frequency ω as a function of pump frequency ω_p (Fig. 3) and the output power W_{AS} as a function of pump frequency ω_p (Fig. 4).

Analyzing the data of frequency measurement we conclude that the generation frequency is proportional to the pumping one:

$$\frac{\Omega}{k} = \frac{\Omega_p}{k_p}. \quad (1)$$

Here $\Omega = \omega - \omega_{ml}$, $\Omega_p = \omega_p - \omega_{mn}$ are the detunings. A typical series of experimental points in Fig. 3 proves dependence (1). At different parameters, no deviation from the linear law was observed and the slope was constant. Some scattering of points is originated from jumps between longitudinal modes of the cavity (about 100 MHz). The detuning range of the Raman laser exceeded 5 Doppler widths ($kv_T = 3.2 \text{ GHz}$). The conversion efficiency at the center was as high as 30%.

The most unexpected feature was observed in the detuning curve, Fig. 4. It was a sharp peak at the center instead of the dip typical for neon atomic lines.¹⁹ The characteristic width of the peak, $500 \div 800 \text{ MHz}$, was much greater than the expected width $\Gamma_{nl} \approx 20 \text{ MHz}$ of forbidden transition. The curve had three-scale structure:

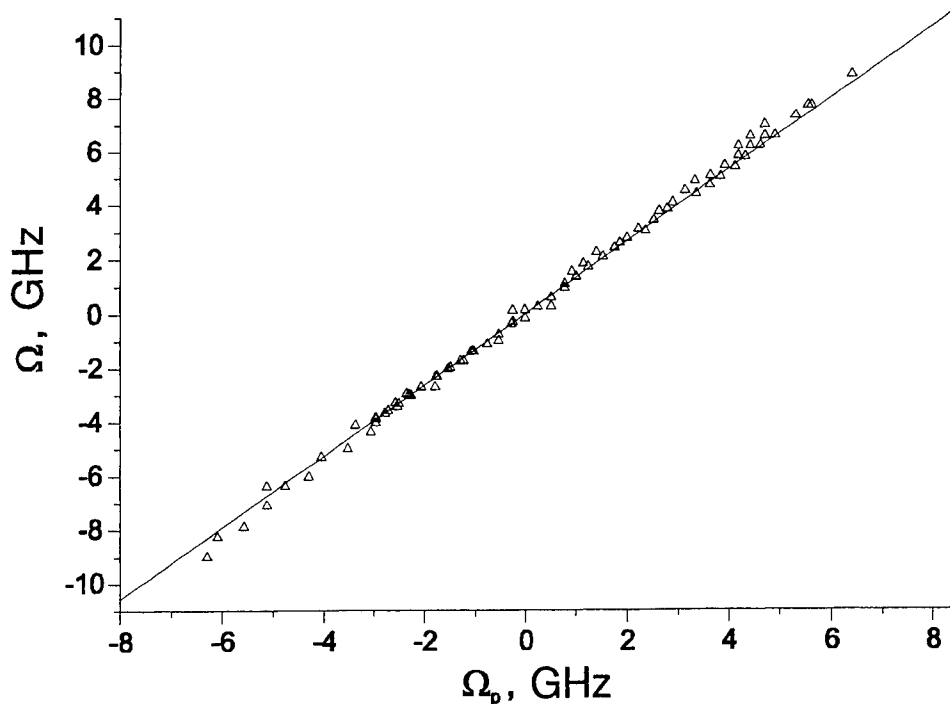


Figure 3. Frequency correlation: the measured dependence of generated frequency detuning $\Omega = \omega - \omega_{ml}$ on the detuning of pumping frequency $\Omega_p = \omega_p - \omega_{mn}$. Solid curve is a straight line with slope k/k_p .

relatively narrow peak at the center, the smooth dip of the nearly Doppler width around, and wide wings. The wings (and consequently, the tunability range of the Raman laser) were almost independent of the discharge parameters and pump power. The dip exhibited more sensitivity to the discharge current and pressure and disappeared at low currents $I \leq 40$ A. It became deeper, on the other hand, with decreasing the pump power. At low-intensity pumping the generation at the center vanished and a gap formed in the detuning curve with the width about $k\nu_T$. Here, the generation remained outside the Doppler width.

Surprisingly, in the "high-Q" cavity ($T=0.3\%$) the generation on ml transition (461 nm) appeared under lower argon pressure $p < 0.1$ torr even without pumping. Note that the continuous laser oscillation at this line was never observed, while pulsed generation has been obtained under specific conditions.²⁴ In our device, long-term operation under low pressure was difficult because of discharge instabilities. Although experiment in this regime was difficult, it was helpful, since it allowed us to find the reason of the dip formation and to provide the Raman lasing in a "low-Q" cavity ($T=7\%$).

It was clarified that the dip in the detuning curve was caused by nonuniform pressure distribution along the discharge axis.²⁶ Cathode and anode bulbs contained colder ions under higher pressure compared to the plasma column. Under condition $N_m \approx N_l$ the contribution of the electrode layers into absorption leads to significant perturbation of the Doppler line for ml transition. In particular, there existed an operation mode with the absorption at the line center and amplification at wings. The effect manifested itself in multimode generation (without pumping): its spectral profile measured near the threshold at high pressure showed a wide dip that disappeared at lower pressure. It means that similar effect should exist in the spectral profile of small signal gain.

Under lower pressure, when the longitudinal distribution was more smooth, the Raman lasing could be observed in the transparent cavity, i.e., at $T=7\%$. When the pump was off, the integral gain was less than the losses for output mirror transmission. The power of dye laser of about 10 mW (intensity 0.4 W/cm^2) was enough for lasing. Experimental curves recorded at different discharge parameters and pump power showed no dip, Fig. 5. A sharp peak was evident against the background of the broad wings. The relative peak height was within 30–50% in the wide domain of parameters. At low pumping power and relatively high pressure a single isolated peak was observed without wings. However, the accuracy of measurement under these conditions was low due to strong fluctuations

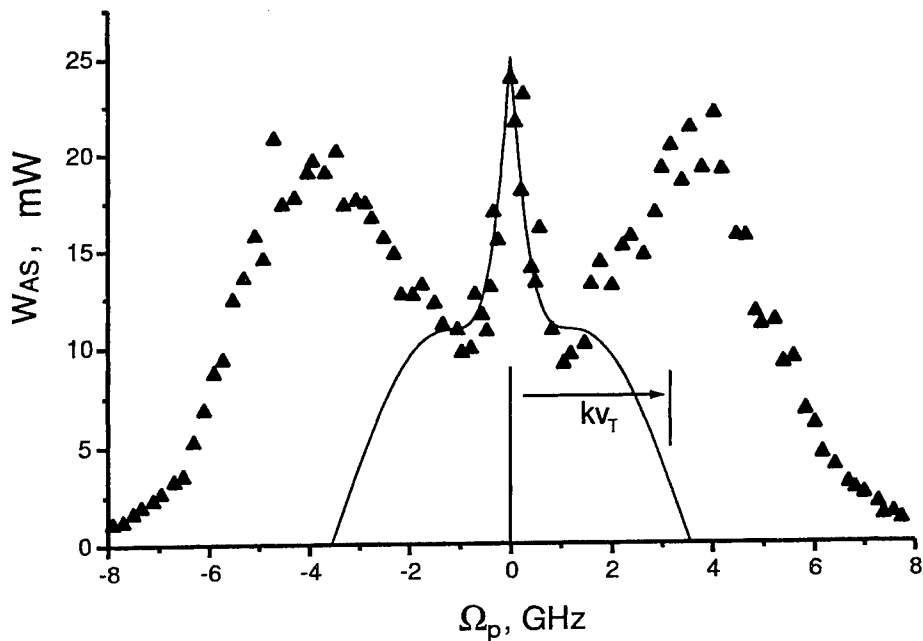


Figure 4. Detuning curve in the “high-Q” cavity ($T = 0.3\%$): the generated power W_{AS} as a function of the pump frequency detuning Ω_p at current 100 A, pressure 0.2 Torr. For comparison, the Doppler width kv_T is shown in the graph. The sharp peak at the center is discussed in Sec. 4.

near the threshold. A model interpreting the peak is discussed in the next section.

3. COULOMB DIFFUSION UNDER A STRONG FIELD

The standing output wave has the form

$$\mathcal{E}(x, t) = \mathcal{E} e^{-i\omega t} (e^{ikx} + e^{-ikx}) + \text{c.c.},$$

where frequency ω is close to Bohr frequency of transition ml , x is the coordinate along the cavity. Let us write the off-diagonal element of the density matrix ignoring higher spatial harmonics $e^{3ikx}, e^{5ikx}, \dots$:

$$\rho_{ml}(x, u, t) = e^{-i\omega t} (e^{ikx} \rho_+(u) + e^{-ikx} \rho_-(u)).$$

Polarizations ρ_+ and ρ_- are induced by the waves running in positive and negative directions, respectively. Here u is the projection of the velocity \mathbf{v} onto the wave vector \mathbf{k} . The power of induced emission is given by the integral over velocities

$$\mathcal{P}(\Omega) = 2\hbar\omega \text{Re} \int du (iG^* (\rho_+(u) + \rho_-(u))), \quad (2)$$

where $G = \mathcal{E}\mu_{ml}/2\hbar$ is the Rabi frequency, μ_{ml} is the dipole moment of transition ml .

In experiment the external pumping field on transition mn enters the cavity

$$\mathcal{E}_p(x, t) = \mathcal{E}_p e^{i(k_p x - \omega_p t)} + \text{c.c.}$$

That is a traveling wave propagated in positive direction. It excites ions from the long-lived level n to the upper level m , increasing, in doing so, the population inversion on the working transition ml .

Amplitudes $\rho_{\pm}(u)$ could be found from the kinetic equation²⁰

$$\begin{aligned}(\Gamma_{lm} - i(\Omega \mp ku))\rho_{\pm} &= \hat{V}\rho_{lm} - iG(\rho_m - \rho_l), \\ \Gamma_l\rho_l &= \hat{V}\rho_l + 2\text{Re}(iG^*(\rho_+ + \rho_-)) + A_{ml}(\rho_m - \rho_m^0) + \Gamma_l\rho_l^0, \\ \Gamma_m\rho_m &= \hat{V}\rho_m - 2\text{Re}(iG^*(\rho_+ + \rho_-)) - 2\text{Re}(iG_p^*\rho) + \Gamma_m\rho_m^0, \\ (\Gamma_{mn} - i(\Omega_p - k_p u))\rho &= \hat{V}\rho - iG_p(\rho_m - \rho_n),\end{aligned}\quad (3)$$

where $\rho_j \equiv \rho_{jj}$ is the population of level j , $\rho(u) = \exp(-i(k_p x - \omega_p t))\rho_{mn}$ is the polarization induced by the pumping field, Γ_j and Γ_{ij} are the relaxation constants for level j and polarization ρ_{ij} , A_{ml} is the Einstein coefficient, $G_p = \mathcal{E}_p \mu_{mn} / 2\hbar$ is the Rabi frequency for pump wave, μ_{mn} is the dipole moment of transition mn , $\rho_j^0 = N_j \exp(-u^2/v_T^2) / \sqrt{\pi}v_T$ is the equilibrium population of level j without the field, which has a shape of 1D Maxwellian distribution with thermal velocity $v_T = \sqrt{2T_i/m}$, where T_i is the ion temperature in the energy units, m is the ion mass. In the equation for the density matrix we drop out the terms proportional to polarization ρ_{nl} at the forbidden transition and contribution of the higher spatial harmonics.

The operator of small-angle ion-ion scattering \hat{V} describes the velocity change of an ion. Random wandering of the ion in the microfield of other charged particles can be presented as a diffusion in velocity space:

$$\hat{V} = D \frac{d^2}{du^2}, \quad D = \frac{8\sqrt{\pi}Ne^4}{3m^2v_T} \Lambda,$$

where D is the diffusion coefficient, N, e are the ion density and charge, Λ is the Coulomb logarithm.²⁷

The pumping field is in resonance with ions having velocity $u_* = \Omega_p/k_p$. Nonlinear correction to the population distribution (the Bennett holes) reaches maximum at $u = u_*$. In a similar way, the generated field is in resonance with ions of velocity $u_* = \pm\Omega/k$ for the wave running in positive (+) or negative (-) direction, respectively. Nonlinear corrections $\delta\rho_j(u) = \rho_j - \rho_j^0$ that appear because of interaction with the fields, have the shape of narrow peaks or dips with extrema at resonant velocities u_* . Since the random velocity change of an ion in plasma follows the diffusion law \sqrt{Dt} , the width of a nonlinear structure cannot be less than the diffusion width $\Delta u = \sqrt{D/\Gamma_j}$. Under typical experimental conditions $\Gamma_j \sim 2 \times 10^8 \text{ s}^{-1}$, $kv_T \sim 2 \times 10^{10} \text{ s}^{-1}$, $Dk^2 \sim (2 \times 10^9 \text{ s}^{-1})^3$, $N \sim 10^{14} \text{ cm}^{-3}$, $T_i \sim 1 \text{ eV}$, we can take advantage of following inequalities

$$\frac{\Gamma_{lm}}{k}, \frac{\Gamma_{mn}}{k_p} \ll \sqrt{\frac{D}{\Gamma_j}} \ll v_T.$$

From the first relation follows that the diffusion width Δu of the corrections is much greater than their collisionless widths. The second relation means that the diffusion width is narrower compared to thermal velocity v_T .

If we neglect ion-ion collisions the gain for the generated wave is induced by optical pumping processes, caused by population transfer from level n to m , and coherent two-photon processes, caused by polarization ρ_{nl} on the forbidden transition. Coulomb scattering leads to a fast growth of uncertainty $\Delta\phi$ in the phase of polarization on allowed transition ρ_{ml} . Dephasing results in the additional damping of ρ_{ml} . The growth of $\Delta\phi$ stems from the uncertainty in the ion coordinate governed by the random velocity change

$$\Delta\phi = k\Delta x = kt\Delta u = k\sqrt{Dt^3}.$$

In characteristic time $t_D \sim (Dk^2)^{-1/3}$, value $\Delta\phi$ reaches the value of the order of π , then after time t_D the polarization is destroyed. The inverse time $t_D^{-1} \sim 2 \times 10^9 \text{ s}^{-1}$ exceeds the relaxation constant at the working transition $t_D^{-1} \gg \Gamma_{ml}$. The polarization decay is determined by the dephasing time t_D . While the parameter is small,

$$\Gamma_{ml}/(Dk^2)^{1/3} \ll 1,$$

the relative contribution of coherence is small compared to the stepwise population processes. This is why coherent processes can be neglected in the kinetic equation (3).

Thus, the gain of the generated standing wave has two peaks at resonant frequencies $\Omega = \pm\Omega_p k/k_p$. Their heights are nearly equal; the width of each is controlled by the diffusion $\Delta\Omega = k\sqrt{D/\Gamma_m}$. The small-signal gain

is independent of the sign of detuning, therefore, both waves seemingly must come to generation. However, even a tiny contribution of coherence effect to the gain coefficient of one wave breaks the symmetry and gives an advantage to one of the two possibilities. This disbalance is enhanced by the nonlinear mode competition,²⁸ as a result the generation occurs only at $\Omega = +\Omega_p k/k_p$. At the same time, the influence of coherence processes on the generation power is negligible provided $|\Omega_p| < k_p v_T$.

The formation of a single peak in the center of the detuning curve (Figs. 4, 5) can be explained merely by population effects. Let us consider the distribution of polarization over velocity u . The population difference $\Delta N_{ml}(u) = \rho_m(u) - \rho_l(u)$ at the maximum of nonlinear correction $\delta\rho_m$, $u = u_* = \Omega_p/k_p$, within the Doppler contour is almost independent of Ω_p . Then, the gain for the co-propagating wave is independent of the detuning, too.

At small detuning $\Omega_p < k_p \sqrt{D/\Gamma_m}$, the wave running in the negative direction may also be amplified due to the population inversion created by the pumping field. Conversely, when the detuning exceeds the diffusion width $\Omega_p = k_p u_* \gg k_p \sqrt{D/\Gamma_m}$ the pumping field creates no inversion for particles with negative velocity $u = -u_*$, i.e., $\Delta N_{ml}(-u_*)$ can be ignored. Then the amplification of the opposite wave is absent. Thus, the frequency dependence of the standing wave gain copies the shape of nonlinear correction $\delta\rho_m$ to the upper level population. Consequently, the deviation from equilibrium occurs even at low output intensity domain, where saturation effects are absent. This feature distinguishes the effect from the Lamb dip.²⁸ The former is nonlinear effect and it requires saturation on the working transition. The saturation in our case makes the quantitative consideration more complicated, however, it does not change the main conclusion about the diffusional nature of the peak.

To derive the expression for detuning curve we take into account the saturation effects on the working transition ml , but restrict our consideration to the linear approximation with respect to the pumping intensity, i.e., ignore saturation on transition mn . The polarization at allowed transitions as a function of velocity u has the shape of narrow contours centered at $u = \Omega_p/k_p = \Omega/k$ for $\rho_+(u)$ and $\rho(u)$ or $u = -\Omega/k$ for $\rho_-(u)$. The width of each contour is determined by the dephasing $\delta u \sim t_D^{-1}/k \sim (D/k)^{1/3} \ll \sqrt{D/\Gamma_j}$. In accepted approximations, kinetic equation (3) gives the integrals for polarizations

$$\begin{aligned} 2\text{Re}(iG^* S_{\pm}) &= \frac{2\pi|G|^2}{k} (\rho_m - \rho_l)|_{u=\pm u_*}, \\ 2\text{Re}(iG_p^* S) &= \frac{2\pi|G_p|^2}{k_p} (\rho_m^0 - \rho_n^0)|_{u=u_*}, \end{aligned} \quad (4)$$

where

$$S_{\pm} = \int du \rho_{\pm}(u), \quad S = \int du \rho(u).$$

In equation (3) for populations, narrow functions can be replaced by δ -functions

$$\rho_{\pm}(u) = S_{\pm} \delta(u \mp u_*).$$

After this replacement the equations for populations take the following form

$$\begin{aligned} \Gamma_l \rho_l &= D \frac{d^2 \rho_l}{du^2} + S + A_{ml}(\rho_m - \rho_m^0) + \Gamma_l \rho_l^0, \\ \Gamma_m \rho_m &= D \frac{d^2 \rho_m}{du^2} - S \\ &\quad - \frac{2\pi|G_p|^2}{k_p} \delta(u - u_*) (\rho_m^0(u_*) - \rho_n^0(u_*)) + \Gamma_m \rho_m^0, \end{aligned} \quad (5)$$

$$\begin{aligned} S &= \frac{2\pi|G|^2}{k} \left[\delta(u - u_*) (\rho_m(u_*) - \rho_l(u_*)) \right. \\ &\quad \left. + \delta(u + u_*) (\rho_m(-u_*) - \rho_l(-u_*)) \right]. \end{aligned}$$

In the Doppler limit $kv_T \rightarrow \infty$ the set is reduced to algebraic equations that can be solved analytically.

First, let us show how to solve set (5) without spontaneous decay ($A_{ml} = 0$), then we treat the general case. We seek the population distributions as two exponential curves

$$\begin{aligned} \rho_j = \rho_j^0 + A_j^+ \exp\left(-\frac{|u - u_*|}{\sqrt{D/\Gamma_j}}\right) \\ + A_j^- \exp\left(-\frac{|u + u_*|}{\sqrt{D/\Gamma_j}}\right). \end{aligned} \quad (6)$$

Substituting (6) into (5) we get the following equations for A_j^\pm

$$\begin{aligned} 2\sqrt{D\Gamma_l}A_l^\pm &= \frac{2\pi|G|^2}{k} (\rho_m(\pm u_*) - \rho_l(\pm u_*)), \\ 2\sqrt{D\Gamma_m}A_m^+ &= -\frac{2\pi|G|^2}{k} (\rho_m(u_*) - \rho_l(u_*)) \\ &\quad - \frac{2\pi|G_p|^2}{k_p} (\rho_m^0(u_*) - \rho_n^0(u_*)), \\ 2\sqrt{D\Gamma_m}A_m^- &= -\frac{2\pi|G|^2}{k} (\rho_m(-u_*) - \rho_l(-u_*)). \end{aligned}$$

Expressing the population difference at point $u = \pm u_*$ in terms of A_j^\pm again, we obtain a linear set of equations for amplitudes A_j^\pm . Calculated amplitudes allow one to find the power generated from the unit volume at working frequency ω as a function of the pump detuning Ω_p using (2), (4)

$$\begin{aligned} \mathcal{P}(\Omega_p) &= \frac{2\pi\hbar\omega|G|^2}{k} [\Delta N_{ml}(u_*) + \Delta N_{ml}(-u_*)] = \\ &= \frac{2\sqrt{\pi}\hbar\omega|G|^2 f_T}{kv_T} \frac{2N_{ml} + PN_{nm}(1 + e^{-z})}{1 + p(1 + q + e^{-z} + qe^{-z/q})}, \end{aligned} \quad (7)$$

where $f_T = \exp(-\Omega_p^2/k_p^2v_T^2)$ is the Doppler factor, $z = 2|\Omega_p|/k_p\sqrt{D/\Gamma_m}$ is the detuning of pumping field normalized to the diffusion width, $q = \sqrt{\Gamma_m/\Gamma_l}$ is the ratio of diffusion widths of levels l and m , $N_{ij} = N_i - N_j$ is the population difference, $p = \pi|G|^2/\sqrt{Dk_p^2\Gamma_m}$ and $P = \pi|G_p|^2/\sqrt{Dk_p^2\Gamma_m}$ are the dimensionless Raman-laser and pump power, respectively.

Expression (7) consists of two terms. The first one describes the linear absorption or amplification and is proportional to the unperturbed (equilibrium) population difference N_{ml} at the working transition. The second term is responsible for amplification induced by the optical pumping and proportional to the product PN_{nm} of the pump power and the population difference between starting and intermediate levels N_{nm} . In our experiments $N_n \gg N_m, N_l, PN_{nm} \gg N_{ml}$, therefore the second term, i.e. the optical pumping, prevails. The pumping induces the peak at $|\Omega_p| < 0.5\sqrt{Dk_p^2/\Gamma_m}$. Its shape is described by a sharp exponential curve, copy of the Bennett peak in the velocity distribution (6). Its height significantly exceeds the linear amplification. In the case of weak saturation $p \ll 1$, the denominator (7) is independent of z . The contrast C of the peak can be defined as the amplification at its center $z = 0$ divided by that at the wings $z \gg 1$. The contrast turns to be $C = 2$.

In the limit of strong saturation $p \gg 1$ we can ignore 1 in the denominator (7). At $q \gg 1$, i.e., for long-lived lower level, the narrow peak in the gain contour induced by the pumping is also observable under strong saturation. Its profile is cusp-like and given by the exponential curve, while its width is determined by the diffusion at the upper level. Its contrast $C = 2$ is the same, but its height is lowered by factor pq . In the opposite limit of short-lived lower level $q \ll 1$, as well as for equal relaxation constants $q = 1$, the cusp in the gain disappears, since factors $(1 + e^{-z})$ in the numerator and denominator cancel out. In the intermediate case the peak can combine with a wide dip. Its width is limited by diffusion at the lower level $\Delta\Omega = \sqrt{Dk_p^2/\Gamma_l}$. Analogous two-scale contour has been discussed concerning experiments on the Lamb dip in ionic spectra of a two-level system with different level lifetimes.²⁰

To derive the expression for self-consistent generation power of the Raman laser let us equate the gain of induced radiation to the losses in the cavity

$$\mathcal{P}(\Omega_p) = \frac{c|\mathcal{E}|^2}{8\pi} \frac{1-r}{L},$$

where r is the reflection coefficient of the coupling mirror, $1-r \simeq T$, L is the length of active part of the medium. Neglecting absorption of the pump wave we get the intracavity power

$$p(z) = \frac{\mathcal{N}f_T + Pf_T(1 + e^{-z}) - t}{t(1 + q + e^{-z} + qe^{-z/q})}, \quad (8)$$

where

$$\mathcal{N} = 2 \frac{N_m - N_l}{N_n - N_m}$$

is the dimensionless population difference on the working transition,

$$t = \frac{c|\mathcal{E}|^2}{8\pi} \frac{1-r}{L} \frac{kv_T}{2\hbar\omega\sqrt{\pi}|G|^2(N_n - N_m)}$$

is the dimensionless level of losses.

While we seek p , we assume the pump power P constant. For a real laser, the pumping field is inhomogeneous along the medium due to absorption. To take absorption into account we should average the calculated exponential dependence over the coordinate $P(x) = P \exp(-\alpha f_T x)$:

$$\langle P \rangle = \frac{1}{L} \int_0^L P(x) dx = P \frac{1 - \exp(-\alpha f_T L)}{\alpha f_T L},$$

where P is the incident intensity of the pump field, α is the absorption coefficient at the line center. If we include also the spontaneous decay at the working transition, the method of calculation is almost identical. The final expression for output including both effects of the spontaneous decay and inhomogeneous pumping field has the following form

$$W_{AS} = c \cdot p(z),$$

$$p(z) = \frac{\frac{\mathcal{N}}{t} f_T - 1 + \frac{\langle P \rangle f_T}{t} (1 + e^{-z} - B)}{1 + q + e^{-z} + qe^{-z/q} - B}, \quad (9)$$

where

$$B = A \frac{q - 1 + qe^{-z/q} - e^{-z}}{q^2 - 1},$$

$A = A_{ml}/\Gamma_l$, $c = TS\sqrt{Dk^2/\Gamma_m}/A_{ml}$ is the dimensional scale factor, S is the average cross-section of the light beam.

This expression, like formula (7), involves two completely different kinds of terms, each can produce the peak. The first term in the numerator, proportional to $\mathcal{N}/t - 1$, is responsible for conventional lasing (without pumping) on the working transition. The second term describes the Raman lasing due to the optical pumping and includes the parameters of all three levels. The first term has a z -dependence in the denominator only, which is caused by saturation. When the gain is above the threshold $\mathcal{N}/t > 1$ and pumping is absent $\langle P \rangle = 0$ we have the Lamb dip in the detuning curve of the two-level laser.²⁸ Generally, the Lamb dip in ionic system has three scales because of different lifetimes of the lower level, upper level, and the duration of dephasing.²⁰ At $\mathcal{N}/t < 1$ the peak appears instead of the dip, analogous to saturated absorption peak.²⁹ In this case, the generation occurs with optical pumping only.

The second term carries a z -dependence stemming from the optical pumping in the numerator. Another z -dependence enters in denominator as a result of saturation. Generally, they lead to formation of a narrow peak with the diffusion width of the upper level and a wide dip with the diffusion width of the lower level. The qualitative behavior at $A \neq 0$ remains the same. Totally new features appear at $A \sim 1$. Even at $q \rightarrow 1$, the factors involving z -dependence do not cancel each other.

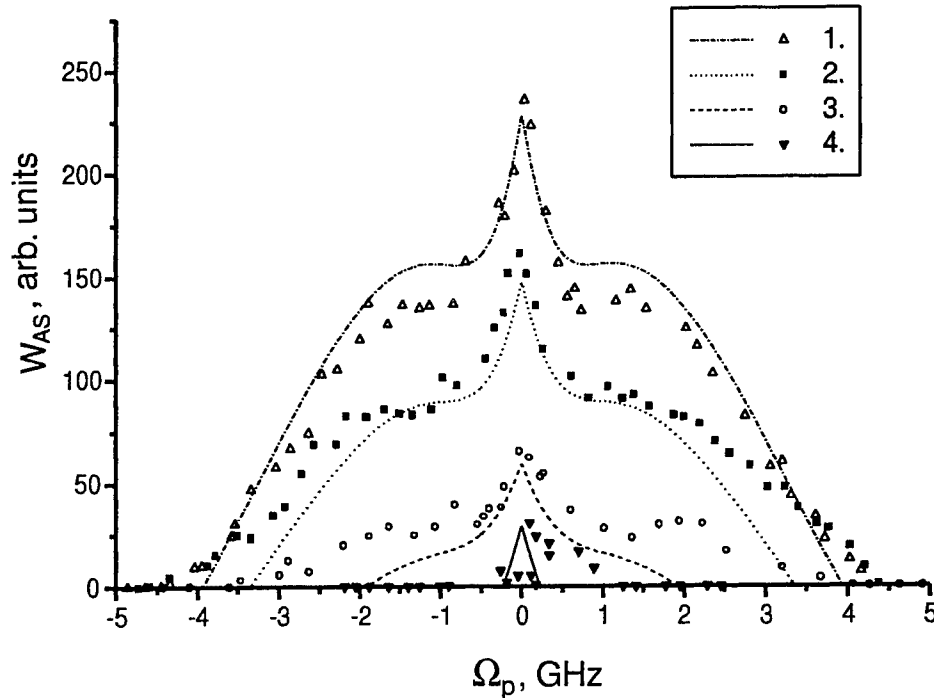


Figure 5. Measured detuning curves in “low-Q” cavity ($T = 7\%$) at current 70 A along with theoretical curves: $P/t = 6.89$ (80 mW), $\mathcal{N}/t = 0.53$ (curve 1); $P/t = 4.65$ (54 mW), $\mathcal{N}/t = 0.53$ (2); $P/t = 2.33$ (27 mW), $\mathcal{N}/t = 0.53$ (3); $P/t = 2.33$ (27 mW), $\mathcal{N}/t = 0.0056$ (4). Pressure was 0.1 Torr (curves 1,2,3) or 0.15 Torr (4).

The second term dominates already at relatively small pumping $\langle P \rangle \gtrsim \mathcal{N} - t$. The generation power is proportional to the pumping. This is a particular feature of the Raman laser in contrast to the two-level laser. Thus, the peak in the detuning curve is formed due to diffusion in the velocity space, provided that the widths of resonant structures on levels m and l are different. This difference exists even for equal relaxation constants $\Gamma_m = \Gamma_l$ if spontaneous emission is taken into consideration. In the next section, the theory is compared with the experimental curves.

4. COMPARISON BETWEEN THEORY AND EXPERIMENT

Detuning curves measured at different pump laser power are shown in Fig. 5. The experiment was performed within the scope of the theory. Three top curves 1, 2, 3 were recorded at the same discharge pressure, while for the bottom curve 4 the pressure was higher. In the same picture, the theoretical curves calculated with formula (9) are also presented. Curves 1,2,3 were fitted by parameter $q = \sqrt{\Gamma_m/\Gamma_l}$ and scale factor c . Parameters P/t and \mathcal{N}/t have been estimated from independent measurements. In the data processing, the following values are assumed: $\nu = 2D/v_T^2 = 0.1\Gamma_m$, $\mathcal{N}/t = 0.53$, $kv_T = 3.2$ GHz, $\alpha L = 1.5$, $A = 0.5q^2$ according to experimental conditions. The fitting was carried out using the central part of the curves ($|\Omega_p| < k_p v_T$), since the approximation underlying the theory is not valid at the wings.

As a result of the least square fitting the common value $q = 1.3$ is obtained for curves 1,2,3. This value corresponds to $\Gamma_m/\Gamma_l \simeq 1.7$ and agrees with the literature. As mentioned in Sec. 2, the data on the lifetime of final level $4s' \ ^2D_{5/2}$ by different authors^{22,23} vary by a factor of 3. The present fitting makes it possible to measure the lifetime ratio more accurately. From known value $\Gamma_m^{-1} \simeq 6$ ns we obtain $\Gamma_l^{-1} \simeq 10$ ns with collisional deactivation included. For the bottom curve 4 value $q = 1.3$ was assumed and \mathcal{N}/t became the fitting parameter. The result is $\mathcal{N}/t = 5.6 \times 10^{-3}$, which almost matches the threshold of linear absorption. The independent measurement in the “high-Q” cavity agrees well with this value.

Fig. 5 confirms that the shape of detuning curve persists at increasing P . The width of the peak is governed by the velocity change on level m : $\delta_m = kv_T \sqrt{\nu/2\Gamma_m} = 0.7$ GHz. We should take into account that the peak in the detuning curve is twice as narrow as the Bennett-type hole in the velocity distribution in frequency units. The

tunability range depends on the excess of the amplification above the generation threshold. The excess is determined by both pumping P and linear gain \mathcal{N} in agreement with (9). The absence of wings under higher pressure is a result of decreased linear gain \mathcal{N} at the same pumping P . The same reason increases the fluctuations: points in series 4 are scattered, since the gain approaches the threshold. Fig. 5 also indicates that the height of the peak is slightly above the theoretical prediction. Possible explanation is the saturation effect with respect to the pumping field ignored in the theory. At $|\Omega_p| > k_p v_T$ the contribution of the coherence effect grows and may lead to the observed deviations at the wings.

Absolute height of the peak (minus the pad) grows up linearly with pumping P . It points to the main role of the second term of formula (9) proportional to the pumping P and indicates that the effects like saturated absorption²⁹ are negligible under experimental conditions. Qualitative understanding of the main processes permits us to compare Fig. 4 with the theory, although the near-electrode plasma absorption is not known exactly. If we fit only central peak, then the least squares yield reasonable parameters $q = 1.2$, $\mathcal{N}/t = -0.5$, as shown by the curve. They agree with the data extracted from Fig. 5 and experimental estimation of absorption, respectively. The deviation from the theory at the wings is aggravated by the observed effect: average absorption along the tube at the working transition and corresponding absolute value of \mathcal{N}/t decreases with the detuning in contrast to the basic assumptions of the theory.

5. CONCLUSIONS

Thus, it is shown that plasma specifics of the active medium fundamentally changes the detuning curve of the ion Raman laser with traveling pump wave and standing output wave. As distinct from neutral gas, a comparatively broad peak is observed instead of a narrow two-photon dip. Its shape corresponds to exponential curve, a copy of the Bennett hole at the intermediate level with its collisional broadening. Its width was about 700 MHz, that exceeds more than by an order of magnitude the width of the forbidden transition.

The theory of Raman lasing is often based on assumption of weak output field compared to the pumping power and ignores the saturation on the working transition. The generation in experiments happened to be strong and so, violated the perturbation theory. The model was developed with, conversely, strong field on the working transition and weak pumping field. The second unusual feature in the theory is collisional dephasing of the forbidden transition polarization. Soft ion scattering in plasma turned to be enough to destroy the coherence effects within the Doppler contour. The theory provides also the answer to the question why the slope of frequency characteristics is preset by the ratio of wavelengths. The coherence effect breaks the symmetry among two counterpropagating waves. Because of nonlinear mode competition the wave parallel to pumping one only is generated.

The proposed model describes well the experimental detuning curves $W_{AS}(\Omega_p)$ for different pump powers and discharge pressures. The sharp peak with contrast 1.5-2 against the smooth pad was observed within the broad domain of parameters. Under some conditions the isolated peak without a pad was registered, or the peak inside a smooth dip. Each case agrees qualitatively with the theory.

The shape of detuning curve is very sensitive to the ratio of working level lifetimes Γ_m/Γ_l and the effective transport frequency ν . That permits one to utilize the effect for determination of one lifetime provided the other is known. Such an estimation has been done in the present paper for an ArII metastable in plasma. If both lifetimes are measured independently, then the collision frequency could be extracted from the peak shape. The effect may also be helpful for plasma diagnostics.

6. ACKNOWLEDGEMENTS

We are grateful to A. M. Shalagin and S. G. Rautian for fruitful discussions, and M. A. Rybakov for technical assistance. This work is partially supported by RFBR Grant: Nos 97-02-00016G, 00-02-17973, and 00-15-96808, and by Russian Ministry of Science and Technology programs: Optics (laser physics 1.53) and Fundamental Spectroscopy (08.02.32). M.G.S. acknowledges the support by INTAS within the program of the International Center for Fundamental Physics in Moscow No 96-0457. Tunable CW dye laser for the experiments is courteously granted by Laser Center "Inversion" (Novosibirsk).

REFERENCES

1. R. Corbalán, J. Cortit, and F. Prati, "Competition and bistability of longitudinal modes in raman laser," *Phys. Rev. A* **53**(1), pp. 481–485, 1996.
2. A. J. Merriam and A. V. Sokolov, "Anti-stokes Raman lasers without inversion," *Phys. Rev. A* **56**(1), pp. 967–975, 1997.
3. V. V. Kozlov, P. G. Polynkin, and M. O. Scully, "Resonant Raman amplification of ultrashort pulses in a V-type medium," *Phys. Rev. A* **59**(4), pp. 3060–3070, 1999.
4. A. Eschmann and R. J. Ballagh, "Intensity squeezing in a Raman laser," *Phys. Rev. A* **60**(1), pp. 559–572, 1999.
5. C. L. Bentley, Jr., J. Liu, and Y. Liao, "Cavity electromagnetically induced transparency of driven-three-level atoms: A transparent window narrowing below a natural width," *Phys. Rev. A* **61**(2), p. 023811, 2000.
6. A. A. Apolonsky, S. A. Babin, S. I. Kablukov, R. V. Markov, A. I. Plekhanov, and A. M. Shalagin, "Lasing on the D₂ line of sodium in a helium atmosphere due to optical pumping on the D₁ line (up-conversion)," *Phys. Rev. A* **61**(3), p. 033408, 2000.
7. I. M. Beterov and V. P. Chebotaev, "Three level systems and their interaction with radiation," *Progress in Quantum Electronics* **3**, p. 1, 1974.
8. B. Wellegehausen, "Optically pumped CW dimer lasers," *IEEE J. Quant. Electr.* **15**(10), pp. 1108–1130, 1979.
9. J. C. White, "Stimulated Raman scattering," *Topics in Applied Physics* **59**, pp. 115–207, 1989.
10. K. S. E. Eikema, J. Waltz, and T. W. Hänsch, "Continuous wave coherent Lyman- α radiation," *Phys. Rev. Lett.* **83**(19), pp. 3828–3831, 1999.
11. U. Hinze, L. Meyer, E. Chichkov, B. Tiemann, and B. Wellegehausen, "Continuous parametric amplification in a resonantly driven double- Λ system," *Opt. Comm* **166**(1-6), pp. 127–132, 1999.
12. M. Jain, H. Xia, G. Y. Yin, A. J. Merriam, and S. E. Harris, "Efficient nonlinear frequency conversion with maximal atomic coherence," *Phys. Rev. Lett.* **77**(21), pp. 4326–4329, 1996.
13. S. F. Yelin, M. D. Lukin, M. O. Scully, and P. Mandel, "Gain without inversion in the frequency up-conversion regime," *Phys. Rev. A* **57**(2), pp. 3858–3868, 1998.
14. A. Feitisch, D. Schnier, T. Müller, and B. Wellegehausen, "Continuous anti-Stokes-Raman laser oscillations in argon-laser plasma," *IEEE J. Quant. Electr.* **24**(8), pp. 507–511, 1988.
15. A. A. Apolonsky, S. A. Babin, A. I. Chernykh, S. I. Kablukov, S. V. Khorev, E. V. Podivilov, and D. A. Shapiro, "Giant Coulomb broadening and Raman lasing in ionic transitions," *Phys. Rev. A* **55**(1), pp. 661–668, 1997.
16. K. Rittner, A. Höpe, T. Müller-Wirts, and B. Wellegehausen, "Continuous anti-Stokes-Raman lasers in a He-Ne-laser discharge," *IEEE J. Quant. Electr.* **28**(1), pp. 342–348, 1992.
17. V. S. Letokhov and V. P. Chebotaev, *Nonlinear Laser Spectroscopy*, Springer Verlag, Heidelberg, 1977.
18. S. G. Rautian and A. M. Shalagin, *Kinetic Problems of Non-Linear Spectroscopy*, Elsevier, Amsterdam, 1991.
19. E. V. Baklanov, I. M. Beterov, B. Y. Dubetsky, and V. P. Chebotaev, "Nonlinear effects in resonant SRS line in a gas in the field of a standing wave," *JETP Lett.* **22**, pp. 134–135, 1975.
20. S. A. Babin and D. A. Shapiro, "Spectral line broadening due to the Coulomb interaction in plasma," *Phys. Rep.* **241**(3-4), pp. 119–216, 1994.
21. S. A. Babin, S. I. Kablukov, and S. M. Kobtsev, "Parameters of metastable levels of ArII in gas-discharge plasma," *Opt. Spekt.* **84**(6), pp. 915–921, 1998.
22. B. F. J. Luyken, "Transition probabilities and radiative lifetimes for ArII," *Physica* **60**(2), pp. 432–458, 1972.
23. A. Hibbert and J. E. Hansen, "Transitions in Ar-II," *J. Phys. B: At. Mol. Opt. Phys.* **27**(15), pp. 3325–3347, 1994.
24. C. C. Davis and T. A. King, "Gaseous ion lasers," *Adv. Quant. Electr.* **3**, pp. 169–454, 1975.
25. M. H. Dunn and J. N. Ross, "The argon ion lasers," *Progr. Quant. Electr.* **4**(prt.3), pp. 233–269, 1976.
26. S. A. Babin and A. E. Kuklin, "Comparison of high-current discharges with axial and transverse gas flow for UV ion lasers," *SPIE Proc.* **1397**, pp. 589–592, 1991.
27. G. I. Smirnov and D. A. Shapiro, "Spectral line broadening due to Coulomb interaction," *Zh. Eksp. Teor. Fiz.* **76**(6), pp. 2084–2093, 1979. [Sov. Phys. JETP, **49** (6) 1054–1058 (1979)].
28. W. E. Lamb, "Theory of an optical maser," *Phys. Rev.* **134**(6A), pp. 1429–1450, 1964.
29. V. N. Lisitsyn and V. P. Chebotaev, "Effects of saturation of absorption in gas laser," *Zh. Eksp. Teor. Fiz.* **54**(2), pp. 419–423, 1968.

New Simulations for COIL lasers from the University of Illinois

D. S. Stromberg, L. A. Fockler, D. L. Carroll, and W. C. Solomon
University of Illinois at Urbana-Champaign

Abstract

Over the past six years we have been conducting detailed studies of a family of closely related supersonic mixing nozzles. These nozzles have performed well in experiments with the VertiCOIL laser. Subtle design changes in these nozzles lead to highly predictable results when compared to the complete CFD calculations for the three designs under study. Our conclusion is that mixing within the jets very near the nozzle throat with nitrogen diluent provides a more efficient lasing process.

Introduction and Background

The first supersonic COIL device was demonstrated in 1987 and reported by the Air Force Research Laboratory in 1988¹ and technology developments were reviewed in a 1992 paper.² A number of earlier computational studies have established the basic modeling approach. Pioneering work with detailed models was performed by Buggeln,³ and Madden,⁴ and Masuda⁵. These researchers and ourselves have taken similar approaches to coupling the COIL finite-rate kinetics with a detailed species molecular diffusion model. Research by Madden,⁴ Fockler,⁶ and Stromberg⁷ using the 3-D Navier-Stokes GASP code modeled enough detail to exactly represent the chemically reacting flowfield of the COIL under non-lasing conditions. This allows one to first determine the nature of the fundamental mixing and reacting flow before coupling the radiation transport to the simulation. Over the series of comparisons with existing VertiCOIL hardware^{8,9} we have established the viability and accuracy of the existing model. We recently applied the general simulation methodology to evaluating new COIL hardware configurations.

Over the past six years we have conducted detailed studies of the flow-fields within COIL lasers. We have chosen to study a family of closely related supersonic mixing nozzles that have performed well in experiments with the VertiCOIL laser. All designs have been tested experimentally to give substance to the computational results. In the present case we compare the operation of the VertiCOIL laser in our laboratory to the computational result for the mixing and reacting flow device operating with nitrogen diluent. In an earlier simulation⁶ a detailed CFD study of this laser in which helium was used as the diluent was conducted.

The Numerical Experiment

A schematic representation of a typical COIL is shown in Fig. 1. Our numerical experiment is designed to match VertiCOIL geometry and flow rates. The singlet-delta oxygen generator in our case is of the rotating disk type. The oxygen generator is close-coupled to the subsonic mixing chamber and molecular Iodine is introduced with a variety of sonic jets into the subsonic portion of the flow. The mixing and reacting flow is expanded through a Mach 2 supersonic nozzle into the laser cavity. The flow is subsequently discharged into a vacuum exhaust scrubber arrangement. Table 1 shows the rate constants of the important 13-reaction rate set within the COIL laser.

The chemical reaction set selected for this study is an updated 13-reaction set originally suggested by Carroll¹⁰ and later modified by Carroll¹¹ to include the new rates for Iodine deactivation measured by Heaven.¹² Our rationale for using this reduced reaction set in the studies covered here is given by Carroll.¹⁰ A close-up view of the important secondary injection-throat region of the nozzle is found in Figure 2. As can be seen we use a tight grid distribution within the sonic injectors and around the important injection region.

The flowfield within the VertiCOIL mixing nozzle is a low Reynolds number, viscous, chemically reacting flow with complex inviscid-viscid flow interactions. The flow is predominantly laminar, and viscous effects dominate a substantial portion of the flowfield. The second aspect consists of the core flow of the underexpanded jet which expands rapidly to form shocks as it decelerates. The third aspect is the transonic flow which produces strong streamwise gradients as the entire flow accelerates

though the nozzle. The Navier-Stokes fluid equations are appropriate to treat this chemically reacting flow, with its strong viscous-inviscid interactions.

Table 1. Reduced oxygen-iodine reaction set; 13 reactions, 10 species [I, I*, I₂, I₂*, N₂, H₂O, O₂(¹Δ), O₂(³Σ), O₂(¹Σ), Cl₂], Refs. 10-12.

<i>k</i>							Rates, cc/molecule-s	
<i>I₂ Dissociation</i>								
1	O ₂ (¹ Δ)	+	O ₂ (¹ Δ)	→	O ₂ (¹ Σ)	+	O ₂ (³ Σ)	2.5e-17
2	I ₂	+	O ₂ (¹ Σ)	→	2I	+	O ₂ (³ Σ)	4.0e-12
3	I ₂	+	O ₂ (¹ Δ)	→	I ₂ *	+	O ₂ (³ Σ)	7.0e-15
4	I ₂ *	+	O ₂ (¹ Δ)	→	2I	+	O ₂ (³ Σ)	3.0e-10
<i>I* Production</i>								
5	I	+	O ₂ (¹ Δ)	→	I*	+	O ₂ (³ Σ)	7.8e-11
6	I*	+	O ₂ (³ Σ)	→	I	+	O ₂ (¹ Δ)	1.04e-10*exp(-401.4/T)
7	I ₂	+	I*	→	I	+	I ₂ *	3.5e-11
8	I*	+	O ₂ (¹ Δ)	→	I	+	O ₂ (¹ Σ)	1.0e-13
<i>Deactivation Losses</i>								
9	I ₂ *	+	O ₂ (³ Σ)	→	I ₂	+	O ₂ (³ Σ)	4.9e-12
10	O ₂ (¹ Σ)	+	H ₂ O	→	O ₂ (³ Σ)	+	H ₂ O	6.7e-12
11	I ₂ *	+	H ₂ O	→	I ₂	+	H ₂ O	1.7e-11
12	I ₂ *	+	N ₂	→	I ₂	+	N ₂	8.2e-12
13	I*	+	H ₂ O	→	I	+	H ₂ O	2.1e-12

We employ a parallel version of the CFD code GASP to perform all the simulations reported in this investigation.^{13, 14} The code has been extensively validated⁴ with stability, accuracy, and efficiency demonstrated. The code has a multiple zone simulation capability that allows the computational domain to be decomposed and adapted to complex geometries in a straightforward manner. GASP employs finite volume discretization of the integral form of the Navier-Stokes equations as a description of the fluid dynamics. Additional equations can be included for species continuity and turbulence closure.⁴ This version is commonly run employing up to 20 processors which corresponds to the zonal decomposition. The speedup is about a factor of 10 over the case when our large 3-D case is run on a single processor.^{7, 14}

The rationale for this investigation is that the original VertiCOIL nozzle design gave a fairly uniform gain distribution in the lasing zone when helium was employed as diluent.⁶ However, when nitrogen was substituted as the diluent, the gain peaked just downstream of the nozzle throat and dropped off fairly rapidly as it reached the laser cavity.⁶ This gain "peaking" upstream of the laser mirrors can be detrimental to laser performance. Thus peak gain upstream of the mirrors can cause a loss of chemical efficiency and high power densities on the upstream edge of the mirror. Moving the injectors downstream offers the potential to reduce this deleterious effect by producing a gain distribution which is more uniform, achieving a maximum within the mirror region. Such a gain distribution would then distribute the power load more uniformly over the mirror surface avoiding the deleterious effects.

Further, there has been significant experience with Iodine injectors where the flow emanating from the jet was directly opposed to its partner on the opposite side of the nozzle. It was not known what the difference in performance might be if these jets were interleaved (or staggered). Thus we included this possibility in both the VertiCOIL experimental arrangement and the "exact" numerical simulation.

Approach

In order to realistically simulate the injection process, a nozzle mixing configuration similar to that conducted in previous studies was employed. The baseline nozzle that we examined for our nitrogen-diluted series had been used in earlier helium experiments and CFD simulations by Madden.⁴ In this nozzle the iodine injector jets are located quite far upstream (1.1 cm) from the nozzle throat and consist of banks of opposed (top and bottom) sonic orifices. To improve the design we moved the large injectors closer to the nozzle throat, 0.47 cm upstream of the nozzle throat, and conducted a second and third numerical experiment.⁷ In this experiment the large injectors were interleaved rather than opposed. The purpose of the latter was to establish the degree of communication (top and bottom) between the jets.

Two additional computational grids (Case II and Case III) were developed for use in this investigation. Both grids were generated using Gridgen software (Pointwise Corp., Version 13), a structured grid generator for use on a Silicon Graphics workstation. The principal difference between the two grids generated is that, here, the second grid has a slightly larger laser nozzle throat with respect to the first grid (0.453" versus 0.353"). Identical grid generation methods were applied to both grids, see Figure 2. The grid generated by Madden was used in the first of the three computations presented here and his grid generation method was followed here.⁴ It is the baseline case from which our study of nitrogen diluted systems departed.

The flow conditions are given in Table 2. All flow conditions for these simulations for Cases I-III are as indicated in this table, except that the pressure is reduced in Case III from 60 to 45 torr. It should be noted that in the actual lab experiments that when the throat height is increased and pressure decreased that the yield increases due to a lower pooling reaction loss. For the purpose of these numerical computations it was desired to study the effects the geometry change has on the fluid mechanics and mixing phenomena without adding the complexity of the increased yield in trying to understand the numerical results.

Table 2. Flow rates for the numerical experiments.

Experimental Flow Conditions: Simulation I	
I ₂	0.85 mmol/sec
Cl ₂	40.6 mmol/sec
Utilization	0.98
N ₂ Primary Flow	164 mmol/sec
N ₂ Secondary Flow	40 mmol/sec
Duct Pressure	60 Torr
Duct Temperature	278 K
P _o secondary	176.6 Torr
T _o secondary	423.2 K
Yield	0.615

When the configuration for Case I is operated as a nitrogen-diluted laser the iodine injector quickly penetrates to the centerline and good utilization of the O₂(¹Δ) within the iodine jet was obtained.⁶ I₂ disappears almost immediately in the subsonic portion of the main flow. The I* concentration builds up inside the high velocity portion of the jet to a very high level and persists down-stream as the jet begins to twist and break up. As a result, the gain builds up and to a very high peak value within the subsonic region of the flow and drops off rapidly as it enters the optical cavity. This occurs because of the slower velocity of the flow in the nitrogen-diluted nozzle than in the helium-diluted nozzle. For this reason we moved the large injectors closer to the nozzle throat, 0.47 cm upstream of the nozzle throat, and conducted a second and third numerical experiment. In these experiments the large injectors were interleaved rather than opposed.

Results

Results from three simulations are reported here: Case I, subsonic injection I₂ with the large injectors located far upstream, 1.1 cm upstream of the geometric throat and a throat height of 0.353"; Case II, subsonic injection of I₂ with the injectors located 0.47 cm upstream of the geometric throat and a throat height of 0.353"; and Case III, subsonic injection of I₂ with the injectors located 0.47 cm upstream of the throat and the nozzle throat enlarged to 0.453".

Case I with the injectors located far upstream (helium diluent baseline^{4,6} nozzle) was run with nitrogen diluent for comparison. We show the penetration by observing the N_2/I_2 stream as it mixes in Figure 3a and 3b. We note that penetration into the main stream is good and reaches the centerline at the nozzle throat. Figures 4a and 4b which provide the I_2 profile show that $O_2(^1\Delta)$ penetration into the jet has resulted in rapid dissociation of the I_2 in the first couple of millimeters of the flow. Figures 5a and 5b show an average gain plot with 2%/cm gains appearing in the subsonic section of the nozzle. Rather obviously, penetration, mixing and reaction are taking place too far upstream of the laser cavity leading to much reduced gains in the cavity. By inference, this is not an efficient lasing situation (which is confirmed by running a Blaze II quasi-2D Fabry-Perot power calculation for this case and by experiment in the laboratory in which the laser efficiency never exceeded 16%^{8,9}).

Our numerical experiment was continued with the re-designed nozzle injectors by moving the Iodine injector further downstream to 0.47 cm upstream of the throat. The calculation was repeated to see how far the gain zone was displaced downstream. Figures 6a-c show the results of the N_2/I_2 study of penetration. Penetration appears to be reasonably complete and Figures 7a and 7b show that I_2 gets as far as the nozzle divergent section before disappearing completely. We see a result of the design change first in the extended passage of unreacted I_2 downstream in Figures 7a and 7b. Penetration of the jets by $O_2(^1\Delta)$ is shown in Figure 8. Here we see that there is about a 50% utilization of $O_2(^1\Delta)$ inside the jets prior to lasing. This represents a fairly complete mixed and reacting flow case. When we look at the gain distributions in Figures 9a and 9b we see that gains exceeding 1.6% occur just upstream of leading edge of the mirror. These gains drop smoothly to 1.1% as they exit the important cavity region. While the increased cavity gain is encouraging with respect to Case I, we note that there is still some room for improvement in our basic design. We also note the highly three dimensional nature of the flowfield in Figure 10 which shows a typical Mach number distribution in this kind of a mixing nozzle.

As a result, we examined Case III, which is identical to Case II as far as location of the I_2/N_2 jets. However we increased the throat height by 28% to 0.453". This lowered the pressure and decreased the penetration into the flow. If one observes the nitrogen traces in the N_2/I_2 jet stream one can immediately see that centerline penetration is not achieved, Fig. 11. Approximately 90% of the flow channel height is filled with the jet within the important laser cavity region, see Figure 11. Figures 12a and 12b for Case III illustrate that the iodine disappearance looks very much like that found in Case II, Figs. 7a and 7b. When one examines the gain plots in Figures 13a and 13b one notes smooth gains curves exceeding 1.25% proceed much of the way through the important cavity region. Thus, from the non-lasing CFD results it is really difficult to tell if case III is an improvement over case II.

Conclusions

In order to determine the relative merits of the three cases studied we compare them with the calculated gain distributions for a helium diluted laser nozzle (analogous flow conditions to that shown in Table 2 were used for this comparison) of the same design as Case I. Figure 14 shows a comparison of the maximum of the average gain of these cases with the helium diluent case because a large number of measurements are available with helium and this helium case should show near optimum performance for this type of nozzle-mixing arrangement. Indeed a smooth gain zone of 1.3% cm^{-1} through the important cavity region is observed for this comparison case. A direct substitution of helium for nitrogen as in Case I of our three new numerical experiments shows that the gain peaks long before reaching the optical cavity to be utilized in the lasing process. Thus, this is the poorest performing laser nozzle for our nitrogen diluent case. The lower velocities and more completed mixing in the predominantly nitrogen stream account for the early peaking of the gain and the lower gain in the cavity region. Case II is nearly identical to Case I, but has injection interleaved and relocated as close to the nozzle throat as was physically possible and still inject upstream of the throat. (Note, we reserve the experiments with injection at the fluid dynamic throat for later comparisons.)

The injection location in Case II forces the gain zone to move downstream so that it fills the lasing zone much better than Case I. This is simply the effect of the delayed injection. Case III is identical to Case II except that the throat height is increased by 28% and the pressure is lower. In this lower pressure case, the temperature is slightly lower and the gain is distributed better throughout the important cavity region. Everything being equal, we would expect best gain performance from Case III. However, due to the larger throat (needed to reduce the pressure) this case underpenetrated by about 10%. So, while we did fill the cavity better we did not quite get the penetration that we desired. It appears that the two effects (better cavity filling and lower penetration) just about compensate for the other.

Our study was not totally conclusive regarding the interleaving of jets versus the opposing geometry. However, it appears that properly penetrated jets do tend to communicate across the centerline.

We have conducted experiments with VertiCOIL hardware configured for Cases I, II and III.⁹ We found that the laser performance was successively improved in each case. The numerical results indicate Case III would likely require increased penetration in order to see any improvement over Case II. We observed about a 15% improvement when this was done in the laboratory. Overall, these findings are consistent with our observations in the laboratory.

Acknowledgments

Portions of this work were supported by the Defense Advanced Research Projects Agency, the National Supercomputing Alliance, and by the Air Force Research Laboratory Small Business Technology Transfer Program.

References

1. Hager, G. D., Watkins, L. J. Meyer, R. K., Johnson, D. E., Bean, L. J., and Loverro, D., "A Supersonic Chemical Oxygen-Iodine Laser" AFWL Technical Report 87-45, Kirtland AFB, NM, (1988).
2. Truesdell, K. A., Lamberson, S. E., and Hager, G. D., "Phillips Laboratory COIL Technology Overview," AIAA 92-3003, AIAA 23rd Plasmadynamics and Lasers Conference, Nashville TN, July, 1992.
3. Buggeln, R. C. and Shamroth, S., Lampson, A. I., and Crowell, P. G., "Three-Dimensional (3-D) Navier-Stokes Analysis of the Mixing Power Extraction in a Supersonic Chemical Oxygen Iodine Laser (COIL) with Transverse I₂ Injection," AIAA 94-2435, 25th AIAA Plasmadynamics and Lasers Conference, June 20-23, 1994, Colorado Springs, Co.
4. Madden, T. J. and Solomon W. C. "A Detailed Comparison of a Computational Fluid Dynamic Simulation and a Laboratory Experiment for COIL Laser," AIAA 97-2387, 28th AIAA Plasmadynamics and Lasers Conference, Atlanta, GA, June, 1997.
5. Masuda, W., Hishida, M., Hirooka, S., Azami, N. and Yamada, H., "Three Dimensional Mixing/Reacting Zone Structure in a Supersonic Flow Chemical Oxygen-Iodine," JSME International Journal Series B-Fluids and Thermal Engineering, **41**, No. 2, pp. 209-215 (1997).
6. Fockler, L. A., "Large Scale Simulations of Chemical Oxygen Iodine Laser Flow Fields Using Nitrogen Diluent", M.S. Thesis, Mechanical Engineering, University of Illinois at Urbana-Champaign, 1999.
7. Stromberg, D. S., "Computational Fluid Dynamic Analysis of a Chemical Oxygen Iodine Laser using Nitrogen Diluent", M.S. Thesis, Aeronautical and Astronautical Engineering, University of Illinois at Urbana-Champaign, 2000.
8. Rittenhouse, T.L., Phipps, S.P., and Helms, C.A., "Performance of a 5 cm gain length supersonic Chemical Oxygen-Iodine Laser", IEEE J. Quantum Electronics, **35**, pp. 857-865 (1999).
9. Carroll, D. L., King D. M., Fockler L., Solomon W. C., Sentman, L. H., and Fisher C. H., "High-Performance Chemical Oxygen-Iodine Laser Using Nitrogen Diluent for Commercial Applications", IEEE J. Quantum Electronics, **36**, pp. 40-51 (2000).
10. Carroll, D. L., "Modeling High Pressure Chemical Oxygen-Iodine Lasers," AIAA Journal, **33**, No. 8, pp. 1454-1462 (1995).
11. Carroll, D. L., "Optimizing High Pressure Chemical Oxygen-Iodine Lasers," Proc. of the International Conf. On Lasers '95, Society of Optical and Quantum Electronics, McLean, VA (1996).
12. Heaven, M.C., "Studies of Energy Transfer Processes of Relevance to Chemically and Optically Pumped Lasers," Emory University AFOSR/NR F49620-92-J-0073 (1994).
13. Fuller, E. J., and Walters, R.W. "Navier-Stokes Calculations for 3-D Gaseous Fuel Injection with Data Comparisons," AIAA Paper No. 91-5072, Dec 1991.
14. Vitt, P. H., Riggins, D. W. and McClinton, C., R., "The Validation and Application to Supersonic Mixing and Reaction Flows" AIAA Paper No. 93-0606, 31st Aerospace Sciences Meeting, January 1993.

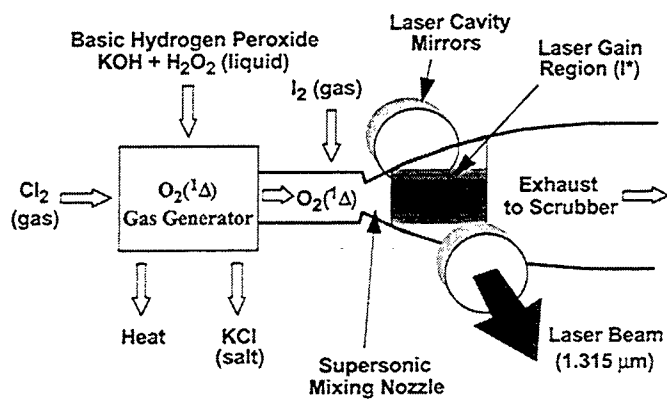


Figure 1. Schematic of a typical COIL device.

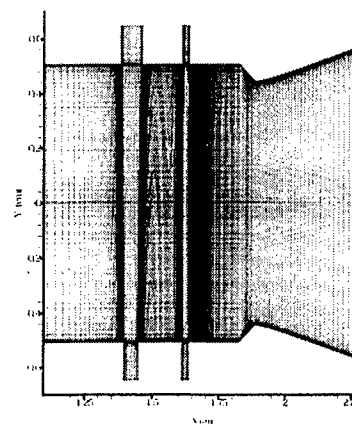
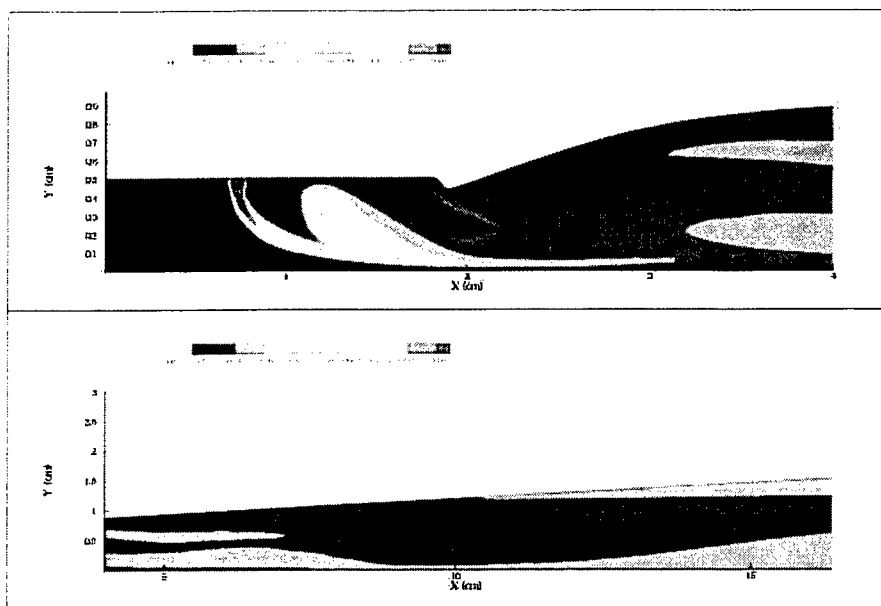
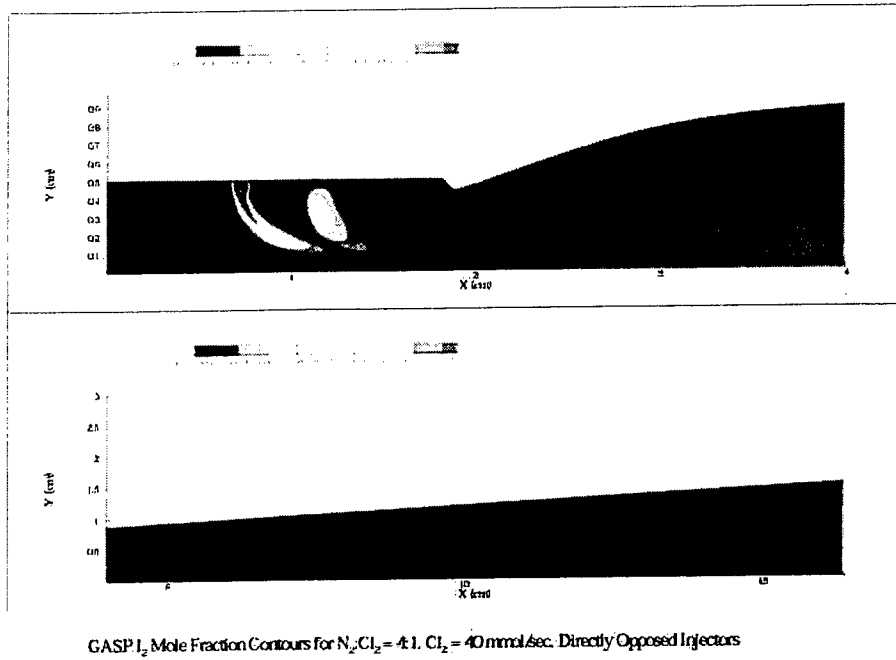


Figure 2. CFD grid in the injector-throat region.

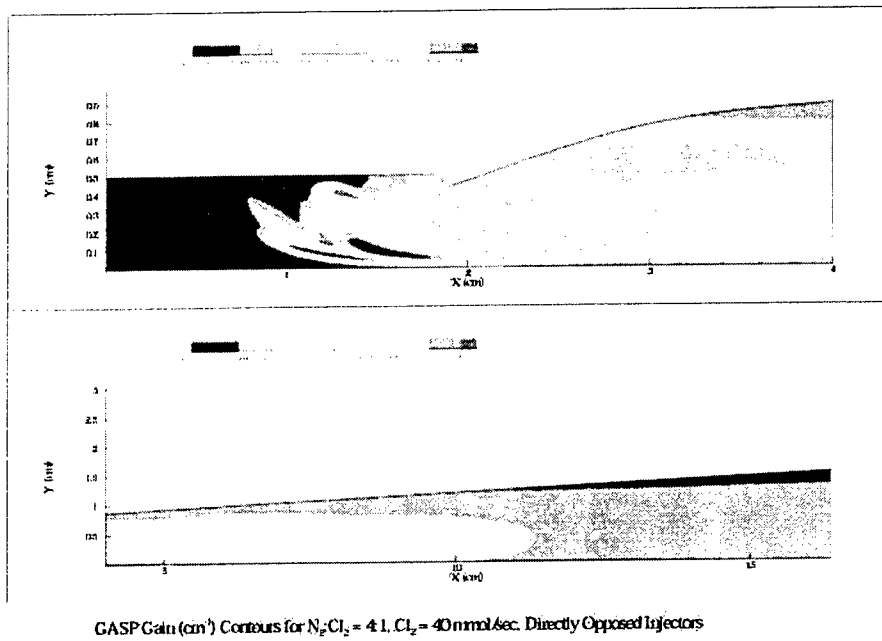


GASP N_2 Mole Fraction Contours for $N_2/Cl_2 = 4:1$, $Cl_2 = 40$ mmol/sec. Directly Opposed Injectors

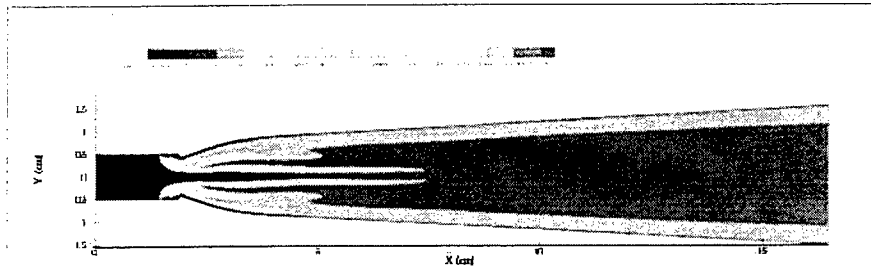
Figures 3a and 3b. GASP N_2 mole fraction contours for $N_2/Cl_2 = 4:1$, $Cl_2 = 40$ mmol/sec. Directly opposed injectors.



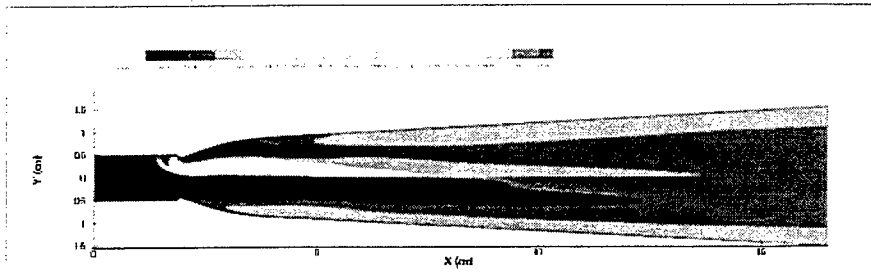
Figures 4a and 4b. GASP I₂ mole fraction contours for N₂/Cl₂ = 4:1, Cl₂ = 40 mmol/sec. Directly opposed injectors.



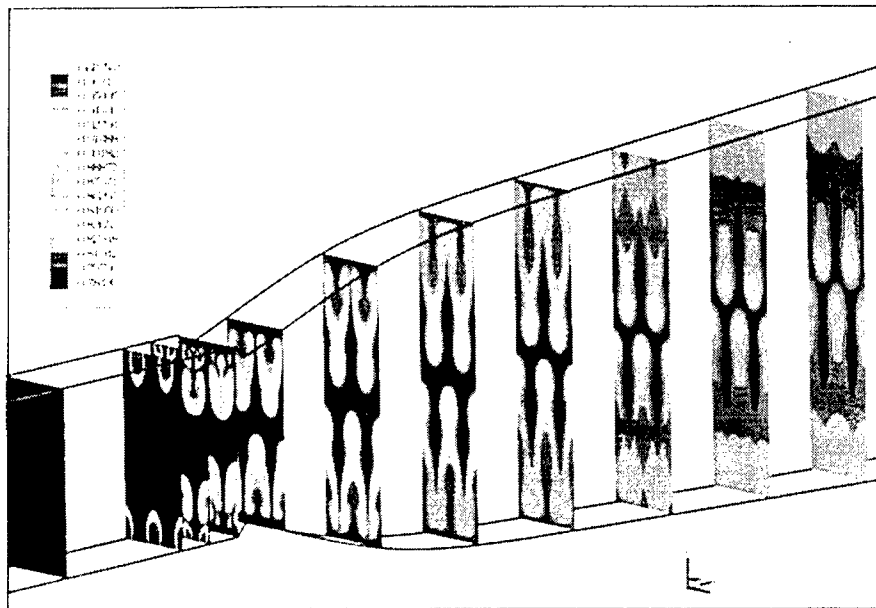
Figures 5a and 5b. GASP gain (1/cm) contours for N₂/Cl₂ = 4:1, Cl₂ = 40 mmol/sec. Directly opposed injectors.



(a): GASP N_2 Mole Fraction Contours for Simulation 1 (Throat Height = 0.353") - Center of Small Injector

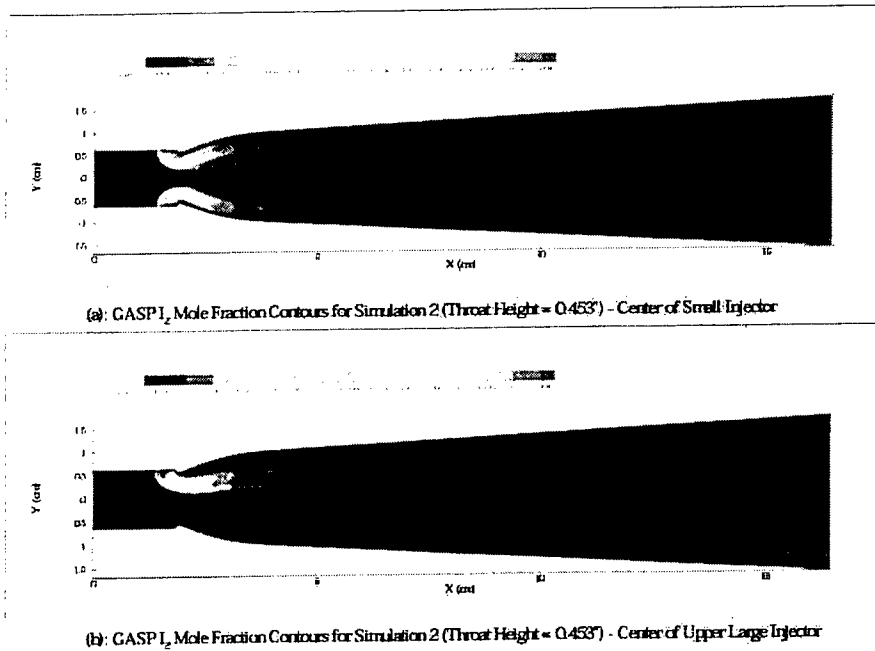


(b): GASP N_2 Mole Fraction Contours for Simulation 1 (Throat Height = 0.353") - Center of Upper Large Injector



(c): GASP N_2 Mole Fraction Contours for Simulation 1 (Throat Height = 0.353")

Figures 6a-c. GASP N_2 mole fraction contours for $N_2/Cl_2 = 4:1$, $Cl_2 = 40$ mmol/sec. Throat height of 0.353". Interleaved injectors.



Figures 7a and 7b. GASP I₂ mole fraction contours for N₂/Cl₂ = 4:1, Cl₂ = 40 mmol/sec. Throat height of 0.353". Interleaved injectors.

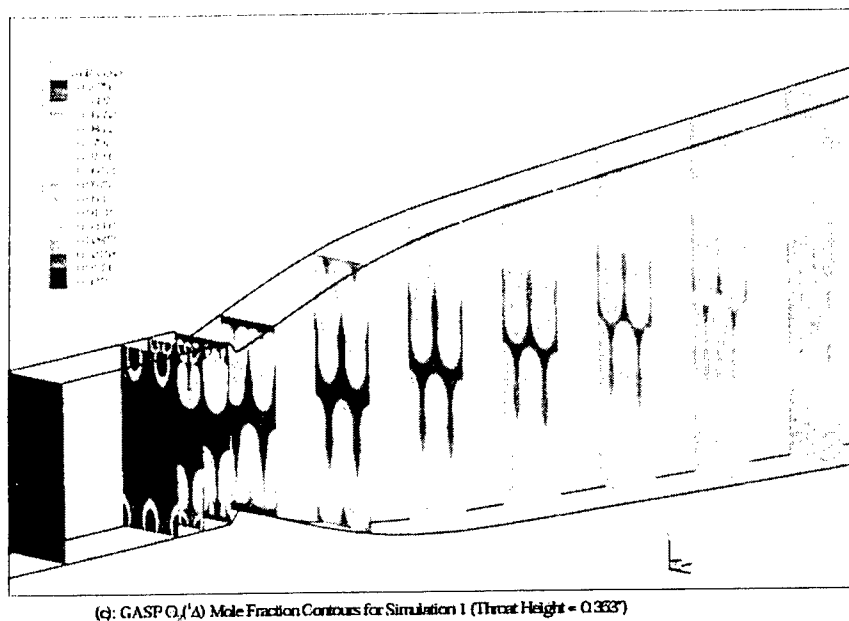
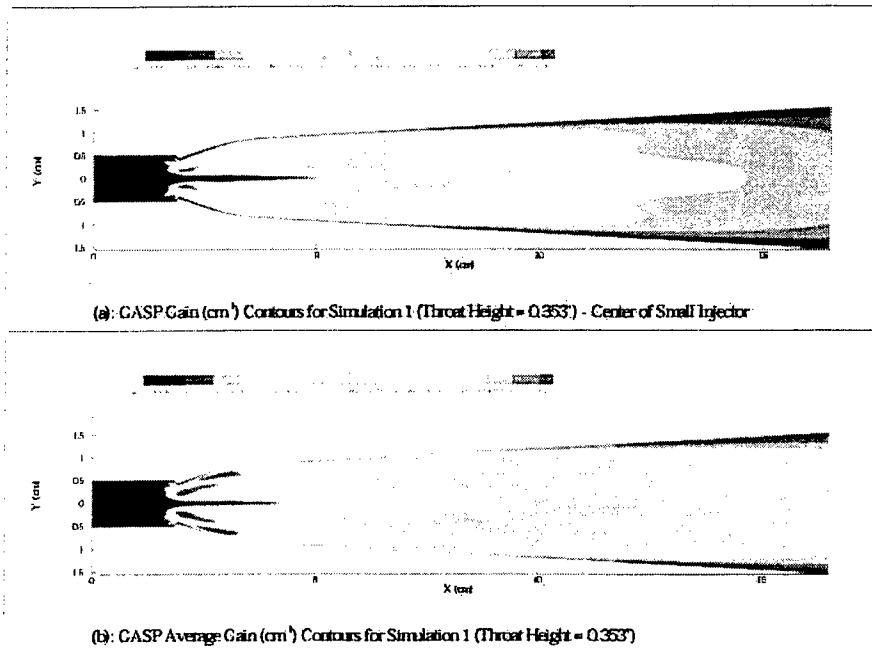


Figure 8. GASP O₂(Δ) mole fraction contours for N₂/Cl₂ = 4:1, Cl₂ = 40 mmol/sec. Throat height of 0.353". Interleaved injectors.



Figures 9a and 9b. GASP gain (1/cm) contours for $N_2/Cl_2 = 4:1$, $Cl_2 = 40$ mmol/sec. Throat height of 0.353". Interleaved injectors.

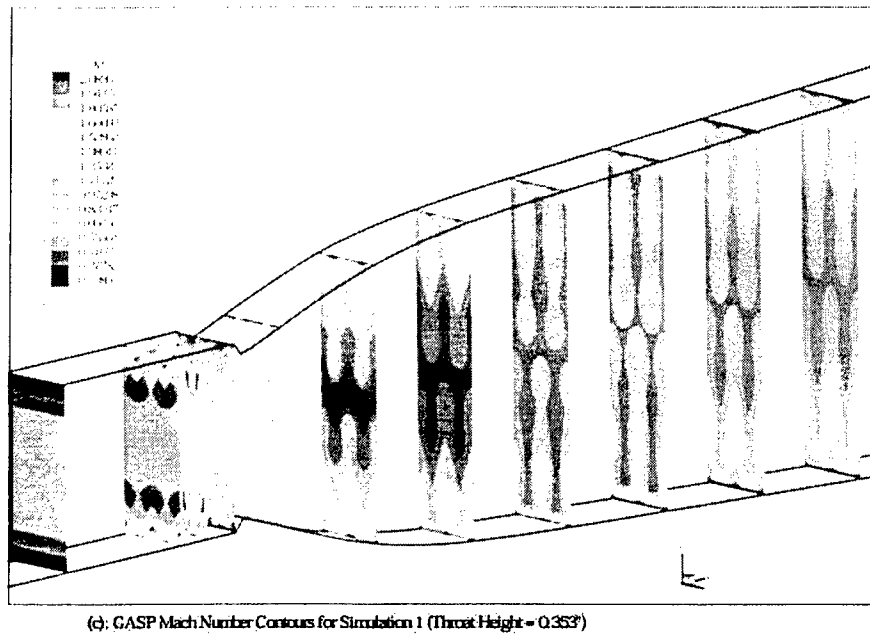
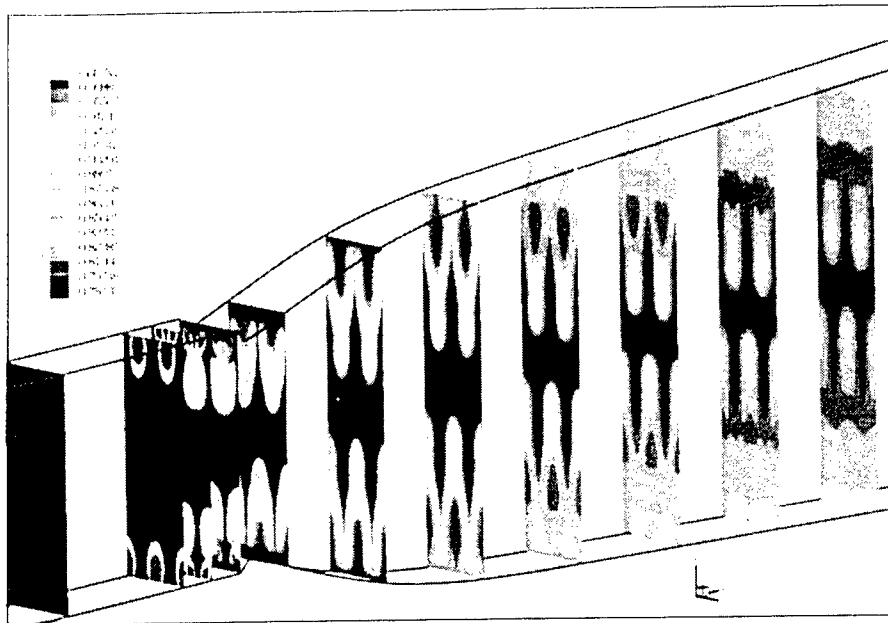
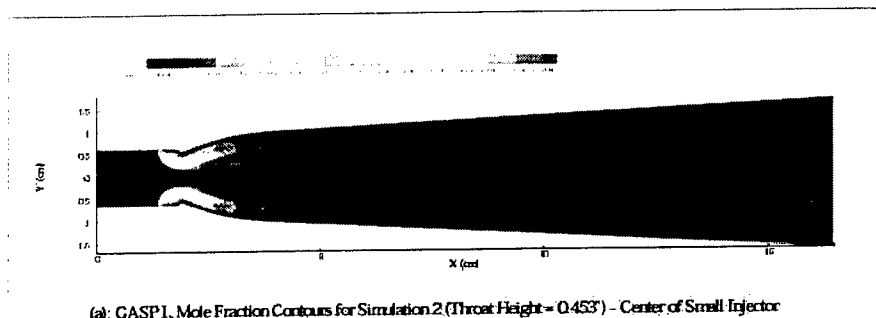


Figure 10. GASP Mach number contours for $N_2/Cl_2 = 4:1$, $Cl_2 = 40$ mmol/sec. Throat height of 0.353". Interleaved injectors.

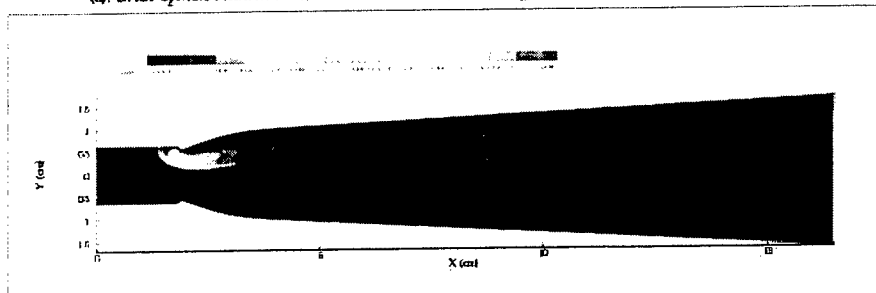


(c): GASP N_2 Mole Fraction Contours for Simulation 2 (Throat Height = 0.453")

Figure 11. GASP N_2 mole fraction contours for $N_2/Cl_2 = 4:1$, $Cl_2 = 40$ mmol/sec. Throat height of 0.453". Interleaved injectors.

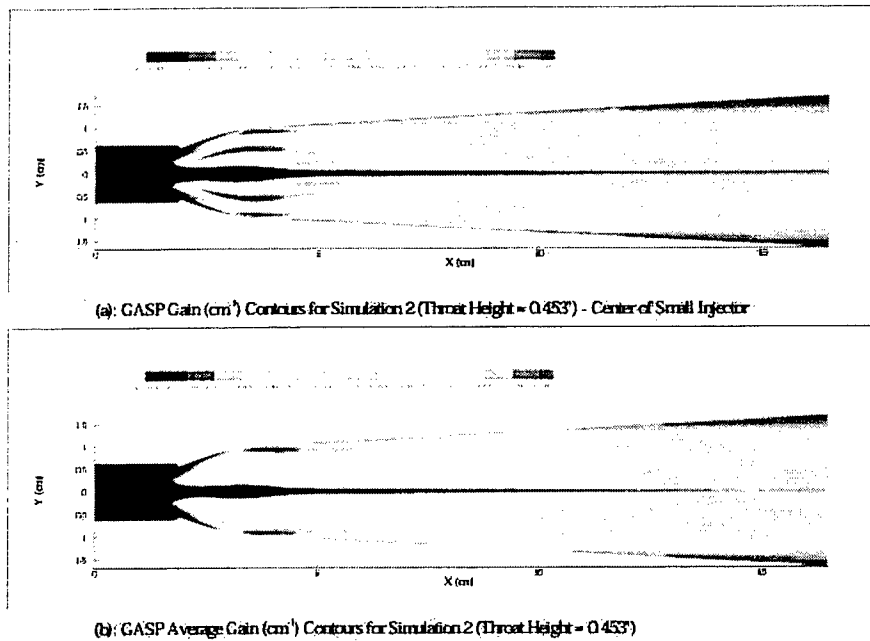


(a): GASP I_2 Mole Fraction Contours for Simulation 2 (Throat Height = 0.453") - Center of Small Injector



(b): GASP I_2 Mole Fraction Contours for Simulation 2 (Throat Height = 0.453") - Center of Upper Large Injector

Figures 12a and 12b. GASP I_2 mole fraction contours for $N_2/Cl_2 = 4:1$, $Cl_2 = 40$ mmol/sec. Throat height of 0.453". Interleaved injectors.



Figures 13a and 13b. GASP gain ($1/\text{cm}$) contours for $\text{N}_2/\text{Cl}_2 = 4:1$, $\text{Cl}_2 = 40$ mmol/sec. Throat height of 0.453". Interleaved injectors.

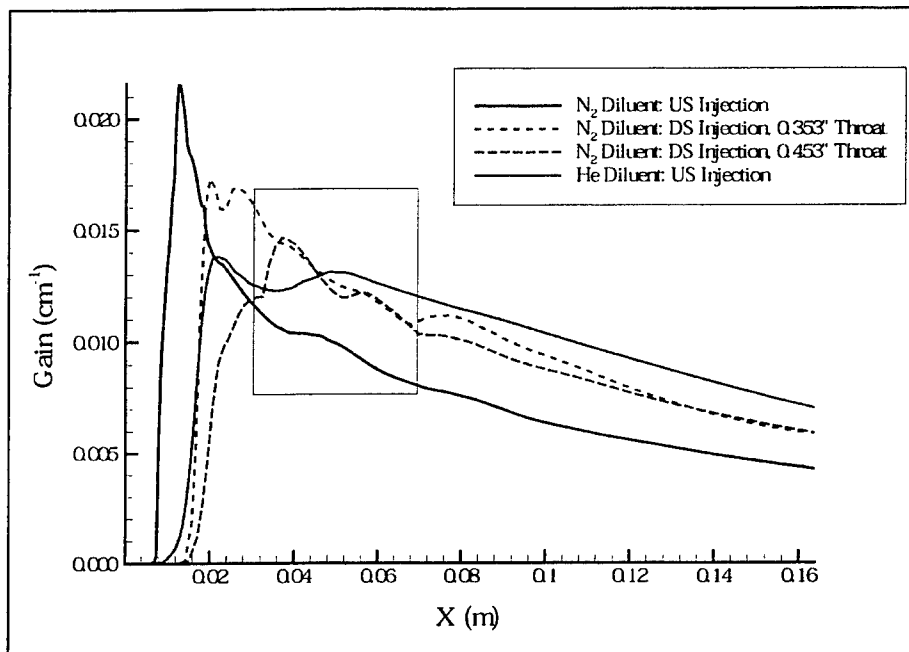


Figure 14. Comparison of the maximum average gain as a function of distance in the flow direction. In all cases, the throat is located at approximately 0.02 m. US denotes I_2 injection 1.1 cm "upstream" of the throat, DS denotes injection further "downstream" at 0.47 cm upstream of the throat.

Current status of chemical oxygen-iodine laser research

S. Rosenwaks, B. D. Barmashenko, D. Furman, E. Bruins and V. Rybalkin
Department of Physics, Ben-Gurion University of the Negev, Beer-Sheva 84105, Israel

ABSTRACT

The chemical oxygen-iodine laser (COIL) is one of the most promising and extensively studied chemical lasers. Nevertheless, the mechanisms governing its operation are not yet fully understood and efforts are underway to find better singlet oxygen chemical generators and improve oxygen/iodine mixing schemes. The latter efforts are briefly reviewed and recent results of parametric studies of an efficient supersonic COIL operating in our laboratory are presented. The laser is energized by a jet type generator, operating without primary buffer gas and applies simple nozzle geometry and mixing of iodine and oxygen at or after the critical cross section.

Keywords: chemical oxygen-iodine lasers, grid nozzle, slit nozzle, transonic mixing, supersonic mixing

1. INTRODUCTION

The operation of the chemical oxygen iodine laser (COIL) [1] is based on an electronic transition of the iodine atom, $I^*(^2P_{1/2}) \rightarrow I(^2P_{3/2}) + h\nu$ (1315 nm), where the upper level is populated by near resonant energy transfer from an $O_2(^1\Delta)$ molecule:



Mixing of the $O_2(^1\Delta)$ (produced in a chemical generator by the reaction of gaseous chlorine with a basic hydrogen peroxide solution) with I_2 molecules results in their dissociation to iodine atoms which are subsequently excited via reaction (1).

Maximum values of both the power (up to 40 kW) and chemical efficiency (~30%) were obtained for supersonic COILs where the primary gas ($O_2 - O_2(^1\Delta) - He$) was brought to supersonic velocity via expansion in a converging-diverging nozzle [2], [3]. Most of the supersonic COILs use a subsonic mixing scheme where the secondary $I_2 - He$ flow is injected into the primary gas in the subsonic section of the nozzle and research in these lasers is described in Refs [2] and [3]. Very often this scheme is not optimal and it is reasonable to move the mixing point downstream to the transonic part of the nozzle. This was done recently in [4], [5] where we reported on an efficient supersonic COIL applying simple nozzle geometry and transonic mixing of iodine and oxygen. This scheme of transonic mixing made it possible to obtain output power of 190 W at 11.8 mmole/s of Cl_2 with no primary buffer gas and very small secondary N_2 flow rate (~ 1 mmole/s). The chemical efficiency, 18%, is about three times higher than that obtained in subsonic mixing without primary buffer gas. The merit of transonic mixing was confirmed in [6], [7] where the power of a supersonic 5 cm gain length COIL was substantially increased by displacing of the iodine mixing point from subsonic to transonic region of the flow (in these studies primary nitrogen was used as a diluent). In [8], a supersonic mixing scheme was studied, where parallel primary and secondary flows with Mach number $M \sim 1.5$ were mixed. Iodine injection in the diverging section of a slit supersonic nozzle was studied theoretically in [9] using three-dimensional CFD code. It was shown that for some conditions this injection scheme demonstrates a performance increase over the traditional subsonic scheme.

To understand the kinetic and mixing processes in supersonic COILs operating without primary buffer gas and different mixing schemes and optimize the output power it is necessary to get information on the small signal gain and iodine dissociation fraction. The gain can be easily measured using diode laser based diagnostic [10], [11]. Indeed, measurements of the gain in supersonic COILs with subsonic injection of iodine were carried out in [10] and [12]. However, it is difficult to measure the dissociation fraction of iodine because the absorption of I_2 molecules in the supersonic portion of the flow is very small, in particular when the gain length is short, as in our laser [4], [5], [10] and

[13]. The most important parameter affecting both the gain and dissociation fraction is the iodine number density and hence the iodine flow rate. The changes in iodine flow mainly affect the rates of chemical reactions and gas temperature and have only weak, indirect (via temperature changes) effect on the flow hydrodynamics.

In the present paper we report on measurements of the gain and temperature in the resonator of a supersonic COIL operating without primary buffer gas and different slit nozzles. Both the gain and the temperature are measured as functions of the iodine flow rate for different schemes of iodine injection, chlorine and secondary buffer gas flow rates, optical axis position along and across the flow and Mach number in the resonator. The results are compared with those obtained in [13] for a grid nozzle. An analytical method was developed in [13] which enables the use of these dependencies for calculation of the iodine dissociation fraction F and the number N of $O_2(^1\Delta)$ molecules lost in the region of iodine dissociation per I_2 molecule. In this paper this method is modified to be applicable to the slit nozzles and applied to results obtained for different mixing schemes.

2. EXPERIMENTAL SETUP

The experimental setup, including a jet-type singlet oxygen generator (JSOG), is similar to that used in [5] and [14]. The BHP is prepared from 4 L 50% wt H_2O_2 + 3.75 L 55% wt KOH (6.9 M HO_2^- and 2.2 M H_2O_2 in excess) and kept at $-20^\circ C$. Two JSOGs are used in this study. The first one, with a flow cross-section of $1.2 \times 5 \text{ cm}^2$ is described in [5] and used mainly for experiments with smaller chlorine flow rate (11.7 mmole/s). The second JSOG has a flow cross section of $1.2 \times 7.5 \text{ cm}^2$ and is connected to an adapter where the flow width decreases from 7.5 to 5 cm. The oxygen produced in the generator flows to a diagnostic cell with a flow cross section of $1 \times 5 \text{ cm}^2$, which serves as an interface between the generator and iodine injectors housing. The $O_2(^1\Delta)$ yield, water vapor fraction, Cl_2 utilization and the temperature of the subsonic flow are simultaneously measured in the diagnostic cell as described in [14].

The iodine-oxygen mixing system is located downstream of the diagnostic cell and uses slit supersonic nozzle. In this paper we study slit nozzles with iodine injection in transonic and supersonic sections of the nozzle and different numbers and diameters of the injection holes. The results are compared with those obtained using grid supersonic nozzle with transonic iodine injection described in [13].

The slit nozzles (Fig. 1) have the same critical cross sections of 2.5 cm^2 as the grid nozzle described in [5]. They have two rows of injection holes in each wall (top and bottom). In slit nozzles No. 1 and 2 iodine is injected at the nozzle throat and in nozzle No. 3 – in the diverging section of the nozzle. The first row of nozzle No.1 has 24, 0.6-mm diameter holes and the second row (lying 1 mm downstream of the first one) has 25, 0.4-mm diameter holes. The total cross section of the injection holes of nozzle No. 1 is close to that of the grid nozzle. The first row of nozzle No.2 has 31, 0.6-mm diameter holes and the second row 62, 0.4 mm diameter holes. Thus, slit nozzle No.2 has a smaller mixing scale but higher total cross section of the injection holes than nozzle No. 1. The first row of nozzle No.3 is located 3 mm downstream of the critical cross section and has 49, 0.5-mm diameter holes. The second row has 50, 0.4-mm diameter holes. The total cross sections of the injection holes for nozzles No.2 and 3 are larger than for nozzle No. 1.

The laser section starts at the nozzle exit plane (flow cross section of $5 \times 1 \text{ cm}^2$) from where the floor and the ceiling diverge at an angle of 8° . The optical resonator is of 5 cm gain length. For the gain diagnostic system we replaced the laser mirrors by optical windows. In most experiments the gain was measured at the optical axis of the resonator, i.e., at the centerline of the flow. Two optical axis positions are available: 4.5 and 8 cm downstream of the nozzle exit-plane. The flow height at the first position of the optical axis is 1.7 cm. The pumps provide a volumetric pumping rate of 1400 L/s, which is 3 times higher than the pumping rate in our previous experiments [5] and [13].

The iodine diagnostic system used in the present work was developed by Physical Sciences Inc [11]. It is based on sensitive absorption spectroscopy by tunable near infrared diode laser monitoring gain for the $I^*(5p^5 \ ^2P_{1/2}, F=3) \rightarrow I(5p^5 \ ^2P_{3/2}, F=4)$ transition at 1315 nm. The laser frequency is scanned over the I transition in a single pass configuration through the gain region in the resonator. The frequency is calibrated in our laboratory using Fabry-Perot resonator. The temperature of the gas in the resonator is found from the width of the Doppler profile of the I transition. It is estimated that the accuracy of the measurements of the gain is $\pm 0.01\%/cm$ and of the temperature $\pm 10 \text{ K}$. The accuracy of the

measurements of the other parameters is discussed in detail in [14].

3. RESULTS AND DISCUSSION

In what follows we present dependencies of the gain g and temperature T in the resonator on the iodine flow rate nI_2 for different flow parameters, types of the nozzles and optical axis positions and find the optimal values of the parameters, corresponding to the maximum gain. Dependencies of F and N on nI_2 and the mixing parameter η (defined in appendix A) are estimated using a simple model presented in Appendix A. Most of the measurements are done for two values of Cl_2 flow rates nCl_2 of ~ 12 and ~ 20 mmole/s. The main results are summarized in Table I.

3.1. Optimal secondary nitrogen flow rate

For any type of nozzle and primary flow conditions there is always some optimal flow rate of the secondary N_2 , nN_2 , corresponding to the maximum value of the gain. To find optimal nN_2 the dependencies of g on nI_2 were monitored at several values of nN_2 . For example, Fig. 2 shows dependencies of g on nI_2 for different values nN_2 for nozzle No.1 at $nCl_2 = 20.1$ mmole/s. It is seen that maximum gain is achieved for optimal nN_2 equal to 8.7 mmole/s. The value of optimal nN_2 depends on the kind of the nozzle, nCl_2 and flow rate of vacuum pump. These dependencies are discussed below.

3.2. Experiments with low pumping rate in the resonator

In our experiments the pumping rate and hence the pressure p in the resonator are controlled by opening a leak downstream of the resonator. Some experiments are carried out with opened leak and hence smaller pumping rate and Mach number in the resonator. It is done to compare our present results with the results of experiments with grid nozzle [13] performed with old pumps having smaller volumetric flow rate of 450 L/s. The opening of the leak is chosen to get the same p (about 1.5 Torr) as in experiments [13] with the grid nozzle at $nCl_2 \cong 11.7$ mmole/s.

Figs. 3 - 5 show dependencies of g , T and F (calculated using the model described in Appendix A) on nI_2 for the slit nozzles No. 1 - 3 at $nCl_2 = 11.7$ mmole/s. Just as in [13], g , and in some cases F , are non-monotonous functions of nI_2 . The maximum gain and corresponding T , F , flow parameters and measured values of the $O_2(^1\Delta)$ yield Y_i , are presented in Table I.

For the slit nozzles the optimal values of nN_2 are higher than for the grid nozzle where the optimal nN_2 was about 1.4 mmole/s. This is because penetration of the iodine jets into the primary flow for the slit nozzles should be larger than for the grid nozzle: larger optimal penetration for the slit nozzle is needed due to the difference in the injection geometry, e.g., the height of the critical cross section of the slit nozzle (0.5 cm) is two times larger than the distance between the injection tubes of the grid nozzle. The optimal nN_2 for slit nozzle No. 2 is higher than for nozzle No.1. This is due to the larger total cross section of the injection holes in the former which necessitate higher nN_2 to reach the same penetration. Nozzle 3 has much higher nN_2 than nozzles No.1 and 2 since the injection point is located in the diverging part of the nozzle where larger penetration is necessary.

The maximum gain for slit nozzles Nos. 1, 2 and 3 under the present conditions is higher than that for the grid nozzle (0.34 %/cm, see [13]). This is probably because the O_2/I_2 mixing parameter for the slit nozzles is higher than for the grid nozzle due to larger optimal penetration, which results in faster initial jet-induced entrainment and mixing. As a result the losses of $O_2(^1\Delta)$, I^* and I_2^* for the grid nozzle are larger than for the slit nozzles. The maximum value of g , 0.53%/cm, is obtained for nozzle No. 1.

nI_2 corresponding to the maximum gain for nozzle No. 3 (iodine injection in the diverging section) is much higher than for nozzles No. 1 and 2, which is due to higher optimal nN_2 (that carries the I_2) for nozzle No. 3. The values of nI_2 corresponding to the maximum g for nozzles No. 1 and 2 are almost the same. However, as seen in Figs. 2 and 3, the value of $nI_2|_{g=0}$ corresponding to zero gain (and hence to the onset of dissociation) for nozzle No. 2 is about 0.2 mmole/s, which is much higher than for nozzle No. 1 where $nI_2|_{g=0}$ is about 0.1 mmole/s. The reason for this behavior is higher value of nN_2 for nozzle No. 2.

The dissociation fraction F for nozzles No. 1 and 2 is higher than for the grid nozzle, which is due to above-mentioned higher mixing parameter in the slit nozzle. For nozzle No. 3, F is much smaller than for nozzles Nos. 1 and 2. This is because of the short residence time of the gas in the volume between the iodine injectors and the resonator optical axis, due to the high jet velocity caused by both high nN_2 and the fact that iodine is injected in the divergent section of the flow.

To determine the values of the mixing parameter η we compared the dependence $N(nI_2)$ with N_{th} as described in Appendix A. These dependencies are shown in Fig. 6 for nozzle No. 1. Just as in [13], $N(nI_2)$ is non-monotonous. Good agreement between N and N_{th} is obtained for η equal to unity. As shown in [13] for the grid nozzle, the best agreement between N and N_{th} is obtained for mixing parameter of ~ 0.5 . Hence the mixing parameter for slit nozzle No. 1 is really higher than for the grid nozzle. The values of η for other nozzles are found the same way and, as shown in Table 1, are close to unity.

The maximum gain increases with increasing chlorine flow-rate as is seen from comparison of runs 3 and 4. To obtain the same penetration as for smaller nCl_2 , the optimal nN_2 also increases with increasing nCl_2 .

The maximum gain decreases as the optical axis is moved downstream. For optical axis located 8 cm downstream of the nozzle exit, maximum g of 0.44 %/cm is obtained for nozzle No. 3 (all flow conditions are the same as in run 4). This value of g is smaller than that measured in run No. 4, where the optical axis is located 4.5 cm downstream of the nozzle exit plane. A possible reason is quenching of I^* and I_2^* (mainly by H_2O) and $O_2(^1\Delta)$ losses with distance. This result is in agreement with the conclusion of [5] that maximum power is achieved when the distance between the optical axis and the supersonic nozzle exit plane is minimal (4.5 cm). That is why all the experiments described below are carried out for optical axis located 4.5 cm downstream of the nozzle exit.

Unlike the gain, the temperature increases monotonously with iodine flow rate (see Figs. 3 – 5). Table 1 shows that the temperature corresponding to the maximum gain is rather high (e.g., in run 1 the temperature is 260 K). This is due to the large heat release in the iodine dissociation reaction and the absence of primary buffer gas.

3.3. Experiments with high pumping rate in the resonator

To obtain maximum pumping rate and Mach number the rest of experiments are carried out with closed leak downstream of the resonator. For high pumping rate the gain measured at 11.7 mmole/s of chlorine is higher than that measured for low pumping rate. This behavior is illustrated comparing the values of the gain obtained in runs Nos. 5 and 6 and Nos. 1 and 2, respectively (Table 1). The values of optimal nN_2 in the runs with closed leak are higher than in the runs with opened leak. A possible reason is that for small nN_2 the static pressure in the resonator with closed leak is too low to achieve large gain. To increase the pressure the value of nN_2 should be larger than for opened leak.

Increase of nCl_2 from ~ 12 mmole/s to ~ 20 mmole/s results in a very small rise of the gain. For example, comparison between the values of g in runs Nos. 5 and 7 shows that for nozzle No. 2 the gain increases from 0.65%/cm to 0.67 %/cm which is within our error limits. Small increase of the gain is also observed for other nozzles, e.g., for nozzle No. 3 and flow conditions of run No. 6, g increases from 0.55 %/cm to 0.60 %/cm.

As seen from Table 1, the maximum values of g for nozzle No.3, with iodine injection in the diverging part of the nozzle, are smaller than for nozzles with transonic injection under similar flow conditions. It should be noted that for high nN_2 ,

the stagnation pressure in the diagnostic cell for nozzle No.3 increases with increasing nN_2 , which means that the flow at the injection location is not supersonic. Hence, although iodine is injected in the diverging part of nozzle No. 3, for large nN_2 the injection is transonic since the N_2/I_2 jets block the primary flow and the critical cross-section moves from the nozzle throat downstream to the iodine injection location. To create supersonic injection the jets should be injected at small angle to the flow direction.

Calculated values of F for closed leak, shown in Table I, are higher than for opened leak. Fig. 7 shows dependencies of g , T and F on nI_2 for nozzle No. 2 at $nCl_2 = 20.1$ mmole/s. It is seen that the maximum value of F is close to unity, the same is correct for all other runs with closed leak. To obtain that calculated F is smaller than one for any nI_2 one should assume that the mixing parameter η is about 0.7 or even smaller, i.e., that mixing is poor. For larger η (close to unity), calculated maximum values of F are larger than one, which is obviously incorrect. The value $\eta = 0.7$ corresponds to the best agreement between N and N_{th} (see Appendix A). As shown in Table I, η is smaller than unity for all runs with closed leak.

To check the above conclusion about poor mixing for closed leak, we measured the gain at a point located 0.2 cm down of the centerline of the flow at equal distances from the centerline and the floor of the supersonic section. The results are presented in Table I, run No.8 (the flow conditions were as in run No. 7). The maximum gain of 0.44%/cm obtained for very high nI_2 , 0.43 mmole/s, is smaller than that obtained in the centerline (0.67%/cm). For $nI_2 = 0.33$ mmole/s (corresponding to the maximum value of g at the centerline), the gain is 0.34%/cm, i.e., only about half of the gain at the centerline, whereas T is only 220 K, i.e., lower than the temperature at the centerline (250 K). That means that for nN_2 corresponding to the maximum gain at the centerline of the flow the elemental iodine is concentrated near the centerline, and the mixing parameter is really small.

That mixing parameter for closed leak is smaller than for opened leak is probably due to higher gas velocity with closed leak because of the larger expansion ratio and nN_2 flow rate. As a result, the residence time of the gas is too small to provide for good mixing.

To optimize the gain, nCl_2 was varied in the range between 12 and 20 mmole/s. The maximum gain of 0.73%/cm was obtained in run No. 9 at nCl_2 of 15 mmole/s.

The values of T corresponding to the maximum g are 245 – 290 K depending on the type of the nozzle and flow conditions and are not much different from the values of T obtained with the opened leak. However, the temperature in the “cold” runs, without adding I_2 to secondary N_2 , T_c (see Appendix A), for closed leak is about 190 K (flow conditions of run No. 7), whereas for opened leak T_c is about 215 K (flow conditions of run No. 1). The difference in T_c is due to different expansion ratios of the flows for opened and closed leak. Using the fact that in the absence of iodine the stagnation temperature T_{0c} (measured in the diagnostic cell and equal to 320 K) does not change along the flow, it is possible to calculate the Mach numbers Ma_c of the flows with opened and closed leak. Ma_c is given by [15]

$$Ma_c = \sqrt{\left(\frac{T_{0c}}{T_c} - 1\right) \frac{2}{\gamma - 1}}, \quad (2)$$

where $\gamma = 1.4$ is a heat capacity ratio. Calculated values of Ma_c are 1.85 and 1.55 for closed and opened leak, respectively.

4. CONCLUSIONS

A parametric study of the gain and temperature in a supersonic COIL operating without buffer gas makes it possible to find optimal values of the flow parameters corresponding to the maximum gain. The gain is studied as a function of the

molar flow rates of various reagents, for different schemes of iodine injection, optical axis position along and across the flow and Mach number in the resonator. Measured values of the gain and temperature in the resonator of the supersonic COIL are used to calculate the iodine dissociation fraction. Maximum gain is achieved when the distance between the optical axis and the supersonic nozzle exit plane is minimal (4.5 cm). For this position of the optical axis maximum gain of 0.73%/cm is obtained at chlorine and secondary nitrogen flow rates of 15 mmole/s and 7 mmole/s, respectively, for a slit nozzle with transonic injection of iodine. For higher chlorine flow rate of 20 mmole/s the maximum gain is a little smaller, 0.67 %/cm. Maximum dissociation fractions in these cases are close to unity.

The value of the maximum gain is almost the same for two slit nozzles (Nos. 1 and 2) with transonic injection and different numbers of injection holes, which means that mixing in the direction of the optical axis is good. However, measurements at a point located down of the flow centerline show that the gain is strongly non-uniform in direction perpendicular to both the flow direction and optical axis, which means that the overall mixing is poor. For slit nozzle No. 3 with iodine injection in the diverging part of the nozzle the values of the maximum gain are smaller than for the nozzles with transonic injection.

Opening a leak downstream of the resonator in order to decrease the Mach number and increase the resonator pressure results in the decrease of the gain and dissociation fraction at the centerline. However, the mixing parameter in this case is close to unity.

The gain is found to be non-monotonous function of the iodine flow rate, whereas the temperature increases with increasing iodine flow. The measured temperatures in the resonator corresponding to the maximum gain are rather high (> 250 K), which is due to the large heat release in the iodine dissociation reaction and the absence of primary buffer gas.

Maximum values of the gain obtained using the slit nozzles are much higher than the values measured in [13] for a grid nozzle where the maximum gain was only 0.34%/cm.

APPENDIX A. MODEL FOR CALCULATION OF F AND N FOR SLIT NOZZLE

The model for calculation of F and N for grid nozzle was presented in [13]. Here this model is modified to be applicable to the slit nozzle. Using the dependencies of g and T on nI_2 we can calculate the I_2 dissociation fraction F at the resonator optical axis. To take into account final mixing rate of iodine, assume that total number density of iodine atoms is non-uniform in direction y perpendicular to both the flow direction and resonator optical axis:

$$[I] + [I^*] = \frac{p}{kT} \frac{nI_2}{n} Ff(y), \quad (A1)$$

$$\int_{-H/2}^{H/2} f(y) dy = H,$$

where n is the total flow rate, $f(y)$ a normalized form-factor and H is the height of the flow duct. Therefore the iodine mixing parameter can be defined as

$$\eta = 1 / f(0). \quad (A2)$$

For uniform iodine distribution both $f(0)$ and η are equal to unity. If the mixing is slow and iodine is concentrated near the centerline one has $f(0) \gg 1$ and $\eta \ll 1$, which means that mixing parameter is small.

The relation between the local gain g , F and the $O_2(^1\Delta)$ yield Y at the optical axis is [13]

$$g = \sigma_0 \left(\frac{300}{T} \right)^{1/2} \frac{p}{kT} \frac{nI_2}{n} F \frac{(2K_e + 1)Y - 1}{(K_e - 1)Y + 1}, \quad (A3)$$

where $K_e = 0.75 \exp(402/T)$ is the equilibrium constant of reaction (1). The following relation connects Y with the yield Y_i before the iodine injection:

$$Y = Y_i - \frac{nI_2 F}{nO_2} N, \quad (A4)$$

where $nO_2 = (nCl_2)_0 U$ is the oxygen flow rate and U the chlorine utilization in the $O_2(^1\Delta)$ generator. Eq. (A4) assumes that since the diffusion coefficient of O_2 is about three times larger than that of iodine, the oxygen is distributed uniformly over y . For the opposite limiting case of slow diffusion of oxygen, nI_2 in Eq. (A4) should be substituted by nI_2/η . However, application of the model to the experimental data shows that the approximation of slow oxygen diffusion results in too small values of Y , and hence in our analysis we use assumption of fast diffusion of oxygen where Y is given by Eq. (A4).

N can be found from the energy conservation equation:

$$c_p [(n_p + n_s)T_0 - n_p(T_{0i})_p - n_s(T_{0i})_s] = q_\Delta nI_2 FN - q_{I_2} nI_2 F - q_{I^*} nI_2 F \frac{2K_e Y}{(K_e - 1)Y + 1}, \quad (A5)$$

where $c_p = 7/2 k$ is the specific heat capacity of diatomic gas, $n_p = (nCl_2)_0 + nH_2O$ and $n_s = nN_2 + nI_2$ are the primary and secondary flow rates, T_0 the stagnation temperature of the flow in the reaction zone, $(T_{0i})_p$ and $(T_{0i})_s$ the stagnation temperatures of the primary and secondary flow, respectively and $q_\Delta = 11,340$ K, $q_{I_2} = 18,400$ K and $q_{I^*} = 10,954$ K are the energy of $O_2(^1\Delta)$, dissociation energy of I_2 and energy of $I^*(^2P_{1/2})$, respectively. The first term in the right-hand-side of Eq. (A5) corresponds to the energy lost by $O_2(^1\Delta)$ in the region of I_2 dissociation, the second term to the energy of I_2 dissociation, and the third term to the energy of excitation of the iodine atoms produced via the iodine dissociation.

Just as in [13], T_0 is given by:

$$T_0 = T_{0c} \frac{\mu}{\mu_c} + T - T_c \frac{\mu}{\mu_c}, \quad (A6)$$

where T_c and μ_c are the static temperature and molecular weight in the "cold" runs without adding I_2 to secondary N_2 . The value of T_c was found by linear extrapolation of $T(nI_2)$, shown in Figs. 3-5, to nI_2 , corresponding to zero gain. For example, for slit nozzle No. 1 (Fig. 3) zero gain is achieved at $nI_2 = 0.15$ mmole/s and T_c is of 215 K.

$$T_{0c} = \frac{n_p(T_{0i})_p + nN_2(T_{0i})_s}{n_p + nN_2} \quad (A7)$$

is the stagnation temperature in the cold runs.

Solving the system of equations (A3) – (A5), with T_0 given by Eqs. (A6) and (A7), we find dependencies of F , N and Y on nI_2 . The mixing parameter η is unknown parameter. To determine the value of η we compared the dependence $N(nI_2)$ with the theoretical value of the number N (indicated below as N_{th}) suggested in [16] and [17]:

$$N_{th} = 1 + 1/\eta_{dis} - \frac{(k_w nH_2O + k_o Y nO_2) \ln(1-F)}{\eta_{dis} k_7 nI_2} + \frac{2K_e Y}{(K_e - 1)Y + 1} \quad (A8)$$

where $\eta_{dis} = k_8[O_2(^1\Delta)] / (k_8[O_2(^1\Delta)] + \sum_M k_{qM}[M])$ is the dissociation efficiency [16], $k_w = 2 \times 10^{-12} \text{ cm}^3/\text{s}$ and $k_o = 10^{-13} \text{ cm}^3/\text{s}$ are the rate constant of quenching of I^* atom by water and singlet oxygen molecules, respectively, $k_7 = 3 \times 10^{-11} \text{ cm}^3/\text{s}$ and $k_8 = 3 \times 10^{-10} \text{ cm}^3/\text{s}$ the rate constants of the reactions (7) and (8), respectively and k_{qM} is the rate constant of quenching of I_2^* by a type M molecule ($M = O_2, N_2$ and H_2O). The values of the rate constants are the same as in [16]. Expression (A8) for N_{th} is correct only for small values of nI_2 when the changes of the yield Y are small and F increases with increasing nI_2 [16].

REFERENCES

- [1] W. E. McDermott, N. R. Pchelkin, D. J. Benard, R. R. Bousek, "An electronic transition chemical laser," *Appl. Phys. Lett.*, vol. 32, pp. 469-470, 1978.
- [2] K. A. Truesdell and S. E. Lamberson, "Phillips laboratory COIL technology overview," *SPIE*, vol. 1810, pp. 476 - 492, 1992.
- [3] N. N. Yuryshev, "Chemically pumped oxygen-iodine laser," *Quantum Electronics*, vol. 23, pp. 583 - 600, 1996.
- [4] D. Furman, B. D. Barmashenko and S. Rosenwaks, "An efficient supersonic chemical oxygen-iodine laser operating without buffer gas and with simple nozzle geometry," *Appl. Phys. Lett.*, vol. 70, pp. 2341-2343, 1997.
- [5] D. Furman, B. D. Barmashenko and S. Rosenwaks, "Parametric study of an efficient supersonic chemical oxygen-iodine laser/jet generator system operating without buffer gas," *IEEE J. Quantum Electronics*, vol. 34, pp. 1068 -1074, 1998.
- [6] M. V. Zagidullin, V. D. Nikolaev, M. V. Svistun, N. A. Hvatov and N. I. Ufimtsev, "Highly efficient supersonic chemical oxygen-iodine laser with a chlorine flow rate of 10 mmole/s," *Quantum Electronics*, vol. 27, pp. 195 -199, 1997.
- [7] D. L. Carroll, D. M. King, L. ockler, D. Stromberg, W. C. Solomon, L. H. Sentman and C. H. Fisher, "High-performance chemical oxygen-iodine laser using nitrogen diluent for commercial applications," *IEEE J. Quantum Electronics*, vol. 36, pp. 40-51, 2000.
- [8] V. N. Azyazov, M. V. Zagidullin, V. D. Nikolaev and V. S. Safonov, "Chemical oxygen-iodine laser with mixing of supersonic jets," *Quantum Electronics*, vol. 27, pp. 491-494, 1997.
- [9] T. G. Madden, G. D. Hager, A. I. Lampson and P. G. Crowell, "An investigation of Supersonic Mixing Mechanizm for the Chemical Oxygen-Iodine Laser (COIL)," in *AIAA 30th Plasmadynamics and Lasers Conf.*, Norfolk, VA, June 28- July 1, 1999, paper 99-3429.

- [10] E. Lebiush, B. D. Barmashenko, A. Elior and S. Rosenwaks, "Parametric study of the gain in a small scale, grid nozzle supersonic chemical oxygen-iodine laser," *IEEE J. Quantum Electronics*, vol.31, pp. 903-909, 1995.
- [11] S. J. Davis, M. G. Allen, W. J. Kessler, K. R. McManus, M. F. Miller and P. A. Mulhall, "Diode laser-based sensors for chemical oxygen-iodine lasers," *SPIE*, vol. 2702, pp. 195 – 201,1996.
- [12] P. B. Keating, B. A. Anderson, C. A. Helms, T. L. Rittenhouse, G. D. Hager, and K. A. Truesdell, "2-D spatial gain maps in a small scale chemical oxygen-iodine laser," in *Proc. Int. Conf. Lasers '96*, Portland, OR, Dec. 1996.
- [13] D. Furman, E. Bruins, B. D. Barmashenko and S. Rosenwaks, "Small signal gain and iodine dissociation in a supersonic chemical oxygen-iodine laser with transonic injection of iodine," *Appl. Phys. Lett.*, vol. 74, pp. 3093-3095, 1999.
- [14] D. Furman, B. D. Barmashenko and S. Rosenwaks, "Diode-laser based absorption spectroscopy diagnostics of a jet-type generator for chemical oxygen-iodine lasers," *IEEE J. Quantum Electronics*, vol. 35, pp. 540-547, 1999.
- [15] A. H. Shapiro, *The Dynamics and Thermodynamics of Compressible Fluid Flow*. New York: Ronald, 1953, vol. 1, pp. 73-110.
- [16] B. D. Barmashenko and S. Rosenwaks, "Power dependence of chemical oxygen-iodine lasers on iodine dissociation," *ALAA J.*, vol. 34, pp. 2569-2574, 1996
- [17] V. Quan, " Analytical evaluation of kinetics in oxygen-iodine laser nozzle flows," *SPIE*, vol. 2989, 114 – 125,1997.

Table I. Typical results of the measured maximum gain g and temperature T in the resonator and estimated iodine dissociation fraction F and gain mixing parameter η for optical axis located 4.5 cm downstream of the nozzle exit plane. In all the runs the chlorine utilization and water vapor fraction are about 0.9 and 0.08, respectively. The accuracy of the measurements is given at the end of section II.

Run No.	Nozzle type	n_{Cl_2} [mmole/s]	n_{N_2} [mmole/s]	n_{I_2} [mmole/s]	Leak	p , [Torr]	Y_i	g [%/cm]	T [K]	F	η
1	No. 1	11.7	2.5	0.26	opened	1.4	0.6	0.53	260	0.6	1
2	No. 2	11.8	4	0.27	opened	1.45	0.55	0.45	240	0.4	1
3	No. 3*	11.7	7	0.38	opened	1.55	0.55	0.40	220	0.25	1
4	No. 3*	20	12.7	0.31	opened	1.9	0.52	0.48	238	0.6	1
5	No. 2	11.8	5.1	0.29	closed	1	0.52	0.65	270	0.93	0.7
6	No. 3*	12	11.5	0.35	closed	1.35	0.5	0.55	290	0.6	0.5
7	No. 2	20.1	8.7	0.33	closed	1.3	0.52	0.67	250	0.9	0.7
8**	No. 2	20.1	8.7	0.43	closed	1.3	0.5	0.44	260	-	-
9	No. 2	15.1	7.1	0.3	closed	1.1	0.52	0.73	245	1	0.75

*Iodine injection in the diverging section.

**The gain is measured at a point located 0.2 cm down of the centerline of the flow, F and mixing parameter are not calculated for this run because the model presented in Appendix A is applicable only to the gain measurements at the centerline of the flow.

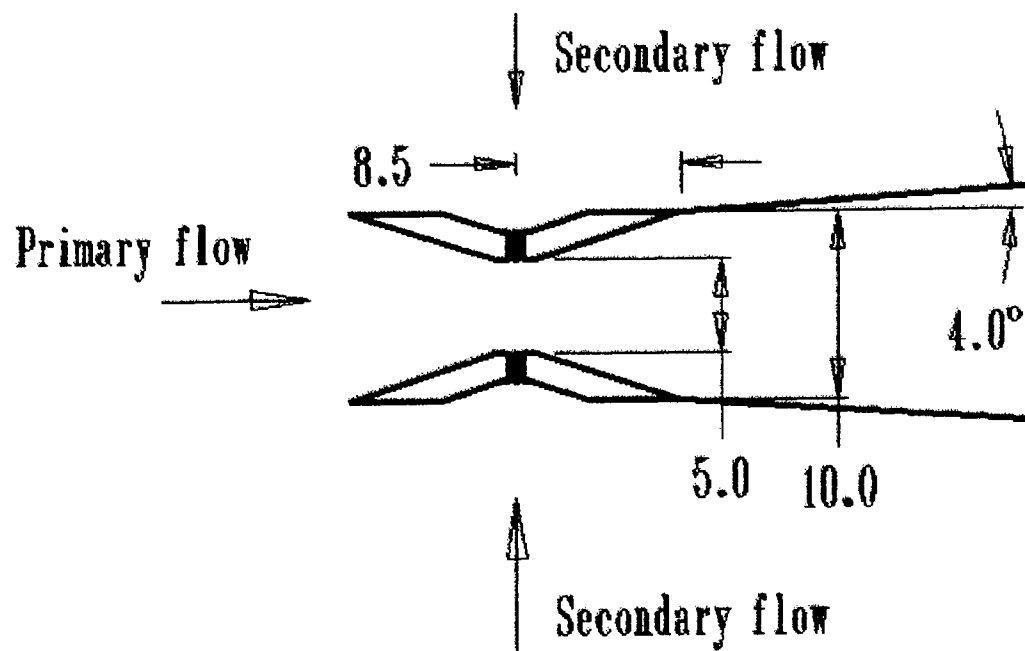


Fig. 1. Schematics of the slit nozzle. All measures are in millimeters.

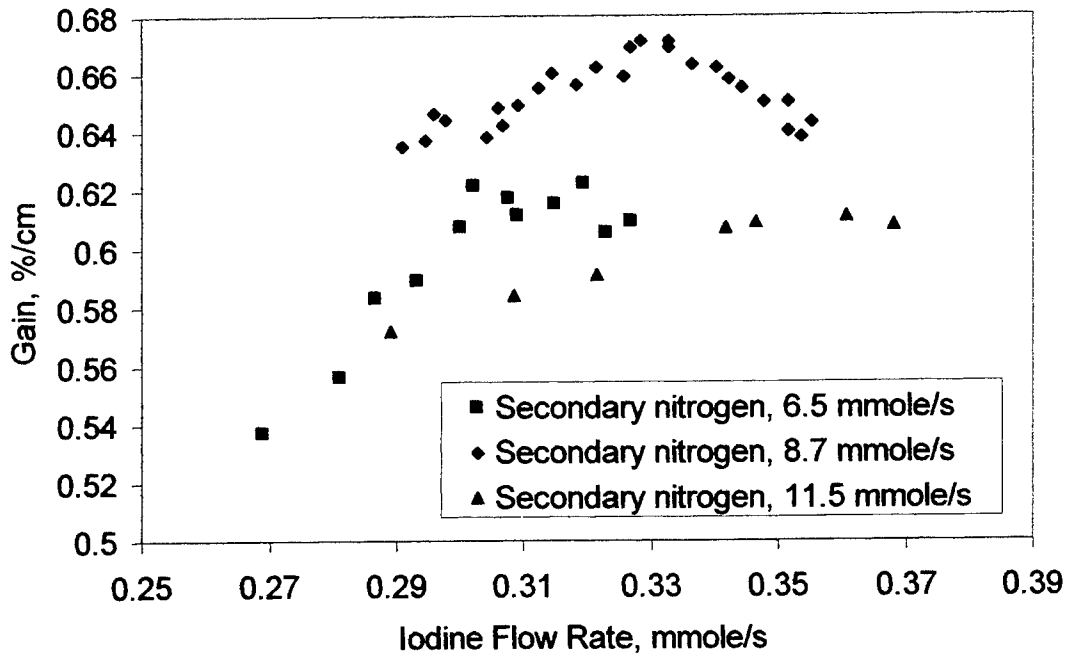


Fig. 2. Dependencies of the gain on the iodine flow rate for different values of the secondary nitrogen flow rate for nozzle No. 2. The chlorine flow rate is 20.1 mmole/s.

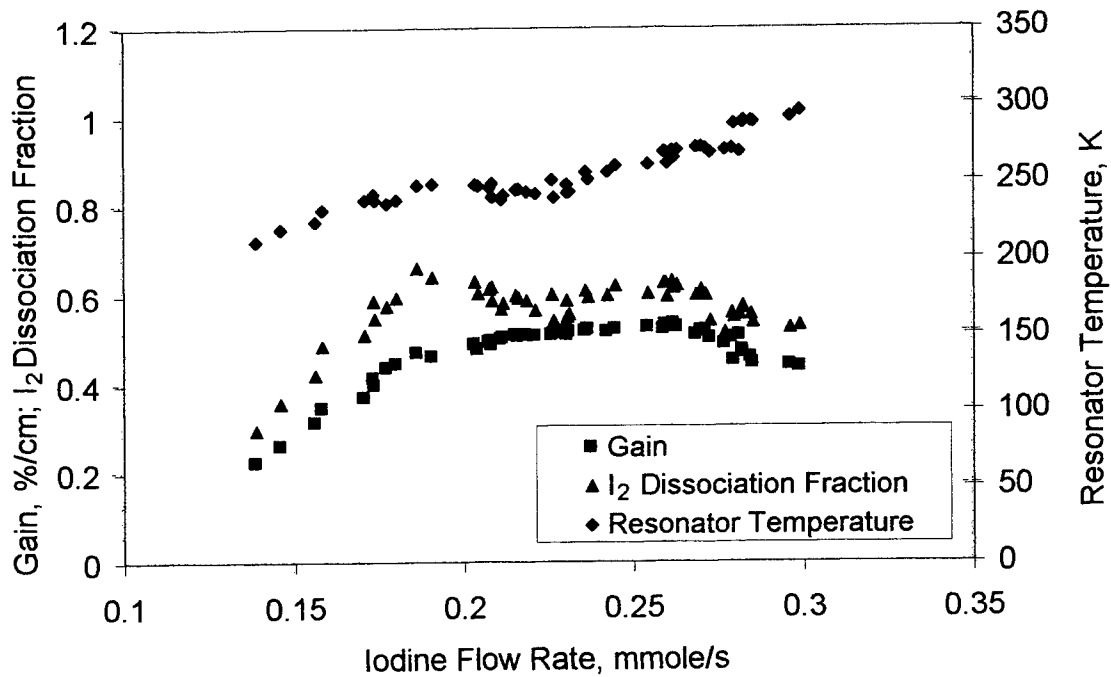


Fig. 3. The gain, temperature and iodine dissociation fraction at the resonator optical axis for slit nozzle No. 1 as a function of the iodine flow rate. The chlorine and secondary nitrogen flow rates are 11.7 and 2.5 mmole/s, respectively, the leak downstream of the resonator is opened (run No. 1, Table I).

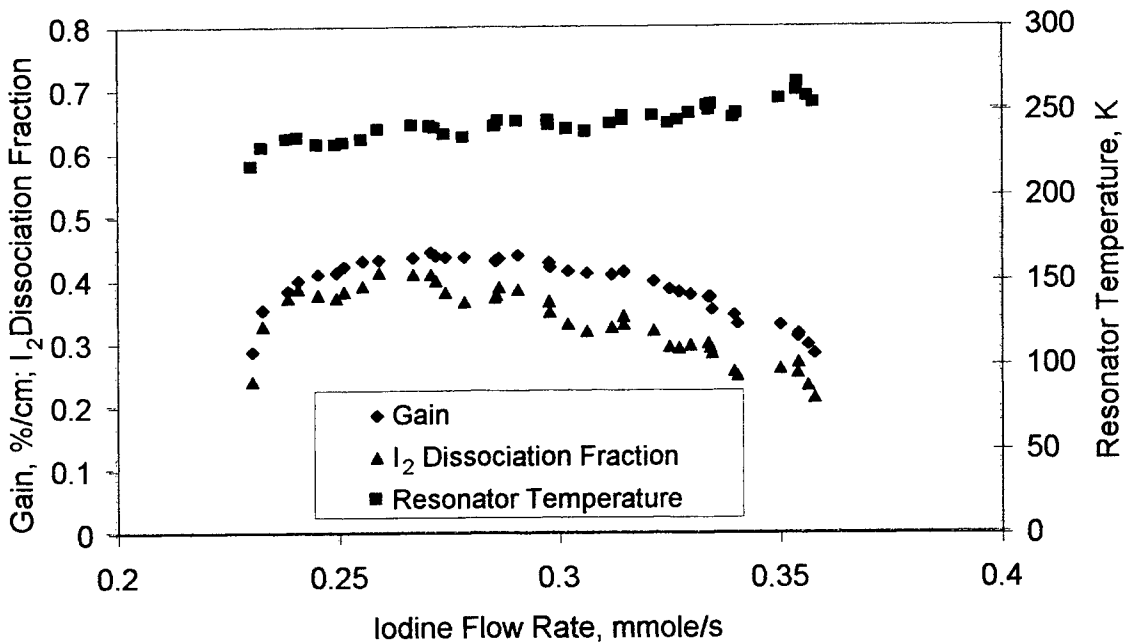


Fig. 4. The gain, temperature and iodine dissociation fraction at the resonator optical axis for slit nozzle No. 2 as a function of the iodine flow rate. The chlorine and secondary nitrogen flow rates are 11.8 and 4 mmole/s, respectively, the leak downstream of the resonator is opened (run No. 2, Table I).

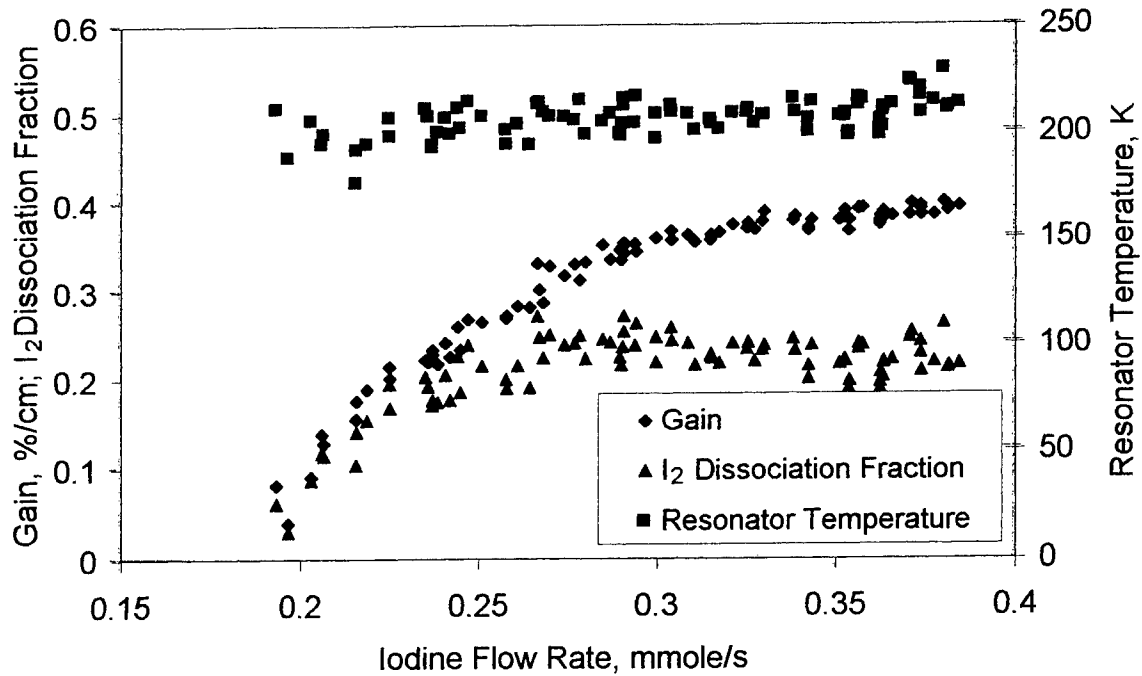
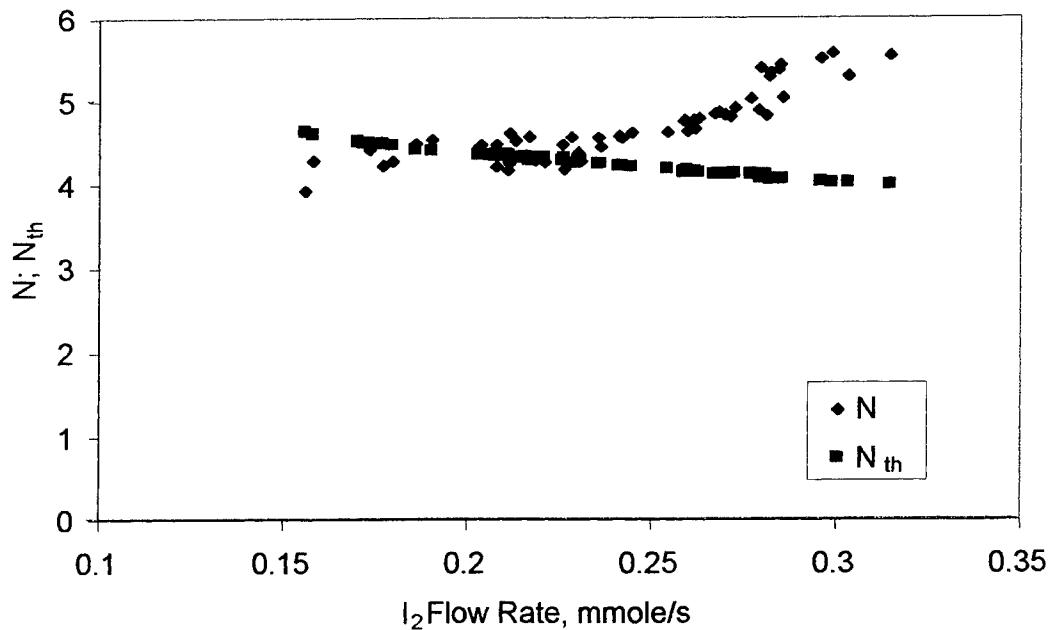


Fig. 5. The gain, temperature and iodine dissociation fraction at the resonator optical axis for slit nozzle No. 3 (iodine injection in the diverging section) as a function of the iodine flow rate. The chlorine and secondary nitrogen flow rates are



11.7 and 7 mmole/s, respectively, the leak downstream of the resonator is opened (run No. 1, Table I).
 Fig. 6. Slit nozzle No. 1 parameters calculated from the experimental (N) and theoretical (N_{th}) numbers of $O_2(^1\Delta)$ molecules lost in the region of iodine dissociation per I_2 molecule as a function of the iodine flow rate for mixing parameter $\eta = 1$. The flow conditions are as in Fig. 3.

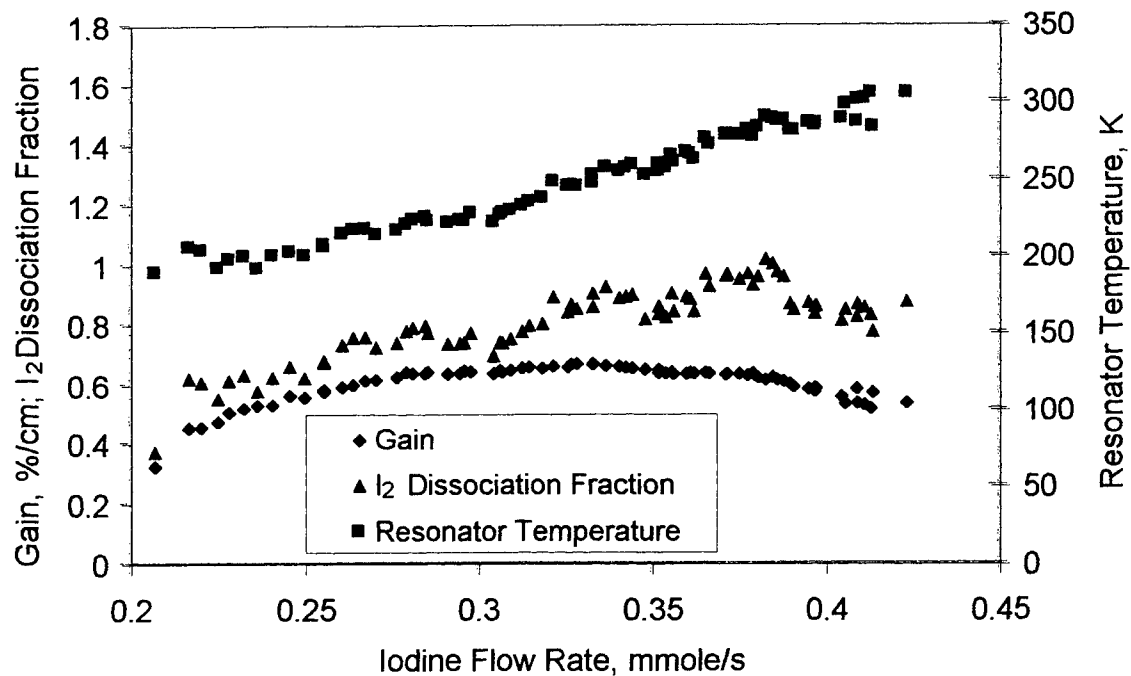


Fig. 7. The gain, temperature and iodine dissociation fraction at the resonator optical axis for slit nozzle No. 2 as a function of the iodine flow rate. The chlorine and secondary nitrogen flow rates are 20.1 and 8.7 mmole/s, respectively, the leak downstream of the resonator is closed (run No. 7, Table I).

AMPLIFICATION OF IMAGE BRIGHTNESS BY MEANS OF THE PHOTODISSOCIATIVE IODINE LASER

Ig.V.Bagrov, O.B.Danilov, S.A.Tul'skii, A.P.Zhevlakov.
Institute for Laser Physics, St. Petersburg, 199034 Russia

ABSTRACT

A possibility of the amplification of image brightness by the active medium of the photodissociative iodine laser have been demonstrated. The brightness of the test-object image with spatial frequency of 10 mm^{-1} was amplified 1600 times for Q-switch lasing action and 250 times for free-running one. The contrast of amplified image was equaled 0.8 in both occasions. The smallest input signal achieved the level of 10^{-13} J per pixel.

Key words: amplifier; iodine laser; amplitude image.

1. INTRODUCTION

The inverted medium of photodissociative iodine laser (PIL) is characterized by a high optical quality of $\Delta n \ll 10^{-6}$ under favorable conditions of laser radiation when the relaxation processes are absent and when it is possible to neglected by the influence of surface gasdynamic waves [1,2]. This fact allows to effectively amplify a signal with determined wave front in schemes of PIL, for example, for the reproduction of a lowly illuminated image. The possibility of amplitude amplification of image brightness by means of one pass iodine amplifier with a lamp pumping was investigated in the present work .

2. EXPERIMENT

The experiments were carried out according to the "master oscillator - power amplifier" scheme as shown in Fig.1. The pump in each of two laser stages was made by non-magnetic coaxial Xe-lamps therefore the concordance of corresponding spectral superfine structure with only one $F=3 \rightarrow F=4$ component was provided [3]. The inner quartz tubes of the both lamps served as a cells for gas mixture $n\text{-C}_3\text{F}_7\text{I}:\text{SF}_6$ at the same time. The active zone diameter and length were respectively 0.8 cm and 50 cm in the master oscillator and 1.8 cm and 100 cm in the amplifier. The pulse durations were $6\mu\text{s}$ for free-running regime and 50 ns for Q-switch one. In the last case the passive Q-switch modulator placed inside the resonator of the master oscillator was made with № 1061-phthalocyanine dye by an initial transmission of 10%. The pinhole of \varnothing 4 mm was installed inside the resonator to form a single mode laser beam.

The investigations were conducted in two stages. At first we studied a quality of an image amplified in iodine inverted medium. The liquid-crystal spatial modulator (LCSM) [4,5] disposed between the master oscillator and the amplifier was used as the test-object (Fig.2,a). This sample of 35 mm diameter was produced on base of two BaF_2 substrates with a strip Cu-electrodes which had a width of 0.3 mm and between distance of 0.1 mm. The dark line being in middle of LCSM picture accords to the region filled by the LC. A single laser pulse was relayed on the test-object by different energy levels. The LCSM-sample was replaced by the standard grid test-object in the other case (Fig.2,b,c) in order to define a whole quantity of the pixels in the view field of this laser imaging system.

An electron-optical converter (EOC) was used to registrate a amplified image in 1315 nm lasing wavelength. The image of the test-object was reproduced on a EOC photocathode with 2^* -magnification by means

of two spherical lenses. The iodine amplifier was mounted between these lenses. The distances were 1.5 m from a master oscillator to a test-object and 0.5 m between a test-object and first lens in front of the amplifier.

On second stage we defined a maximal sensitivity of our quantum amplifier to the input signal transmitted through the standard grid. The radiation energy level after the master oscillator was varied in the diapason of six orders, i.e. from 0.1 J to 0.1 nJ, by means of the calibrated glass filters. The germanium photodiode with a low noise electron-amplifier by a coefficient $K_u = 300$ as a detector was located at 10 m far from out pupil of the iodine amplifier to decrease the intensity of lamp emission as a noise. The additional lens was disposed in front of the detector for the collection of laser radiation.

3. RESULTS

The brightness of the test-object image was amplified 1600 times for Q-switch lasing action and 250 times for free-running one. The contrast of an amplified image was produced as well as 0.8 in both regimes (Fig.2,a,b). The input signal on the amplifier entrance had been reduced to the level of 10^{-10} J for the Q-switch lasing action. There are 10^3 pixels in a total view field. Thus, we reached the value of 10^{-13} J per pixel as a smallest signal on the entrance to the iodine amplifier. In this case the contrast of the amplified image have been decreased down to 0.4. Fig.2,c illustrates that the fragment of number 10 with a spatial frequency of 10 mm^{-1} was reproduced through the iodine amplifier by rather good quality. This magnitude of the spatial resolution corresponds to the diffraction limit defined by the size of the amplifier aperture.

4. CONCLUSION

Our experimental results showed a possibility for the effective use of inverted medium of the photodissociative iodine laser for a registration of the image of the feebly illuminated objects. This fact is conditioned by such specific characteristics of the iodine active medium as a low level of the noise, a power amplification of the small signal and a high optical quality, providing diffraction accuracy of the image.

REFERENCES

1. O.B.Danilov, A.P.Zhevlakov, S.A.Tul'skii, Ig.L.Yachnev. - An investigation of a high-efficiency free-running photodissociation laser.- *Kvantovaya elektronika* 1982, 9, № 6, p.1245-1250 (Russia).
2. O.B.Danilov, A.A.Artemov, A.P.Zhevlakov. -Problems of efficiency and scaling for iodine pulse-repetitive flash-lamp pumped laser. - *Proc. SPIE* 1993,v.1980, 41-48.
3. V.G.Bespalov, O.B.Danilov, S.A.Tul'skii, A.P.Zhevlakov. - Four-wave mixing in inverted medium of the iodine photo- dissociative amplifier. - *Proc. SPIE* 1996, v.2771, p.202-206.
4. P.V.Adomenas, S.F.Saluchko, V.V.Danilov, A.P.Zhevlakov, D.O.Leschenko, D.A.Savel'ev.- Intracavity control of laser radiation by means of modulator based on microcapsulated LC.- *Sov. J. of Optical Technology* 1991, vol. 58, no. 1, p.9-11.
5. Ig.V.Bagrov, M.V.Gryaznova, V.V.Danilov, A.P.Zhevlakov, E.N.Sosnov, S.A.Tul'skii. - Liquid-crystal modulators as laser-optics elements for the muddle IR range.- *Optics and spectroscopy*, 1999,vol.87, no.5, p. 779-789 (translated from Russian *Optika i spektroskopiya*, 1999, vol.87, no.5, p.853-864).

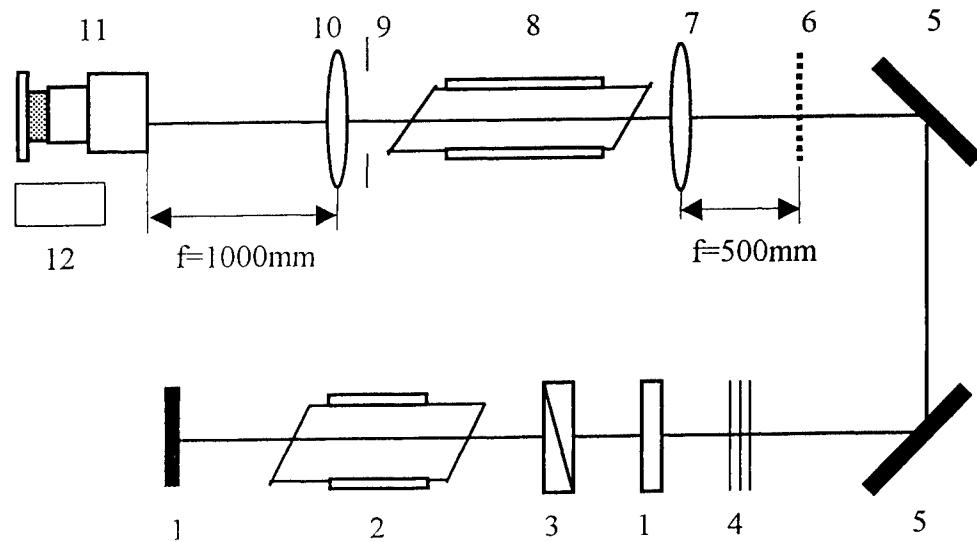
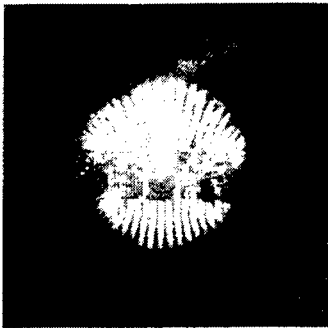
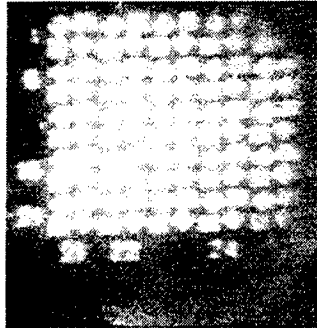


Fig.1 Experimental setup.

1-cavity mirrors; 2-master oscillator head; 3-Q-switch; 4-glass filter; 5-rotate mirrors; 6-test object; 7,10-lenses; 8-amplifier head; 9-pinhole $\varnothing 18\text{mm}$; 11-electron-optical converter with photocamera; 12-photodetector.



a



b



c

Fig.2. Amplified image of the test objects.
a-sample of LCSM; b, c – standard grid by the different illumination intensity (c-magnified scale)

Possibility of realizing fullerene-oxygen-iodine laser with solar pumping (Sun-Light FOIL)

O. B. Danilov, I. M. Belousova, A. A. Mak, V. Yu. Zalesskiy, V. A. Grigor'ev,
A. V. Kris'ko, E. N. Sosnov, V. P. Belousov

Research Institute for Laser Physics
12 Birjevaya line, 199034, St. Peterburg, Russia
E-mail: danilov@ilph.spb.ru

We consider the possibility to design the fullerene-oxygen-iodine laser with optical pumping (solar, particularly) [1]. It is assumed that singlet oxygen is formed at pass of molecular oxygen through (and interaction with) mixture of lower and higher fullerenes in the triplet metastable state obtained at illumination of fullerenes. The presented results of estimates by a photokinetic model show the opportunity to reach the efficiency of the FOIL with solar pumping at the level of several tens of percents. We present the results of experimental and theoretical studies of singlet oxygen yield at interaction of optical pumping with fullerene in solutions. Laser radiation with wavelength of 532 nm and wideband lamp radiation for imitation of solar radiation were used as pumping.

Keywords: fullerene-oxygen-iodine laser, solar pumping.

1. Introduction

Paper [2] was probably the first publication, which presented the photochemical kinetics of the photodissociative iodine laser with solar pumping in details. Conceptual design of the space-based photodissociative laser with power of 50 kW and power density per weight of 5 W/kg was suggested in [3]. This result can be considered as satisfactory, since it is based on very low efficiency of photodissociative laser with solar pumping (in [2,3] it was lower than 0.1%). There are two main reasons of such low efficiency: 1) strong mismatching between solar radiation spectrum and spectrum of alcyliodide molecule absorption and 2) large value of Stokes losses (ratio of pumping photon energy to lasing photon energy for the photodissociative iodine laser is about 5). We realized the maximum efficiency of photodissociative laser (about 2%) by specially designed high-efficiency UV Z-pinch pumping source and specially selected photochemical kinetics with minimization of pumping losses, losses of excited atomic iodine, and losses due to the optical inhomogeneities of the active medium [4]. However, we had no opportunity to diminish the Stokes losses.

Here we consider the other photochemical scheme of the iodine laser such as kinetic scheme of the fullerene-oxygen-iodine laser that allows us to essentially increase the efficiency of the iodine laser with optical pumping, including the solar one. Simultaneously we present some experimental and theoretical results of studies on formation of singlet oxygen at interaction of oxygen molecules with optically excited fullerene molecules in the triplet state obtained at irradiation of sample by as pulsed laser source, so pulsed lamp, imitating the solar radiation.

2. Kinetic scheme of Sun-Light FOIL, main reactions and constants

Figure 1 presents kinetic scheme of the fullerene-oxygen-iodine laser with

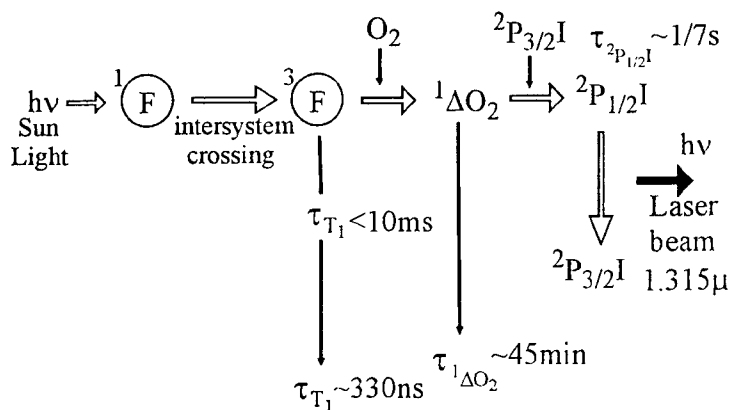


Figure 1. Kinetic scheme of Sun-Light FOIL

optical, including solar, pumping. The pumping photon with wavelength in the area of 300-700 nm is absorbed by fullerene in the channel of singlet states (1F). Fullerene transits in the lower triplet state (3F) during the time interval of about 1 ns. By data of [6], the radiative lifetime of 3F state may reach 10^{-2} s. This lifetime essentially depends on the quencher presence. The molecular oxygen is one of the strongest quenchers. In its presence, the lifetime of the triplet state reduces down to 330 ns, whereas the molecular oxygen transits into the singlet state (mainly, $^1\Delta O_2$) with quantum yield up to 0.96 [5,6]. Further operation of the laser is performed in accordance with the usual scheme of the continuous oxygen-iodine laser (COIL). The key part of the considered scheme is the part, which can be called as generator of the singlet oxygen with optical pumping. First of all, we outline some moments in the kinetic scheme presented in Fig. 1. In the case of solar pumping, application of fullerene C_{60} enables effective absorption of about 60% of the input energy. Using the mixtures of fullerenes, containing C_{60} , C_{70} , C_{76} and so on, it is possible to absorb and utilize more than 90% of the solar energy, concentrating excitation at the lower metastable triplet state of each fullerene type, from which excitation transfers to the oxygen molecule with its transition into the $^1\Delta O_2$ state. Such type pumping results in significant reduction of the effective Stokes losses relative to the case of optical pumping of the photodissociative iodine laser.

The principle of design of singlet oxygen generator is very important. One of the possible generator variants is a multilayer membrane of fullerene mixture illuminated by photon flux. The oxygen flow passes through the membrane towards the pumping radiation, as it is shown in Fig. 2, with output of the singlet oxygen into the volume of lasing (cavity).

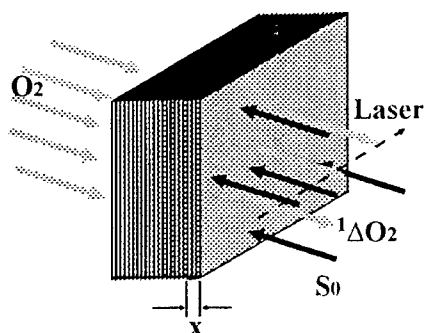
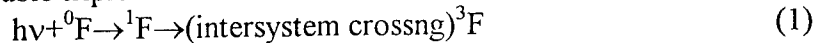


Figure 2. Principle of design of singlet oxygen generator

Concentration of fullerenes in the membrane can reach up to $3 \cdot 10^{21} \text{ cm}^{-3}$. In this case, photons of the optical pumping are absorbed in the first 500-1000 layers of fullerenes with total thickness of $(0.5 \div 1) \times 10^{-4} \text{ cm}$. At oxygen flow speed of several meters per second, oxygen molecule passes this distance during less than 1 μs , i.e., during the time, compatible with the lifetime of metastable triplet state of fullerene in the oxygen presence. The formed singlet oxygen inputs the zone of laser beam formation. The prehistory of

fullerene pass does not play any role, since energy transfer takes place only at the last section of membrane layer. Assuming possible creation of the superpure fullerene membranes, we can consider the following three reactions as the main reactions of the photochemical kinetics in kinetics of singlet oxygen generation:

1. Absorption of pumping photons by fullerenes in the ground state 0F in the channel of singlet states 1F with further non-radiative transfer of this excitation to the metastable triplet state 3F :



Effective cross section of this process as a whole can be estimated as $\sigma_{\text{eff}} \sim 5 \times 10^{-18} \div 10^{-17} \text{ cm}^2$.

2. Interaction of fullerene in metastable triplet state 3F with molecular oxygen in the ground triplet state with formation of singlet oxygen $^1\Delta O_2$ and fullerene in the ground singlet state 0F :



This reaction constant is $K_2 \approx 3.3 \times 10^{-12} \text{ cm}^3 \text{ s}^{-1}$ [5].

3. Quenching of singlet oxygen by fullerene in the ground singlet state 0F :



This reaction constant is $K_3 \approx (4 \div 8) \times 10^{-16} \text{ cm}^3 \text{ s}^{-1}$ [5].

On the base of these three reactions, we can make preliminary estimates of efficiency both for singlet oxygen generator on fullerenes with optical pumping and for the fullerene-oxygen-iodine laser as a whole. It is necessary to note that opportunity of chemical reaction between singlet oxygen and fullerene were studied in [8]. The obtained results show that chemical reactions between fullerenes and other components of the mixture can be neglected.

In the stationary case of the continuous pumping, we can simply obtain the estimate of the singlet oxygen flow value at the output of the membrane $I_0(^1O_2)$:

$$I_0(^1\Delta O_2) \approx \sigma_{\text{ef}} S_0 \nu / K_3, \quad (4)$$

where the speed of oxygen flow through the membrane ν is selected by the condition:

$$\nu \sim 1 / (\sigma_0 [^0F] \tau_2), \quad (5)$$

Here τ_2 is the lifetime of metastable triplet fullerene state in the oxygen presence, which depends on the oxygen concentration, $[^0F]$ is the concentration of fullerenes in the ground singlet state in the membrane, S_0 is the pumping photon flow, and σ_0 is the cross section of light absorption by fullerenes (it can coincide with σ_{ef}).

The important estimate is the ratio of concentrations of singlet oxygen and oxygen in the ground state at the membrane output:

$$[^1\Delta O_2] / [O_2] \sim (K_2 [^3F]) / (K_3 [^0F]) \quad (6)$$

The performed estimates show that at illumination of the multilayer fullerene membrane by radiation with power density, corresponding to the solar constant (1370 W/cm^2 , i.e., $S_0 \sim (3 \div 4) \times 10^{21} \text{ m}^{-2} \text{ s}^{-1}$), we can realize the flow of singlet oxygen I_0 up to 0.05 m/s at ratio $[^1\Delta O_2] / [O_2] \sim 10$. Analysis of the numerous experimental data

(for instance, [9]) shows that in this case we have the real opportunity to design oxygen-iodine laser with output power of about 400-700 W. It means that the efficiency of the FOIL with solar pumping (including solar) may reach 30-50%.

This estimate is rather optimistic, but all presented considerations are very essential stimulus for performance of experiments.

3. Experimental measurement of singlet oxygen yield at optical pumping of fullerene C₆₀ in solution

The first stage of the experimental work was devoted to study of photochemical kinetics in interaction of fullerenes with pumping radiation and oxygen. They were carried out, as in [5], with solutions of fullerene (mainly, C₆₀) and oxygen in different solvents, transparent both for pumping radiation and for luminescence lines of singlet oxygen. After preliminary experiments, we selected CCl₄, which has the best

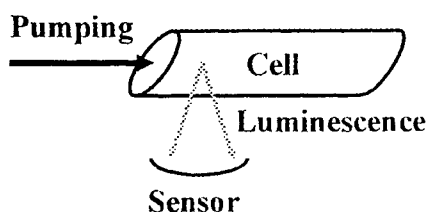


Figure 3. Schematic of the experiment.

solvability of oxygen and fullerene. C₆₀ concentration in the studied sample was $3.7 \times 10^{17} \text{ cm}^{-3}$ (it was defined experimentally by absorption and optical limiting). Oxygen concentration in the solution was $6 \times 10^{18} \text{ cm}^{-3}$ (it was calculated on base of physical and chemical data [10]).

Figure 3 presents the schematic of the experiment. The optical pumping was performed by two ways:

- By second harmonics of a neodymium laser with pumping wavelength of 532 nm and pulse duration of about 10 ns; the energy density in the experiments was $\leq 0.6 \text{ J/cm}^2$.
- By xenon lamp, spectrum of which was corrected with filters to close it to solar-like spectrum. Pulse duration in these experiments was 250 μs , radiation energy at the sample reached 14 mJ (power density was varied in the range of 5-35 W/cm^2). The chosen duration of the pumping pulse in this case, according to photochemical kinetics, practically imitated the continuous operation mode.

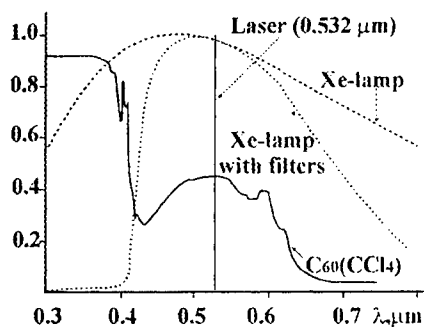


Figure 4. Main spectral parameters of the system

Figure 4 presents the main spectral parameters of the system elements: spectrum of C₆₀ absorption in CCl₄, line of the second harmonics of the neodymium laser, spectrum xenon lamp emission before and after correction.

In these experiments, we measured intensity of luminescence of singlet oxygen at wavelength of 1.268 μm (state $^1\Delta\text{O}_2$) and 0.762 μm (state $^1\Sigma\text{O}_2$). All measurements were performed in absolute units that gave us the opportunity to perform thorough comparison with results of computer simulation of photochemical kinetics with account of solvent

action on lifetimes of fullerene and singlet oxygen. All measurement equipment was preliminary tested and calibrated. We measured spatial parameters of pumping radiation and luminescence signals that enables correct account of geometrical actors. It is necessary to note that application of calibrated pumping radiation (laser pumping by pulses with different energy) at comparison of measurements performed in absolute units with results of computer simulation allows us to analyze correctness of selecting constants for the main reactions. The simulation also take into account other processes of singlet oxygen quenching, such as homogeneous quenching at collisions in volume, heterogeneous relaxation on the cell walls, and so on.

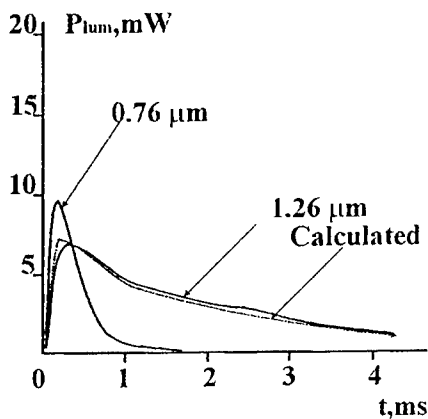


Figure 5. Pulse shape of the singlet oxygen luminescence power.

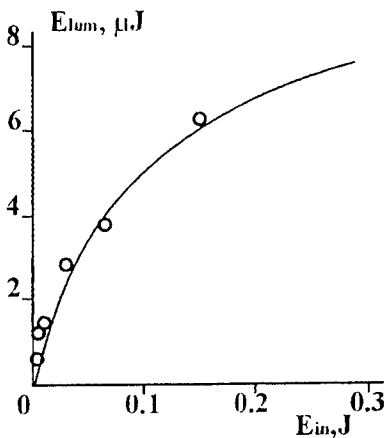


Figure 6. Luminescence energy as function input energy: curve is calculated data, points are experimental data.

Figure 5 presents pulse shape of the singlet oxygen luminescence power at wavelengths of 1.268 and 0.762 μm . For comparison, it also shows the example of calculated shape of luminescence signal obtained at simulation of

the corresponding experimental conditions.

Figure 6 presents the measured singlet oxygen luminescence pulse energy as a function of pumping laser pulse energy. It also shows the calculated results carried out with the corrected model of interaction of pumping, fullerene, and oxygen in solution of CCl_4 .

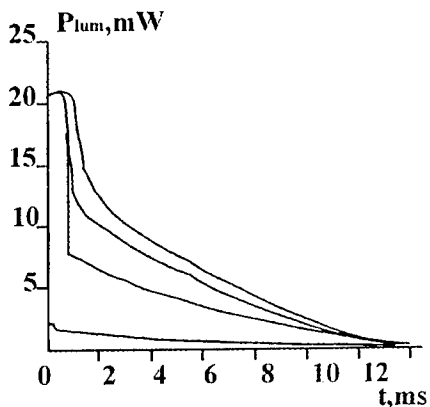


Figure 7. The pulse shape of the singlet oxygen luminescence at solar-like pumping.

First of all, it is necessary to note that the suggested kinetic model satisfactorily describes the process of singlet oxygen generation. Presence of saturation in the luminescence pulse energy with pumping energy increase (Fig. 6) proves this. The saturation manifests itself at sufficiently high pumping energy densities due to the effect of reverse saturable absorption (RSA) of pumping photons in the channel of fullerene triplet states [10] that results in additional losses of efficiency, since the absorbed energy does not go on increase of concentration of fullerene molecules in the triplet state. Test measurements of optical limiting in fullerene solution in CCl_4 carried out

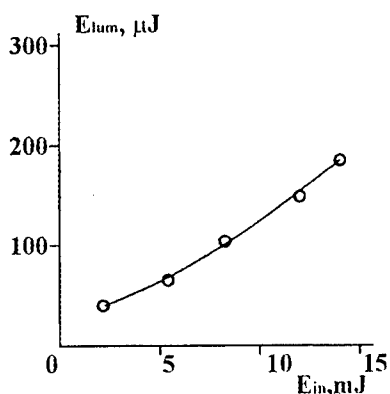


Figure 8. Energy of luminescence as a function of solar-like pumping energy.

by standard technique [10] have shown good correlation with data presented in Fig. 6.

Figure 7 presents the pulse shape of the singlet oxygen luminescence at solar-like pumping. It is necessary to note that at the initial part of the luminescence signal, one can see the noise induced by the pumping pulse. To exclude the contribution from this noise to the luminescence energy, we perform calibrating experiments in the analogous conditions in the system without oxygen in the solution.

Figure 8 presents the measured luminescence energy as a function of solar-like pumping energy. Comparing these results with

data obtained with laser pumping, we must outline essential increase of both singlet oxygen yield and total efficiency of this process.

Analysis of the photochemical kinetics shows that this takes place due to practical absence of nonlinear optical phenomena at light absorption.

4. Conclusion

1. We considered the opportunity to design fullerene-oxygen-iodine laser with solar pumping and presented the results of estimates, showing the possibility to obtain the efficiency of such a laser, reaching tens of percents.
2. The presented experimental data on generation of singlet oxygen at optical (laser and solar-like) pumping of fullerene C_{60} show significant increase of singlet oxygen yield and process efficiency at transition to the solar-like pumping. We assume that it is caused by practical absence of nonlinear optical phenomena, which results in losses of energy in the channel of triplet fullerene states, typical for laser pumping case.

5. References

1. I. M. Belousova, O. B. Danilov, A. A. Mak. The claim of the patent of Russian Federation, Research Institute for Laser Physics, St.-Petersburg, Russia, 20.06.2000, n 2000115512.
2. V. Yu. Zaleskii. Iodine laser pumped by solar radiation, *Sov. J. of Quantum Electronics*, 1983, **13**, n6, p.70.
3. S. H. Choi, J. H. Lee, W. E. Meador, E. J. Conway. A 50-kW module power station of directly solar-pumped iodine laser, *J. of Solar Energy Engineering*, 1997, **119**, p.304.
4. O. B. Danilov, A. A. Artemov, A. P. Zhevlakov. Iodine photodissociative pulse-repetitive laser: problems of efficiency, *Proc. SPIE*, 1992, **1980**, p.41.

5. J. W. Arbogast, A. P. Darmanyany, Ch. S. Foote, et al. Photophysical properties of C_{60} , *J. Chem. Phys.*, 1991, **95**, p.11.
6. J. W. Arbogast, Ch. S. Foote. Photophysical properties of C_{70} , *J. Am. Chem. Soc.*, 1991, **113**, p.8886.
7. H. T. Etheridge, R. B. Weisman. C_{70} triplet excimers: evidence from transient absorption kinetics, *J. Phys. Chem.*, 1995, **99**, p.2782.
8. L. Juha, V. Hamplova, J. Kodymova, O. Spalek. Reactivity of fullerene with chemically generated singlet oxygen, *J. Chem. Soc., Chem. Commun.*, 1994, p. 2437.
9. V. V. Kalinovsky, G. A. Kirilov, V. V. Konovalov, V. D. Nikolaev. High power oxygen-iodine laser, *Proc. SPIE*, 1992, **1980**, p.138.
10. V. P. Belousov, I. M. Belousova, V. P. Budtov, V. V. Danilov, O. B. Danilov, A. G. Kalintzev, A. A. Mak. Fullerenes: structural, physical-chemical and nonlinear-optical properties, *J. of Opt. Technology*, 1997, **64**, n12, p.2.

Technical proposals of Industrial High-Power CO Lasers

I. Ya. Baranov*

Baltic State Technical University

6, Gribalevoj st., Apt.15, St.-Petersburg, 194100, RUSSIA

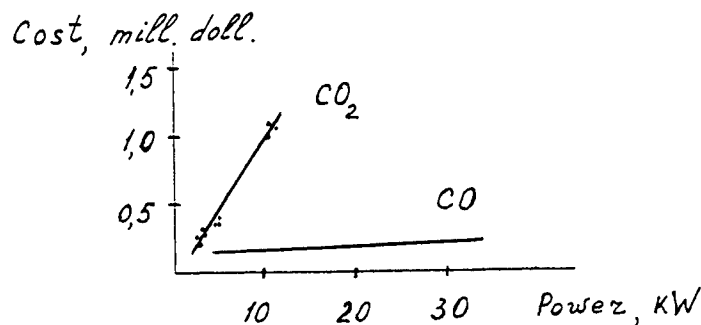
ABSTRACT

The commercial lasers with power 20kW and up are created by scaling of well-developed electrodischarge kilowatt CO₂ laser with circulating of gas. However, there occurs two negative moments: loss of the optical beam quality and significant increase of laser cost. The first moment is connected not so much with increase of laser beam path between resonator's mirrors as with quantum efficiency of CO₂ molecule, which is 0.41, and also with conversion of irremovable vibrational energy to heat in a resonator. The cost of lasers with power 10kW and higher is considerably increased in scaling of kilowatt CO₂ lasers. This is associated with the necessary increase of consumption of active medium, resulting not only in a change of circulating system, but in a change of regeneration system, source of power supply, cooling system, system of extracting radiation, etc. as well. It is known that the production of high power, high efficiency, high specific energy and high optical beam quality can be obtained in the experimental systems of a quasi-cw electro-ionisation CO laser with cooling a CO mixture by its expansion in the nozzles. The quantum efficiency of CO molecule is substantially higher (0,95). Moreover, at supersonic speed of CO mixture flow the radiation can be removed from a resonator before the conversion of vibrational energy to heat. The way of transfer to industrial high-power CO lasers is proposed by the present author through the use of continuous formation of a CO laser mixture during laser operation and by excitation in a radio-frequency (RF) electric discharge without an electron gun. The given conception was used on a small-scale model system to demonstrate that the laser radiation was possible in a CO mixture with combustion products and air, which are excited by RF discharge in a supersonic flow. The possibilities for scaling the experimental system and the creation of industrial high-power CO laser were considered. The lower cost for the proposed laser system can be made by using the system with small sizes without special circulating units, electron gun, sectionalised electrodes, ballast resistance, block of mixture regeneration and with possibility of using the optic manipulators with fibre-optic cable and hence standard robots. In spite of the open working cycle of laser, high specific energy and high efficiency define reasonable service expenses with high stability of radiation parameters without ejecting toxic CO into the atmosphere by converting CO molecules to CO₂ ones. Estimated cost of proposed laser is cost of kilowatt CO₂ laser.

Keywords: industrial, high-power lasers, electrodynamic CO laser, radio-frequency discharge

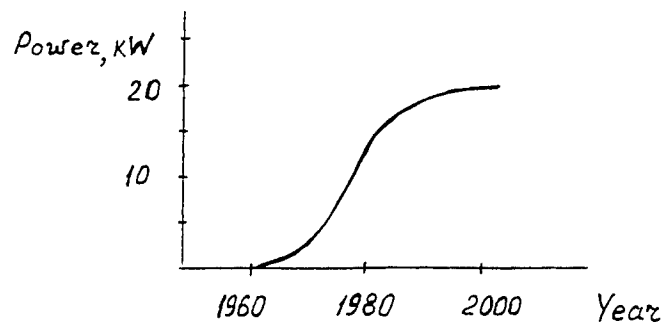
The technical proposal is developed for industrial high-power electrodynamic CO laser with power 20÷40 kW, cost ≈ 100.000 US dollars and open working cycle.

The cost of industrial CO₂ lasers higher one million US dollars at the power higher 10 kW:



* E-mail: komdep@bstu.spb.su

Power growth of industrial CO₂ lasers on years:



The reasons of saturation of power growth:

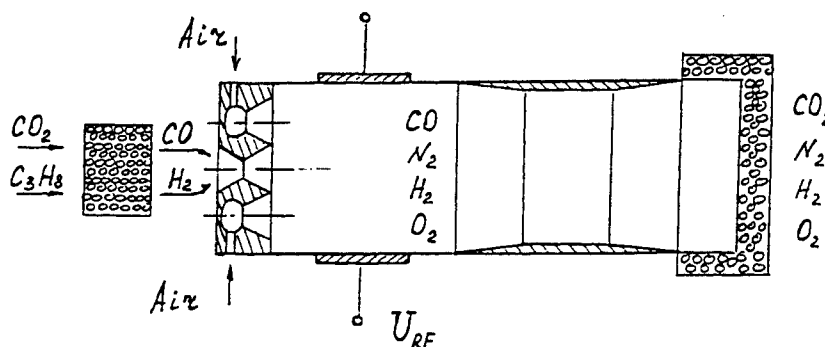
- high cost of CO₂ lasers with power higher 10 kW;
- deterioration of optical quality of a beam at growth of power by increasing an optical path.

- | | |
|---|--|
| Hansen C.F.,
1973 | A electrogasdynamic laser as a combination of gasdynamic laser with Efficiency less than 1% and electric-discharge laser was proposed. |
| Bhaumik M.L.,
Lacina W.B.,
Mann M.M.,
1972 | $P_{out} \sim 100$ kW and electric-optical Efficiency $\sim 50\%$ were obtained experimentally from quasi-cw electrogasdynamic CO laser installation with an electron gun.
(A unique properties of the CO molecule provide low divergence θ). |
| Monson D.J.,
1976 | Calculations of the closed working cycle and the open working cycle in an electrogasdynamic CO laser were made:
Efficiency of closed cycle < Efficiency of open cycle. |
| Hertzberg A.,
1978 | Problem of a CO mixture recirculation was noted in the closed working cycle because of the high chemical activity of the CO molecules, the increase of contamination in an active medium and attachment of beam electrons.
(A problems of the open working cycle cover the release of a toxic CO mixture into the atmosphere, availability of an electron gun and prior formation of the mixture). |
| Baranov I.Ya.,
And his colleagues,
1993 | Model installation of an electrogasdynamic CO laser was used to demonstrate practically that a laser radiation was possible in an installation with combustion products and air and with radio-frequency (RF) discharge in a supersonic gas flow ¹ .
It makes possible continuous formation of a laser CO mixture during laser operation and excitation of this mixture without an electron gun ² . |
| Baranov I.Ya.,
1994 | Multipurpose self-contained industrial high-power laser system with formation of a laser mixture by combustion of a chemical fuel and air during the operation of the laser was proposed ³ . |
| Baranov I.Ya.,
1998 | Technical proposals were developed for the industrial high-power laser on combustion products and air with power supply from electrical socket and conversion of oxide (CO) molecules to carbon dioxide (CO ₂) ones for ejecting the gas into the atmosphere ⁴ . |
| Baranov I.Ya.,
2000 | The continuous formation of carbon oxide (CO) mixture is offered with using the catalytic decomposition of molecules of carbon dioxide (CO ₂) and propane (C ₃ H ₈). |

The low cost in the proposed CO laser gets by using:
 -open working cycle of laser;
 -RF-discharge in a supersonic gas flow.

In this laser there is absent following: closed contour;
 pumping system on a closed cycle;
 system of mixture regeneration;
 electrode sectionalized;
 active ballast resistance;
 electron gun.

The open working cycle of laser is put into effect by following:
 -continuous formation of a CO mixture (air \approx 90%) using the catalytic decomposition of molecules CO_2 and C_3H_8 (propane);
 -the conversion of molecules CO to CO_2 for ejecting the gas into the atmosphere.



The condition of effective laser operation on the mixture of $(\text{CO}:\text{N}_2:\text{H}_2:\text{O}_2)^5$ is following:

$$\tau_{VV} \ll \tau_{eV_{\text{CO}}} < \tau_p < \tau_{eV_{\text{N}_2}} < \tau_{eV_{\text{H}_2}} \leq \tau_{eV_{\text{O}_2}} \leq \tau_{VT} \approx \tau_a \quad (1)$$

where τ with different indices are the characteristic times of excitation, VV^- , VT^- , eV^- -processes and electron attachment, respectively.

The conditions (1) for the times is satisfied by selecting the values of E/N and the composition of a mixture:

$$E/N \approx 10^{-16} \text{ Vcm}^2, \quad \text{CO} > 10\%, \text{N}_2 < 90\%, \text{O}_2 < \text{CO}, \text{H}_2 < 90\%$$

The feasibility of using the available electric-field energy in direct excitation of CO molecules in a mixture with N_2 molecules has been reported:

- Dolina V.I., Koterov V.N., Pyatakhin M.V., Urin B.M.;
- Islamov R.Sh., Konev Yu.B., Kochetov I.V., Kurnosov A.K.;
- Hall R.J., Eckbreth A.S.;
- Iyoda M., Sato S., Saito H., et.al.

The competitiveness of proposed CO laser in comparison with CO₂ lasers with power ≥ 20 kW consists in following:

- simplicity and reliability of a design at use of catalytic decomposition of accessible gases (CO₂, C₃H₈);
- acceptable operating costs caused by high specific energy and efficiency of laser and use of atmospheric air;
- high quality of laser radiation as a result of the small sizes, low pressure and properties of CO molecules;
- high stability of radiation parameters owing to continuous reproduction of a CO mixture;
- the ecological safety, which is caused by absence of ejecting the toxic CO molecules into the atmosphere by converting CO molecules to CO₂ ones;
- the low cost of proposed CO lasers, which is connected to simplicity and small sizes of the installation and opportunity of using serial standard elements.

Estimated cost of proposed laser is calculated as the sum of following:

-gasdynamic laser with similar sizes: (Proceedings SPIE 3092 456 (1997))	75.000 USD
-RF electro-generator:	20.000 USD
-air compressor:	10.000 USD
-gas-discharge chamber:	10.000 USD

CONCLUSIONS

The scaling of well-developed industrial CO₂ lasers with power ≥ 20 kW has two negative moment: significant increase of laser cost and deterioration of optical quality of laser radiation.

Industrial CO lasers with power ≥ 20 kW, low cost and high optical quality of radiation can be created with open working cycle and continuous formation of CO mixture excited by RF-discharge in a supersonic flow.

Laser mixture is formed of atmospheric air ($\approx 90\%$) and the products of catalytic decomposition of accessible gases (CO₂ and C₃H₈ (propane)). At the same time for one hour of laser operation it is required on one cylinder of each gas (40 liters).

REFERENCE

1. G. A. Baranov, I. Ya. Baranov, A. S. Boreisho, I. V. Timoshchuk, "Supersonic CO combustion-product laser with a high-frequency excitation," *Quantum Electron.* **23**, pp.189-199, 1993.
2. I. Ya. Baranov, "Method of CO laser active medium making," Russian Patent no.2.002.346, in *Inven. Bull.*, no.39-40, p.174, awarded Oct.30, 1993.
3. I. Ya. Baranov, "Multipurpose high-power electrogasdynamic CO laser," *Quantum Electron.*, **24**, pp.536-539, 1994.
4. I. Ya. Baranov, "The conception for creation of industrial high-power lasers with continuous formation of CO mixture and RF discharge in a supersonic flow," Proceedings of SPIE, **3686**, pp.1-9, 1998.
5. I. Ya. Baranov, "Generalised scaling of an electrogasdynamic CO combustion-product laser," *Quantum Electron.*, **24**, pp.673-676, 1994.
6. I. Ya. Baranov, "Stimulation of chemical reactions in shock waves with preliminary excitation of a supersonic gas flow in a high-frequency discharge," *Plasma Phys. Rep.*, **22**, pp.964-968, 1996.

High-power high optical quality RF-excited slab CO₂-lasers

A.I.Dutov, A.A.Kuleshov, S.A.Motovilov, N.A.Novoselov,
N.L.Orlov, V.E.Semenov, A.A.Sokolov

199034, Research Institute for Laser Physics, Birzhevaya, 12, St.-Petersburg, Russia.
Phone: (812) 328-10-93. Fax: (812) 328-58-91. E-mail: dutov@ilph.spb.su

ABSTRACT

For the various pumping rates and for the various heights of the gap were calculated the average value of the small-signal gain and its profile across the gap. For the high power slab CO₂-lasers, RF-excited at 40.68 MHz, were analyzed the ranges of their geometry parameters variation, providing for the possibility of diffraction limited performance. In theory and in experiment was shown the possibility to select the basic waveguide mode of radiation.

Keywords: slab CO₂-laser, small-signal gain, mode selection, radiation losses.

1. INTRODUCTION

Today the RF-pumped slab CO₂-lasers have a well-established positions at the market of material-processing lasers. High efficiency and beam quality of such lasers stimulate the search for the approaches to their cost reduce. For the higher output power of such lasers the problem of laser beam quality becomes more emphasized, and thus the problem of optimization of laser parameters becomes more important.

The majority of published results indicates that the main advantages of slab CO₂-lasers are realized for the discharge gap height (*h*) about 2 mm when the laser gas excitation frequency (*F*) lies within the range of 81 - 125 MHz¹⁻³. For such values of gap along the slab coordinate one observes the waveguide mode of light propagation, while along the width coordinate the light propagates as in the free space. In the space between the butt-ends of electrodes and optical resonator mirrors the light also propagates as in the free space. For the optimal design of slab laser the parameters *F* and *h* are tied by definite relationships⁴. The values of these parameters influence onto the size of laser head and onto laser reliability and cost.

In the paper⁵ was shown that it is reasonable to excite the high-power slab CO₂-laser of kW-power range by the RF power with *F*=40.68 MHz. The reason is that this frequency is, on the one hand, the one permitted for the technology applications, and, on the other hand, its use makes it possible to simplify RF generator, to make it cheaper and to reduce the accuracy requirements to the laser head design. Obviously, for the smaller *F* the larger is the RF-wavelength (for *F*=40.68 MHz λ_{RF} =7.3 m), and thus the mode of RF-wave propagation is more close to the mode of DC-excitation. So in practice for such *F* it is more simple to provide the uniform excitation along the discharge length, than for, say, *F*=81 MHz. The latter is especially important in the case of high-power slab lasers, which have long (~ 1m) active medium. In some papers, for example in papers^{4,5}, it was shown that for such frequency it is reasonable to use the gap height of *h* ≥ 4 mm. However, for the standard geometry of the discharge gap (two plain parallel electrodes) with such height it is impossible to provide the single-mode generation. For example, in the already mentioned work⁵ the authors did not manage to provide for the high quality of the output beam – some 50% of the generation power went to the third waveguide mode. In the said paper it was proposed to use the new type of electrodes. These electrodes, acting together with the optical resonator mirrors, were creating a kind of interferometer, selecting the basic mode. However, in the said work the authors still had to use the spatial filter at the laser head output so as to provide final separation of the basic mode.

Worth mentioning, that the use of lower radio frequencies has its disadvantages. In this case one meets the growing danger of discharge transformation to the unstable α - γ stage⁶, when for the large specific energy deposition the discharge current and the average energy of electrons are growing very fast. The increase of the gap height from, for example, 2 to 4 mm, also results in corresponding reduce of the specific energy output, related to the unit of the discharge surface¹, because one has to reduce the energy deposition so as to prevent overheating of active medium.

Note also, that the provision of the high generation efficiency in slab laser requires positioning of the resonator mirrors as close to the butt-ends of electrodes as possible so as to reduce the losses. (Typical distance $\Delta z=5-15$ mm). In this case the mirror surfaces are subjected to the action of discharge plasma ions, which shortens the lifetime of mirrors and leads to gradual reduce of the laser output power. So the choice for the optimal value of Δz is also very important.

In this paper we present the theoretical and experimental study of the problem of the generation mode formation. We discuss the selective properties of the discharge gap butt-end, which works as the slot diaphragm. These properties were studied in their dependence upon the resonator mirror curvature and upon the distance from the mirror to the gap butt-end.

2. NUMERICAL SIMULATION AND EXPERIMENTS

The mathematical model and calculation algorithms, used for the numerical simulation of the physical processes in the slab CO_2 -laser with the diffusion cooling of active medium, were described in the paper⁷. The software package consists of four main parts, simulating

1. structure of RF-discharge;
2. processes of inversion formation;
3. laser radiation propagation through the resonator;
4. and chemical reactions in plasma.

The first code makes it possible to calculate the characteristics of the RF-discharge: "current - voltage - input power". The output parameters of the kinetics code are the profiles of the temperature and the gain across the height of the discharge gap and also the output radiation power. The calculation of the light propagation inside the resonator makes it possible to study the modal structure of radiation, the angular distribution of the output power, to calculate the radiation losses and also to obtain the near-field and the far-field distribution patterns.

The calculations, which were done with the use of this package has shown good correlation with the results of some published experiments^{3,6}. In particular, the calculations of the radiation parameters for the conditions of the paper⁵, have confirmed, that under such conditions some 30-50% (depending upon the pumping level) of generation power go to the third waveguide mode. According to the analysis, under the intense pumping and for the gap height of 4 mm, used in the said work, in the neighborhood of the resonator axis the active medium is overheated and the small signal gain in the central zone is depleted. These processes are illustrated by the calculations of $T(x)$ and $g(x)$, made for $h=2, 3$ and 4 mm for two rates of pumping (Fig. 1a,b,c).

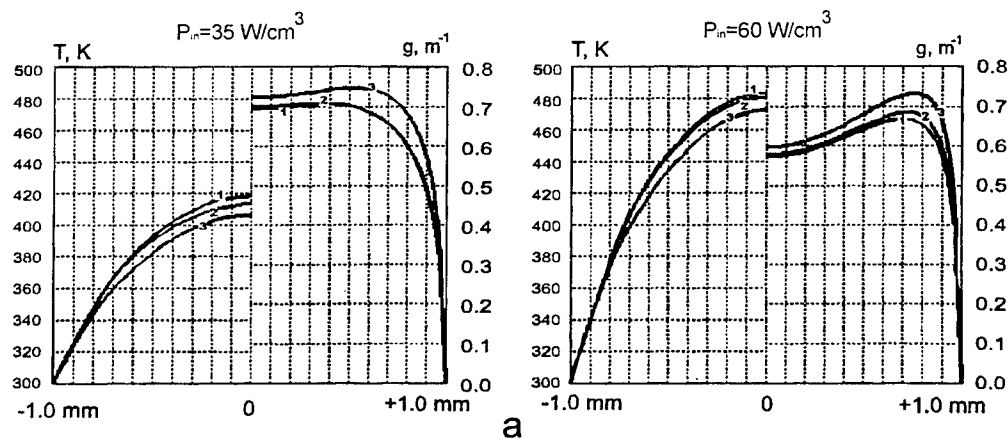


Fig. 1a. Distributions of $T(x)$ and $g(x)$, calculated for two values of the power, put in the discharge and for:
(a) $h=2$ mm, 1 - $F=41$ MHz, 2 - $F=81$ MHz, 3 - $F=125$ MHz.

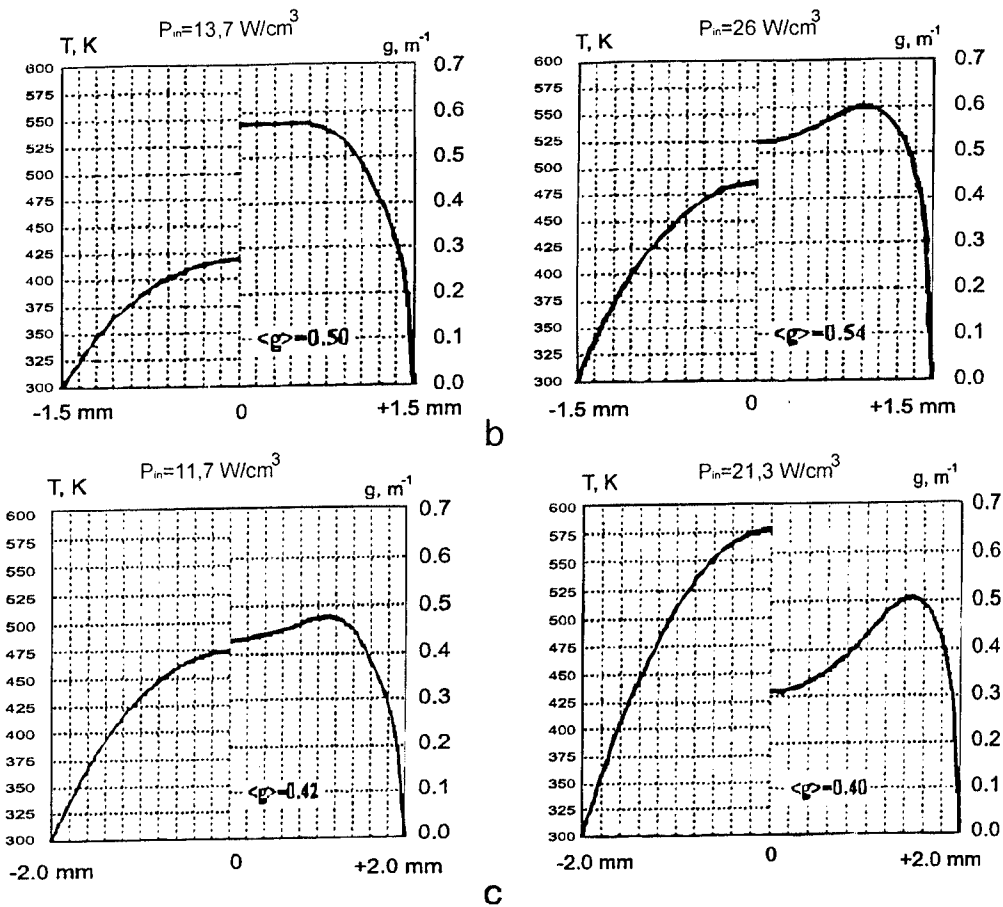


Fig.1b,c. Distributions of $T(x)$ and $g(x)$, calculated for two values of the power, put in the discharge and for: (b) $h=3 \text{ mm}$, $F=41 \text{ MHz}$ and (c) $h=4 \text{ mm}$, $F=41 \text{ MHz}$.

The calculations were carried out for the active mixture of $\text{CO}_2:\text{N}_2:\text{He}:\text{Xe}=1:1:6:0.4$, for the gas pressure of 50 Torr and for rate of CO_2 molecules dissociation 60%. Under the conditions of the insufficient selection of the basic mode ($h=4 \text{ mm}$, $\Delta z=13 \text{ mm}$) the third mode efficiently competes with the basic mode. In Fig.2 is shown the light field distribution at the resonator mirror, calculated for the conditions of experiment⁵.

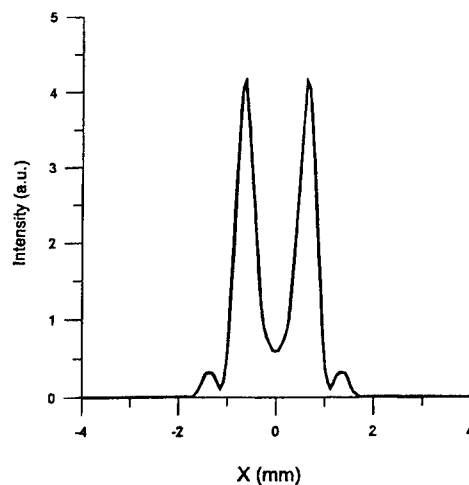


Fig.2. Calculated distribution of the light field at the resonator mirror for the conditions of the experiment⁵ ($h=4 \text{ mm}$, $P_{out}=800 \text{ W}$).

The value of the small-signal gain $g_0(x)$ is influenced not only by the gap height, but also by the rate of CO_2 molecules dissociation in the discharge δ . In Fig.3 are shown the values of the gain, averaged across the gap $\langle g_0(x) \rangle$, for the set of heights from 3 to 6 mm, calculated in their dependence upon the pumping power, varied in the range from 5 to 40 W/cm^3 . One can see that changing of δ value from 60% to 80% (typical values for the high power slab CO_2 -lasers, results in $\langle g_0(x) \rangle$ reduce in 2 and more times.

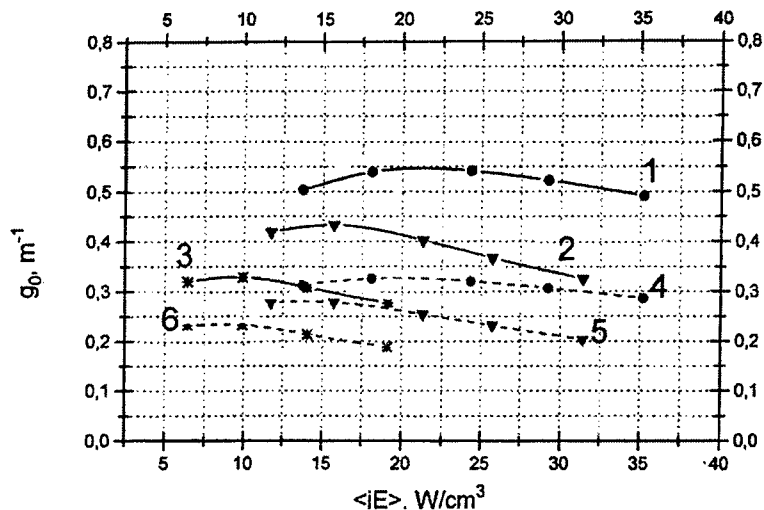


Fig.3. Calculated value of small signal gain, averaged across the discharge gap $\langle g_0 \rangle$. Curves 1 and 4 correspond to the height $h=3.0$ mm, 2 and 5 - $h=4.0$ mm, and 3 and 6 - $h=5.0$ mm. Solid lines correspond to the rate of CO_2 -molecules dissociation $\delta=60\%$ and dotted lines - to $\delta=80\%$.

According to the calculations, one can observe the depletion of $g_0(x)$ in the central zone of discharge gap even for the gap height $h=2$ mm, when the specific energy deposition is some $50\text{-}60 \text{ W/cm}^3$ - quite typical values for the slab laser. This process can reveal itself in experiment as the instability of the average generation power within the range of some 5-10%. We explain it by the competition of the basic and third waveguide modes.

According to our experiments, this process is also accompanied by the instability of angular divergence of laser output. Excess of pump leads to the divergence aggravation. It is well seen from Fig.4a,b, shown the far-field distribution of radiation from the slab CO_2 -laser "Olymp-250". The images were taken by the matrix of photosensors (SPIRICON production), providing the possibility of real-time observation of radiation power re-distribution from the basic to the nearest third symmetrical waveguide mode.

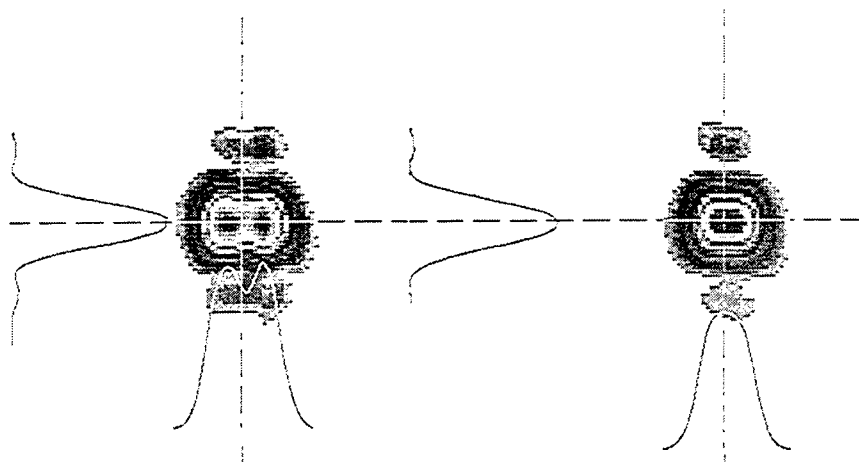


Fig.4. Far-field (focal length 1 m) distribution of laser output, (a) $P_{\text{out}}=250 \text{ W}$, maximal output power and (b) $P_{\text{out}}=230 \text{ W}$, optimal output power.

We have already said in the Introduction, that for the slab CO₂-lasers it is important to optimize the distance Δz between the butt-end of the discharge gap and the resonator mirror. This problem has two aspects. The first of them is the influence of the resonator mirror curvature onto the distortion of the modal structure due to the wave interaction with the mirror. The second one deals with filtration of modes by the butt-end of the discharge gap. The distortions of the modal structure at the mirror can be rather high, because in the compact slab lasers with the short active medium the curvature of resonator mirrors can be rather high. After reflection from such a mirror even the basic mode is substantially attenuated, because some part of laser energy is transferred to the higher order (3, 5 etc.) modes. One can see from the experiment⁵ (see Fig.2), that up to 50% of the power can be transferred to 3rd and 5th modes for the typical case of mirror radius $R \sim 1$ m and gap height $h=4$ mm. According to the calculations, for the height $h=2$ mm and the same radius of the mirror, the total energy of higher (3,5,7) modes is about 1% of that of the basic mode. So it is obvious that the increase of the discharge gap height results in substantial deterioration of selective properties of the discharge gap butt-end.

At the same time advantages of the use of the high ($h=3-5$) discharge gaps, which we have outlined earlier, indicate the necessity of more thorough study of the problem, aimed onto the search of the approaches, providing the preservation of the high beam quality. According to the calculations, one can provide the efficient performance of the slab CO₂-laser with the gap height of both 2 and 4 mm, when the distance to mirrors Δz fills to the range from 20 to 55mm. However, its realization requires the very accurate choice of the curvature radiuses R of the resonator mirrors. In Fig.5 are shown the dependencies of the loss of the basic mode energy vs. the mirror curvature, calculated for the various values of the distance from the butt-end of the electrodes to the mirror Δz (gap height $h=2$ mm).

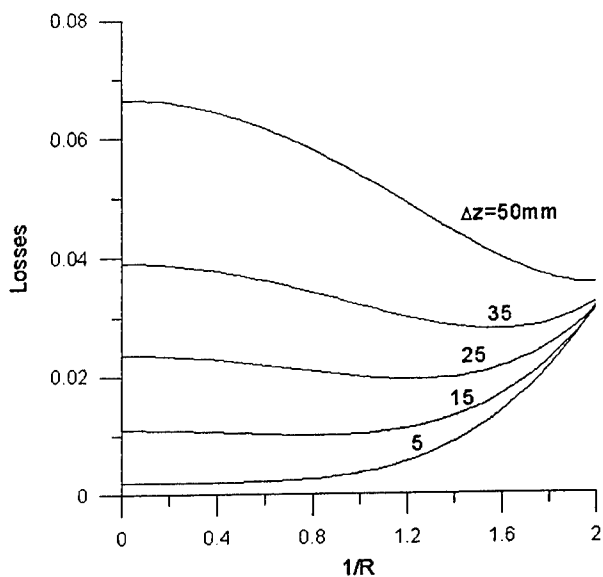


Fig.5. Calculated dependencies of the basic mode energy losses at the butt-end of electrodes versus the curvature of the concave mirror of resonator. $h=2$ mm.

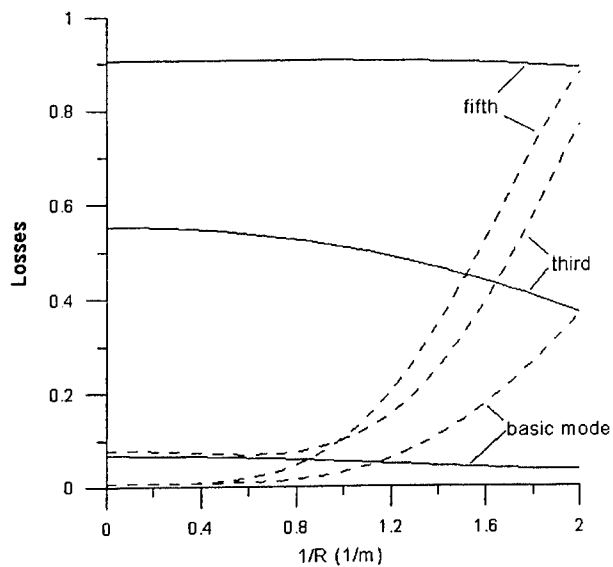


Fig.6. Calculated dependencies of the energy losses for three symmetric modes at the butt-end of electrodes versus the curvature of the concave mirror of resonator for $\Delta z=50$ mm. Solid lines correspond to the gap height $h=2$ mm, and the dotted lines - to $h=4$ mm.

For the large Δz , for example, for $\Delta z=50$ mm; see Fig.6, the optimal shape of the resonator mirror can be not the spherical one, but some toroidal ($R_x \neq R_y$). The proper choice depends upon the relationship between the length of active medium and the discharge gap height. This approach was confirmed by the experiments. The slab laser with the active medium dimensions $3(4) \times 60 \times 600$ mm, pumped by RF-frequency $F=40.68$ MHz, provided the output generation power of

150-170 W with the efficiency 9-10%; beam divergence was nearly diffraction limited. The resonator was comprised by toroidal mirrors, placed at the distance 50 mm from the electrodes. The magnification of the unstable resonator (gap width coordinate) was $M=1.17$. In Fig.7 is shown the 3-D far-field distribution of laser output, registered by means of Spiricon matrix.

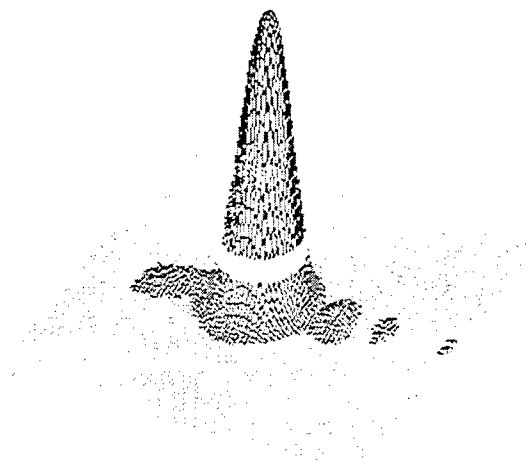


Fig.7. Experimentally measured 3D plot of far-field ($f=1$ m) radiation intensity distribution.

3. CONCLUSIONS

Influence of the active medium excitation frequency, of the discharge gap height and of the specific input power onto the small signal gain distribution across the discharge gap was studied by means of numerical simulation. It was shown that the shape of $g_0(x)$ distribution influences onto the mode structure of the slab CO_2 -laser radiation. The dependence of laser radiation losses upon the curvature of the resonator mirrors and upon the distance between the mirror and the discharge gap butt-end was studied. In theory and in experiment was shown that for the chosen gap with the height $h=3-5$ mm and the excitation frequency $F=40.68$ MHz it is possible to select the basic waveguide mode by means of proper choice of the mirrors' curvature along the slab coordinate and of the distance from the mirror to the butt-end of electrodes.

REFERENCES

1. D.R.Hall, H.J.Baker, "Area scaling boots CO_2 -laser performance", *Laser Focus World*, **25**, no.10, p.77-80, 1989.
2. R.Nowack, H.Opower, U.Shafer et al., "High power CO_2 waveguide laser of the 1 kW category", *Proc.SPIE*, **1276**, CO_2 Lasers and Applications II, p.18-26, 1990.
3. A.D.Colley, H.J.Baker, D.R.Hall, "Planar waveguide, 1 kW cw carbon dioxide laser excited by a single transverse RF-discharge", *Appl.Phys.Lett.*, **61**, no.2, p.136-139, 1992.
4. P.Vitruk, D.R.Hall, H.J.Baker, "Similarity and scaling in RF-excited CO_2 -lasers", *IEEE Journ. of Quantum Electronics*, **30**, no.7, p.1623-33, 1994.
5. P.Vitruk, J.Schemmer, S.Byron, "700 W diffusion cooled, large area, 40.68 MHz excited CO_2 -laser employing split-wave hybrid confocal resonator", *Proc.SPIE*, **3343**, p.677-686, 1998.
6. P.Vitruk, D.R.Hall, H.J.Baker, "The characteristics and stability of high power transverse radio frequency discharges for waveguide CO_2 slab laser excitation", *J.Phys.D: Appl.Phys.*, **25**, p.1767-1776, 1992.
7. A.I.Dutov, V.N.Ivanova, S.A.Motovilov et al., "Computer simulation of RF-excited diffusion-cooled slab CO_2 laser", *Proc.SPIE*, **2713**, p.58-66, 1995.

About particularities of intensities distribution in cross-section of powerful laser beams

V.A.Gurashvili^a, P.V.Korolenko^b, A.P.Napartovich^a, S.P.Pavlov^a, A.V.Rodin^a, N.E.Sarkarov^a,
A.M.Zotov^b

^aTroitsk Institute For Innovation and Fusion Researches, Troitsk, Moscow Region, 142092,
Russia

^bMoscow State University, Moscow, 119899, Russia

ABSTRACT

The physical nature and manifestation of several types of instabilities and fluctuation processes in the cavity of the fast-flow CO₂-laser are considered. It was established by experiment that optimal design of optical and gas-dynamic laser sections depresses totally the high frequency fluctuations and reduces low-frequency fluctuations to the level 6-10%. It was shown that inhomogeneities in the laser cavity are apt to complicate appreciably the space-temporary structure of output laser radiation. To interpret the experimental results influence of phase aberrations on the process of formation of caustics and wavefront dislocations in laser beam is considered.

Keywords: unstable cavity, laser beam, diffraction, wavefront dislocation, caustic, power instabilities.

1. INTRODUCTION

The actual now-a-days actual problem of the improvement of the characteristics of high power technological lasers is closely connected with the investigation of the physical nature of optical inhomogeneities and instabilities in laser cavities as well as with their influence on radiation structure. High peak intensity values inherent in high power fast-flow lasers reinforce the optical inhomogeneity of the active medium, cause termodeformation of the cavity mirror and generate nonlinear self-action effects and multimode lasing in active media^{1,2}. The important role in development of generation instability in fast-flow lasers is played self-modulation processes. They are typical for the devices with cross flow of active medium using a cavity with an unstable configuration under the condition of separate pumping and generation. The auto-oscillations of the power having the period close to time of medium crossing the cavity offer the depth of power modulation up to 100 %^{3,4}. Speed inhomogeneities of an active medium flow can result in stabilisation of a generation mode⁵. However speed inhomogeneities strengthen the phase inhomogeneities of the medium⁶. Aforesaid testifies that there are a lot of factors, which influence negatively on stability and quality of laser radiation. The result of this influence is usually estimated by analysis of the far-field radiation structure. At the same time much less attention is paid to the study of the light field characteristics in the near diffraction zone, the length of which for wide-aperture beams is rather significant. In this paper the spatial-temporary structure of CO₂-laser beam of the near field diffraction zone is considered.

2. CHARACTERISTICS OF LASER AND EXPERIMENTAL RESULTS

As a source of radiation the technological electrocharge CO₂ - laser of continuous action with flowing active medium and wavelength $\lambda=10,6\mu$ was used. The design of the laser investigated was similar to that described earlier⁷. Active medium in the resonator cavity was formed by replenish of CO₂ gas components to a binary mix N₂+He, previously exited in a discharge chamber. The flow speed of active medium varied in the range of 100-150 m/s. It was possible to change the pumping mode as well as the gas formula and optical cavity characteristics. The depth of energy-input modulation in the discharge did not exceed 5 %. The instability of gas-dynamic parameters was not more than 3 %. To pick up the energy from active medium of the laser several constructions of unstable resonators with magnification number $M=1,12-2,2$ were used. Depending on the scheme of the resonator the scope of active medium of the laser was carried out by single or double passage of

radiation through the active volume. In the optical scheme of the double passage unstable resonator the angle reflectors consisting of two or three flat mirrors were used. The application of such reflectors not only allows to fill effectively the active medium with radiation, but also to level the intensity distribution in cross section of a beam by the rotation of a field in the cavity. It was possible to form radiation at the resonator output as a rectangular, square or circular with the central part shadowed by the output mirror.

Measuring of power fluctuation value and the intensity distributions in the cross section of the output radiation was carried out in the previously weakened laser beam. To attenuate the high power radiation the grooved gratings made on the mirrors base, diffraction couplers on the basis of mirrors with regular sieve structure were used, as well as couplers in the form of narrow fringes of spherical mirrors ensuring the scanning of a laser beam over a small aperture of the photoreceiver. In case of insufficient value of radiation attenuation the edges of optical plates made of KCl or ZnCe were applied. Depending on the power of weakened laser beam the registration of radiation was carried out directly or by using the integrating sphere. The time of the beam aperture scanning was about $10^{-2} - 10^{-3}$ s. On occasion to measure the intensity distribution in the beam cross-section the small spherical mirrors with the diameter of about 5 – 10 mm were placed instead of mirror fringes. It allowed to scan the output beam aperture thus give the opportunity to register the intensity distribution with the resolution of about 3 – 7 mm in any given beam scan.

It was established that the average value of power fluctuations does not exceed 6-10 % under the magnifying factor equal to $M = 1,5$. The varying of the magnification number in the limits $M=1,4-2,2$ did not result in appreciable changes of the character of temporal power behaviour. Under such conditions the power picked off the laser active medium decreased with increasing of M because of insufficient power density in the cavity. The reduction of the magnification number of the unstable resonator from $M=1,4$ up to $M=1,12$ resulted in increasing of power fluctuations. The same effect was observed when the reduction of the cavity aperture along the flow took place. However the power modulation depth in this case did not exceed 20 %. It is important, that in all experiments the generation power modulation was conducted in the low-frequency band (up to 10 Hz) and did not contain spectral components corresponding to the time of medium crossing the cavity. One can explain this effect by the fact that at the high power levels an increasing of the effective mode volume and averaging over generation area all effects, which decrease of the power stability.

Contrary to the temporal behaviour of the total power the intensity in the beam cross-section was extremely unstable. Besides its transverse distribution was very complicated. The spatial modulation of intensity distribution in the beam cross-section in the near zone varied with the distance from the plane of measurement in relation to the output aperture of the resonator.

The registration of intensity distribution in cross section has shown, that in this distribution the "hot spots" with intensity much higher than its average value may randomly occur. In some cases intensity in such spots differed from average value by 5-10 times. The quantity of such spots in cross section of a beam varied. From one up to six such spots was registered. At registration of distribution of intensity on distance 19m from a output aperture of laser cross size of spots varied in a range 10-20mm. They occurred by a random way in a various areas of the aperture of a beam.

To improve the registration of channels with high meanings of intensity the special aerosol chamber was designed. It allowed to visualise the spatial fragments of the beam which intensity surpasses the certain level. As working medium in the aerosol chamber the fine particles of corundum weighed in air were used. To increase density of power and to achieve a threshold level of a luminescence corundum, the radiation was directed through the aerosol chamber, being previously focused with the help of a long-focal-length a mirror. Such technique allowed by character of a luminescence corundum to investigate transformations of spatial distribution of intensity in a laser beam. In fig. 1 the typical photo-picture of a luminescence of corundum particles in a converging laser beam is given. In it the channels with high meanings of intensity are precisely visible. The amount and position of such channels in process of generation are varied.

Simultaneously with registration of spatial distribution of intensity of radiation the research of features of phase distribution using the help shift interferometer was carried out. The analysis of interferograms has shown, that alongside with essential phase aberration on the wave front screw dislocations are formed. Their identification was carried out on points of branching of interference fringes. In fig. 2 interferogram of wave front with the screw dislocation is given. The registration of screw dislocation is in the consent with the earlier discovery^{8,9} of topological distortions of wave front in laser radiation of a rather wide class of lasers.

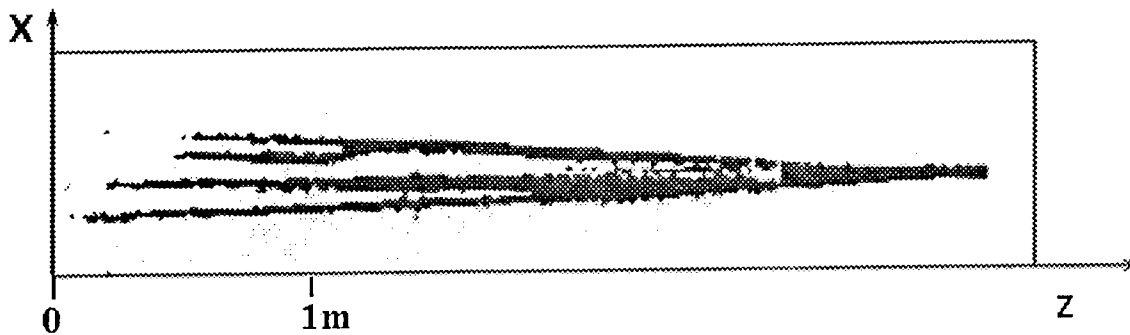


Fig. 1. Structure of the convergent laser beam.

Thus, investigated type of the laser at a stable level of total output power has the complex and unstable form of distribution of amplitude and phase in cross section of radiation. The mechanisms of stochastisation of a amplitude-phase structure of a beam and formation of channels with high meanings of intensity radiation can be different. One of them is connected to excitation of a superposition of transverse modes² in a laser cavity. Another mechanism of formation of complex distribution of amplitude and phase in the near zone can be caused by the presence smooth distortion of wave front of the laser beam near output mirror.

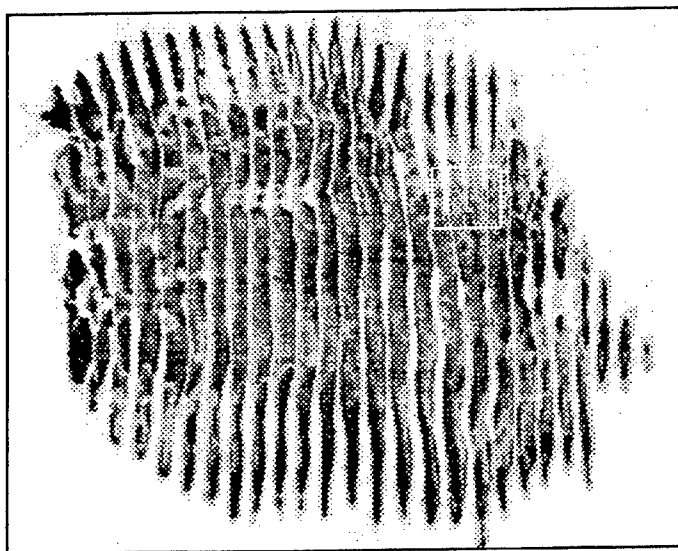


Fig. 2. Transverse shift interferogram of the laser beam.
Block—screw dislocation.

3. DIFFRACTIONAL MECHANISM OF FORMATION OF CAUSTICS AND PHASE DISLOCATIONS IN LASER BEAMS

Let's consider in more detail the process of formation of caustics and dislocations in the field of a laser beam. The general representation about character of considered process can be received on an example about propagation of a gaussian beam, the phase of which varies in an initial plane on the harmonic law. The amplitude of a field of such wave under longitudinal coordinate $z=0$ is

$$\Psi(x, y) = \exp\{-(x^2 + y^2)/w_0^2 + im/2 \cdot \sin(2\pi x/a)\}, \quad (1)$$

where m - is a parameter describing the depth of phase modulation, x, y - are cross coordinates, a - is period of modulation. At the distance z from the initial plane the field can be presented as a superposition of gaussian beams¹⁰:

$$\Psi = \sum_{q=-\infty}^{\infty} J_q(m/2)G(x', y, z'), \quad (2)$$

where J_q - is the bessel function about q order, $G_q(x', y, z')$ - is a function, which describes a field of a gaussian beam¹¹,

$$\begin{aligned} x' &= z \sin(q\alpha) + x \cos(q\alpha), \\ z' &= z \cos(q\alpha) - x \sin(q\alpha), \\ \alpha &= a/\lambda. \end{aligned}$$

Using for calculations of the characteristics of a field expression (2), and also the ray method used in work¹², it is possible to establish the basic features of transformation of initial amplitude - phase distribution. The calculations show, that even at small depth of a phase modulation in an initial section the diffraction effects result in significant spatial redistribution of intensity. So, at meaning $m = 0.1$ the contrast K ($K = I_{\max}/I_{\min}$) of the picture of intensity distribution is equal to $K=1.28$, and at $m=0.5$ $K=2.82$. At excess of the certain critical level of modulation there are qualitative changes in wave structure. At $m>1$ in a field of a wave occur the beak-shaped caustics¹² occur, and at $m>\pi/2$ near of caustic generatrix edge dislocations (ED), in which wave phase jump is equal to π , begin to form.

ED is located symmetrically relatively to the axes of beak-shaped caustic. Their arrangement in relation to the caustic generatrix corresponds to phase structure of a field given in work¹³. In this work the field is calculated on base of Persy integral. With increase of initial modulation depth of a phase the number of ED grows. The appropriate dependence is given by fig. 3. Longitudinal structure of intensity distribution is given by fig. 4 for $m=1.2$ and $w_0/a=5$. From it one can see, that the phase modulation results in formation of the longitudinal channels. These channels are extended along a propagation direction of the beam and have power density much greater than its average meaning. The axes of these areas coincide with the axes of symmetry of beak-shaped caustic.

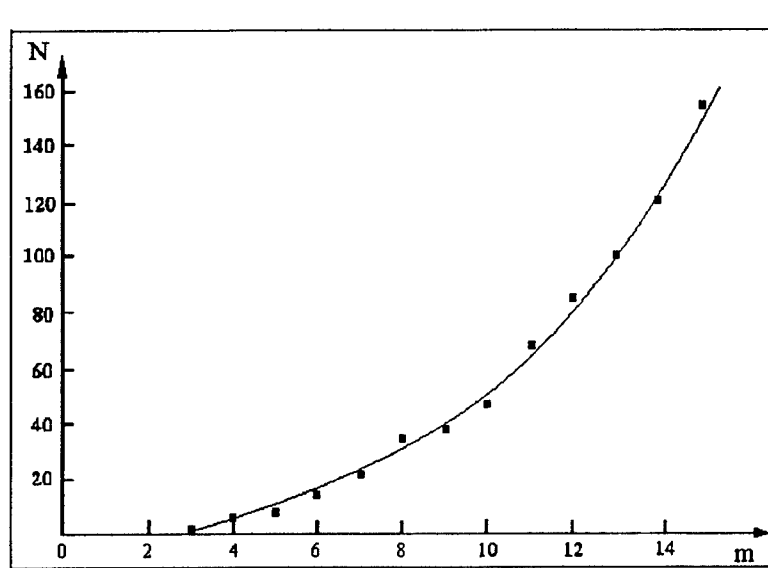


Fig.3. Dependence of edge dislocations number on the phase modulation depth.
The length of the counting range - is $a^2/2\lambda$, width - is a .

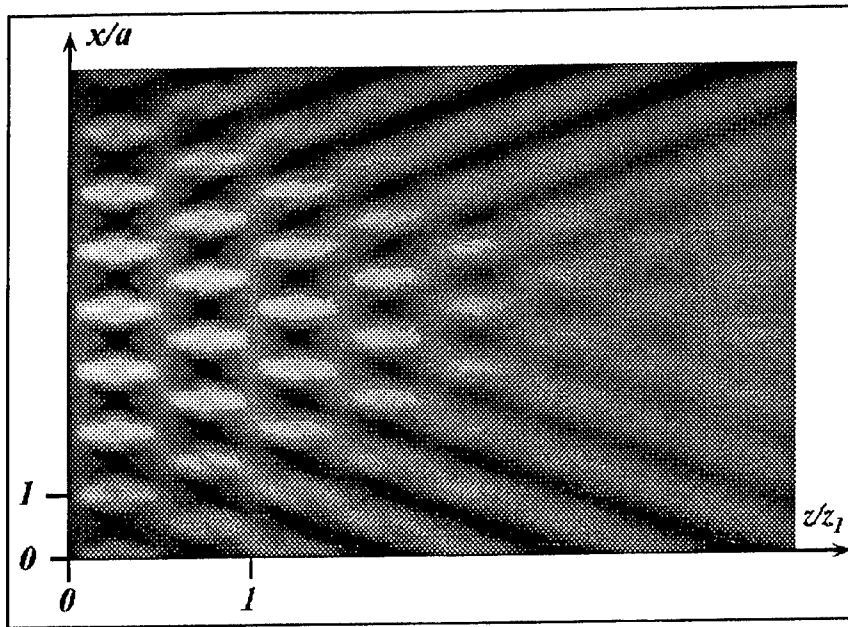


Fig. 4. Longitudinal structure of intensity of modulated gaussian beam. $z_1=2a^2/\lambda$.

If the phase modulation in an initial plane is taking place not on one, but in two cross coordinates there is an opportunity of formation of screw dislocation² (SD) of wave front. SD differ from ED fundamentally by topological structure (at path-tracing around SD a phase varies by 2π). In fig.5,a the equiphase lines structure of wave front in an initial plane is given, if the distribution is as follows:

$$\Psi_{\Sigma}(x, y) = \Psi(x, y) + i\chi\Psi(y, x) + C. \quad (3)$$

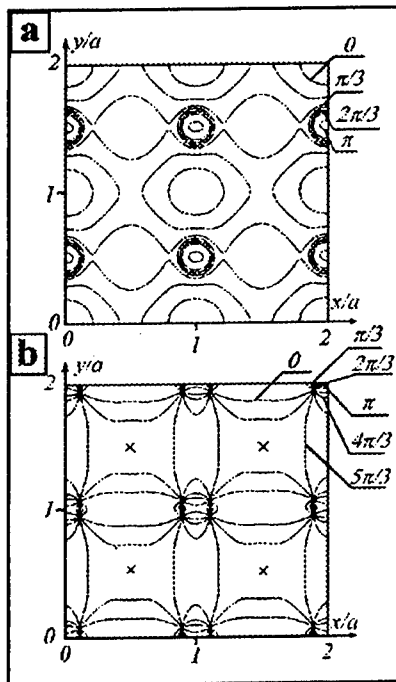


Fig.5. Structure of equiphase lines in initial (a) and $z=a^2/2\lambda$ (b) planes, xx-caustics.

The function $\Psi(y,x)$ coincides with function $\Psi(x,y)$ at replacement of cross coordinate x on cross coordinate y , C , χ are constants. The structure of equiphase lines in fig.5,a is constructed for $C=0.2$, $\chi=1$, $w_0/a=5$ and $m=2$. The position of lines testifies the presence of smooth regular distortions of wave front. In fig. 5,b the equiphase lines structure at the distances $z = a^2/2\lambda$ are represented. SD are located in points of equiphase lines crossing.

They form the original quadrupoles, each of which consists of four SD. Two of them have positive signs (are "right" ones), the other two - negative signs (are "left" ones). Quadrupoles surround the axes of caustics. As well as ED, screw dislocations arise only as the depth of initial wave front modulation exceeds certain critical meaning. If to designate through $\Delta\Phi$ a difference between the maximal and minimal meaning of a phase in an initial plane (when modulation by one coordinate $\Delta\Phi$ coincides with m), SD arise, when $\Delta\Phi > \pi/2$. Contrary to ED, each of which, in the strict sense, is formed in the certain plane $z = \text{Const.}$, SD are characterised by certain longitudinal length. Fig. 6 represents the dependence of SD length changes and their longitudinal positions on parameter m in the region with width a and length $a^2/2\lambda$. It is clear that some dislocations have a large length compared with value a^2/λ , length of the other are very small.

Process of formation of wave front dislocations was investigated also by using the stochastic theoretical model. The wave with uniform amplitude and stochastic phase in one transverse coordinate in initial

plane was considered. Fig 7 shows the dependence of average amount of ED n in phase correlation interval R_{cor} on the root mean square σ of phase in initial plane. Value n was estimated in plane $z=A^2/2\lambda$, where A – period of largest harmonic of wave front disturbances. It is seen that n tends to unity under σ tends to five. However individual dislocations are formed in laser beam even if σ is equal to unity.

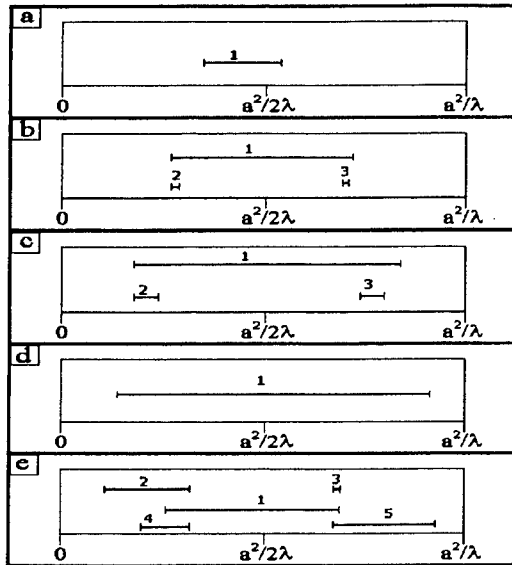


Fig. 6. Longitudinal dimensions of screw dislocations a- $\Delta\phi=2.0$, b- $\Delta\phi=2.5$, c- $\Delta\phi=3.0$, d- $\Delta\phi=3.5$, e- $\Delta\phi=4.0$. 1,2,3,4,5-labels of dislocation.

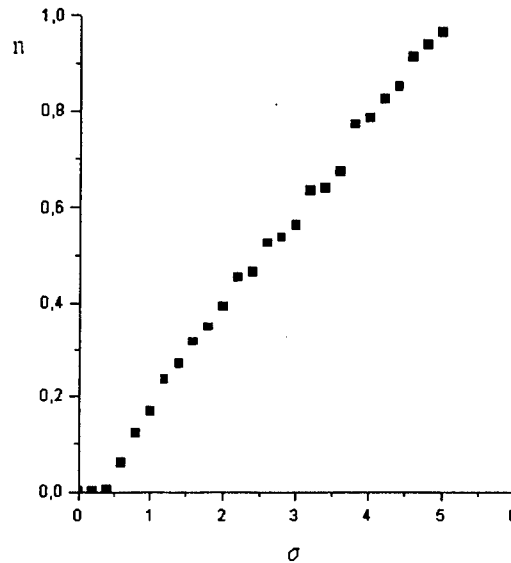


Fig. 7. The dependence of average amount of ED n in phase correlation interval R_{cor} on root mean square of phase σ .

4. CONCLUSIONS

The results of computations specify the important role, which the smooth small-scale disturbances of wave front play in transformation of an amplitude-phase structure of radiation and formation of caustics and dislocations. The occurrence of caustics and dislocations of wave front is of threshold character and is directly connected with the depth of initial phase modulation. For practice it is important that the occurrence of the specified formations in a laser beam is connected to formation of narrow channels, in which the intensity of radiation considerably exceeds its average meaning. These results have shown agreement with experimental data concerning fast-flow CO_2 laser. Thus, the problem of improvement of wave front quality in output laser beam as well as stabilisation of total power is very vital.

5. ACKNOWLEDGEMENTS

The present work was supported by the Russian Fund for Support of Leading Scientific Schools (grant N 00-15-96679) and Russian Ministry of Science (project 1.61 of the program "Physics of quantum and wave processes").

REFERENCES

1. V.S.Golubev, F.V.Lebedev, "On stability of the radiation from fast-flow gas-discharge technological CO₂-lasers. (Review article)", *Rus. J. Kvantovaya Electronica*, **12**(4), 663-671, (1985).
2. V. V. Valuev, A. I. Kutsenko, A. P. Naportovich, V. G. Naumov, S. P. Pavlov, N. E. "Investigation of multimode stimulated emission from powerful CO₂ lasers", *Rus. J. Kvantovaya Electronica*, **25**(3), 221-224 (1998).
3. U. A. Drejzin, A. M. Dikhne. "Self-oscillation instability of generation of fast-flow lasers based on unstable cavity", *Rus. J. Pisma JETF*, **19**, 818-821, (1974).
4. A. V. Artamonov, V. G. Naumov. "On Stability of the Stimulated Emission from the Fast-Flow Transverse-Priming CO₂ Laser", *Rus. J. Kvantovaya Electronica*, **4** (1), 178-180, (1977).
5. V. V. Lichansky, A. P. Napartovich. "On dynamic of radiation of fast-flow CO₂ lasers with unstable cavity", *Rus. J. Izv. AN SSSR, Phys. Ser.* **45**, 399-408 (1981).
6. A. V. Artamonov, A. P. Napartovich. "Dynamic Characteristics of a Fast-Flow Electric-Discharge CO₂ Laser", *Rus. J. Kvantovaya Electronica*, **6**(7), 1554-1556 (1979).
7. G. A. Abilsiitov, E. P. Velikhov, V. S. Golubev, F. V. Lebedev. "Perspective schemes and methods of pumping powerful CO₂ technologic lasers. (Review article)", *Rus. J. Kvantovaya Electronica*, **8**(12), 2517-2539 (1981).
8. P. V. Korolenko, V. N. Tikhomirov. "On the structure of wave front of coupled mode systems", *Rus. J. Kvantovaya Electronica*, **18**(9), 1139-1141, (1991).
9. B. D. Bobrov, E. I. Dmitriev, G. Yu. Snezhkov. "Topology of phase defects of radiation of technologic CO₂-lasers with stable and unstable resonators", *Rus. J. Kvantovaya Electronica*, **20**(7), 680-688, (1993).
10. J. W. Goodman. *Introduction to Fourier Optics*. Department of Electrical Engineering Stanford University. McGraw-Hill Book Company San Francisco, New York, St. Louis, Toronto, London, Sydney 1968.
11. D. Marcuse. *Light Transmission Optics*. Van Nostrand Reinhold Company. New York, Cincinnati, Toronto, London 1977.
12. U. A. Kravtsov, U. N. Orlov. *Geometrical Optics of Heterogeneous Media*. Moscow, Nauka, 1980.
13. L. M. Brekhovskih. *Waves in Stratified Media*. Moscow, AN SSSR, 1957.

Construction and characterization of a CO₂ wave guide laser with a special electrode design for materials processing

J.L.Jiménez Pérez ^a, M.A. Algatti ^b, J.G. Mendoza-Alvarez ^{a,c}, A. Cruz Orea ^{a,c}

^a CICATA-IPN, Legaria 694, México D.F. 11500, México.

^b Departamento de Física e Química, Universidade Estadual Paulista

"Júlio de Mesquita Filho" Campus de Guaratinguetá 12500-000 Guaratinguetá, SP, Brazil

^c Departamento de Física, CINVESTAV-IPN, Apdo. Postal 14-740. México D.F. 07300, México.¹

ABSTRACT

We describe the design and construction of an efficient tunable CO₂ wave guide laser which was used for thermal graving of predigitalized images over polymeric materials. The small internal diameter of the cylindrical wave guide allowed the laser operation in high pressure regime ranging from 50 Torr to 100 Torr, which gives higher gain per cavity length. The operation of the laser at 80 Torr with the gas composition CO₂:N₂:He::11:9:60 gave a 400 MHz laser linewidth. For the proposed laser design we used an electrodes configuration which provides a symmetric discharge. The laser cavity, divided into three pieces, show great light coherence.

Keywords: gas lasers, industrial applications, optical waveguides

1. INTRODUCTION

Wave guide lasers have interested the scientific community since many years ago due to their great applicability in high resolution molecular spectroscopy,¹ optical pumping of far infrared (FIR) lasers,² high temperature plasma diagnostics,³ controlling of pollutant in atmosphere⁴⁻⁸ and materials processing.⁵ The main feature of this kind of laser is that it may operate in a pressure range higher than the conventional one, giving a higher gain per unit length,⁹ allowing the construction of very compact light sources that may operate as sealed-off devices.¹⁰⁻¹³ These characteristics of such lasers make them the candidates for several applications in materials processing due to its inherent low operational cost. Another important feature of such lasers is that under the high pressure operation regime the collision-broadened laser linewidth is wider than the separation between two consecutive longitudinal oscillating modes inside the laser cavity, allowing one to realize a continuous tuning over the spectral range that may exceed 1GHz.¹⁴ Such tunable coherent light source may be used as a local oscillator in heterodyne detection of weak light signal coming from the interstellar gas clouds.¹⁵

In this paper is described the project of a compact CO₂ wave guide laser that may be used in a wide range of applications encompassing high resolution spectroscopy as well as material processing. The present project was used together with a computer-controlled x-y translator for thermal graving of plastic materials.

The design of the optical cavity using a 2.7 mm of inner diameter and 300 mm long cylindrical quartz wave guide allowed the operation at pressures ranging from 50 Torr up to 100 Torr. This pressure regime gives higher gain per cavity length than the conventional CO₂ lasers, due to the more efficient cooling processes by heat diffusion through the cavity walls. In this regime of operation the pressure-broadened laser linewidth is larger than the longitudinal intermode separation allowing one to explore a continuous tunability in a frequency range of 490 MHz around the central line. The laser works with a current of 10 mA at a voltage of 10 kV giving an output power of 2.5 watts. The coaxial aluminium disk electrodes provide a singular stable discharge. The laser uses a 99 % reflector gold mirror and 89 % reflector Ge mirror built at the IEAv-CTA research group contributing for the total nationalization of the laser project. It is also presented and discussed the characterization and the operational advantages of this easily handling laser as well as its application in thermal graving of predigitalized images.

¹ Further author information-

J.L.J.P: Email: jimenezp@mail.cicata.ipn.mx or jimenezp@fis.cinvestav.mx

M.A.A: Email: algatti@feg.unesp.br

J.G.M.A: Email: jmendoza@fis.cinvestav.mx

A.C.O: Email: orea@fis.cinvestav.mx

2. LASER PARAMETERS

The schematic diagram and the photograph of the laser cavity is shown in FIG. 1. It consists of a 300 mm long cylindrical quartz tube with 2.7 mm of internal diameter divided into three pieces (two of 60 mm and one of 180 mm). The cavity has two coaxial aluminum electrodes separated by a 180 mm-long quartz piece. The electrode thickness is 3 mm. The optical cavity is formed by the quartz waveguide and two mirrors. The 100 % reflector mirror is made of a gold film sputtered over a Pyrex™ substrate with flatness of $\lambda/4$ (for $\lambda=6328 \text{ \AA}$ He-Ne laser line). The 89 % reflector mirror is made of a polished concave ($R=10\text{m}$) Ge substrate whose surface was covered by several dielectric layers in order to improve its reflectivity. The quartz wave guide has lower losses than the Pyrex™ wave guide ($\alpha_{\text{quartz}} = 2.5 \times 10^{-4} \text{ cm}^{-1}$; $\alpha_{\text{pyrex}} = 1.8 \times 10^{-3} \text{ cm}^{-1}$), for infrared radiation propagation.¹⁵ The wave guide is formed by a Pyrex™ jacket inside which circulates water for cooling purposes. The aluminum electrodes have internal channels for circulating cooling liquids as distillate and de-ionized water or high voltage transformer oil. The advantage of using such kind of electrode configuration is that one may work in cold high current regime, minimizing the oxide and silicate formation over the electrode surface that is in contact with the quartz tube inside the laser cavity. The ring-shaped electrodes provide a extremely uniform and symmetric discharge avoiding the appearance of hot points caused by electric field inhomogeneities. Such discharges are more efficient in transferring electron energy to the molecule internal degrees of freedom.

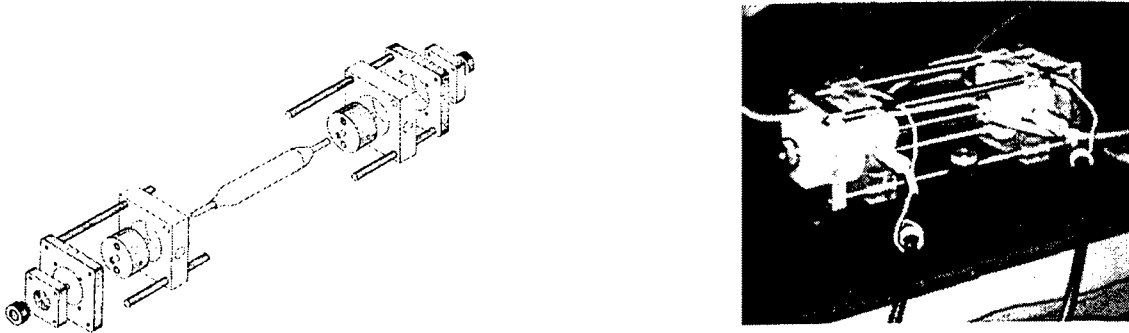


Figure 1 a-) Schematic diagram of the laser cavity showing the terminal blocks, the disk shaped electrodes, the quartz waveguide and the Pyrex™ jacket as well as the stainless steel bars used for mechanical stabilization of the laser cavity. b-) Photograph of the assembled CO₂ waveguide laser showing the high voltage cables and the PVC tubes used for electrodes and waveguide cooling.

The rigid laser structure is constituted by four stainless steel bars that hold the terminal aluminum blocks where mirrors are fixed. This layout may be optimized from the mechanical stability point of view by using invar or quartz bars which have a thermal expansion coefficient about one order of magnitude smaller than the stainless steel, assuring a stable laser operating condition even in the absence of any dynamical cavity length stabilization system.¹⁶ The output mirror is adapted to a piezoelectric transducer that is used for cavity tuning. The output power fluctuation due to the cavity thermal expansion could be controlled by applying a voltage to the piezoelectric ceramic through a stabilized high voltage DC power supply. The laser electrodes are electrically insulated by two acrylic resin blocks with a dielectric rigidity of 15 kV/mm, assuring a non-risk accidental operating condition. The electrodes are cooled by bi-distilled water and de-ionized water circulating in an appropriate closed loop, with a flow rate of 50 liters/hour. The laser waveguide is cooled by water at 17°C, circulating in an open circuit. The waveguide cooling may be improved by circulating a more volatile fluid in a closed loop, like CH₃OH for instance.

The laser power supply whose schematic diagram is shown in Fig.2 is basically a complete wave form rectifier with a capacitive filter operating at a maximum voltage of 15 kV and 10 mA current with a ripple less than 2%. The power supply is connected in series with the laser tube through a 325 kΩ ballast resistor that keeps the current at reasonable levels after the dielectric breakdown of the gas mixture inside the laser cavity. The voltage drop through the laser tube is controlled by varying the voltage applied to the primary stage of the high voltage transformer. Typical operating values are 8 mA for 7.5kV.

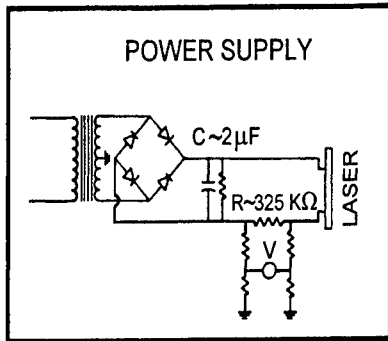


Figure 2- Schematic diagram of the laser power supply showing the complete waveform rectifier, the capacitive filter and the load resistor.

The optical cavity was aligned using a He-He laser through an appropriate experimental set up that allowed simultaneous monitoring of the position of the near and the front mirrors. The position of each laser's mirror was adjusted through three screws that defined the mirror's plane. The final adjustment was performed maximizing the laser output power and optimizing the shape of the far field mode pattern that could be seen like a dark spot over the surface of a fluorescent screen. The gas circuit operated in an open flux regime was composed by a double stage mechanical pump whose pumping speed is 40 liters/min. The gas flux within the laser cavity was controlled through three needle valves. Typical values of gas flux were 8.4 liters/min at 80 Torr of total gas pressure.

3. CHARACTERISTICS OF WAVE GUIDE LASER OPERATION

To characterize the operational condition of the waveguide CO₂ laser it was necessary to measure simultaneously the current and the voltage applied to the laser tube for several gas mixtures at different pressure as well as the output power variation with current and voltage. Typical results are presented in Figs. 3 to 5.

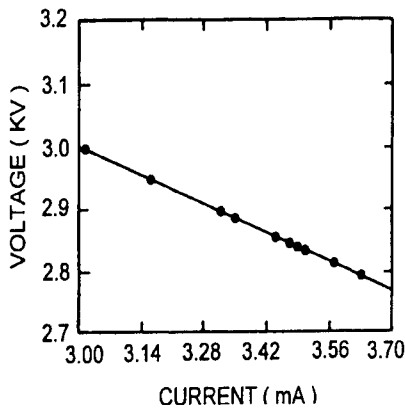


Figure 3- The voltage vs. current dependence for total pressure of 55 Torr and gas mixture composition (in Torr) CO₂:N₂:He;19:10:26. The curve shows the non-ohmic behavior of the discharge for this pressure range of operation. The output power is 2.1 watts.

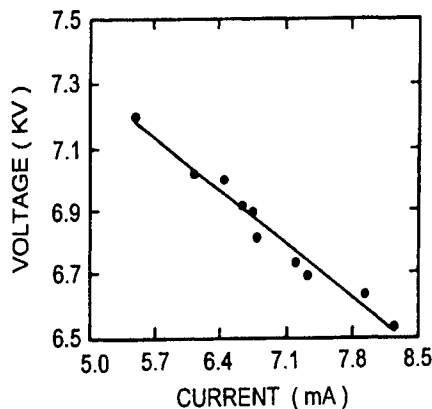


Figure 4- The voltage vs. current dependence for total pressure of 80 Torr and gas mixture composition (in Torr) CO₂:N₂:He;11:9:60. The curve shows the non-ohmic behavior of the discharge for this pressure range of operation. The output power is 1.6 watts.

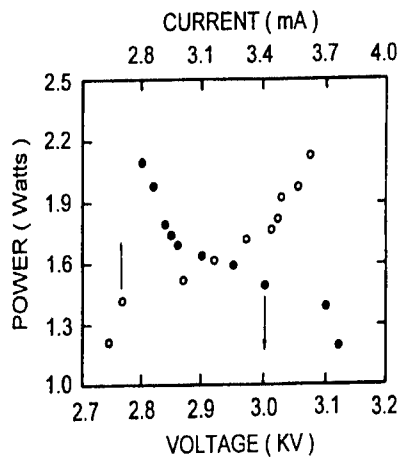


Figure 5- The power vs. voltage and power vs. current dependence for total pressure of 55 Torr and gas mixture composition (in Torr) $\text{CO}_2:\text{N}_2:\text{He};19:10:26$. The curves show the non-ohmic behavior of the discharge.

Figure 3 presents the voltage vs. current characteristic for a total gas pressure of 55 Torr and a mixture composition in the proportion (in Torr) of $\text{CO}_2:\text{N}_2:\text{He};19:10:26$, giving a maximum output power of 2.1 watts. Quite similar results are presented in Figure 4 for a total gas pressure of 80 Torr with proportions $\text{CO}_2:\text{N}_2:\text{He};11:9:60$, giving a maximum output of 1.6 watt. It can be seen from the results that the discharges present a non-ohmic behavior for those values of applied voltage, since the current increases as the voltage decreases. This behavior is closely related to the electron stripping and acceleration by the electric field. In order to reach the discharge's electrical breakdown, very high values of voltage are applied to the laser tube, producing high energy electrons that are inefficient in exciting the metastable upper laser level. These high energy electrons contribute significantly for the molecular fragmentation through inelastic collisions. Many of these inelastic processes contribute for the decreasing of the current inside the laser cavity. As the voltage applied to the laser tube is decreased, the current increases favoring the inelastic processes resulting in upper laser level excitation. Therefore it is reasonable that current should increase with the voltage decrease.

The output power dependence on voltage and current, for a total gas pressure of 55 Torr and composition mixture of $\text{CO}_2:\text{N}_2:\text{He};19:10:26$ is presented in Figure 5. It can be seen that the output power decreases with voltage increasing and increases with current increasing, in close agreement with the discharge behavior presented in Figs. 3 and 4. Therefore the decrease of voltage produces electrons within discharge that are much more effective in converting kinetic energy into radiant energy through inelastic collisions.

The increasing of current and output power when the voltage decreases is observed in all the voltage range below the discharge breakdown. This behavior follows the same trend, up to the values above those when the discharge turns off. The disruption of the discharge happens before reaching the optimum value of the voltage and current, for that the output power and the current should decrease after reaching the optimum value, which is different for other values of total pressure and gas mixture composition.

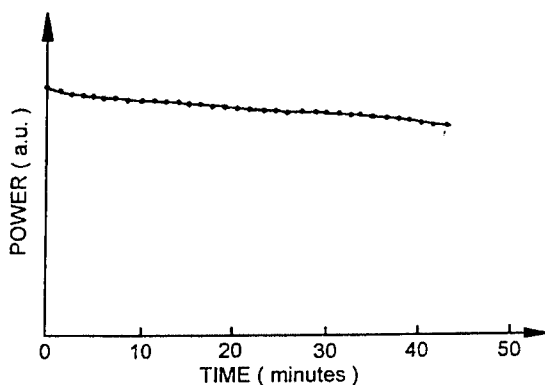


Figure 6- The time dependence of laser output power, (in arbitrary units), for a PZT adjustment performed in each one minute or one minute and half. The main agent responsible for power fluctuations is the thermal expansion of the laser cavity.

The output power was monitored using a power meter and the fluorescent screen to follow simultaneously the change in the output power and in the far-field transversal mode shape. The results obtained are shown in Fig. 6 It was observed during the

measurements that the thermal fluctuations causing cavity expansion is the main responsible for the laser output power oscillations. These fluctuations may be corrected by applying a voltage to the piezoelectric ceramic in order to maximize the output power. It is seen from figure 6 that the power was kept almost constant during approximate 40 minutes applying the correction voltage for a period of one minute to one minute and half. The main agent responsible for cavity length variation is the Nylon end blocks that hold the mirrors.

The tuning curve of the laser cavity is shown in Figure 7. The PZT ceramic was calibrated using an He-Ne interferometer giving an expansion rate of $8 \mu\text{m/kV}$. The distance between two minimum correspond approximately to 500 V applied to PZT. This gives a laser linewidth of about 400 MHz. This result is in close agreement with the expected by the phenomenological model proposed by Abrams and Bridges.¹⁷

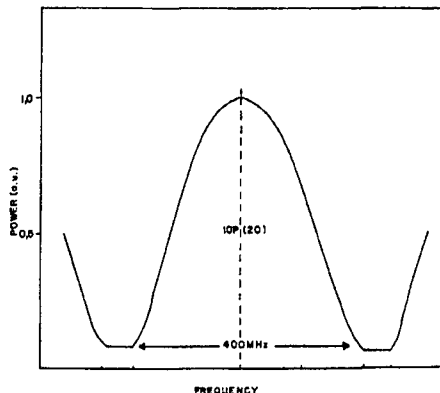


Figure 7- The tuning curve for the 10P(20) laser line. The cavity longitudinal mode separation is approximately 500 MHz. The collision-broadened laser linewidth is smaller than the intermode separation for the operating gas pressure.

4. LASER APPLICATIONS

Infrared Lasers operating in the 9-10 μm region of the electromagnetic spectrum at lower power level, i.e., around 1 or 2 watts, may be used in thermal processing of many kind of polymers and plastics such as polyethylene, polypropylene, polyvinylchloride and so on. This thermal processing includes, for instance, materials drilling, cutting holding and graving.

In this paper the CO_2 waveguide laser was used for thermal graving of a thermal plastic resin commonly used in thermographs, in order to demonstrate its capability of creating a permanent register of a digitalized image previously stored on a personal computer (PC).

The PC controlled two step motors that drive a x-y positioning table. The step motors were controlled through an appropriate analogic/digital card (A/D converter) designed and built at our laboratory. The laser beam was focused by a germanium lens with a focal distance of 6.4 cm. The spot size of the laser beam over the thermoplastic resin sensibilized a circular area of approximately $100 \mu\text{m}$ of diameter. This area was scanned driving the step motor over 32 steps. The variation of the period of time that a region of the plastic surface was exposed to the laser beam allowed one to get the colors contrast needed for the image definition. The thermal graved image over the thermoplastic surface, realized at the atmospheric pressure is shown in Figure 8. It can be appreciated that the contrast obtained with a maximum exposition time of 8 ms and a minimum exposition time of 2 ms is very good, allowing one to get the complete definition of the image. It also can be observed two vertical cuts resulted from the over exposition to the laser beam (approximately 16 ms) at the point where the positioning system reverses the direction of the sample translation.



Figure 8- Photograph of the thermal graved digitalized image of "Mr. Spock" from "Star Trek" TV's series. The laser beam is focused over a thermoplastic resin that is moved by a computer controlled x-y positioner. The variation of the time that the sample is exposed to the laser beam, between 2 ms and 8 ms allowed one to get the contrast enough to define the image.

5. CONCLUSIONS

To summarize, this paper describes the construction and the characterization of a CO₂ waveguide laser. The operation of the laser at 80 Torr with the gas composition of CO₂:N₂:He;11:9:60 gave a 400 MHz laser linewidth. The results obtained are in close agreement with those predicted by phenomenological models. Also this laser was applied to the thermal graving of a plastic material. These small coherent light source allowed one to get a compact computer controlled thermal marker that may be used for drawing patterns over several kinds of surfaces in very small areas. The system may also be used for drilling and cutting several kinds of plastics and polymers as well as to produce thermal induced oxidation over metal surfaces.

6. ACKNOWLEDGEMENTS

We would like to thank Prof. Dr. Carlos Schwab from Instituto de Estudios Avanzados-Centro Tecnológico Aeroespacial (IEAv-CTA) for building the Ge mirror that allowed the complete nationalization of the laser project. One of us, J.L.J.P. would like to thank CICATA-IPN, CINVESTAV-IPN, Consejo Nacional de Ciencia y Tecnología (CONACYT)-México and Conselho Nacional de Desenvolvimento Científico e Tecnológico (CNPq)-Brazil for financial support. Also J.L.J.P. would like to thank Prof. Gabriel Peña-Rodríguez for his help in the images.

7. REFERENCES

1. W. Demtroder, "Laser Spectroscopy", Springer-Verlag 1988.
2. J. Stellan, *Infrared Physics*, **29**, pp. 853-874, 1989.
3. K.W. Gentle, *Rev. Mod. Phys.* **67**, pp. 809-874, 1995.
4. P.L. Meyer and M.W. Sgrist, *Rev. Sci. Instr.* **61**, pp.1177-1807, 1990.
5. I.G. Calasso, I. Delgadillo, M.W. Sigrist, *Chem. Phys.* **229**, pp. 181-191, 1998.
6. B.L. Zimering, A. C. Boccara, *Inst. Sci. & Tech.* **26(2&3)**, pp. 261-279, 1998.
7. B.L. Zimering, A. C. Boccara, *Appl. Opt.* **36**, pp. 3188-3194, 1997.
8. B.L. Zimering, A. C. Boccara, G.C. Pandey, *Progress in Natural Science* **6**, pp. S606-S608, 1996.
9. P.A. Atanasov, *Opt. Eng.* **34m**, pp. 2976-2990, 1995.
10. J.J. Degnan, *Appl. Phys.* **11**, pp. 1-33, 1976.
11. D.H. Hall and C. A. Hill, in "*Handbook of Molecular Lasers*", edited by Peter K. Cheo, Marcel Dekker, Inc., New York, 1987.
12. P.V. Salvo, *Industr. Laser Rev.* **7m** pp. 9-19, 1992.
13. W.J. Witteman, "*The CO₂ Laser*", Springer Series in Optical Science, vol. 53, Springer-Verlag, Berlin, 1987.
14. R. Abrams, in "*Laser Handbook*", vol. 3, edited by M.L. Stich, North-Holland Publishing Company, Amsterdam, 1979.
15. E.E. Matinero and M. Stuke, *Optics Commun.* **30**, pp. 349-380, 1979.
16. R. Genzel, D. Hollenbach and C. H. Townes, *Rep. Prog. Phys.* **57**, pp. 407-531, 1994.
17. R.L. Abrams and W. B. Bridges, *IEEE J. Quantum Electron.* **QE-9**, pp. 940-946, 1973.
18. P.T. Woods and B. W. Jolliffe, *J. Phys. E, Sc. Inst.* **9**, pp. 395-402, 1975.

Energy Parameters and Resource of High-Power Pulse-periodical Sealed-off TEA-CO₂ Lasers

Boris A.Kozlov, Sergei G.Fomin
Electronic Eng. and Techn. Dept., Radio-Engineering Academy
59/1 Gagarin str., Ryazan, 391000, GSP, RUSSIA

ABSTRACT

Physical processes proceeding over the active electrode surfaces and their influence on a spatial plasma homogeneity of the volume discharge as well as the energy parameters and the resource of sealed-off pulse-periodical TEA-CO₂ lasers have been investigated. Microstructures of the active electrode surfaces which lead to the increase of autoelectronic emission have been found to be formed under the influence of the volume discharge plasma and the products of plasma chemical reaction. The increased values of these currents initiate the formation of local channels in the cathode area of a volume discharge and initiate complete transition of volume discharge into a local one. The electrode materials, which provide the formation of stable volume discharges are determined and a maximum resource of sealed-off TEA-CO₂ lasers is achieved.

Keywords: sealed-off TEA-CO₂ lasers; volume discharge; spatial plasma homogeneity; plasma-chemical processes; photo- and autoemissivity processes; microstructure of the active electrode surfaces; local channels; electrode materials; resource.

1. INTRODUCTION

One of the most urgent problems which arise in developing the sealed-off TEA-CO₂ lasers and in determining the range of their possible applications is referred to the question of providing their high-resource. The solution of this problem is closely connected with generating a spatial and homogeneous volume discharge, stable to localization under the conditions, when an accumulation of plasma chemical reaction secondary products in laser mixture takes place¹⁻³.

The sealed-off TEA-CO₂ lasers resource is actually determined by the time when it is possible to form a spatial and homogeneous volume discharge. The localization of a volume discharge is believed to occur due to the development of plasma instabilities when secondary compounds are accumulated in the working mixtures of TEA-CO₂ lasers. This point of view is not universal.

As it is shown in a number of publications the localization of a volume discharge in the active mixtures of sealed-off TEA-CO₂ lasers can be also caused by the processes occurred on the active electrode surfaces^{1,4-6}.

The investigation results of the interrelated processes, initiating volume discharge transformation into a local one and limiting the energy and resource characteristics of pulse-periodical sealed-off TEA-CO₂ lasers are presented in this experimental work.

2. Experimental Set-up

The experimental investigations were conducted in the following directions:

1. A long-term visual and photographic observations of a spatial volume discharge plasma structure.
2. Microstructure investigation of the active electrode surfaces for a volume discharge forming.
3. The electron emissivity energy measurements out of the active electrode surfaces.
4. Studying the autoelectronic characteristics of the cathodes.
5. Choosing the electrode materials and the resource testing of different types of sealed-off TEA-lasers.

The investigations were conducted in an experimental set-up which consisted of a discharge chamber with ten identical discharge gaps and with electrodes made of different materials; it contained a pulse generator for exciting the volume discharges in investigated gaps; a system of pumping out and filling in a discharge chamber by the gases being examined; a measurement device of electron emissivity energy out of the active electrode surfaces; an optical and raster electronic microscopes; an autoelectronic currents meter and the measuring devices for determining laser parameters.

We used Al, Mg, stainless-steel, Cu, Ni, Mo, Ti, Ta, Nb and W as cathodes materials for excitation the volume discharges. The height of every gap was 0,7 cm, cross-section $-0,8 \text{ cm}^2$. A volume discharge of a nanosecond duration was simultaneously excited in all discharge gaps at 40 Hz pulse repetition rate and energy density up to $250 \text{ mJ}\cdot\text{cm}^{-3}$. Blowing of laser gas mixtures into a discharge chamber was done by an "electrical wind"^{7,8}. The volume discharges were being glowed in mixtures with an initial composition of $\text{CO}_2:\text{N}_2:\text{He}=1:1:8-1:1:2$ and at the total pressure $P=1-1,2 \text{ Atm}$.

The control of plasma spatial homogeneity of volume discharge was being done within definite time intervals according to the photos of plasma glowing made by a microphotometer MF-4. In order to make measurements of autoelectronic currents out of cathodes the discharge chamber was evacuated up to residual pressure $P < 10^{-7} \text{ Torr}$ and interelectrode gaps were decreased up to $d=1 \text{ mm}$. The condition of electrodes surfaces were observed with the help of optical microscope (Carl Zeiss, $m < 500$) or a raster electronic microscope (JOEL-7, $m < 5000$). For this reason the discharge chamber was opened and the investigation of microstructure was carried out in the open air (optical microscope) or in the vacuum (electron microscope). The measurements of electron emissivity energy out of active electrode surfaces were simultaneously conducted with the method of "vibrating condenser"⁹ according to a contact potential difference. These measurements were carried out in the vacuum ($P < 10^{-7} \text{ Torr}$). The value of electron emissivity energy out made it possible to define a coefficient of amplification of the electrical field on the cathode surface and an area of emissive centers on the basis of the Fowler-Nordheim equation^{10,11}. The control of chemical composition of working mixtures in the TEA- CO_2 lasers operation process was made by a monopolarity mass-spectrometer.

3. Experimental Results

3.1. Volume Discharge Resource

Fig.1 shows the photographs of volume discharge plasma glowing in $\text{CO}_2:\text{N}_2:\text{He}=1:1:4$ mixture, in the initial mixture (a) and in the mixture with chemically stable composition after 10^6 discharge pulses (b). The structure of volume

discharge plasma in the initial mixture is characterized by a high spatial homogeneity with the increased glow brightness in the cathode zone in all discharged gaps. It means that a space plasma homogeneity of a volume discharge in the mixtures without secondary compounds does not depend on the type of electrode material.

As the number of discharge pulses in the volume discharge cathode area is being increased the thread-like channels with a fixed position to the anode side are being formed. The length of these channels are being increased as the number of discharge pulses is being increased. After 10^6 discharge pulses the thread-like channels completely overlap the discharge gaps formed by Al, Mg and stainless steel electrodes. In the gaps formed by the copper and nickel electrodes the linear dimensions of the thread like channels reach ~20-40 % of the interelectrode gap value. When making molybdenum, titanium, tantalum, niobium and tungsten electrodes a plasma spatial structure of volume discharge does not undergo the visible changes. As the number of discharge pulses is increased a structure of the active electrode surfaces is significantly changed.

Fig.2 shows a state of the active surfaces of electrodes made of Al and Ni after being acted upon them by a volume discharge plasma (a) and after 10^4 (b) and 10^6 (c) discharge pulses. These photos are obtained by means of a raster electron microscope. In the photos we see that when the electrode surfaces are effected by a volume discharge plasma it results in visible disruptions of the electrode surface. Numerous island-like formations consisting of oxide compounds appear on it. The measurements of their geometrical sizes after 10^6 discharge pulses showed that they achieved $0,03 - 0,1 \text{ mm}^{10}$.

The microstructure changes of electrode working surfaces result in the increase of autoelectron currents from these surfaces. In order to determine the nature of these phenomena the autoelectronic currents from these surfaces and a value of electron emissivity energy were measured in synchronism with the change in a microstructure of the active surfaces. The volt-ampere autoelectron current characteristics in Fowler-Nordheim coordinates^{5,6,11} for aluminium, nickel, copper, molybdenum, tantalum and tungsten cathodes prior to the effect of a volume discharge plasma on them and after 10^6 discharge pulses are shown in fig.3. The given volt-ampere characteristics obtained in the result of the measured electron emissivity energy values allow easily determine the amplification coefficient of the electric field over the microheterogeneities β .

The measurements of the electron emissivity energy prior to the effect of a volume discharge plasma on the electrode surfaces and after 10^6 discharge pulses showed that the electron emissivity energy changes only to 0,05 - 0,2 eV. It makes it possible to state that the main contribution to the change of autoelectronic currents is made by a value of the electrical field β . Some experimental values of the amplification coefficient of the electrical field over microheterogeneities prior to the effect of volume discharge plasma $-\beta_0$ and after the affect of volume discharge plasma $-\beta_1$ on the electrode working surfaces are given on the diagrams in fig.3.

The highest changes of the amplification coefficient of the electric field after the affect of a volume discharge plasma on the electrode working surfaces are observed at aluminium, nickel and copper. The value of the amplification coefficient on the electrodes made of molybdenum, tantalum and tungsten are changed insignificantly. The comparison of autoelectron values of the currents coming out of the investigated material surfaces while changing the electron emissivity

energy to 0,05-0,2 eV together with corresponding current changers in the case of increasing the amplification coefficient indicates that the increase of autoelectronic currents are mostly connected with the increase of the local values of electrical field occurred on the microheterogeneities being formed. These results directly point out that it is advisable to make the sealed-off TEA-CO₂ lasers electrodes using such materials as molybdenum, tantalum, tungsten and niobium. These results indicate that the resource of sealed-off TEA-CO₂ lasers is determined by the period of time during which the plasma-generated microinhomogeneities at the surface of the electrodes are achieved of the value enough for transition of the autoelectronic emission current to an explosive one.

The formation of the local channels in the volume discharge area and the increase of their geometrical dimensions synchronically with the increase of the amplification coefficient of the electric field on the microheterogeneities, appeared as a result of volume discharge plasma effect, witness of the leading role of autoelectron emission in a volume discharge localization in the sealed-off TEA-CO₂ lasers in the process of their functioning.

According to the electron explosive emission concept the regeneration process can be developed in the following way. Small values of autoelectron currents at "natural" microheterogeneities on the electrode surfaces are increased as far as the geometrical dimensions of microheterogeneities and changes of their electric properties such as density, conductivity, heat capacity and electron emissivity energy are increased. When the threshold autoelectron current value is achieved the emitter heat destruction takes place, forming plasma in evaporated material vapours where the concentration of charge carriers is increased to several orders⁴⁻⁶.

The electrical field in the case when autoelectron emission current is transformed into electron explosive emission current, initiating correspondingly the regeneration of the volume discharge into local one, has the value of $10^7 - 10^8$ B*cm⁻¹^{4-6,11}, that is

$$E_{AV} * \beta = 10^7 - 10^8, \quad (1)$$

where E_{AV} – is an average value of electrical field in the "anode-cathode" vacuum gap or an average value of electrical field in the range of cathode potential drop of the volume discharge;

β - the amplification coefficient of the electrical field in the range of emitter (on the cathode area).

The initial values of the amplification coefficient of the electrical field that is the values which are typical of electrode surfaces prior to the effect of a volume discharge plasma are $\beta_0 \sim 10^1 - 10^2$. If we suppose that the amplification coefficient β_t of the autoemitter electric field under the influence of the volume discharge plasma is changed according to the law:

$$\beta_t = \beta_0 * (1 + a * t^n), \quad (2)$$

where a – is a parameter, characterizing the change velocity of the field amplification coefficient and is determined by the grow velocity of microheterogeneities geometrical dimensions;

t – is the total time of volume discharge plasma interaction with a cathode surface.

We can have an expression for a volume discharge resource and for the sealed-off TEA-CO₂ lasers resource respectively as:

$$T = ((\beta_t - \beta_0) / a * \beta_0)^{1/n} \quad (3)$$

As we know the initial meaning of the amplification coefficient of the electric field and the value, corresponding to an autoelectron emission transfer into an explosive one as well as the value "n" we can determine the resource value of the sealed-off TEA-CO₂ lasers volume discharge.

The value $(\beta_t - \beta_0) / \beta_0$ in the expression (3) can be used as a parameter, characterizing an "initial stability" of the volume discharge to localization.

As far as it is problematic to determine the "a" and "n" values in the expression (3) theoretically then we can get the information about the resource only from the experimental research results.

Resource tests were conducted at two types of small-size sealed-off TEA-CO₂ lasers operating at a repetition pulse rate of $F = 20 - 50$ Hz (metall-ceramic TEA-CO₂ lasers with gases mixture blowing by "electrical wind") and $F = 0,5 - 2,5$ kHz. In both cases the volume discharge was formed in the gap, having the following geometrical dimensions $V_a = 18 * 0,8 * 0,8$ cm³. The ratio of the volumes of the active elements to the discharge exciting zone was respectively, $k_1 \sim 155$, $k_2 \sim 830$. Aluminium, nickel, copper and tantalum were used as electrodes material. The working mixtures consisted of CO₂:N₂:He in proportions of 1:1:6 and 1:1:8 at a total pressure $P = 1$ Atm. Spatial plasma homogeneity of volume discharge was inspected visually through optical resonator and special windows, being located along the discharge gap. Photographing of a volume discharge plasma glow was made in the definite time intervals.

The results of the research showed the following. The volume discharge in the gaps of aluminium electrodes saves its spatial heterogeneity during 3-7 hours. For the active laser element, operating at a repetition pulses rate $F = 40$ Hz it corresponds $N \sim 4,3 * 10^5 - 10^6$ pulses. For the active element with $F = 10^3$ Hz the resource has close values in time, the number of discharge pulses, however, is increased up to $N \sim (1,1 - 2,5) * 10^7$ ones. The formation of a volume discharge between copper and nickel electrodes results in the increase of a resource up to 50-80 hours. The highest resource - $T = 120 - 130$ hours ($N \sim (4,3 - 4,6) * 10^8$ pulses) was achieved when the electrode was made from tantalum. These results were obtained when the formation of a volume discharge was made in a CO₂:N₂:He = 1:1:8 mixture. The use of CO₂:N₂:He = 1:1:6 mixture results in the two fold decrease of the resource.

The chemical composition measurements of the working mixtures after the resource testing was done, showed very low amounts of oxygen concentration in all cases.

The refilling of the active elements with fresh mixture without changing electrodes, after having been done the resource testing, and the repeated resource measurements showed that the glowing time of a spatial volume discharge (volume discharge resource) has from 2 to 5 fold decrease.

The results obtained indicate that the volume discharge resource in CO₂-laser mixtures at atmospheric pressure is determined by the type of electrodes material and the chemical composition of the working mixture. The highest resource is achieved when the electrodes are made of materials less affected by plasma interaction, containing the "active" forms of oxygen and nitrogen oxides.

3.2. Sealed-off TEA-CO₂ Lasers Resource

Fig 4 shows the dependence of pulse radiation energy on operation time of a small-size TEA-CO₂ laser with an exciting zone of a volume discharge $V_a = 18 \cdot 0,8 \cdot 0,8 \text{ cm}^3$ and the aluminium (a), copper (b), nickel (c) and tantalum (d) electrodes. The active laser element was made of ceramic 22XC with the diameter of 8 cm and the length of 35 cm. The initial mixture consisted of CO₂:N₂:He in relation to 1:1:5 at total pressure of $P = 1 \text{ Atm}$. The gas mixture regeneration was conducted by means of two palladium catalysts.

“Transversal” blowing of gas mixture in the active element was carried out by the “electrical wind”. TEA-CO₂ laser operated at a pulse repetition rate $F = 40 \text{ Hz}$. The active laser element was cooled by an air stream.

It is seen that the radiation energy in the pulse does not directly depend on the type of electrode material after switching the laser on and after achieving the stationary value. Laser resource with aluminium electrodes is $\sim 7,5$ hours ($N \sim 1,08 \cdot 10^6$ pulses). In the laser with copper electrodes, the geometrical dimensions of which are identical, the radiation energy drop in the stationary mode pulse occurs 37 hours later ($N \sim 5,33 \cdot 10^6$). The use of nickel electrodes provides the laser resource for ~ 52 hours ($N \sim 7,5 \cdot 10^6$ pulses). At last forming the volume discharge between the tantalum electrodes continuous laser operation is provided within ~ 78 hours ($N \sim 1,12 \cdot 10^7$ pulses).

The filling of the active element with mixtures CO₂:N₂:He in proportion of 1:1:6 and 1:1:7 ($P = 1 \text{ Atm}$) and the use of tantalum electrodes allow to increase the total operation time for lasers to 90-120 hours at a pulse repetition rate from 40 to 50 Hz¹².

The dependencies of the average radiation power on time of two TEA-CO₂ lasers, operating at a pulse repetition rates $F = 0,5 \text{ KHz}$ and $F = 1 \text{ KHz}$ are shown in fig 5. The volume discharge in these lasers was excited between a profiled tantalum cathode and grid copper or nickel anode. The dimensions of the excitation zone of the volume discharge consisted respectively of $V_{a1} = 28 \cdot 2 \cdot 0,6 \text{ cm}^3$ (curve 1) and $V_{a2} = 45 \cdot 2,5 \cdot 0,8 \text{ cm}^3$ (curve 2). The active elements of these cylindrical lasers had the following dimensions: diameter $d_1 = 32 \text{ cm}$, the length $l_2 = 40 \text{ cm}$; diameter $d_2 = 22 \text{ cm}$, the length $l_2 = 70 \text{ cm}$. The first active element was made of stainless-steel, the second -of aluminium. Heat release from the active elements was obtained by air-cooled copper heat exchangers with the area of plate surfaces $S_1 = 5 \text{ m}^2$ and $S_2 = 8 \text{ m}^2$ and the water consumption up to $5 \text{ l} \cdot \text{min}^{-1}$.

The working mixture of the first laser consisted of CO₂:N₂:He in proportion of 1:1:7. Mixture regeneration was obtained by a set of catalysts of the palladium origin. The working mixture of the second laser consisted of CO₂:N₂:He in proportion of 1:1:8 and being regenerated by catalysts of the (CuO*MnO₂) and adding carbon monoxide to the initial mixture. The working pressures of the mixtures in the lasers active elements were equal to atmospheric.

With a flow of operation the average radiation power of both lasers is decreased monotonously. The breaks in the function of the lasers lead to the changes in the stationary power level not more than 10%. In spite of the high excitation energy density, radiation power drop of the first laser ($V_1 = 28 \cdot 2 \cdot 0,6 \text{ cm}^3$) (see Fig.5, curve 1) occurs lower than of the second one. Such behaviour can be stipulated by a large volume of gas area in the active element against the excitation zone of a volume discharge and the kind of coating material of the active element (stainless steel).

The increase of a drop speed of the average radiation power after 70 hour uninterrupted work of lasers is connected with the destruction of the plasma spatial homogeneity of the volume discharge. After a hundred hour uninterrupted work of lasers the length of the microchannels in the cathode area of the volume discharge (macro-heterogeneous zone) achieves ~5-7 mm. In their further functioning over that hundred hour time-period the dimensions of these channels are rapidly increased and a discharge gap is completely overlapped by a highly current local discharge, causing a breakdown of the laser radiation generation. In TEA-CO₂ laser with $V_a = 15 \times 1,2 \times 0,5 \text{ cm}^3$ and electrodes made of copper at pulse repetition rates of up to 3 kHz (average power of laser radiation $P_{av} < 20 \text{ W}$) the lifetime of 30 hours is obtained.

4. CONCLUSION

Experimental results corroborate the autoelectronic nature of a local increase of the volume discharge current density and microinhomogeneities and their liding role in localization of the volume discharge and in limitation of the energy parameters and resource of sealed-off TEA-CO₂ lasers. Much more effective the formation process of microinhomogeneities takes place over the electrode surfaces made of Al, Mg, stainless-steel, Cu and Ni. The formation of microinhomogeneities over the electrode surfaces made of Mo, Ti, Ta, Nb and W becomes much more slower. Polishing of active surfaces of electrodes of Mo, Ta, W and the decrease in oxygen concentration of the laser mixture enable to gain the higher resource of sealed-off TEA-CO₂ lasers.

The resource tests conducted with the two types of sealed-off TEA-CO₂ lasers, such as small-size ones with metal-ceramic envelope and blowing of gas mixtures by "electrical wind" ($F = 25 - 50 \text{ Hz}$, radiation energy in pulse $W = 25 - 50 \text{ mJ}$) and high-frequency ones ($F = 0,5 - 1 \text{ kHz}$, average radiation power $P > 120 \text{ W}$) showed that the minimum resource is typical of TEA-CO₂ lasers with electrodes made of Al and Cu. The highest resource $T = 100 - 120$ hours is achieved while producing the tantalum cathodes.

REFERENCES

1. G.A.Mesyats, V.V.Osipov, V.F.Tarassenko, "Pulse-Operating Gas Lasers", 272 p., Nauka, Moscow, 1991.
2. K.Smith, R.Tomson, "Computer Modeling of Gas Lasers", 516 p., Mir, Moscow, 1981.
3. V.A.Vizir', V.V.Osipov, V.A.Tel'nov, G.M.Khamidulin, "A Compact-High-Pulse-Repetition-Rate CO₂ laser", -*Quantum Electronics*, V.15, No.6, pp. 1256-1260, 1988.
4. Yu.D.Korolyov, G.A.Mesyats, "Autoemissive and Explosive Processes in the Gas Discharge", 243 p., Nauka, 1982.
5. G.A.Mesyats, "Ectons", part 1, 262 p., Nauka, Yekaterinburg, 1994.
6. Yu.D.Korolev, G.A.Mesyats, "Physics of pulse breakdown in gases", 224 p., Nauka, Moscow, 1991.
7. B.A.Kozlov, V.I.Solovyov, A.A.Fedotov, "Pulse-Periodical Gas Laser", Patent Russian Federation No 9301-6340/25, March 30, 1993.
8. S.B.Gorkin, B.A.Kozlov, V.I.Solovyov, "Sealed-off Compact Repetitively Pulsed TEA-CO₂ Lasers Using "Electrical Wind" Effect for Gas Transport", -*Izvestiya of Russian Academy of Sciences. Phys. Series*, V.58, No.2, pp. 42-45, 1994.
9. S.G.Kalashnikov, "Electricity", 576 p., Nauka, Moscow, 1985.
10. B.A.Kozlov, M.E.Nelyubin, "Foto- and Autoemissive Properties of the Electrodes Sealed-off TEA-CO₂ Lasers". -*Proceedings of All-Russian Symposium on Emission Electronics*. -Ryazan, RUSSIA, 17-19 Sept., pp.132-133, 1996.
11. M.I.Elinson, G.F.Vasiljev, "The Autoemissive Electronics", 272 p., GIFML, Moscow, 1958.
12. B.A.Kozlov, V.I.Solovyov, A.V.Kozlov, "Life-time characteristics of small-sized sealed-off TEA-CO₂ lasers", *Proceedings of SPIE*, Vol. 3574, pp.161-166, 1998.

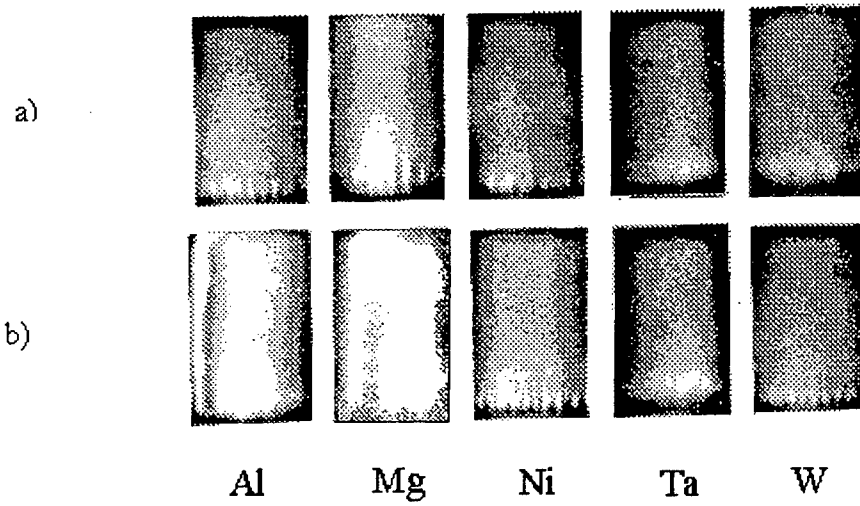


Fig.1. Plasma glowing of the volume discharge in an initial mixture (a) and after 10^6 discharge pulses (b). All the cathodes are placed at the bottom of all photos.

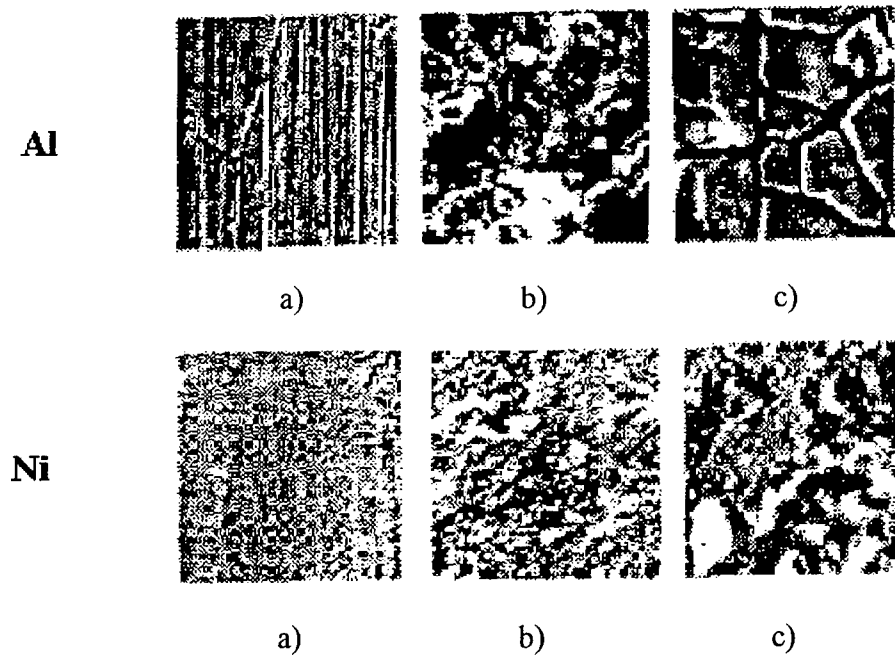


Fig.2. A microstructure of the electrode surfaces of Al (an upper row) and Ni (a lower row) before influence of plasma of the volume discharge on them (a), and after 10^4 (b) and 10^6 (c) pulses of the volume discharge.

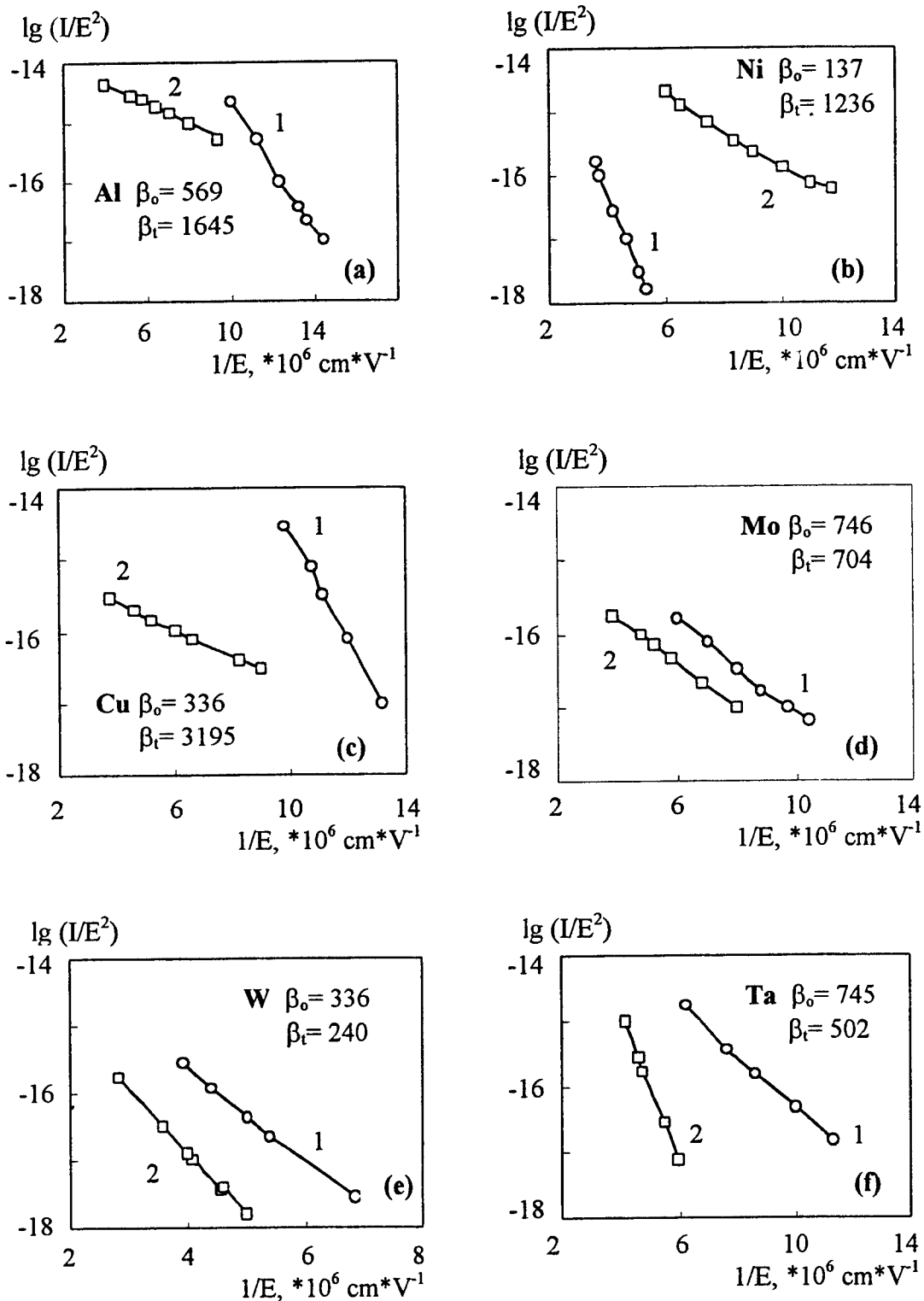


Fig.3. Volt-ampere characteristics of cathodes made of Al (a), Ni (b), Cu (c), Mo (d), W (e) and Ta (f) before influence of plasma of the volume discharge (1) on them and after 10^6 discharge pulses (2).

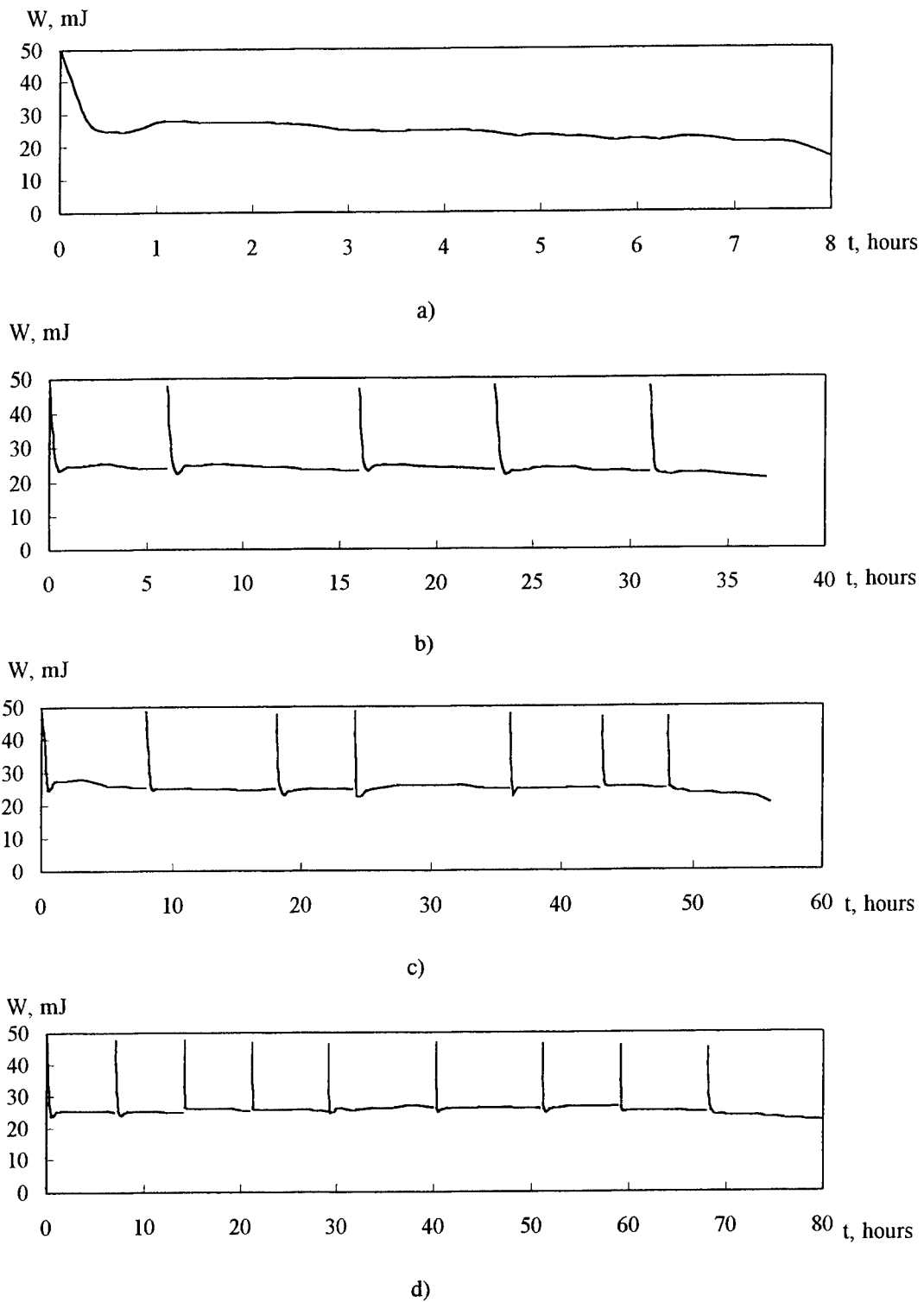


Fig.4. Dependencies of the lasers radiation energy versus the operating time of laser when the electrodes of Al (a), Cu (b), Ni (c) and Ta (d) are used. Initial mixture composition $\text{CO}_2:\text{N}_2:\text{He}=1:1:5$; total pressure $P = 1$ Atm; pulse repetition rate $F = 40$ Hz.



Fig.5. Dependencies of the average radiation power in stationary mode versus the operating time of TEA-CO₂ lasers with $V_{a1}=28*2*0.6 \text{ cm}^3$ (1) and $V_{a2}=45*2.5*0.8 \text{ cm}^3$ (2).

1. Initial mixture composition -CO₂:N₂:He =1:1:7, total pressure $P=1\text{Atm}$. Electrode materials: cathode - Ta; anode - Cu. Pulse repetition rate $F=1\text{kHz}$.
2. Initial mixture composition- CO₂:N₂:He =1:1:8, total pressure $P=1\text{Atm}$. Electrode materials: cathode - Ta; anode - Ni. Pulse repetition rate $F=0.5 \text{ kHz}$.

Improvement of the optical quality of the free vortex aerodynamic windows.

A.S. Boreisho, A.V. Trilis

Institute of Laser Technique and Technology of Baltic State Technical University
1, 1st Krasnoarmeyskaya str., 198005, St.Petersburg, Russia
tel. +7 812 2512162, fax +7 812 2512257, e-mail office@iltt.ru

V.M. Khailov, R.I. Sericov
Central Institute of Aircraft Engine Construction,

ABSTRACT

The aerodynamic windows are intended for a high power extraction from the gas laser optical cavity, where the pressure is much lower than environment pressure.

The main requirements for the aerodynamic windows are to satisfy a low level of optical disturbances in a laser beam extraction channel and an air leakage absence into the optical cavity.

One way of the optical quality improving consists in density drop decrease by working gas heating. Optimum heating of the jet gas improves the optical quality of aerodynamic windows. In this case they became useful for powerful DF, HF chemical lasers and COIL. Registered aberrations of the aerodynamic windows are insignificant for divergence quantity of the laser beams with wavelength from 1 to 10 microns.

1. INTRODUCTION

The description of "free-vortex" aerodynamic window has been published 25 years ago¹. Maximal pressure ratio on the aerodynamic window is 600³. It's achieved by using double stage window. Interferometry investigation of free vortex aerodynamic windows has been showed good optical quality² for CO₂ lasers with wavelength 10,6 microns but not so good quality for shot wavelength range.

Usually for stream geometry choice a reason of minimum working gas flow rate maintenance is used. Such approach is justified in case of aerodynamic windows using as output element for high power CO₂ lasers with wavelength 10,6 microns. The registered aberrations in a visible wavelength range were insignificant for 10,6 microns laser beam.

In case of aerodynamic windows using for extraction of power with 3,8-4,2 microns wavelength gas-dynamic inhomogeneity become more significant. And the parameters of the flow in aerodynamic window have to be chosen in accordance with reasons of minimal optical aberrations in output laser beam.

The experimental data analysis shows that the main aberrations introduced in aerodynamic windows on a free vortex are directed along a stream. Across a stream the main perturbation is observed near the walls, that is related to a boundary layer presence.

The inhomogeneity of the aerodynamic windows can be divided on large-scale, related to a stream curvature, and small-scale, related with a turbulent mixing layer. The large-scale perturbations are stationary in time and space. The curvature of gas stream boundaries generates a cylindrical lens presence in the aerodynamic window with a free vortex. The small-scale aberrations are non-stationary in time and rise downstream.

2. ANALYSIS

Let's consider a flow pattern schematically shown in fig. 1 to estimate large-scale inhomogeneity. The medium is divided on three parts by jet boundaries:

- 1 - ambient air
- 2 - gas stream
- 3 - gas in a low-pressure cavity.

Jet boundaries divide gases with various densities, and hence with various refraction indexes.

Area 1 is a dispersing lens with a focal length $\frac{R_+}{n_1 - 1}$ and a matrix $\begin{bmatrix} 1 & 0 \\ \frac{n_1 - 1}{R_+} & 1 \end{bmatrix}$.

where n_1 is the ambient air refraction index. R_+ is an external radius of a vortex.

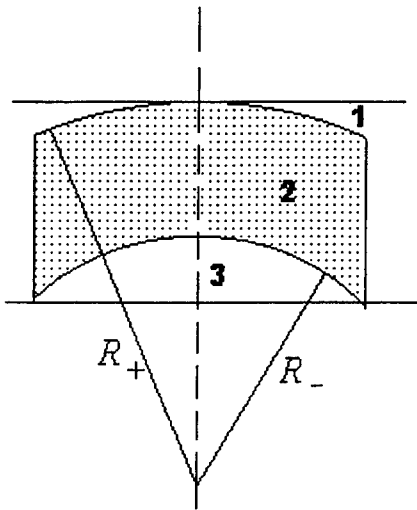


Fig. 1 Main parts of flow in aerodynamic window

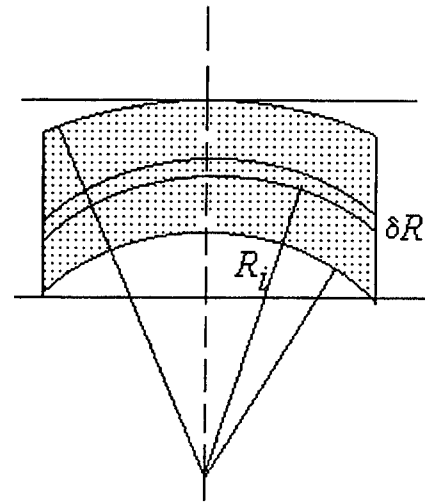


Fig. 2. Flow pattern.

Similarly area 3 is a collecting lens with a matrix
$$\begin{bmatrix} 1 & 0 \\ -\frac{n_3-1}{R_-} & 1 \end{bmatrix}.$$

Area 2 has a variable on a radius refraction index. The radial matrix of area 2 can be received, having divided it on thin layers δR and having multiplied layers matrixes.

Considering a refraction index of an elementary layer δR to constant (fig. 2), the layer matrix will look like a matrix of a dispersing lens:

$$\begin{bmatrix} 1 & 0 \\ \frac{(n_i-1)\delta R}{R_i^2} & 1 \end{bmatrix},$$

where n_i - refraction index of gas flowing on a radius R_i .
The overall stream matrix is an all layers matrix product

$$\prod_i \begin{bmatrix} 1 & 0 \\ \frac{(n_i-1)\delta R}{R_i^2} & 1 \end{bmatrix} = \begin{bmatrix} 1 & 0 \\ \prod_i \frac{(n_i-1)\delta R}{R_i^2} & 1 \end{bmatrix}$$

If δR directs to 0, the product will pass into an integral

We'll calculate integral, using a theorem of mean.

$$\lim_{\delta R \rightarrow 0} \prod_i \frac{(n_i-1)\delta R}{R_i^2} = \int_{R_-}^{R_+} \frac{(n_i-1)dR}{R_i^2}$$

$$\int_{R_-}^{R_+} \frac{(n(R)-1)dR}{R^2} = (\bar{n}-1) \int_{R_-}^{R_+} \frac{dR}{R^2} = (\bar{n}-1) \left(\frac{1}{R_-} - \frac{1}{R_+} \right),$$

where \bar{n} - some average refraction index

The refraction index in jet is changed with a radius and depends on stream density only.

$$n(R)-1 = A\rho(R),$$

where A is an air refraction coefficient; $\rho(R)$ is an air density on a radius R .

The density is changed with a stream velocity $\rho(\lambda) = \rho^* \left(1 - \frac{k-1}{k+1} \lambda^2\right)^{\frac{1}{k-1}}$, where λ - reduced flow velocity

$\lambda = v/a^*$; k is a specific heat ratio.

In a vortex the velocity is changed inverse proportional to a radius $\lambda = \frac{const}{R} = \frac{C}{R}$ (C is a constant of

vortex), and the refraction index with a radius R is changed under the law $n(R) - 1 = A \rho^* \left(1 - \frac{k-1}{k+1} \left(\frac{C}{R}\right)^2\right)^{\frac{1}{k-1}}$,

ρ^* is a gas stagnation density.

Taking into account a smooth refraction index changing with a radius it is possible to calculate approximately

$$\bar{n}, \tilde{n} \approx \frac{n(R_-) + n(R_+)}{2}.$$

As a result the layer matrix will take on form:

$$\begin{bmatrix} 1 & 0 \\ \frac{(n-1)(R_+ - R_-)}{R_- R_+} & 1 \end{bmatrix} = \begin{bmatrix} 1 & 0 \\ \frac{(n(R_-) + n(R_+) - 2)(R_+ - R_-)}{2R_- R_+} & 1 \end{bmatrix}$$

The total matrix of perturbations in the window is received after a multiplication of matrixes of three parts.

$$\begin{bmatrix} 1 & 0 \\ -\frac{1}{f_\Sigma} & 1 \end{bmatrix} = \begin{bmatrix} 1 & 0 \\ -\frac{1}{f_3} & 1 \end{bmatrix} \begin{bmatrix} 1 & 0 \\ -\frac{1}{f_2} & 1 \end{bmatrix} \begin{bmatrix} 1 & 0 \\ -\frac{1}{f_1} & 1 \end{bmatrix} = \begin{bmatrix} 1 & 0 \\ -\frac{1}{f_3} - \frac{1}{f_2} - \frac{1}{f_1} & 1 \end{bmatrix},$$

f_Σ is a focal point of a total lens, f_1, f_2, f_3 are lens focuses of appropriate areas.

Let's carry out a numerical evaluation of a lens speed and we'll find out the most significant part.

$$\frac{1}{f_1} = -\frac{n_1 - 1}{R_+}$$

$n_1 = 1.000257$ - the refraction index of the air for normal conditions.

$$\frac{1}{f_3} = \frac{n_3 - 1}{R_-}$$

n_3 - refraction index of the rarefied air.

The density behind a jet is equal to 1/20 density of the ambient air for the free vortex jet with the pressure ratio 20.

$$\frac{n_3 - 1}{n_1 - 1} = \frac{\rho_3}{\rho_1} = \frac{1}{20}$$

For upper and lower stream bound radiuses for the jet with pressure ratio 20 we have:

$$\frac{R_+}{R_-} = \frac{\lambda_-}{\lambda_+} = 1.35$$

The focuses of lenses created by an external and internal lens ratio is:

$$\frac{1}{|f_3|} : \frac{1}{|f_1|} = 0.067$$

Thus, the lens power produced by the internal air is very small in comparison with the lens power produced by the external air.

For the lens produced by a supersonic jet we have

$$\frac{1}{f_2} = - \frac{(n(R_-) + n(R_+) - 2)(R_+ - R_-)}{2R_-R_+}$$

$$\frac{n(R_-) - 1}{n_1 - 1} = \frac{\rho_-}{\rho_1} = \frac{P_0}{P_a} \varepsilon(\lambda_+) = 1.6$$

$$\frac{n(R_+) - 1}{n_1 - 1} = \frac{\rho_+}{\rho_1} = \frac{P_0}{P_a} \varepsilon(\lambda_-) = 0.17$$

P_0 - full pressure in a jet, P_a is the ambient pressure

$\varepsilon(l)$ is a gas-dynamic function: $\varepsilon(\lambda) = \left(1 - \frac{\kappa - 1}{\kappa + 1} \lambda^2\right)^{\frac{1}{\kappa - 1}}$

$$\frac{n(R_-) + n(R_+) - 2}{2} : (n_1 - 1) \approx 0.8$$

$$\frac{R_+ - R_-}{R_-R_+} : \frac{1}{R_+} = 0.25$$

$$\frac{1}{|f_2|} : \frac{1}{|f_1|} \approx 0.2$$

Thus we have $\frac{1}{|f_3|} : \frac{1}{|f_2|} : \frac{1}{|f_1|} = 0.067 : 0.2 : 1$

It is easy to see, that generally the lens is formed by an external air and $\frac{1}{f_\Sigma} \approx 1.1 \frac{1}{f_1}$.

The obtained results concern to the idealized case and indicated evaluations of the lens power appear hardly overestimated, but they give actual concepts about major factors influencing to large-scale optical aberrations. On the ground of indicated reasonings it is possible to make two conclusions:

1. the lens is formed by an external air layer, the lens speed practically does not depend on gas refraction index of a stream, and depends only on a external jet boundary curvature.
2. In case of linear scaling of the window an induced lens is scaled.

The absolute value of small-scale aberration is smaller and linearly increase downstream and can be estimated from interference fringes contrast loss. So the bands become invisible, if the probing beam wavefront ripple becomes comparable with $\lambda/2$, where $\lambda=0,63$ microns is a probing wavelength.

The ratio of jet boundary gas density to ambient gas density is equals $\rho_{jet}/\rho_{atm} \approx 1.8$. To decrease the density ratio it necessary to warm jet gas. The optimal gas warming lies in limits of $T^*/T_a = 1.4 - 1.8$, where T^* is a working gas stagnation temperature, T_a is an ambient air temperature. The working gas warming reduces small-scale aberrations, because the density difference of a supersonic jet and an ambient air decreases. The turbulent density ripples and hence also refraction index ripples are decrease in a mixing zone.

3. EXPERIMENTAL RESULTS

The shearing interferometer was used for wave front disturbance measurements in aerodynamic windows (see Fig.3). The interferograms were fixed by the digital video camera and were transmitted to the personal computer, where they were processed. The double stage aerodynamic window was used as the test object. The window size was 50mm downstream. To decrease cylindrical lens the free vortex angle was 22° .

Aerodynamic window interferograms for hot and cold working gas are showed in Fig. 4. The interferogram fringes are invisible if use cold working gas and become visible if working gas has been heated in 1.6 times. In this case the refraction difference between ambient gas and stream gas is smaller and boundary turbulent pulsation become invisible. The average fringes luminosity decreasing along the flow is showed in Fig.5.

Wavefront reconstructed from interferograms for hot working gas is represented in Fig 6. "Free vortex" produces cylindrical lens aberration. The maximal wavefront phase difference is not exceed 0.18μ .

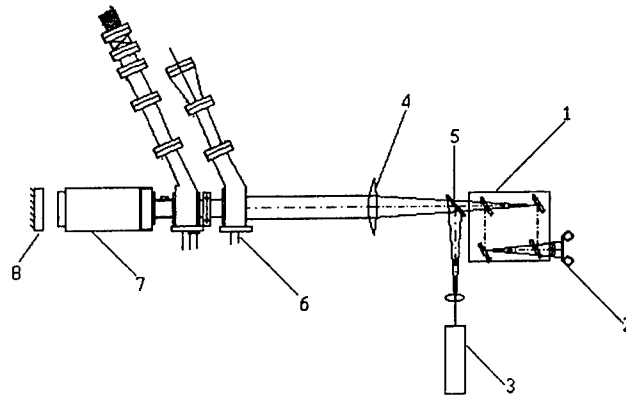


Fig. 3. Scheme of the interferometric measurements.
 1 – Shearing interferometer; 2 - Camera; 3 - Laser; 4 - Collimating lens; 5 – Beam splitter;
 6 – Aerodynamic window; 7 – Volume; 8 - Mirror.

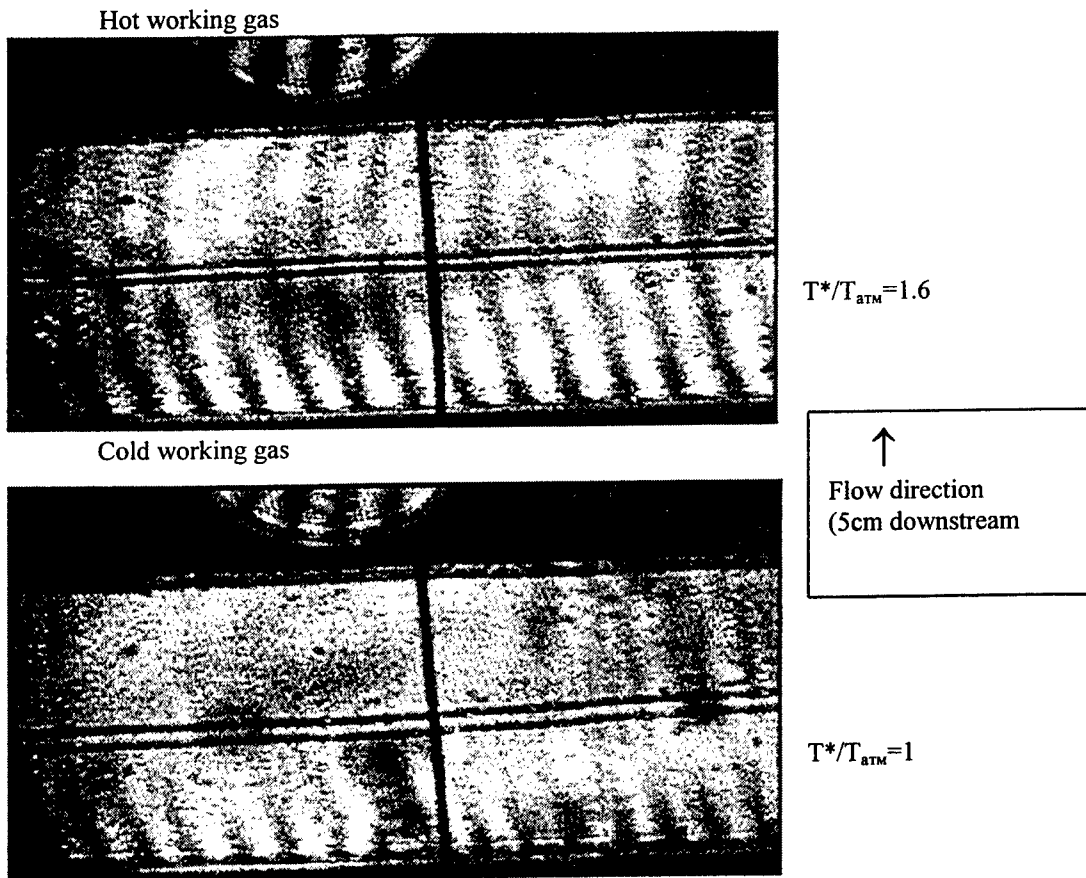


Fig.4. Aerodynamic window interferogram for hot and cold working gas

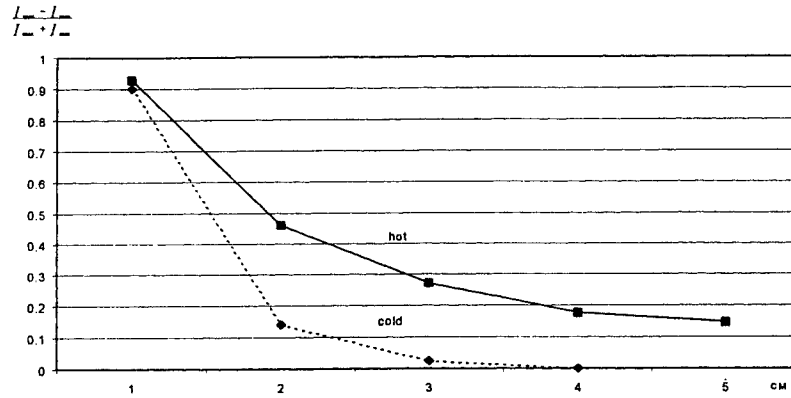


Fig. 5 The fringes luminosity decreasing along the flow.

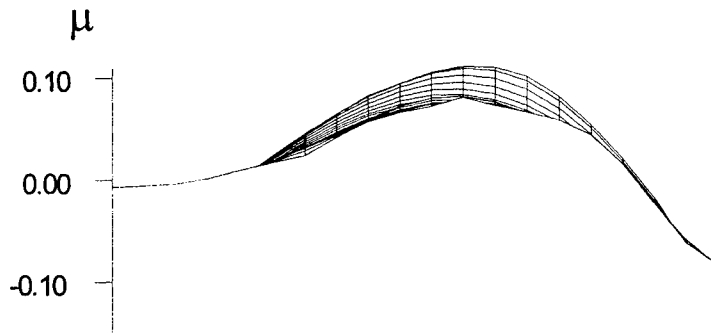
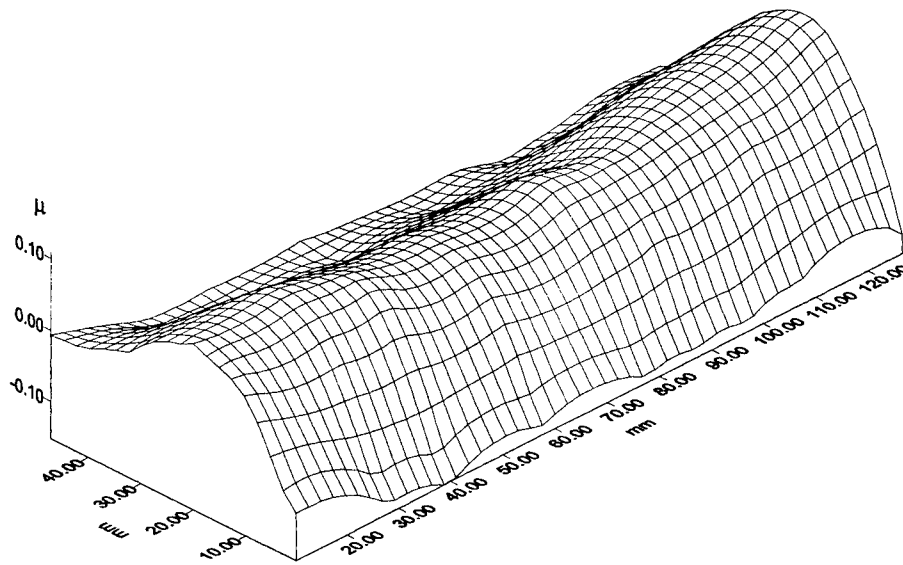


Fig.6. Wavefront reconstructed from interferograms for hot working gas

4. CONCLUSIONS.

Heating of the jet gas improves the optical quality of aerodynamic windows. In this case they became useful for powerful DF, HF chemical lasers and COIL. Registered aberrations of the aerodynamic windows are insignificant for divergence quantity of the laser beams with wavelength from 1 to 10 microns.

REFERENCES

1. Guile R. N., Hilding W. E. "Investigation of free-vortex aerodynamic window," AIAA Paper №75-122. 1975
2. Khailov V.M., Shelomovskiy V.V. "Aerodynamic window with the pressure ratio more than 500. Journal of engineering physics," № 6, V.61, 1991, p.947-952
3. Gilerson A.A., Panchenko V.I., Rafikov V.G., Sericov R.I., Khailov V.M. "Optical characteristic investigation of free vortex aerodynamic window." Journal of technical physics. №12, Vol.60, 1990, pp.29-34

Small-sized TEA -N₂ and TEA-Xe Lasers with High-Average Radiation Power

Boris A.Kozlov, Roman I.Ashurkov
Electronic Eng. and Techn. Dept., Radio-Engineering Academy
59/1 Gagarin str., Ryazan, 391000, GSP, RUSSIA

ABSTRACT

The conditions of forming the spatial homogeneous volume discharges in N₂:He; Xe:He; Kr:He and Ar:He mixtures at total pressures of P = 0,5 - 1,5 Atm and at pulse repetition rates up to F = 7 kHz are investigated. The influence of macro- and microinhomogeneities of the volume discharge plasma on the maximum pulse repetition rates and average radiation power of TEA-lasers are determined. A maximum value of the average radiation power of P_{AV} = 20 W on molecular nitrogen (λ = 337 nm) and P_{AV} = 28 W on transitions of neutral atoms of Xe (λ = 1-5 μm) are obtained.

Keywords: TEA-N₂ lasers; UV-laser radiation; pulse periodical volume discharges; macro- and microinhomogeneities; pulse repetition rate; laser average radiation power, "electrical wind".

1. INTRODUCTION

A powerful laser radiation of the near UV- and IR- ranges of spectrum may be effectively used in laser chemistry of polymers, technique of isotopes separation, laser microtechnologies, optical location and ecology.

A high resource and stability of energy parameters of pulse radiation are of great importance in developing lasers with high level pulse radiation and average radiation powers. The active media such as molecular nitrogen and the mixture of inert gases having the minimum chemical transformations due to the volume discharge plasma meet these requirements to a great extent.

The aim of this work was to determine the conditions which help to reach the maximum levels of radiation power in small-sized sealed-off TEA lasers with "electrical wind" (F_{max} ~ 100 Hz) and with high-speed blowing of gas mixtures (F_{max} > 1 kHz) on N₂:He, Xe:He; Kr:He and Ar:He mixtures at total pressures up to 1,5 Atm.

2. Experimental set-up

The research work has been conducted with two types of TEA-lasers. The first type is small-size sealed-off TEA-lasers with a metal-ceramic envelope, the discharge excitation zone V_a = 18*0,8*0,3 cm³ and "transverse blowing" of the gas mixtures with the "electrical wind"¹⁻³. The second type - TEA-lasers with envelopes made of aluminium and stainless steel (32 cm in diameter and 40-70 cm at length) and excited volumes V_a = 42*1,2*0,5 cm³, V_a = 28*2*0,6 cm³ and V_a = 45*2,5*0,8 cm³. The "transverse blowing" of gases mixtures N₂:He, Xe:He, Kr:He and Ar:He at the total pressure of 0,5-1,5 Atm through a discharge gap was done by small-size electrical fans at a velocity of 15-50 m*s⁻¹.

The excitation of active atoms and molecules with large partial concentrations of helium at pressures up to 1,5 Atm was connected with the necessity of convective release of great quantities of heat out of the discharge gap.

In order to increase the rate of energy dissipation into plasma of the volume discharge a circuit inductance of "peaking condensers - volume discharge plasma" was decreased to values L < 1 nH. Peaking condensers were placed immediately on the discharge chamber and connected to the main electrodes up to 74 inputs. Maximum amplitude of high voltage pumping pulses was 40 kV. A volume discharge of a nanosecond duration and energy density W = 100-150 mJ*cm⁻³ was being formed with pulse transformers. 5 thyatrons with an auxiliary discharge TGI2-500/20 were used as switches⁴. In a number of experiments the magnetic compression chains were used. The volume discharge had been initiated between Bruce profiled electrodes. In some experiments one of the main electrodes was the grid with the transparency ratio of ~50%. Preionization of the gas mixture had been performed by an auxiliary crown or spark discharges, which can be placed at the side of the main discharge gap or behind the grid electrode. Initiation of the main

discharge and the auxiliary one was proceed by independent pulsed generators. Metal mirrors with the curvature value of $R = 5 - 20$ m and the plain plates of quartz or germanium were used as the resonator mirrors.

3. Experimental results

3.1. Macro- and microinhomogeneities of plasma of the volume discharges

We consider macroinhomogeneities as the areas with a higher brightness of plasma glowing of a volume discharge. These areas are commensurable with a value of a discharge gap⁵. In so doing the volume discharge plasma within these areas has a spatial homogeneity. The macroinhomogeneities of the volume discharge plasma are mostly visible in the process of a volume discharge formation at "increased" pulses repetition rates. For example, the macroinhomogeneities of the volume discharge plasma are formed at 25-30 Hz pulse repetition rate in the TEA lasers with a transverse pumping of gas mixtures produced by the "electrical wind" and at a maximum pulse repetition rate of 50-70 Hz. We observe the plasma macroinhomogeneities visually at 0,6 - 1 KHz pulse repetition rate in TEA lasers with a high-speed pumping of gas mixtures and at a maximum pulse repetition rate of 3-5 kHz.

The redistribution of a current density of the volume discharge over a discharge gap length disturbs the optical properties of the active atmosphere, resulting in the decrease of its effective length. The latter influences the conditions when the increase of active media correlates with the optical resonator parameters and leads to an appreciable decrease of laser radiation power in a pulse.

Besides, the macroinhomogeneities of a volume discharge plasma initiate the local channel formation and the subsequent complete regeneration of a discharge in the local area and the break-down of the generation. This process is accelerated by the increase of pulse repetition rate and (or) pumping density.

The investigations showed that plasma macroinhomogeneities of a volume discharge are caused by the thermal inhomogeneities over the cathode area and in the gas flows and by the inaccuracies in the process of the electrodes production and their positioning.

Fig.1 show the examples of the macroinhomogeneities of the volume discharge.

To remove a thermal contact with the main electrodes and the gas flow as well as to use the "distributed" pre-ionizers results in the increase of spatial plasma homogeneity of volume discharge at higher pulses repetition rates. The electrodes production or the inaccuracies of more than 20 μm at a gap length of $d = 1,5 - 2$ cm appearing in the process of volume discharge set-up also lead to the formation of volume discharge plasma "macroinhomogeneities".

When is in the range of $\delta \sim 20-30$ μm the most intensive plasma glowing of a volume discharge at the "increased" pulse repetition rates is observed in the central part of a discharge gap. A preliminary caving of electrodes in the central part results in balancing of a volume discharge plasma and allows to reach the higher pulse repetition rates. The formation of macroinhomogeneities in the central part of a discharge gap may be connected with a thermal deformation of the electrodes resulted from their heating in the "inner" discharge side with respect to plasma.

In order to define the qualitative values of the size of the electrodes caving when they are being heated by the warmth releasing in a volume discharge plasma the following theoretical model was used:

- the electrode is a flat plate with a thickness of "d" fixed at the edges;
- the temperature of the "external" electrode wall is being kept constant and equal to T_0 .

The heat flow leaving plasma acts on the "inner" surface of the electrodes and is proportional to the electric power releasing in a pre-electrode area of the volume discharge. While calculating the T_1 on the inner surface of the electrode and the length corresponding to this temperature we can determine the size of the electrode caving in its central part. This value is:

$$h_{\text{max}} \sim 0,5 \cdot (2 \cdot I_0 \cdot \Delta l)^{0,5}, \quad (1)$$

where Δl -the length increment of the heated part of the electrode;

l_0 - the length of the electrode.

The size of the electrode caving depends on their length, thickness and the type of material. The maximum cavings of electrodes made of Al, Ni, Co and W with the length of $l = 50$ cm have the following values correspondingly: $\delta \sim 10-100$ μm ; $\delta \sim 18-180$ μm ; $\delta \sim 5-50$ μm ; $3-30$ μm at heat flows leaving plasma 100 W and 1000 W. The highest cavings are typical for the Al and Ni electrodes which have the low heat conductivity coefficient. The minimum cavings are typical for W having the average heat conductivity coefficient and the lowest heat extension coefficient.

The theoretical and experimental investigations made in ⁶ showed the following:

-inhomogeneities of the electric field in a discharge gap are proportional to the inhomogeneities of the inter-electrode gap;
-the 0,2% inhomogeneities of the electric field, being caused by the inter-electrode gap inhomogeneity of $\delta = 120 \mu\text{m}$ when the gap is 6 cm, result in the inhomogeneities of pumping energy density by more than 50%.

So the heating of the electrodes by the volume discharge warmth can cause the electrodes thermal deformation large enough for the noticeable redistribution of the current density of a volume discharge, that is the formation of plasma "macroinhomogeneities" of a volume discharge, and create the conditions for the subsequent complete regeneration of the volume discharge into the local one.

The plasma microinhomogeneities of a volume discharge or individual spark channels are formed in the main discharge gap as a result of voltages mismatches^{7,8} that is in the "afterglow" of the volume discharge plasma.

The main danger of the spark channels formation at the increased pulse repetition rate in the main discharge gap lies in the fact that they initiate the subsequent complete regeneration of a volume discharge into the local one and limit the excitation rate of the volume discharge at the level of ⁹:

$$F = a * B * (L * C * U)^{-1}, \quad (2)$$

where a - temperature conductivity coefficient of electrodes material;

B - constant (for air $B \sim 10^{-8}$);

L - complete inductance of a discharge contour;

C and U - the value of storage capacitance of pulse generator and the voltage of the capacitance charge.

The existence of such interaction between the maximum rate of a volume discharge stable formation and the electrophysical parameters of the pulse pumping generator points at the expediency of gap discharge sectioning and volume discharge excitation by the independent pulse generator in every gap^{8,9}.

3.2. Generation characteristics of small-sized TEA lasers on N₂:He and Xe:He mixtures

Generation characteristics of small-sized TEA-N₂ lasers with blowing of gas mixtures by "electrical wind" are shown in Fig.2 - Fig.8. These dependencies of the average radiation power upon the period of time are achieved for various experimental conditions. The dependencies shown in Fig.2 are gained using the TEA-N₂ laser without a heat-exchanger. Excitation of the volume discharge was effected in geometrical dimensions of $V_a = 18 * 0.8 * 0.3 \text{ cm}^3$. The active mixture consisted of N₂ and He at total pressure $P = 1 \text{ Atm}$. Partial pressure of N₂ was 65 Torr (an optimal value).

It is obvious that the average radiation power is linearly increased with the pulse repetition rate and does not change its meaning during 30 minutes at pulse repetition rates up to 20 Hz. At $F = 25 \text{ Hz}$ a decay of power in relation to time is observed, which is bound up with the redistribution of the current density of the volume discharge ("macroinhomogeneities").

Fig.3 shows the average radiation power versus the time for TEA-N₂ laser with a heat-exchanger made of Cu plates of total area $S = 1500 \text{ cm}^2$ and water is not supplied to the heat-exchanger. Presence of the heat exchanger helps to noticeable increase the radiation power of the laser. As it was earlier a few minutes later after laser switching-on the average radiation power at pulse repetition rate $F = 25 \text{ Hz}$ begins monotonously to decrease.

Water supplying to the heat-exchanger (Fig.4) results in increasing of the average radiation power.

The heat-exchanger from Ni ($S = 1500 \text{ cm}^2$) placed in the laser tube helps to increase the average radiation power (Fig.5, 6) at other similar conditions.

Fig.7 shows the average radiation power versus the pulse repetition rate for the heat-exchanger of Cu (1) and Ni (2). The results gained show that usage of the heat-exchanger made of Ni results in increase of the average radiation power by $\sim 10 \%$ (in comparison with the Cu heat-exchanger). Usage of the heat-exchangers with plates area $S = 1500 \text{ cm}^2$ enables to increase the average radiation power of small-sized sealed-off TEA-N₂ lasers by a factor of 1.5 -1.8 compared to lasers without heat-exchangers.

When SF₆ was added to a mixture of N₂:He (optimal pressure of 7.6 Torr) the initial value of average radiation power was significantly increased. However, during 2.5 hours of continuous laser operation it is decreased by a factor of 2.5. The results achieved are shown in Fig.8.

Fig.9 shows the average radiation power of a small-sized TEA-Xe laser versus the pulse repetition rate for various pumping conditions. The laser radiation was registered at all wavelengths. The active mixtures were consisted of Xe and He at partial pressures of 20 Torr and 760 Torr correspondingly. With laser in operation at the pulse repetition rates of up to 100 Hz the average radiation power increases linearly with the pulse repetition rate. Energies of radiation in a pulse decrease and a "saturation" of the average radiation power is observed. Such behaviour of energy parameters is connected with a break in spatial homogeneity of plasma of the volume discharge. Dependencies are finished at pulse repetition rates, above which the volume discharge becomes a local one.

3.3.Generation characteristics of TEA lasers on N₂:He, Xe:He, Kr:He and Ar:He mixtures on high pulse repetition rates

The increase of the velocity of gases mixtures blowing in discharge gap $V_a = 42 \cdot 1,2 \cdot 0,5 \text{ cm}^3$ up to $25 \text{ m} \cdot \text{s}^{-1}$ allowed to increase the excitation rate of the volume discharge up to 2 kHz and reach the average radiation powers of $P_{AV} = 2,8 \text{ W}$ ⁸.

Fig.10 shows the dependence of the average radiation power on the operating time of TEA-N₂ lasers at different pulses repetition rates (a) and on pulse repetition rate (b). These dependencies had been got at the optimal ratio N₂:He = 1:23 and at the total pressure of $P = 1 \text{ Atm}$. The average radiation power of TEA-N₂ lasers operating at the $F=250 \text{ Hz}$ pulses repetition rate (curve 1 on Fig.10a) is weakly changed within the time. At the initial moment the radiation energy in a pulse has the value of $W=1,6 \text{ mJ}$. Within 10 minutes the radiation energy in a pulse is 1,5 mJ. The average radiation power (curve 2, Fig.10a) at the pulses repetition rate of $F= 500 \text{ Hz}$ is decreased by ~ 20% within 10 min. The initial value of radiation energy in a pulse is 1,5 mJ. At the initial moment the average radiation power is 1,5 W at the pulses repetition rate of $F=1 \text{ kHz}$ (curve 3, Fig.10a) and it reaches the stationary value of 0,75 W for 5 minutes. In doing so the initial value of radiation energy is 1,5 mJ. At the maximum pulses repetition rate of 2 kHz the initial value of the average radiation power is 2,8 W. Within 3 minutes the average power is decreased up to quazi-stationary level of 0,8 W. The initial value of radiation energy in a pulse is 1,4 mJ, the stationary one is 0,4 mJ.

At the initial moment the laser efficiency has a value of $3 \cdot 10^{-4}$ but at a stationary mode its efficiency at the pulses repetition rate of 2 kHz is $9 \cdot 10^{-5}$. Such low efficiency values are the result of the ineffective energy transfer from the pumping generator into a volume discharge plasma (the pumping energy is dissipated from 20 up to 30% in a clipper circuit) and the input of the most part of pumping energy into the discharge not in the breakdown period.

Fig.10b shows the dependencies of the average radiation power of TEA-N₂ laser on the pulses repetition rate obtained at the initial moment (curve 1) and at the stationary mode (curve 2). One can see that at the initial moment, after switching on the laser, the average radiation power is linearly increased alongside with the pulses repetition rate. At the stationary mode the average radiation power aims at some value at the level of $P = 0,8 \text{ W}$.

The dependence of the average radiation power on the time, which we observe, while increasing pulses repetition rate may be connected with the insufficiently effective separation of metastable states of molecular nitrogen on the heat exchangers plates which is intended for releasing the average heat power of 3,5 kW out of active area.

The increase of geometrical dimensions of the volume discharge area ($V_a = 45 \cdot 2,5 \cdot 0,8 \text{ cm}^3$), the speed of gas mixture blowing ($50 \text{ m} \cdot \text{s}^{-1}$) and the heat exchanger parameters (a release heat power 12 kW) as well as the improvement of the matching terms of the pulse pumping generator with a discharge gap allowed to increase pulse repetition rate up to 3-5 kHz and reach the average power of laser radiation at the initial moment and at a quazi-stationary state 7-12 W (Fig.11)⁸.

The excitation of the volume discharge at the segmented gaps (5 sections) allowed to increase pulses repetition rate up to 7 kHz but we could not however reach the higher levels of average radiation power.

The main factors limiting the level of average radiation power of TEA-N₂ lasers are the insufficient effectiveness of pumping energy input into the volume discharge plasma and the speed of heterogeneous deexcitation of the metastable states of molecular nitrogen. The solution of one of these problems will allow to obtain the average powers at the level of 20 W and even more on molecular nitrogen at a stationary mode.

Fig.12 shows the average radiation power of a TEA-Xe laser with $V_a = 42 \cdot 1,2 \cdot 0,5 \text{ cm}^3$ in range of 0,6-2,2 kHz for optimal relations Xe:He = 1:1000¹⁰. A value of a peaking condenser acts as a variable parameter. Value of pumping energy was supported as unchangable and equal to 1 J. The average radiation power (at all wavelengths) is greatly dependent on the peaking condenser and proportional to the pulse repetition rate. A maximum average power $P_{AV} = 2 \text{ W}$ is achieved at

pulse repetition rate $F = 2$ kHz with the value of the peaking condenser $C = 5$ nF. Laser energy has a maximum value $W = 1$ mJ in that case.

Fig. 13 shows pulse oscillogramms of laser radiation at all wavelengths for various values of a peaking condenser. The first peak corresponds to radiation at the wavelength ($\lambda = 2,027$ μm and its value and duration very slowly depend on value of the peaking condenser. Radiation in a pulse "tail" is focused at wavelengths $\lambda = 2,65$ μm , $\lambda = 3,51$ μm , $\lambda = 3,65$ μm . The energy value at those wavelengths is defined by value of the peaking condenser.

Energy parameters of laser radiation at transitions of Kr and Ar atoms are greatly lower. Maximum average radiation powers at these atoms are $P_{\text{Kr}} = 0,3$ W and $P_{\text{Ar}} = 0,05$ W, correspondingly.

Increase in velocity of energy dissipation in plasma of a volume discharge, increase of pulse repetition rates and increase in excited volumes of gas mixtures have made it possible to raise greatly the radiation power level at transitions of neutral atoms Xe, Kr and Ar.

Fig. 14 shows an average radiation power versus the pulse repetition rate of TEA-Xe lasers with the active volumes $V_a = 28 \times 2 \times 0,6$ cm^3 and $V_a = 45 \times 2,5 \times 0,8$ cm^3 . Active mixtures of Xe and He were in relations as 1:1500 (1), 1:1200 (2), 1:1000 (3) and 1:900 (4). Total pressure was 1,5 Atm. Maximum average radiation power $P_{\text{AV}} = 28$ W is gained in a TEA-Xe laser with $V_a = 28 \times 2 \times 0,6$ cm^3 on the pulse repetition rate 6 kHz. Such a result is connected with provision of the better matching between a pulse pumping generator and plasma of the volume discharge of a laser with smaller geometrical dimensions of the active zone.

Maximum average radiation powers $P_{\text{Kr}} = 3$ W and $P_{\text{Ar}} = 0,5$ W are achieved with mixtures of Kr:He and Ar:He, correspondingly.

4. Conclusion

The research results showed that the governing factors of the limitation rate of the stable formation of the volume discharge and a level of the average power are macroscopic inhomogeneities connected with a redistribution of the current density in the main gap due to inaccuracies in manufacturing and mounting of electrodes and in creation of local discharges during "afterglow" of the volume discharge under the influence of mismatch voltages. Application of pre-ionizers disturbing a homogeneous distribution of temperature in a gas flow or temperature at the electrodes in order to form a volume discharge also results in the macroscopic redistribution of the current density in the volume discharge. In order to increase the ignition rate of the volume discharge and to improve a level of the average power measure were taken to reduce the mismatch voltages and to improve an accuracy of electrode manufacturing and their mounting.

Average radiation power of TEA- N_2 lasers are limited by the insufficient effectiveness of pumping energy input into the volume discharge plasma at high pulse repetition rates and the low speed of heterogeneous deexcitation of the metastable states of the molecular nitrogen. Mixtures N_2 :He with partial pressure molecular nitrogen 40-70 Torr provide the maximum average radiation power.

An average power of TEA-lasers working with mixtures of inert gases when the proportions of the mixture components and the pumping energy are fixed is increased linearly with the pulse repetition rate. The laser energy value per pulse depends on a concentration of helium in a mixture and the capacitance value of the sharpening condenser and reaches a maximum value in mixtures with helium content exceeding a concentration of the "working" atoms by a factor of $(1-2) \times 10^{-3}$. An optimal value of capacitance of the sharpening condenser is 25-40% of the value of the capacitance of the storage condenser.

A formation of a stable volume discharge at the pulse repetition rates up to 5-7 kHz made it possible to reach a maximum average power of 12-22 W in mixtures N_2 :He $\sim 1:20$ and 28 W (at all wavelengths) in mixtures Xe:He = 1:1000-1:1200 at the total pressure of 1-1,5 Atm. A maximum value of the average power in mixtures of Kr:He and Ar:He are 3 and 0,5 W correspondingly.

REFERENCES

1. B.A.Kozlov, V.I.Solovyov, "Limiting Frequencies of the Volume Discharge Firing in the Sealed-off TEA- CO_2 Lasers with Transverse Gas Blowing by "Electrical Wind". - *Proceedings of the 6-th Conference on Gas Discharge Physics*, Kazan, RUSSIA, June 23-25, part I, pp.14-15, 1992.

2. B.A.Kozlov, V.I.Solovyov, A.A.Fedotov, "Pulse-Periodical Gas Laser", *Patent Russian Federation* No 9301-6340/25, with a priority of March 30, 1993.
3. S.B.Gorkin, B.A.Kozlov, V.I.Solovyov, "Small-sized Sealed-off TEA-CO₂ Lasers Using "Electrical Wind" Effect for Gas Transport". - *Izvestiya of Russian Academy of Science. Physical Series*, V.58, No.2, pp.42-45, 1994.
4. B.A.Kozlov, M.E.Nelyubin, "Switching Characteristics of Pulse Hydrogen Thyratrons with a Preliminary Discharge". - *Proceedings of ISDEIV*, V.II, pp.1025-1028, (1996).
5. B.A.Kozlov, A.V. Kozlov, "Volume Discharges in High-pressure Mixtures N₂:He at Pulse-repetition-rates up to 5 kHz". - *Proceedings of the 9-th Conference on Gas Discharge Physics*, Ryazan, RUSSIA, June 3-5, part I, pp.68-69, 1998.
6. D.A.Goryachkin, V.M.Irtuganov, V.P.Kalinin, "Electrode-system influence at Spatial Homogeneity of the Volume Discharge". - *J. Technical Physics*, V.59, issue 6, pp.46-50, 1989.
7. B.A.Kozlov, M.E.Nelyubin, V.I.Solovyov, "Small-sized Sealed-off TEA-lasers of IR- and UV-ranges with increased pulse repetition rate". - *Proceedings of the Third Russian-Chinese Symposium on Laser Physics and Laser Technology*, Krasnoyarsk, RUSSIA, October 8-10, pp.52-53, 1996.
8. B.A.Kozlov, "Pumping Features of TEA- N₂ Lasers at Pulse Repetition Rates up to 5 kHz". - *Proceedings of SPIE*, V. 3574, pp. 637-643, 1998.
9. B.A.Kozlov, D.I.Ponomaryov, "Generation Characteristics of the Sealed-off Pulse-periodical TEA-CO₂ Lasers with High-pumping Density". - *Izvestiya of Russian Academy of Science. Physical Series*, V.60, No.2, pp. 77-84, 1996.
10. B.A.Kozlov, D.I.Ponomaryov, V.I.Solovyov, "Pulse-periodical TEA-lasers based on the inert gases: energetic properties and pulses repetition rate". - *Proceedings of SPIE*, V.2619, pp.39-44, 1996.

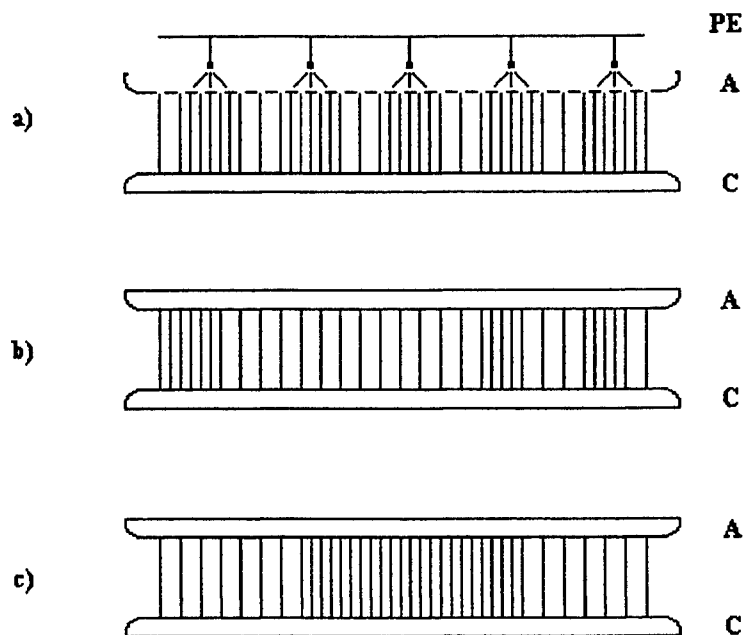


Fig. 1. Macroinhomogeneities of the volume discharge initiated by auxiliary corona discharge (a), inaccuracies of the electrodes productions or interelectrode gap positioning (b) and thermal deformations of the main electrodes (c). PE - auxiliary electrode.

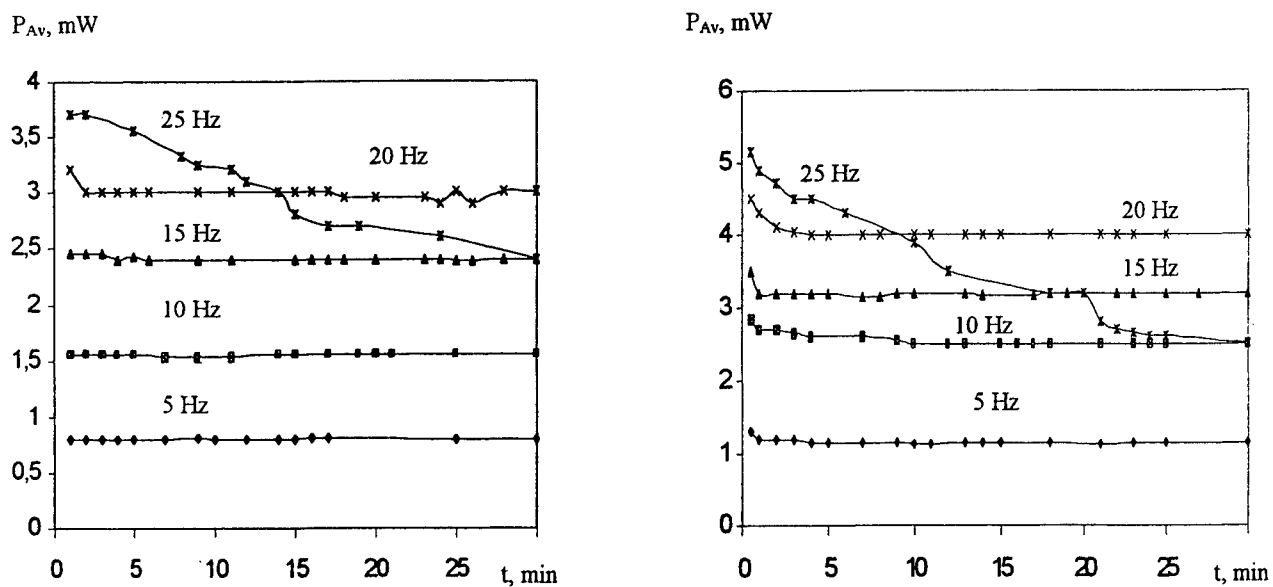


Fig. 2. Dependencies of the average radiation power as a function of operating time for TEA-N₂ laser without heater-exchanger. Working mixture: N₂:He = 65:700 Torr.

Pulse repetition rates: F = 5 Hz - 25 Hz. C₀ = 10 nF, U_c = 20 kV.

Fig. 3. Dependencies of the average radiation power as a function of operating time for TEA-N₂ laser with Cu heater-exchanger and without water cooling. Working mixture: N₂:He = 65:700 Torr.

Pulse repetition rates: F = 5 Hz - 25 Hz. C₀ = 10 nF, U_c = 20 kV.

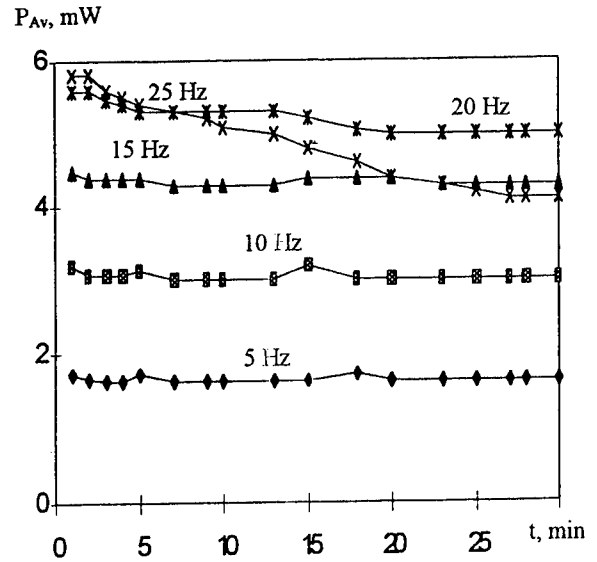
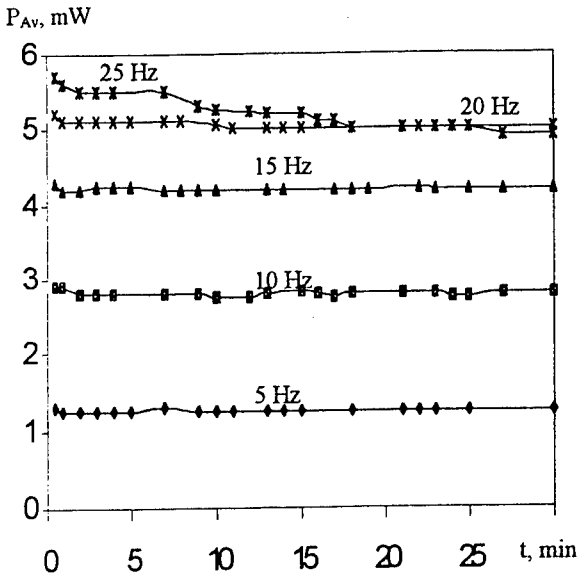


Fig.4. Dependencies of the average radiation power as a function of operating time for TEA-N₂ laser with Cu heater-exchanger and water cooling. Working mixture: N₂:He = 65 :700 Torr. Pulse repetition rates: F =5 Hz -25 Hz. C_o =10 nF, U_c =20 kV.

Fig.5. Dependencies of the average radiation power as a function of operating time for TEA-N₂ laser with Ni heater-exchanger and without water cooling. Working mixture: N₂:He = 65 :700 Torr. Pulse repetition rates: F =5 Hz -25 Hz. C_o =10 nF, U_c =20 kV.

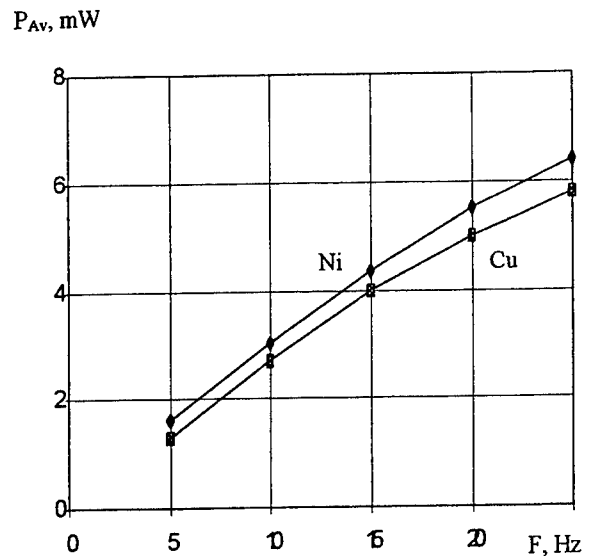
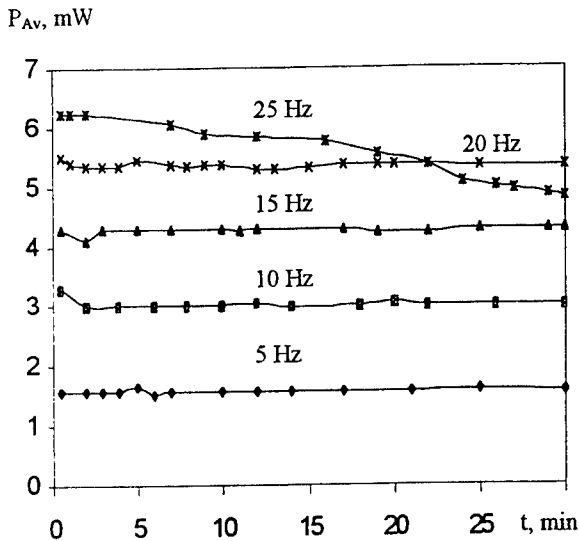


Fig.6. Dependencies of the average radiation power as a function of operating time for TEA-N₂ laser with Ni heater-exchanger and water cooling. Working mixture: N₂:He = 65 :700 Torr. Pulse repetition rates: F =5 Hz -25 Hz. C_o =10 nF, U_c =20 kV.

Fig.7. Dependencies of the average radiation power as a function of pulse repetition rate for TEA-N₂ laser with Cu and Ni heater-exchanger and water cooling. Working mixture: N₂:He = 65 :700 Torr. C_o =10 nF, U_c =20 kV.

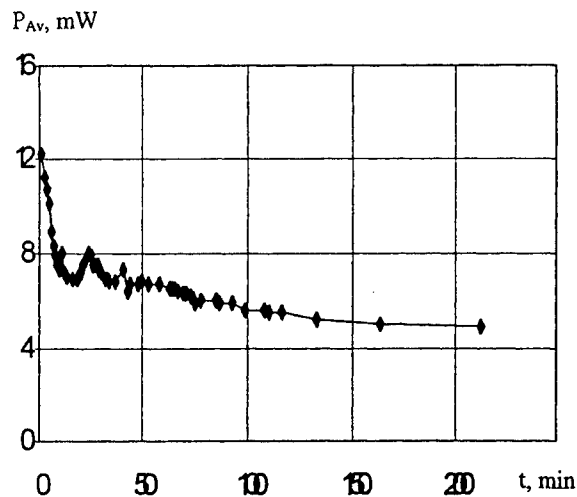


Fig. 8. Dependence of the average radiation power as a function of operating time for TEA- N_2 laser with adding SF_6 . Working mixture: $N_2 : He : SF_6 = 65 : 700 : 7.6$ Torr. Pulse repetition rate: $F = 25$ Hz. $C_0 = 10$ nF, $U_c = 20$ kV.

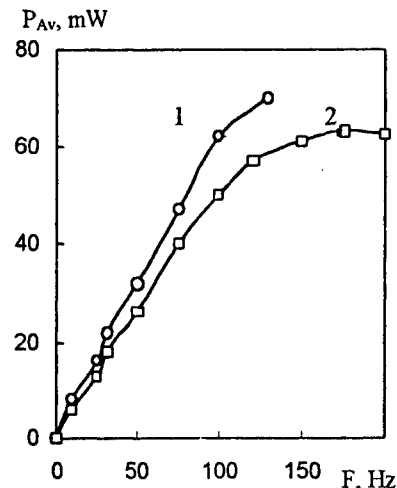
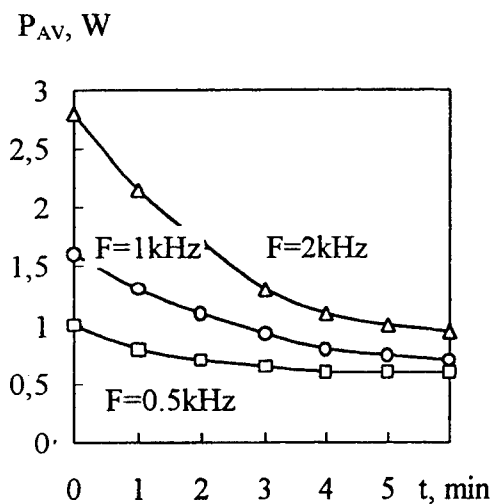
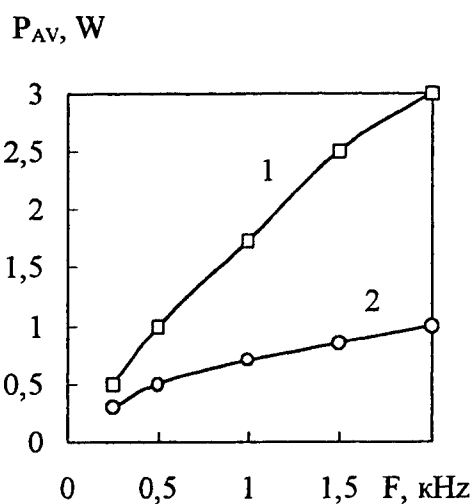


Fig. 9. Dependencies of the average radiation power of a small-sized TEA-Xe laser with "electrical wind" on pulse repetition rate. Working mixture: $Xe : He = 1 : 38$, $P_T = 780$ Torr. 1 - $C_0 = 10$ nF, $U_c = 7$ kV; 2 - $C_0 = 6$ nF, $U_c = 10$ kV.



a)



b)

Fig. 10. Dependencies of the average radiation power as a function of operating time (a) and pulse repetition rate (b). Discharge volume $V_a = 40 \times 2 \times 0.5$ cm³. 1 - initial level of the lasers average radiation power; 2 - stationary mode. Working mixture - $N_2 : He = 1 : 12$, total pressure $P = 1$ atm.

P_{AV}, W

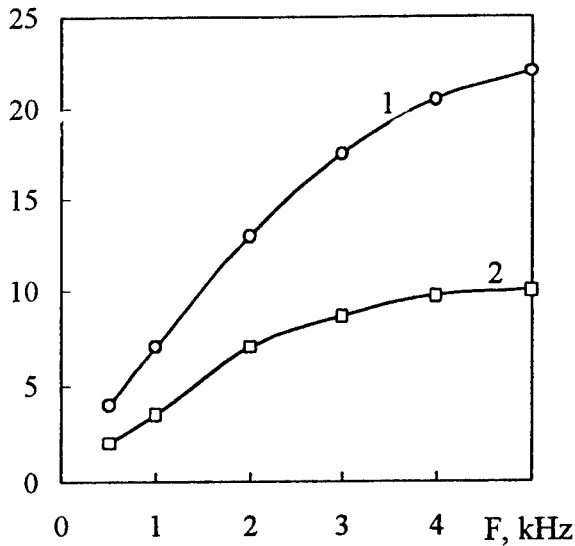


Fig. 11. Dependencies of the average radiation power upon pulse repetition rate.
 Discharge volume: $V_a = 45 \times 2.5 \times 0.8 \text{ cm}^3$.
 1 - initial level of the lasers power;
 2 - stationary mode.
 Working mixture: $N_2:He = 1:16$, total pressure - $P = 1 \text{ Atm}$.

P_{AV}, W

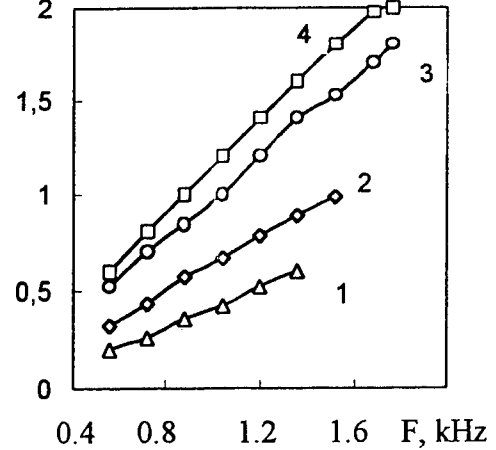


Fig. 12. An average radiation power of TEA-Xe laser as a function of pulse repetition rate for all wavelengths and for various values of peaking condensers:
 1 - $c_p = 0 \text{ nF}$; 2 - $c_p = 1.5 \text{ nF}$; 3 - $c_p = 3 \text{ nF}$;
 4 - $c_p = 5 \text{ nF}$; $c_\Sigma = 10 \text{ nF}$.

$P(t), \text{arb. units}$

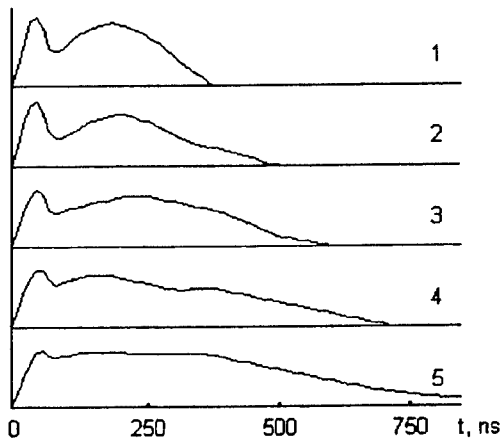


Fig. 13. Oscillogramms radiation pulses of Xe:He lasers for all wavelengths and various values of peaking condensers for a fixed pumping energy.
 1 - $C_p = 2 \text{ nF}$; 2 - $C_p = 4 \text{ nF}$; 3 - $C_p = 6 \text{ nF}$; 4 - $C_p = 8 \text{ nF}$;
 5 - $C_p = 10 \text{ nF}$; $C_\Sigma = 20 \text{ nF}$.
 Mixture Xe:He = 1:1200; $P_\Sigma = 760 \text{ Torr}$.

P_{AV}, W

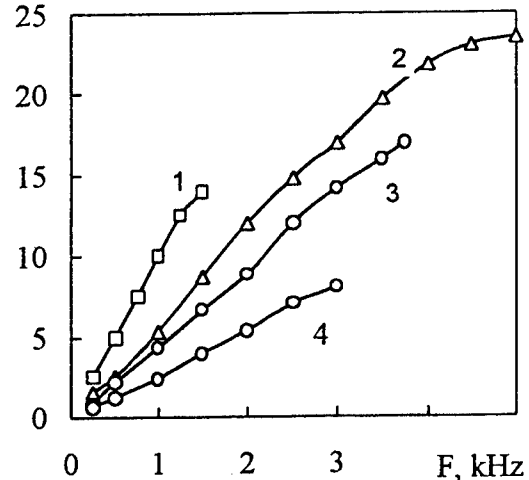


Fig. 14. Average radiation power of TEA-Xe lasers with active volumes $V_a = 4.5 \times 2.5 \times 0.8 \text{ cm}^3$ (1.4) and $V_a = 28 \times 2 \times 0.5 \text{ cm}^3$ (2.3) as a function of pulse repetition rate for all wavelengths.
 Mixtures - Xe:He = 1 - 1:1500; 2 - 1:1200;
 3 - 1:1000; 4 - 1:900; $P_\Sigma = 760 \text{ Torr}$.

IR lasers in a struggle against of the dangerous cosmic objects

Boris A. Kuzyakov
Moscow State University of Technology "STANKIN",
"SPO ASTROPHYSIKA"

ABSTRACT

Humanity can struggle with the small dangerous cosmic objects in our time and its parameter knowledge are needed. A present paper deals with prospects for the perspective of the laser methods applications for a dangerous asteroids discovering and a remote sensing and for the course correction systems of the influence expedients. The cosmic IR lasers will be used for remote sensing measurement of the various cosmic objects parameters: dimensions are more then 50 m, velocity is more then 10 km/s. The laser methods have the good perspectives among a large fleet of diagnostics technical means. The more effective CO₂ - laser parameters were defined for the solar systems smaller bodies velocity analysis. The laser is supplied with modulated laser radiation and an automatic tuning optical system. The CO₂ - lidars are needed for the asteroids detections and remote sensing at the distances of 30 000 km to 1 Mkm. A laser Doppler anemometer method with adaptive selection is used. The power calculations were made for the various asteroids in a cosmic space.

The possibilities are estimated for remote sensing and for the course correction systems of the influence expedients also. The such system must be good for the distances nearby 12600 km, as the asteroids velocity can be more than 70 km/s.

Keywords: Asteroids, laser, solar energy, cosmic platform, sensing systems, influence expedients

1. INTRODUCTION

Three hundred or so large craters^{1,2} and a geological record stretching over billions of years provide ample evidence that, time and again, explosive impacts by asteroids or comets have devastated large parts of the planet, wiped out species and threatened the very existence of terrestrial life. Astronomers are all too aware that more large hulks are out there, hurtling through space, some of them ultimately destined to collide with Earth.

Civilization as we know it will come to end, if a asteroid with dimensions more than 1-2 km hits our planet. When it comes to asteroids wreaking disaster on Earth, the real question is not if, but when. Therefore, developing the ability to detect and destroy or divert asteroids is needed.

Planetary scientists have developed a new means of conveying the risks associated with asteroids and comets that might collide with the Earth. A risk-assessment scale will assign values to celestial objects moving near Earth. The scale³ will run from zero to 10. A near Earth dangerous object (NEO) with a value of zero or one will have virtually no chance of causing damage on Earth, the 8-10 means a certain global climatic catastrophe.

The total asteroids kinetic energy $(MV^2) / 2$ will be transform to the explosion energy in during of the impact process as we know. Therefore it is very important to know the general asteroids mass, structure and velocity. The modern astronomical data were used for an estimation of the known integral M_{int} asteroids mass.

The several common programs are exist in the world today. NASA's search program designed to discover 90% of NEO population within 10 years is the biggest. Note the significant increase in the discovery rate in late 1998 due primarily to the linear program almost according to NASA websites. However, the such function can be approximate by the MathCad program more exactly. The fig.1 below shows the commutative total known near-Earth objects (NEO) v_{y_j} versus time v_{x_j} and versus in month within 2 last years. A double scale is used on fig. 1 for a MathCad procedure illustration.

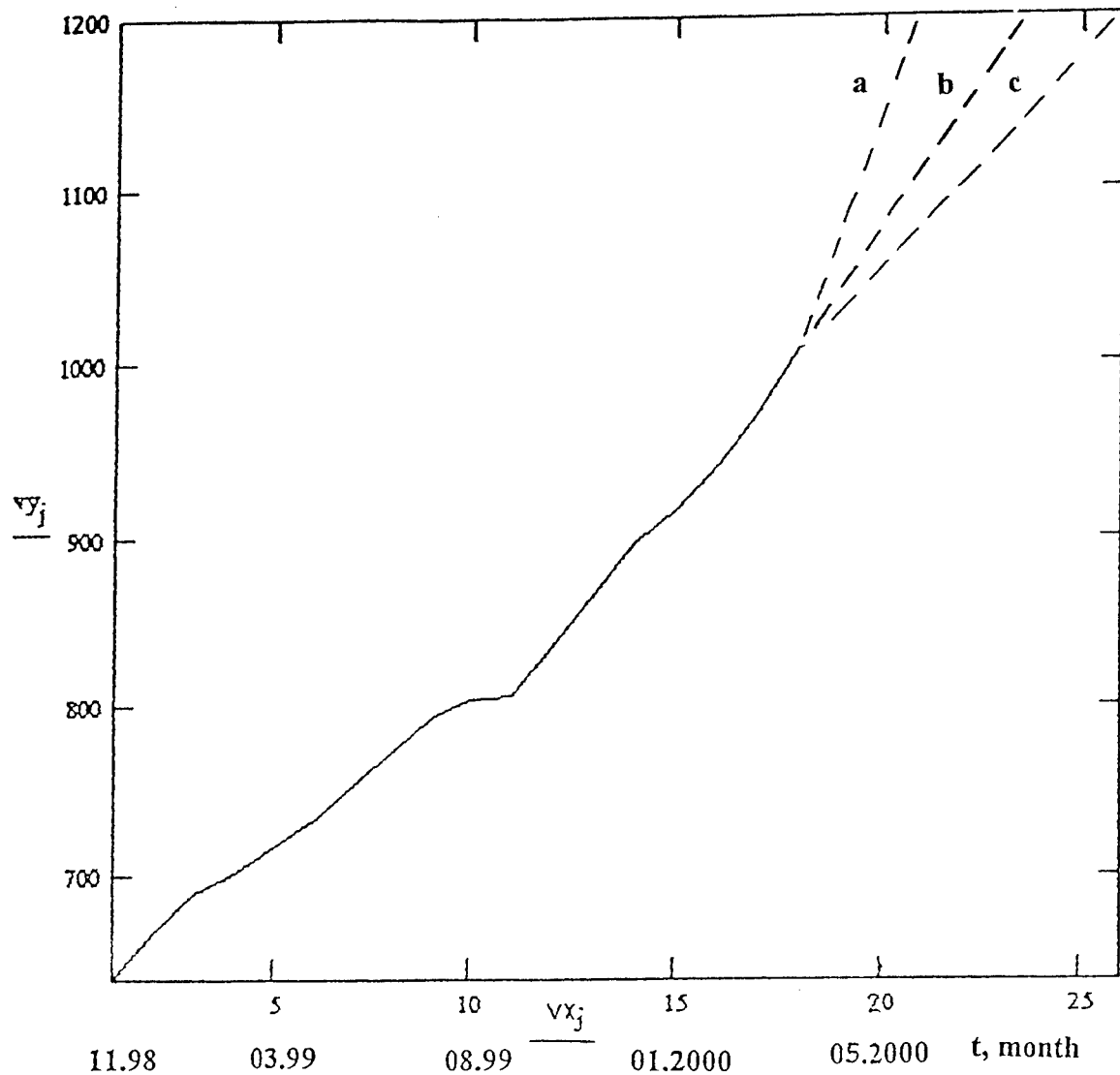


Fig. 1. The commutative the total known and the prediction NEO's
The known number- solid line, the prediction number - dotted line

It may be the several prediction versions, but only three of there are shown on fig. 1 by the dotted lines. It can be used the such polynomial function with the computing coefficients, for example:

$$VY_j(x) = 0.761 x^3 - 24.968 x^2 + 259.018 x \quad (1)$$

The such function (1) is the best approximation of the $VY_j(x)$ function.

The asteroids dimensions distribution is known today. The such distribution function can be approximate by the MathCad service. The very good results were recieved under «linfit» procedure. The polinomial koeffisients were computing by the such procedure. It can be used the next polinomial function:

$$\log(VY_j) = vx_j = 0.061 x^2 - 3.628 x + 8.023 (1+x)^{1/2} \quad (2)$$

The asteroids dimensions distribution $\log(VY_j)$ is shown on fig. 2. The such function (2) is the best approximation of the $\log[VY_j(x)]$ function. A double scale is used on fig. 2 for a MathCad procedure illustration also.

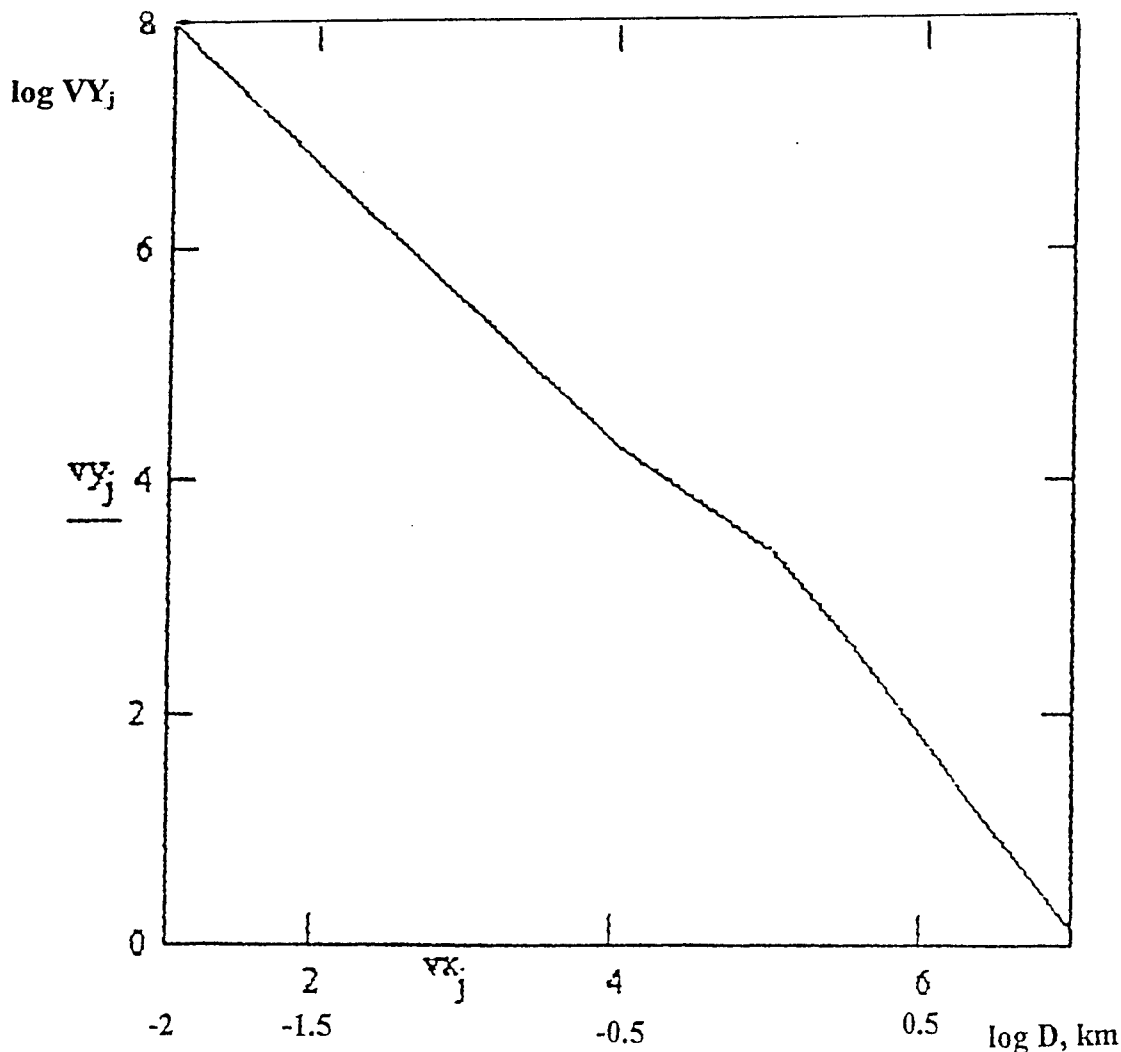


Fig. 2. The best probable asteroids dimensions distribution

The asteroids by dimensions more then 100 m can reach the Earth surface. The asteroids known number with dimensions more then 1000 m are more then 5 hundred as it is shows on fig. 2. The various asteroid materials are known today: stone, ice, different metals etc. Therefore it can be received an estimation of a middle asteroids density $\rho_{mid} \sim 3.6 \text{ ton/m}^3$. The estimation of the asteroids integer mass, with a sphere suggestion of the all asteroids, $M_{i \text{ int}} = (\rho_{mid} \pi D_{ia}^3 / 6)$ can be received at the such suggestions. The asteroids integer mass $M_{1 \text{ int}}$ is nearby $2 \cdot 10^{14} \text{ kg}$ has been taken by an integration of function $\log(VY_j)$ for $D_i \sim 10 \text{ m}$ (upper left plot on fig. 2). The mass $M_{2 \text{ int}}$ is nearby $6 \cdot 10^{15} \text{ kg}$ has been taken by an integration of function $\log(VY_j)$ for $D_i \sim 10^3 \text{ m}$ (middle

plot on fig. 2). The mass $M_{3 \text{ int}}$ is nearby $4 \cdot 10^{15}$ kg has been taken by an integration of function $\log(VY_j)$ for $D_i \sim 10^4$ m (bottom right plot on fig. 2). The maximum mass contribution in M_{int} are got the large asteroids (D_i is more then 500 m) in according to the such estimations. The such no complicated estimations and it a combination with the function vy_j on fig.1. are shown that the known asteroids mass M_{int} is arisen very quickly, a $M_{i \text{ int}}$ rise velocity across time in month is more then $\sim t^{-1}$.

Humanity can struggle with the small dangerous cosmic objects in our time and its parameter knowledge are needed. A present paper deals with prospects for the perspective of the laser methods applications for a dangerous asteroids discovering and a remote sensing and for the course correction systems of the influence expedients. The cosmic IR lasers will be used for remote sensing measurement of the various cosmic objects parameters: dimensions are more then 50 m, velocity is more then 10 km/s. The laser methods have the good perspectives among a large fleet of diagnostics technical means.

Now, the laser methods of objects velocity measuring are elaborated sufficient well and its can be used in the velocity measuring systems of the small particles⁴ so as of the other objects. Sufficient progress in understanding of a cosmic space was achieved by humanity during the 40 last years. The cosmic information systems are developed intensively and they can contain over 10 cosmic apparatus on the polar or the helio-stationary orbits. A humanity can struggle with the dangerous cosmic objects in our time, but the its parameters knowledges are needed. Therefore, the tasks of their monitoring are very urgent at present time. The laser methods have the good perspectives among a large fleet of diagnostics technical means.

2. DISCOVERING SYSTEM

A present paper deals with prospects for the cosmic IR lasers using for the remote discovering measurements of the various cosmic objects parameters: dimensions are up 1000 m, velocity is up 30 km/s. The cosmic diagnostic systems must have the minimum dimensions and weights. The optimization procedures are needed for this. A CO_2 -laser under solar energy pumping was elaborated⁵. The more effective CO_2 -laser parameters were defined for the solar systems smaller bodies velocity analysis. The laser is supplied with an automatic tuning optical system. Possibilities are estimated for diagnostic measurements with using modulated laser radiation⁶. The CO_2 lidars are needed for the asteroids detections at a distances of 30 000 km to 1 Mkm from an Earth surface. A laser Doppler anemometer method with adaptive selection is used. A laser field sounding is made by adaptive space unfolding of a laser beam focusing sounding. An exit laser power and a divergence are the lidar complex main parameters. The peak transmitted optical power is given by :

$$W_T = \pi 64 R^n Y_s / (P_T S_o \eta \epsilon_{\text{opt}} B^2 \sum Y_i) \quad (3)$$

where R is the range to the object, n is a degree index, Y_s is the postdetection electrical-signal power, P_T is the transmitter antenna gain, S_o is the effective object cross section, B is the aperture diameter, η is the space line transmittance, ϵ_{opt} is the optical efficiency of the system. The value Y_s depends on photoreceiver parameters.

The photodetectors with a coolant up to 77 K were used usually in the CO_2 -lidar systems. The high sensitivity (1000 V/W) photoreceivers without a cooling can be used for the sputnik diagnostic systems today. A photoreceiver with Cd Hg Te crystal is a best. The crystal is made as an optical resonator itself and it uses an avalanche injection effect. The total photoreceiver noise $\sum Y_i$ are include various components: Y_t is the thermal-noise power, Y_a is the power of the electronic postdetection amplifier noise, Y_d is the detector dark-current-noise power, Y_{sh} is the signal shot-noise power, Y_b is the background-illumination shot-noise power. The two last terms are unaffected by the Y_s for a such photoreceiver.

The main cosmic system components, are shown on fig. 3.

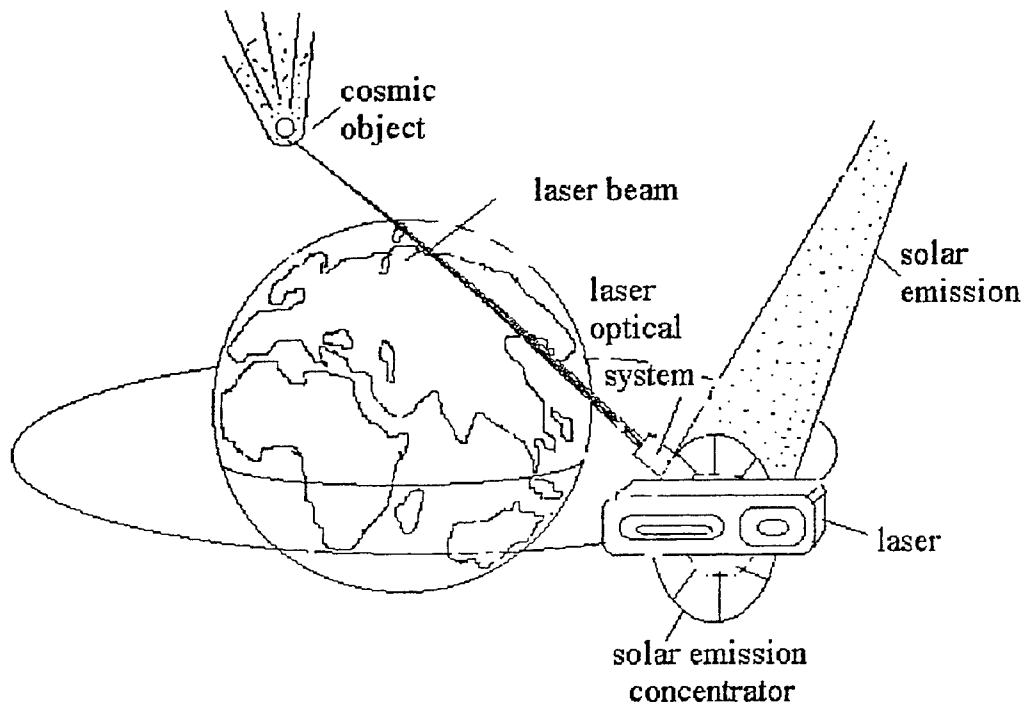


Fig. 3. Laser system general setup for an asteroids discovering

The power calculations were made with using Eq. (3) for the asteroids in a cosmic space. The η is nearly equal 1 for the wavelength $\lambda = 10,6 \mu$ in this case. Substituting the values for $R = 10^5 \text{ km}$, $S_o = 1,6 \text{ km}^2$, $B = 20 \text{ m}$, $P_T = 1500$, $W_r = 9,5 \cdot 10^{-9} \text{ W}$ into Eq. (3), yields $W_T = 100 \text{ kW}$, for example. Therefore, a such diagnostic task can be solved by the measuring system utilization which contains a power laser and the new ⁷ photoreceivers. The constant CO_2 lasers exit power are upper 100 kW, at present. The such diagnostic systems can found application for the asteroids velocity measurements and for the various cosmic and aerophysical measurements in a cosmic space.

3. THE MORE SUITABLE LASER GENERATORS

The various type of the high power lasers under solar pumping can be used in the such systems, its are discussed below. But each of the these laser types can be used in a general optics system.

3.1. Optics System

A high power laser beam is on the its output window. An exit laser beam is a ring type laser beam ($[R - r] \ll R$) at our system ^{8,9}. Then, it input in a laser beam transformer axicon. A transformed laser beam ($[D - d] \sim D$) is created at a axicon output. After that, a laser beam put on a scanning system that is discussed below. Then a laser beam put on a laser beam expander ¹⁰. A high power laser, laser beam transformer, a laser beam scanning system and laser beam expander are a part of general laser optical system (fig. 4) example. Our scanning system is made on a tradition chime. The high power laser beam can be scanned to the field that we want detect. The receive light beam of this direction of our scanning field is collected by the objective and it is scanned back to the fixed beam by the line and frame scanner, at the same time. The one of the beam splitters reflects most of the fixed beam to the focal lens. The letter focuses the whole receive light and local laser to the photoreceiver. A high power laser beam with needed parameters (origin diameter and origin divergence) is created by the such optical system.

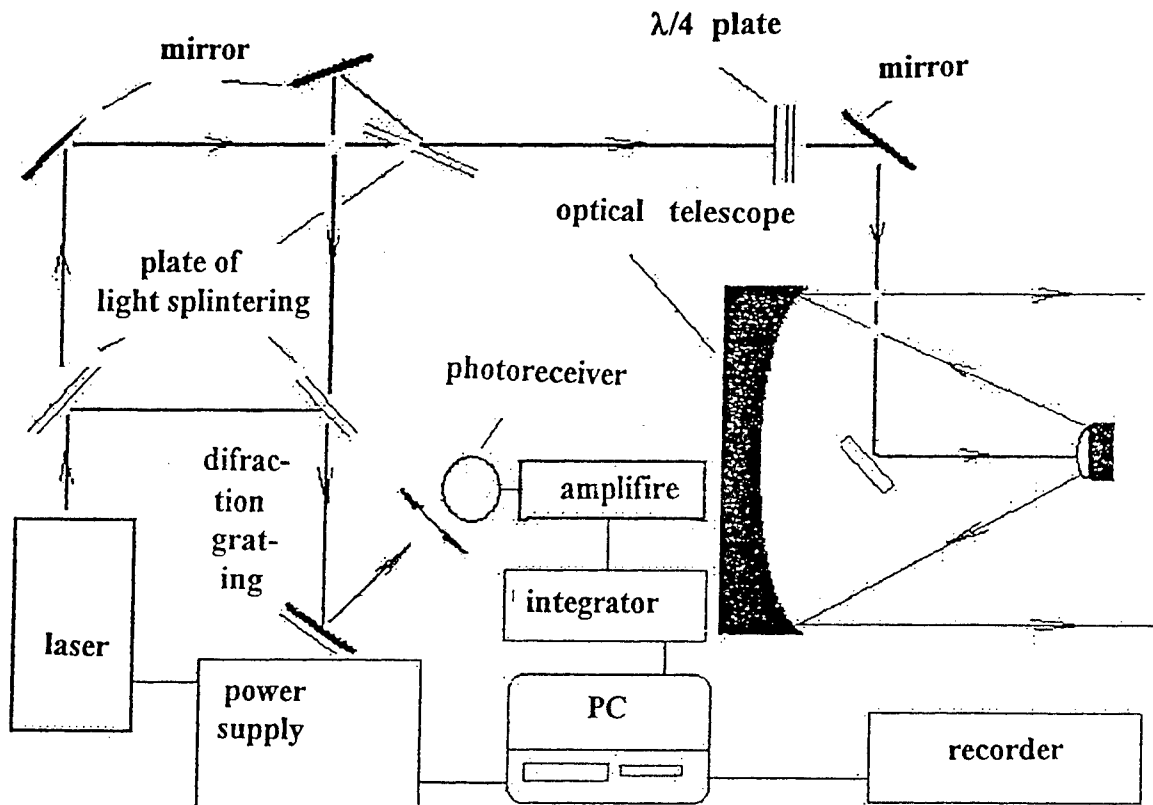


Fig. 4. Laser system scheme

3. 2. The Lasers Pumped by blackbody emission

At earth orbit, the solar flux W_s , well known to be about $\sim 0,14 \text{ W/cm}^2$, which ultimately provides the energy source with which to pump the solar laser system. The lasers pumped through an IR absorption spectrum, the use of an intermediate blackbody offers substantial and important advantages¹¹. The undesirable energy losses in the laser tube can be controlled. If materials such as ZnSe or KCl could be used in the laser construction, the optical absorption losses of these materials are small, and the utilization of the solar spectrum may be increased many orders of magnitude. If the re-radiation losses were the only loss mechanism, the utilization of the sun's energy for laser pumping could be as high as 98 % for black body temperature $T_{BD} = 1500^\circ \text{ K}$. The necessary collector size S for laser power $W_l = 100 \text{ kW}$ is $S = W_l (W_s \rho)^{-1} = 100 \times 100 \text{ m}^2$, if the overall efficiency $\rho = 10^{-3}$. It would seem that the indirect solar pumping has great promise for IR lasers.

3.3. The Gas Lasers with R.F. Excitation

Now, various company produces a range of CO_2 lasers from 1 W to 30 000 W, using Radio

Frequency (R.F.) power excitation. These lasers are compact, low voltage devices which can easily be integrated into systems and supplied with a sophisticated micro-processor control systems. Output power may be adjusted continuously from 0% to 100 % in few millisecond time duration. Voltage of power supplies is very small - 20 - 60 V. Therefore, the solar cell modules can be used in such power supplies⁸. Some specifications of solar cells provided by industry supplies are presented in the Table 1 (for the earth surface normal conditions).

Table 1.

Solar module type	Power, W	Power / Square, W/m ²	Power/Weight, W/kg
MC-550	50	100	6,9
MC-870	70	114	7,8
СЭУ-1	220	80	2,4

The front surfaces of solar modules are coated with long-lasting polymeric material. No fragile materials like glass or single crystal silicon plates are used. Modules design ensures reliable operation even if only the part of its surface is illuminated. The warranty period for flexible amorphous silicon solar cells is 3 years. For the system which consists of 4 lasers 30 kW laser power each for 100 kW cosmic laser system the solar cell module (as MC-870) with dimensions 140 x 140 m² is need for such laser system power supply. The such plate dimensions is not too large for the laser cosmic systems and can be made in our time already. This is the real scientific project as the solar power modules cost will be less 0,3 \$ / W near 2005.

The several scientific works were realized for solving the such tasks. The modern technology scheme for silicon solar cells was developed in our Institutes. The such solar power cost will be less 2\$ / W in 2001, by our estimations. In the same time our solar cells are more lighter then its were 2 years ago, according to table 1.

3.4. The Various Solid State Lasers

We are developing the solid state lasers under solar pumping also. In one of a such laser model is used a single solid state rod at phosphate glass, its length is near 0,5 m, laser wavelength is 1.06 μ. The optics waveguides with the selective properties and ceramic laser chamber are using at a such laser construction. A general mirror concentrator has selective covering also. The such laser construction can be base for 1 - 5 kW solid state laser under solar pumping. If we can combine the several such lasers, we can produced a high power laser module. The examples of the such laser modules are shown in Table 2.

Table 2.

Version	Power, kW	Laser number	General power, kW
N 1	5	20	100
N 2	10	10	- « - « -
N 3	30	4	- « - « -
N 4	50	2	- « - « -
N 5	100	1	100

4. THE SOME ASPECTS FOR THE COURSE CORRECTION SYSTEMS OF THE INFLUENCE EXPEDIENTS

The possibilities are estimated for the course correction systems of the influence expedients also. The such system must be good for the minimal distances nearby 12600 km, as the asteroid velocity can be more than 70 km/s. The laser power for the course correction systems of the influence expedients may be nearby 30 kW in according to

expression (3). Therefore for the such tasks may be used as the same modules which are shown in Table 2, so as the other types modules, which are shown in Table 3.

Table 3.

Version	Power, kW	Laser number	General power, kW
N 1	3	10	30
N 2	5	6	- « - « -
N 5	10	3	30

5. CONCLUSION

In our paper cosmic orbits CO₂-lasers and solid state lasers are discussed because of the ecological requirements. A cosmic system with the such lasers has some advantages and may be used in the object velocity remote sensing systems and for the Earth defense problems solutions in the nearest future. Therefore, the possibilities of the three types of high power lasers with solar pumping are discussed. The possibilities of the other various types lasers with solar pumping were described at several early works^{11,12}.

ACKNOWLEDGEMENTS

This work had been supported partially by Russian Foundation of Basic Research under Grant N 96-02-18776.

REFERENCES

1. «A dangerous asteroids scale». *Science*, 1999, 285, pp. 655.
2. A.V. Vityazev. «The Impacts in an early and a modern Earth history». *Earth and Universe*, N 2, pp.9-17, 2000.
3. «The shock craters on the Moon and on the planets». Moscow, Science, 200 p., 1983.
4. B.A. Kuzyakov, "The IR lasers in the plasma and ions flows investigations». *III All country scientific-technical conference «The optical methods of the flows investigations»*, pp. 88, Moscow, 1995.
5. I.I. Klimovskii, B.A. Kuzyakov, «Laser with a solar emission pumping». Patent, Russia, No. 2 098 980, *Invention Bulletin*, No. 25, pp. 355, 1997.
6. V.V. Grigor'yans, M.E. Zhabotinskii, B.A. Kuzyakov, « A Waveguide Carbon Dioxide Laser With Modulated Parameters ». *Quantum Electronics (Russian J.)*, 9, pp. 1496-1501, 1982.
7. K. Kikushi, «A modern high sensitivity photoreceiver», *Infrared Phys. Technol.*, No. 1, pp. 33-37, 1994.
8. I.I. Klimovskii, Y.B. Konev, B.A. Kuzyakov, «Advanced concept for effective power supply to the polar regions from the near-earth space». *International conference on scientific and technical problems of cosmonautics and rocket engineering. Book of Abstracts*, Kaliningrad, Moscow region, TSNIIMASH, pp. 103-104, 1996.
9. I.I. Klimovskii, Y.B. Konev, B.A. Kuzyakov, «Laser complex perspective». *XIII International conference «The matter condition equations»*, Terskol, pp. 80-81, 1998.
10. B. Kuzyakov, V. Batenin, I. Klimovskii, Y. Konev, «New perspectives of solar pumped high power gas lasers for cosmic energy systems». *International conference «High-power lasers and applications» (LASE'98)*, San Jose, California USA, pp. 44, 1998.
11. V.M. Batenin, I.I. Klimovskii, Y.B. Konev, B.A. Kuzyakov, » High power lasers under solar energy pumping». *IV Between country symposium on radiation plasma dynamics (RPD-97)*, Moscow, pp. 10-11, 1997.
12. A.L. Golger, I.I. Klimovskii, « Lasers with solar emission pumping. [Review] ». *Quantum Electronics (Russian)*, 11, pp. 233- 256, 1984.

Influence of the competition of rotational-vibrational transitions on a two-wave CO₂ laser generation mode

Vladimir O. Petukhov^a, Vadim A. Gorobets^a, Konstantin V. Kozlov^b

^aB.I. Stepanov Institute of Physics, NASB, Scaryna Ave.68, 220072, Minsk, Belarus

^bJoint Stock Company "Peleng", Makayonok Str. 23, 220032, Minsk, Belarus

ABSTRACT

With the aim of a parameters control of multiwave lasers the influence of the competition of CO₂ molecule rotational-vibrational transitions on the original two-channel technique has been investigated experimentally. The strong competition of transitions is observed only at two-wave generation on lines of one band, for example, 00⁰1-10⁰0. At the two-wave lasing on lines of various bands the competition of transitions can be essential weak.

Keywords: two-wave CO₂ laser, competition of rotational-vibrational transitions, dynamics of the connected systems.

1. INTRODUCTION

Laser sources which operate at two or more wavelengths are required in various fields. For example, lasers oscillating on several rotational-vibrational transitions in the mid-IR are of interest for vibrational excitation and dissociation of molecules, remote and local gas analysis, metrology, nonlinear conversion in crystals, effective optical pumping of FIR lasers. For these and number of other appendices it is important to receive multiwave generation with the stable output. However, in the case of molecular gas lasers achieving simultaneous oscillation on several given lines with stable output parameters, is a complicated problem due primarily to the strong competition between rotational-vibrational transitions.

With the purpose of achievement of a steady mode the certain methods allowing to avoid influence of a competition are used, for example, light beams diversity in the active medium. However in some cases the competition can play and positive role, for example, at study of dynamics of the connected systems¹, generation of pulses of the special form², intracavity gas analysis³. Therefore it is important to study the mechanism of a competition of transitions, that then, depending on a circle of soluble tasks to have an opportunity to operate a mode by multiwave generation.

In the given work the results of experimental researches of a two-wave mode of generation in the low pressure cw CO₂ laser with the longitudinal discharge are submitted. The features of such mode were studied in the two-channel cavity with independent adjustment everyone on the certain line, and in active medium the two-wave radiation was distributed strictly on one ways. On the basis of mutual influence of channels of generation the competition of transitions for various combinations of rotational-vibrational lines is investigated.

2. COMPETITION BETWEEN ROTATIONAL-VIBRATIONAL TRANSITIONS

It is known that a cw CO₂ laser with a nonselective cavity oscillates spontaneously on one or several rotational-vibrational transitions⁴. The spectral distribution of the output is changed at random due to competition between these transitions. Two main processes are at the heart of this competition effect, firstly a deviation from the Boltzman rotational distribution or quasi-equilibrium distribution of particles among vibrational levels by laser field. Secondly, rotational or vibrational relaxations which are trying to restore the equilibrium state. To obtain stable cw oscillation on several given lines simultaneously, it is necessary to choose laser parameters correctly, considering the competition and relaxation processes.

In our recent papers, on simultaneous oscillation of two and more rotational-vibrational lines in a pulse TEA CO₂ laser, it was shown both theoretically and experimentally that stable multiline operation is possible at high laser intensities. Under these conditions, due to a rotational bottleneck effect, the competition influence on the laser stability is weakened considerably⁵⁻⁹. To moderate the competition it is necessary for the intracavity intensity to reach the saturation intensity (I) for the transition. This intensity can be estimated from the expression:

$$I_S = c\pi\gamma/\tau B \quad (1)$$

where c is the speed of light, g is the collisional halfwidth at halfmaximum, τ is the collisional relaxation time, and B is the line center Einstein coefficient. This mechanism, which we named the "field mechanism", is applicable both to rotational transitions of one band and of various bands including nonregular bands 00⁰2-02⁰1, 00⁰2-10⁰1, 01¹1-11¹0. In the last case it is simplest to moderate the competition influence on laser stability. In this case the vibrational bottleneck effect operates at

significantly smaller values of the saturation intensity due to slower vibrational relaxation processes.

Despite of the study of multiline oscillation in a TEA CO₂ laser, the temperature model used for calculations⁹ is also applicable to cw CO₂ lasers. On the other hand our results are in a good agreement with earlier theoretical works on multiline oscillation in a cw CO₂ laser^{10,11}. Calculations^{10,11} showed that in order to weaken the competition, among transitions with Lorentzian-shape line broadening, it is necessary to generate conditions such that the laser field disturbs the Boltzman rotational distribution. Thus, in our opinion, the field mechanism is universally applicable and can be used to explain the multiline oscillation in both TEA CO₂ (pulse duration of approximately 1 microsecond) and other cw molecular gas lasers with Lorentzian line broadening. It should be noted that for lasers with the Doppler line broadening different volumes of the active medium can be responsible for the oscillation on different lines.

In this work the field mechanism approach is applied to explain the experiments of the simultaneous oscillation on two lines in a cw CO₂ laser where the line broadening is close to homogeneous. The stability of this system has been studied in a multichannel cavity taking into account the mutual influence of lasing channels. To explain the peculiarities of the multiline oscillation in a cw CO₂ laser, the competition effect has been studied for various combinations of rotational-vibrational lines over a wide spectral range. To demonstrate the principle multiline laser systems, this paper presents a two-wave CO₂ laser for study of nonlinear dynamic effects, designed according to conclusions of this investigation.

3. EXPERIMENTAL SETUP

The experimental setup for investigating the simultaneous oscillation on two lines is schematically shown in Fig.1. The experiments were conducted using a commercial sealed-off discharge tube GL-501 cooled by water. The length of the active medium was 1.2 m. The discharge tube was powered by a stabilized high-voltage power supply. The cavity was formed by a totally reflecting mirror 2 installed in the tube, a 150 lines/mm grating 3 operating in first order in a non-Littrow arrangement, and mirrors 4 (λ_1) and 5 (λ_2) set at small angles to the cavity axis. The reflectivity of the grating in the first diffraction order was greater than 90%. The laser output was approximately equally distributed between the 00 and 00'-orders of the diffraction grating (see Fig.1).

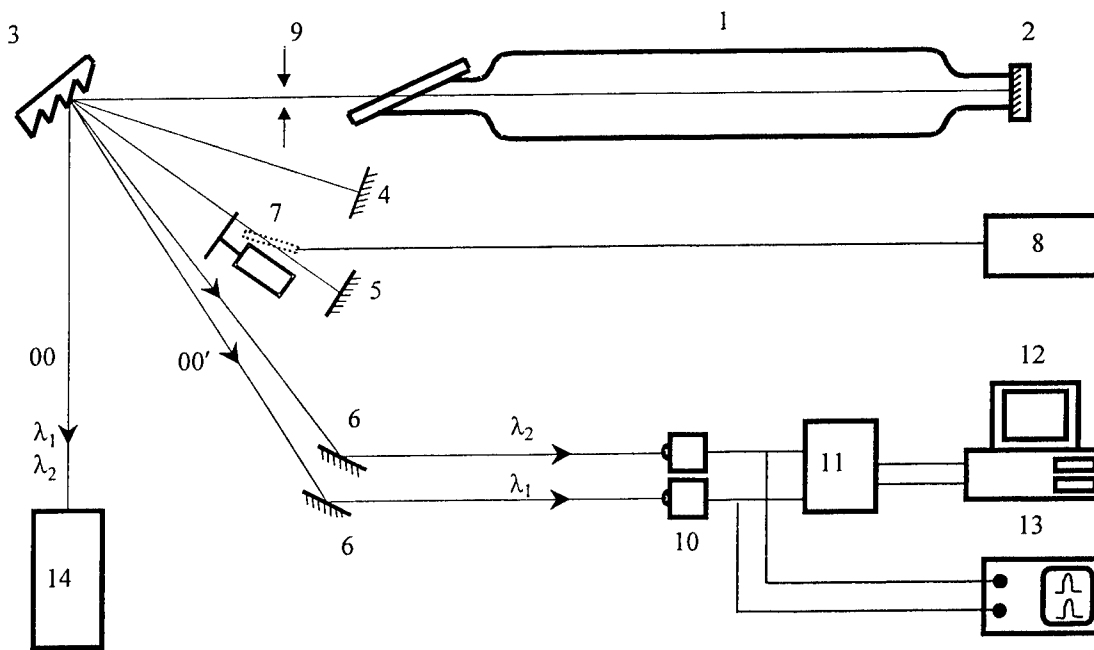


Fig. 1. Experimental setup. 1- discharge tube; 2- nontransmitting mirror; 3- diffraction grating; 4, 5, 6- mirrors; 7- chopper or acousto-optical modulator; 8- generator; 9- iris aperture; 10- photodetectors; 11- two-channel analogue-digital converter; 12- computer; 13- dual-trace oscilloscope; 14- spectrum analyser.

When this system operates with the 00-order of the grating, radiation of different wavelengths, λ_1 and λ_2 , propagates along the same optical path. Radiation output using the 00'-order provides spatial separation between λ_1 and λ_2 components so that we could investigate multiline oscillation. Using this arrangement for the cavity it was possible to tune the lasing channels to a desired line independently and analyse the oscillation on several lines simultaneously

With the help of additional mirrors 6 the 00'-order output was directed to Ge:Au detectors 10 cooled by liquid nitrogen

with a bandwidth of ~ 10 MHz. The electrical signal from these detectors reached a two-channel analogue-digital converter 11 and then a computer 12. Additionally we used a dial-trace oscilloscope 13. To analyze the spectral characteristics of a laser, the 00-order radiation modulated by an electromechanical chopper and directed through a SPM-2 monochromator 14.

Loss modulation in the active channel was performed by an electromechanical chopper 7 or an acousto-optical modulator 7 made of KRS-5 crystal. An ultrasonic wave in this modulator was excited by a generator 8.

4. RESULTS AND DISCUSSION

An investigation of the stability of simultaneous oscillation on various transitions was carried out for various pairs of lines belonging to different vibrational bands $00^0_1-10^0_0$ and $00^0_1-02^0_0$. The vibrational bands and the rotational (J) quantum number were varied. Typical measurement results of the competition of rotational-vibrational transition on a two-wave CO_2 laser generation mode are given in Fig. 2. To investigate the effect of one lasing channel on the other the following procedure was used. Two channels were adjusted to the lines at λ_1 and λ_2 by alignment of mirrors 4 and 5. Then the intracavity loss modulation in the active channel was performed by an electromechanical chopper 7. In case of small frequencies of modulation (up to ~ 5 kHz) in the active channel the quasi-stationary generation is observed, i.e. the Q-switch regime is not shown. Thus the amplitude of pulses correspond to generation output in a continuous mode, when the modulation is absent.

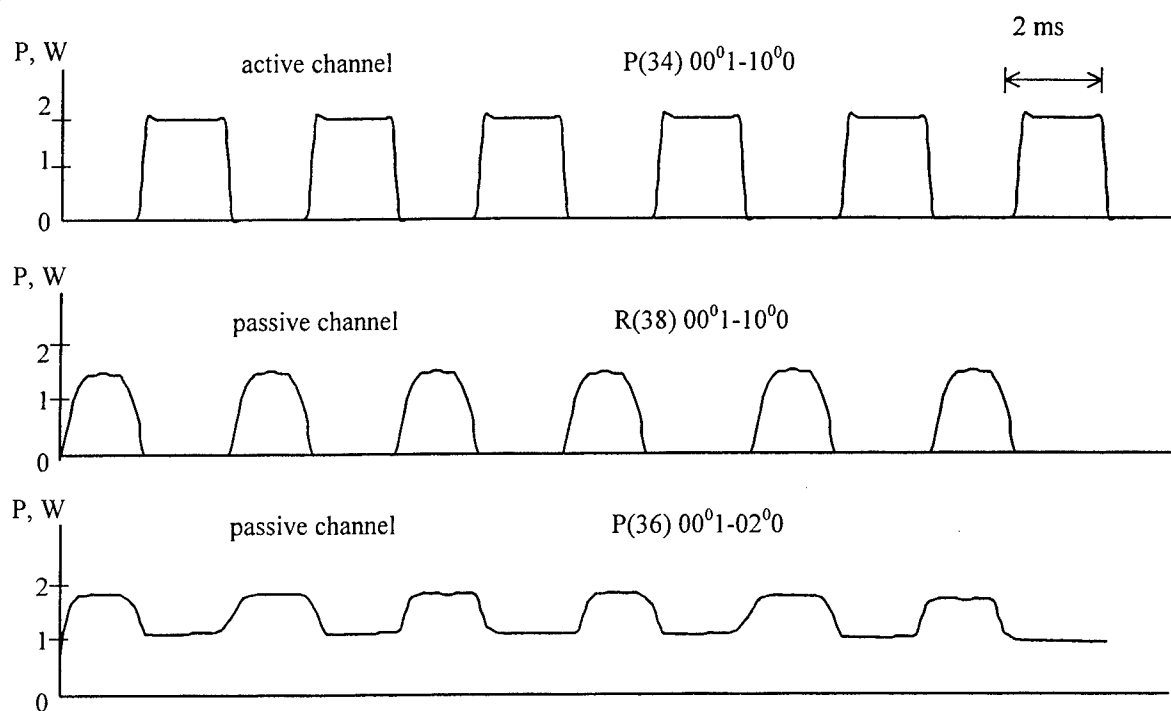


Fig.2. Generated pulses of a two-wave CO_2 - laser with loss modulation (modulation frequency $f_m = 250$ Hz) in one of the channel (active channel) and tuning the other channel (passive channel) on generation lines.

The competition between rotational-vibrational transition should result to synchronous oscillations of the output radiation intensity in the passive channel. And, laser pulses in the passive channel will follow in an anti-phase laser pulses of the active channel¹. The depth of modulation in the passive channel should characterize degree of a transition competition. At the less modulation depth the transitions are less connected.

Studying the interaction between the lasing channels has shown that tuning the cavity mirrors to various vibrational bands, independently of the rotational line choice, leads to modulation depth of the passive channel output radiation intensity far less than 100% (bottom curve on Fig. 2). And the modulation depth has a common tendency to reduction in process of increase of frequency of modulation (f) and aspires to 0 at $f \sim 1,5$ kHz. However exists the high depth of modulation ($\sim 70\%$) is abnormal at $f \sim 500$ kHz. It can be caused by resonant properties of the used laser system or by relaxation processes in active medium.

The most significant interference of the channels was observed when lasing on various rotational lines of the same band (see Fig. 2). In this case the competition resulted in a 100% output power modulation in the passive channel irrespective of loss modulation frequencies down to 40 kHz. At the large frequencies are observed complex nonlinear-dynamic effects¹.

The observed difference in the competition effect on interference between channels for various combinations of rotational-vibrational lines can be explained on the basis of the field mechanism criteria introduced earlier by expression (1). To do this compare the value of saturation intensity I_s and the laser field intensity I achieved in the cavity. Notice, that I_s is dependent upon the transitions probability and relaxation rates.

For CO₂ the absence of the competition effect on interference between channels may be only observed at channel tuning to different bands which are not connected by common vibrational states, e.g. 00⁰1-10⁰0 and 01¹1-11¹0, 00⁰2-10⁰1 and 00⁰1-02⁰0, and so on. Calculations have shown that at intensities ~ 100 W/cm² attained in the cavity and a relatively low V-V exchange rate ($\sim 10^6$ s⁻¹ x Torr⁻¹)¹² for CO₂ under typical conditions of low-pressure cw lasing "vibrational bottleneck" takes place and the competition between the transitions weakens. In the case of transitions which are coupled through a common vibrational state, for example 00⁰1-10⁰0 and 00⁰1-02⁰0, the output power, as illustrated in fig. 2, is dependent on the presence of oscillation in the neighboring channel. For these transitions the output power of the passive channel already begins to feel the competition between the transitions.

The rate of rotational relaxation is several orders of magnitude higher than the rate of vibrational relaxation (about of 100 times higher for experimental conditions), and the radiation intensity I is inadequate to produce the "rotational bottleneck" ($I \ll I_s$) and consequently for the reducing the competition between rotational transitions.

A theoretical analysis is required to explain the observed dependencies more accurately. However, the detailed numerical analysis of multiline oscillation in the cw CO₂ laser, as was done for the TEA CO₂ laser⁹, is complex owing to the quasiequilibrium vibrational distribution in the electrical discharge.

4. APPLICATION OF THE TWO-WAVE CW CO₂ LASER

One more possible application of a multiline system is using them to study nonlinear dynamics processes. Single line cw CO₂ lasers have been used to investigate many types of nonlinear dynamics processes¹³. In our opinion, it would be useful to investigate the problem of a few coupled oscillators system¹ with the help of a multicavity system coupled through the common active medium. In this case the coupling efficiency can be easily varied from low (lines belong to the different vibrational bands) to high (lines belong to one vibrational band).

Such a two-wave laser with independent tuning, in each channel, to a specific rotational-vibrational line in various vibrational bands of the CO₂ molecule represents a system of two coupled "optical" oscillators undergoing forced oscillations¹. Consequently, the proposed method provides new opportunities for investigating the relationships governing the nonlinear response (doubling of the period and of the repetition frequency of the pulses, deterministic chaos, etc.) in the specific case of coupled oscillatory systems.

In this work experimental investigations were made of nonlinear dynamic regimes of the operation of the two-wave CO₂ laser described above. Our laser system made it possible to tune the cavity channels to various lines in the traditionally investigated 00⁰1-10⁰0(02⁰0) and nontraditional 01¹1-11¹0 and 00⁰2-10⁰1(02⁰1) bands. Figure 3 gives the experimental time dependencies of the outputs P_{active} and $P_{passive}$ when the laser was tuned to a pair of lines P(16) (passive channel) and R(18) (active channel), in the 00⁰1-10⁰0 band. The output powers of the lines obtained in the fundamental mode regime were approximately the same and amounted to ~ 2 W (coupling via the 00' order) in the case of cw lasing without loss modulation. When the losses were modulated, the peak power reached 12 W.

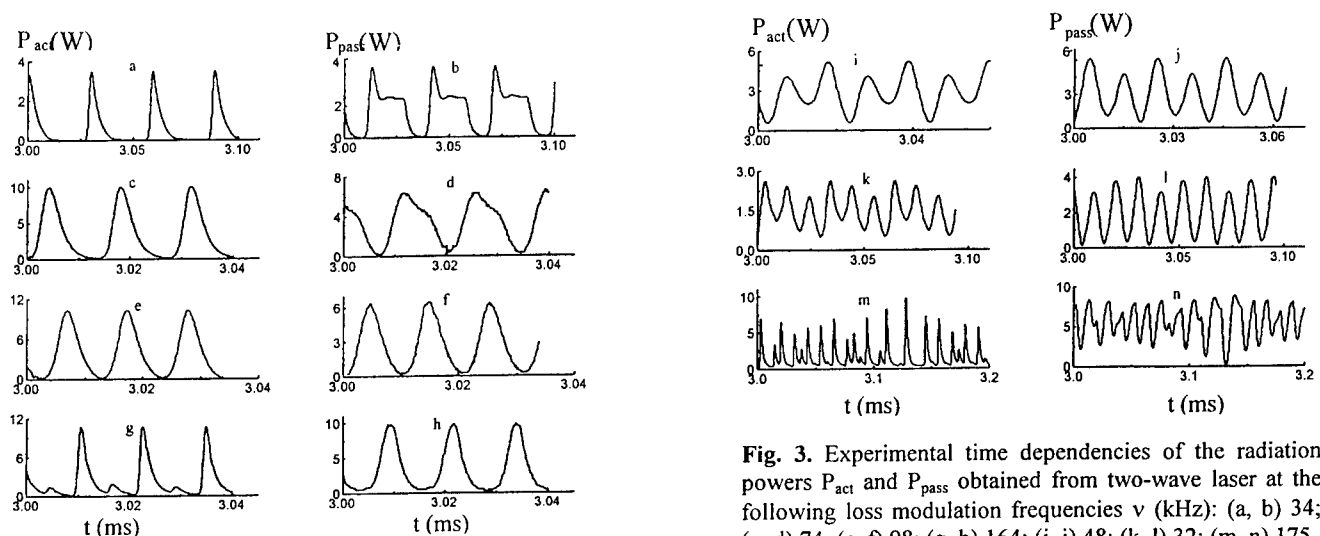


Fig. 3. Experimental time dependencies of the radiation powers P_{act} and P_{pass} obtained from two-wave laser at the following loss modulation frequencies ν (kHz): (a, b) 34; (c, d) 74; (e, f) 98; (g, h) 164; (i, j) 48; (k, l) 32; (m, n) 175.

Nonlinear dynamics of the laser was investigated as a function of the loss modulation frequency in the active cavity channel. Nonlinear amplitude- frequency characteristics of each of the laser channels have two low- frequency resonance spikes, associated with forced linear oscillations of two coupled oscillators, and high-frequency spikes, corresponding to doubling of the period of the output radiation oscillations. These nonlinear amplitude-frequency characteristics are differed fundamentally from the corresponding characteristics obtained in the one wave lasing regime. It was established that at low loss-modulation frequencies the oscillations of the output radiation in the coupled channels are in antiphase. At high modulation frequencies the dynamics is cophasal. Under certain conditions, we observed such nonlinear dynamic effects as doubling of the period and of the repetition frequency of the pulses, as well as deterministic chaos.

5. CONCLUSION

In this work multiline oscillation on two transitions in a cw CO₂ laser was investigated by use of a multichannel cavity. The field mechanism approach was applied for experimental data analysis. It was shown that the influence of competition between transitions on the laser stability is weakened considerably at high laser field intensity (higher than the saturation intensity), when a vibrational bottleneck effect is induced.

The field mechanism approach may be useful when considering simultaneous multiline oscillation in other molecular gas lasers (e.g. CO, N₂O, HF, DF, etc.). It should be noted that in the case of simultaneous oscillation of two orthogonal polarised waves on the same transition ⁶, to enable competition weakening one needs to switch on the polarisation bottleneck effect which is defined by the orientation constant of the transition dipole moment.

It is also possible to apply our approach to investigate simultaneous oscillation on different molecular components in the same active medium (CO-CO₂, CO₂-N₂O, ¹²CO₂-¹³CO₂) where a common reservoir of stored vibrational energy is used jointly ¹⁴. In this case the bottleneck effect is determined with an intermolecular vibrational exchange. Preliminary experiments with a cw CO-CO₂ laser which has an output containing 5.4 and 10.6 μm radiation confirm this conclusion.

6. ACKNOWLEDGEMENTS

The authors wish to express much appreciation and thanks to Dr. B.F. Kuntsevich for much assistance with the work and discussions and Dr. V.N.Chizhevsky for his interesting idea and helpful discussion of nonlinear dynamics aspects.

The work was partly supported by a grant from the Fundamental Research Foundation of the Republic of Belarus

7. REFERENCES

1. V.A. Gorobets, K.B. Kozlov, B.F. Kuntsevich, V.O. Petukhov, "Nonlinear dynamic effects in a two-wave CO₂ laser", *Quantum Electronics* 29 (4), pp. 303-308, 1999.
2. V.A. Gorobets, K.B. Kozlov, B.F. Kuntsevich, V.O. Petukhov, "Lasing of right-angled pulses in a two-wave CO₂ laser" *Proc. of the IV Inter. Conf. "Laser Physics and Spectroscopy", Grodno, Belarus*, pp. 156-158, 1999.
3. A.P.Voitovich, V.B. Dunaev, A.P. Prokopov, "Use of a two-wave CO₂ laser for detection of small gas concentrations" *J. Appl. Spectroscopy* 42(3), pp. 369-372, 1985(in Russian).
4. W.J. Witteman, "The CO₂ Lasers", Springer-Verlag Berlin Heidelberg New York London Paris Tokyo, 1990, - pp. 360.
5. I.M.Bertel', V.O.Petukhov, S.A.Trushin, V.V.Churakov, "Simultaneous stimulated emission of high-power pulses at lines of regular and sequence bands in a TEA CO₂ laser", *Sov.J.Quantum Electron.* 11, pp. 209-214, 1981.
6. I.M.Bertel', V.O.Petukhov, A.P.Prokopov, S.Ya.Tochitsky, V.V.Churakov, "Energy, spectral and temporal performances of two-wave TEA CO₂ laser", *J.Appl.Spectroscopy* 46, pp. 245-249, 1987.
7. V.O.Petukhov, S.Ya.Tochitsky, V.V.Churakov, "The simultaneous efficient stimulated emission at two lines of different sequence bands in a TEA CO₂ laser", *Sov.J.Quantum Electron.* 17, pp. 389-393, 1987.
8. V.V.Churakov, V.O.Petukhov, S.Ya.Tochitsky, "Two-colour TEA CO₂ laser oscillation on the lines of regular and hot bands", *Appl. Phys. B* 42, pp. 245-251, 1987.
9. B.F.Kuntsevich, V.O.Petukhov, S.Ya.Tochitsky, V.V.Churakov, "Field mechanism of simultaneous oscillation on several transitions in TEA CO₂ laser", *Sov. J. Quantum Electron.* 23, pp. 481-488, 1993.
10. B.I.Stepanov: *Journal of Applied Spectroscopy*, 8, pp. 549-554, 1968.
11. V.P.Kabashnikov, "Spectrum of the Steady-State Output of a CO₂ Laser" *Izd. IF Akad.Nauk BSSR, Minsk*, 1971.
12. A.V.Eletskiy, B.M.Smirnov. *Physical Processes in Gas Lasers, Energoatomizdat, Moscow* pp. 3-150, 1985 (in Russian).
13. C.O.Weiss, R.Vilaseka. "Dynamics of Laser" VCH, Weinheim, p. 292. 1991.
14. V.O.Petukhov, N.N.Sazhina, A.M. Seregin, V.S.Starovoitov, S.A.Trushin, N.V.Chebурkin, V.V.Churakov, "An investigation of the gain and oscillation spectra of the TEA ¹⁸CO₂laser", *Journal of Applied Spectroscopy* 47, pp. 782-788, 1988.

Action of pulse-periodic and continuous IR radiation on light-controlled vanadium dioxide mirrors.

O.B.Danilov^a, A.I.Sidorov^a, D.Titterton^b, S.N.Tulsky^a, I.L.Yachnev^a, A.P.Zhevlakov^a

^aInstitute For Laser Physics, St.-Petersburg, Russia

^bDERA, United Kingdom

ABSTRACT

The results of an experimental research of action of the intensive mid IR-range pulse - periodic laser radiation on VO₂-mirrors are represented. The damage thresholds of VO₂-mirrors are defined for pulse-periodic and continuous radiation and the analysis of the mechanism of their destruction is carried out. The results of numerical simulation of dynamics of switching of VO₂-mirrors under the action of pulse - periodic radiation are presented.

Keywords: vanadium dioxide mirror, damage threshold, mid IR range

1. INTRODUCTION.

The vanadium dioxide(VO₂) mirror represents a multilayer interference system with a film VO₂ as the command element¹. The modulation of a reflection coefficient in such system is achieved at the expense of a reversible modification of optical parameters of VO₂ during the semiconductor – metal phase transition, which happens in a temperature interval 60-70°C². In an association from a type of an interference system of a mirror it the reflection coefficient can vary from R_{min} < 1 % up to R_{max} = 95-98 %, and, as with positive, and negative magnitude of dR/dT¹. The switching of VO₂-mirrors from one state into another can be carried out at the expense of heat by the thin-film heater, electronic ray, or by laser radiation.

The controlled VO₂-mirrors and modulators on their basis are perspective devices for laser radiation control. Among a series of applications of similar devices it is necessary to mention the intracavity control of the laser beam direction^{3,4}, control of the shape and duration of laser action pulse⁵, and also the limiting of intensity of a laser radiation⁶. It is obvious, that one of the basic parameters of optical switches on the base of VO₂-mirrors is their stability under the action of an intensive laser radiation. In this paper the outcomes of an experimental and theoretical research of the destruction of VO₂-mirrors are represented under the action of pulse – periodic and continuous laser radiation of mid IR-range, and also the analysis of the influence of conditions is carried out of pulse – periodic exposures on dynamics of switching of VO₂-mirrors.

2. DAMAGE THRESHOLDS OF VO₂-MIRRORS BY A LASER RADIATION.

Experimental research of damage thresholds of VO₂-mirrors were carried out in the 3.6-4.2 μm spectral region. As an action source the continuous supersonic DF-laser with a duration of laser action 5 and 10 seconds was used. To obtain the pulse – periodic regime the radiation was modulated with the help of gyrating of a mirror. The pulse repetition rate of a radiation in this regime varied from 0.5 up to 2.5 kHz and the pulse duration varied from 1.2 up to 0.3 μs.

The optical schemes in the experiments included two channels. The first channel was for a measurement of parameters of a laser radiation - energy or intensity, pulse duration and distribution of a radiation in near-field zone. Samples of VO₂-mirrors were placed in the second channel of the optical scheme. The radiation flux, incident on the samples, varied with the help of calibrated attenuators.

The damage thresholds were obtained on the base of the real spatial distribution of a radiation in a plane of a sample. A diameter of the irradiated zone on the samples was 1-5 mm. The presence of irreversible modifications on a surface of the sample was determined by the following methods: visually - with the help of microscope, on a modification of spatial distribution of a radiation in a probe beam of the He-Ne laser (λ= 0.63 μm), reflected from area of laser action, and - on a modification of the modulation characteristics of a VO₂-mirror at the exploration of the irradiated zone by a

radiation with a wavelength hitting in spectral area of modulation of a mirror. For these purposes the continuous He-Ne laser with $\lambda = 3.39 \mu\text{m}$ was used.

In the experiments the VO_2 -mirrors with $dR/dT > 0$ were investigated. The mirrors were made so that spectral area, in which the modulation of their reflection coefficient is maximum, coincides the spectral area of an acting radiation. The interference systems of mirrors had the following construction: $(HL)_n\text{-H1-VO}_2\text{-H2-M}$. Here H and L – are the quarter wave dielectric layers with a high and low index of refraction respectively, $n = 1 \dots 2$, M – the film of metal with a high reflection coefficient. The whole optical thickness of layers H1 and H2 is close to $\lambda/2$. A principle of work of such mirrors and detailed definition of their constructions are presented in¹. As dielectric layers ZnS, ZnSe, BaF_2 , Al_2O_3 and Ge films were used. A thickness of the VO_2 film was $0.25\text{-}0.35 \mu\text{m}$. The samples of VO_2 -mirrors on a quartz glass, germanium, aluminum and copper substrates were investigated.

The researches have shown, that the irreversible modifications of the surface of VO_2 -mirrors under the action of one radiation pulse pass three stages with growth of radiation power. On the first stage there are no visible modifications of a surface and the modulation characteristics of a VO_2 -mirror at the working wavelength do not vary. However, at exploration of the irradiated zone by a radiation with $\lambda = 0.63 \mu\text{m}$, in space distribution of a reflected radiation occur interference rings. In some cases rings arise only at 10-20 s after the laser action. Most frequently this effect is exhibited at an exposure of VO_2 -mirrors intended for $10 \mu\text{m}$ spectral range. At the increase of the action intensity the second stage of irreversible modifications is observed – the arising in the irradiated zone of single dot destructions of dielectric layers of the mirror. The further increase of intensity produces the third stage of modifications - continuous destruction of film coatings in the irradiated zone.

In spite of the fact that on the first stage of irreversible modifications the change of modulation characteristics of a VO_2 -mirror does not take place, the intensity, appropriate to this stage, was determined as the damage threshold. When the first stage of modifications was not observed, the damage threshold was determined on the arise of single dot destructions on a surface of a sample.

In the Table 1 some experimental damage thresholds of VO_2 -mirrors under the action of pulse – periodic and continuous laser radiation are presented. For the pulse - periodic regime - τ_p – pulse duration, f - pulse-repetition frequency, Q_{thr} - radiation energy density on a sample for one pulse. For a continuous regime of an exposure the threshold intensities on a surface of a sample are presented. The VO_2 -mirrors on a copper substrate at pulse - periodic and continuous action of a radiation have damage thresholds exceeding the magnitudes which are listed in table. For a comparison in a table the data on the destruction of mirrors by a single pulse radiation also are presented.

Table 1. The damage thresholds of VO_2 -mirrors under the action of laser radiation.

$R_{\text{max}}, \%$	Substrate	Mode	$\tau_p, \mu\text{s}$	f, kHz	T_{act}, s	$Q_{\text{thr}}, \text{J/cm}^2$	$T_{\text{max}}, ^\circ\text{C}$
96	Ge	S	4	-	-	14	630
96	Ge	S	50	-	-	21.7	350
94	Ge	P-P	1	2	10	0.6	570
94	Cu	P-P	1	2	10	>1.9	-
94	Ge	C	-	-	10	3.3 kW/cm^2	640
94	Cu	C	-	-	10	>3.8 kW/cm^2	-

Notes: S, P-P, C – single pulse, pulse - periodic and continuous regimes; T_{max} - calculated temperature of a surface of a mirror appropriate to the damage threshold.

The results, represented in a table, allow to reveal the following regularities:

1. The increase of a thermal conduction of a substrate of a VO_2 -mirror reduces in the increase of the damage threshold.
2. To the same result led the increase of R_{max} for VO_2 -mirrors with $dR/dT > 0$.
3. The decrease of a thickness of an interference system is accompanied by the increase of the damage threshold.

A character of destructions of VO_2 -mirrors by a radiation and the regularities of a modification of a damage threshold allow us to make a conclusion, that for the considered conditions of action the thermal mechanism of destruction of mirrors is dominant. The part of an energy of an acting radiation absorbed by an interference system of a mirror, reduces in significant heat of interference layers. As VO_2 -mirrors used in experiments, had zero transmittance, the energy of a radiation absorbed by an interference system, can be presented as:

$$Q = Q_0 \cdot [1 - R(T)] \quad (1)$$

Here Q_0 – the incident energy of a radiation, $R(T)$ - reflection coefficient of a VO_2 -mirror. From here follows the strong influence of the reflection coefficient of a mirror after completion of the phase transition (at $T > 70^\circ\text{C}$) on a damage threshold.

Because of the difference of temperature coefficients of the extension of layers, in an interference system, during heating by the radiation, arises the mechanical strengths reducing in a stratification of the layers and the bend of the surfaces of the mirror in irradiated zone takes place. It is the reason of the appearance of interference rings in distribution of a reflected radiation of the probe laser. As a modification of a thickness of an interference system is small ($\Delta H \ll \lambda_0$, λ_0 - operation wavelength of a VO_2 -mirror), it weakly acts on modulation characteristics of a mirror. However, the mechanical strength in stratified area reduces in emerging of cracks in layers, which are the contributors of dot destructions of a surface of a mirror. Another contributor of dot destructions are the imperfections of a structure of layers and inclusions having an increased absorption and calling a local overheating of a surface.

With a diminution of a thickness of an interference system of a mirror the damage threshold is increased. It is connected with magnification of effectiveness of remove of heat into substrate. Besides the smaller thickness of recordings ensures the increased mechanical strength of the whole interference system and reduces the possibility of a stratification. The influence of a thermal conductivity of a substrate and duration of acting pulse on a damage threshold also is connected to a velocity and effectiveness of remove of heat from layers into substrate during action of a radiation.

3. THERMAL MODEL OF ACTION OF INTENSE RADIATION ON VO_2 -MIRRORS.

The process of heat of a VO_2 -mirror by an intense laser radiation consists of three stages. On the first stage, at temperatures below phase transition, the VO_2 -mirror has a constant reflection coefficient equal R_{\min} for mirrors with $dR/dT > 0$; the second stage corresponds to a temperature interval of phase transition in VO_2 film, where the modification of a reflection coefficient of a mirror happens; and the third stage - at temperatures higher than temperature of completion of phase transition ($T > 70^\circ\text{C}$), where the reflection coefficient of a mirror again becomes to constants and equal R_{\max} for mirrors with $dR/dT > 0$. On each stage of heat the amount of energy absorbed by a mirror, is various and is determined by the reflection coefficient. However, as have shown in the experiments and calculation, for radiation intensities of hundreds kW/cm^2 , the duration of first two stages of heating does not exceed 100 ns, and the amount of an energy of a radiation absorbed on these stages, is several percents from a full energy in a pulse. Therefore, at numerical simulation it is possible with a rather high degree of an exactitude to consider, that the VO_2 -mirror initially is in a switch on state appropriate to a metal phase of the VO_2 film, and has a constant reflection coefficient.

The simulation of heating of a multilayer mirror by a radiation can be carried out in view of distribution of a field of a light wave and heat release in each layer (for example, Ref. 7). However, such approach is meaningful, in basic, for pulses of a radiation of small duration. Let's consider the distribution of temperature on a thickness in a semi-infinite body at its surface heating by square pulse of a radiation. A profile of temperature for the mentioned above conditions can be calculated with the help of expressions⁸:

$$T(z, t) = \frac{2P\sqrt{t}}{\eta} \cdot F\left(\frac{z}{2\sqrt{at}}\right). \quad (2)$$

$$F(x) = \frac{\exp(-x^2)}{\sqrt{\pi}} - x \cdot \left[1 - \frac{2}{\sqrt{\pi}} \cdot \int_0^x \exp(-u^2) du \right], \quad \eta = \sqrt{dck}$$

Here P - specific power of a surface heat source, d - density, c - specific heat, k - thermal conductivity, a - temperature conductivity.

Fig. 1 shows the distributions of temperature through 100 ns and 1 μs after a beginning of action of pulse of radiation for film materials with a low thermal conductivity (VO_2 , ZnS , BaF_2) and material with a high thermal conductivity (Ge). It follows from the Figure, that for time of heating in hundreds and more nanoseconds and thickness of layers, characteristic for VO_2 -mirrors of mid IR-range, the heat, released in one layer, has time to be redistributed on adjacent layers. It allows to consider an interference system as homogeneous during calculations. The average was produced on all layers which are included in an interference system, with weight factors which are taking into account the thickness of layers.

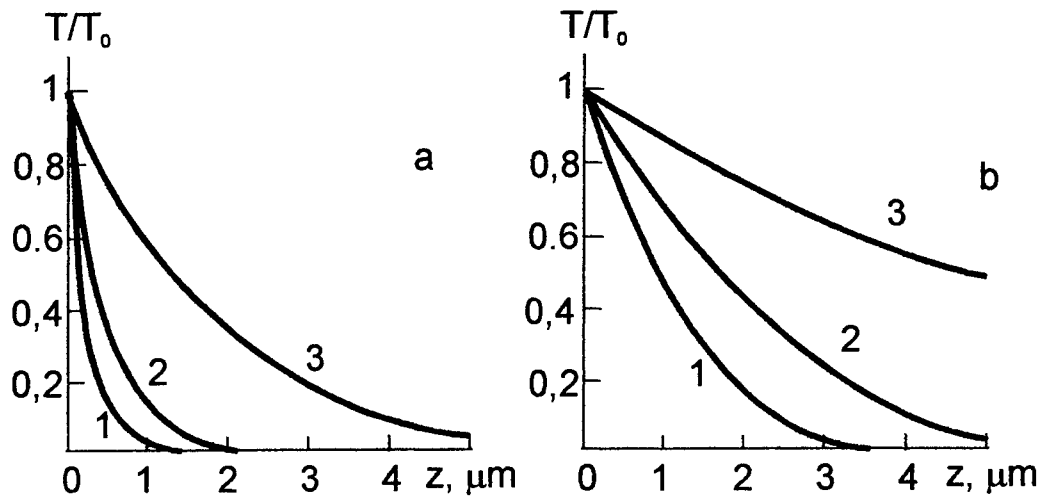


Fig.1. Calculated distribution of temperature on depth of a layer after 100 ns (a) and 1 μ s (b) beginning of heating by a radiation. 1 - ZnS, 2 - VO₂ and BaF₂, 3 - Ge.

The tentative estimations have shown, that under the action of intense laser pulse the surface of a VO₂-mirror is heated up to hundreds degrees. At such modification of temperature noticeably vary a thermal conduction and thermal capacity of materials which are included in a structure of an interference system. Therefore at simulation the temperature dependence of a thermal conduction and thermal capacity of these materials were taken into account.

Thus, the thermal model of a VO₂-mirror for the considered conditions can be shown to an approximation of a thin homogeneous slice with the ideal thermal contact to a semi-infinite body and which is heated up by the constants heat source. For the case of a rectangular distribution of a radiation the modification of temperature in such model can be represented as⁸:

$$T(z,t) = \frac{(1-R)}{\sqrt{\pi \cdot \eta_1}} \cdot \left\{ \sum_{n=0}^{\infty} M^{n+1} \cdot \int_0^t \frac{Q_0(t)}{\sqrt{t-\tau}} \cdot \exp \left[-\frac{(2nh+h-z)^2}{4a_1(t-\tau)} \right] d\tau + \right. \quad (3)$$

$$\left. + \sum_{n=0}^{\infty} M^n \cdot \int_0^t \frac{Q_0(t)}{\sqrt{t-\tau}} \cdot \exp \left[-\frac{(2nh+h+z)^2}{4a_1(t-\tau)} \right] d\tau \right\}, \quad M = \frac{1-K}{1+K}, \quad K = \frac{\eta_2}{\eta_1}$$

Here index 1 concerns to a slice, and index 2 - to a semi-infinite body (substrate), $Q_0(t)$ - an energy density of an incident radiation, R - reflection coefficient of a VO₂-mirror at $T > 70^\circ\text{C}$, H - thickness of a slice.

From this model the maximum temperature (T_{\max}) was defined which is achieved in interference system of a mirror to an end of laser pulse at energy densities of a radiation appropriate to a damage thresholds obtained in experiments, and also in experiments on action of radiation at 10-micron spectral range. The average magnitude T_{\max} is approximately 600°C . An exception are the cases of VO₂-mirrors on Ge and Al substrates for which at $\tau_p = 50 \mu\text{s}$ T_{\max} have smaller values.

Fig.2 shows the calculated damage thresholds of VO₂-mirrors by a single pulse laser radiation for $\lambda = 3.6-4.2 \mu\text{s}$. At calculation it was stated, that temperature appropriate to a damage threshold is 600°C . From the Figure it is evident, that for VO₂-mirrors on substrates with a low thermal conductivity (quartz glass) the calculated results are well agreed with experimental data. For VO₂-mirrors on substrates with a high thermal conductivity (germanium) at $\tau_p = 50 \mu\text{s}$ calculated results of damage threshold approximately twice exceed experimentally measured. One of the reasons of such divergence can be that at $Q_0 > 20 \text{ J/cm}^2$ the damage threshold depends on uncontrollable contamination of a surface of a mirror (particles of a dust, thin film of an atmospheric moisture etc.), possessing the increased absorption and lowering a damage threshold.

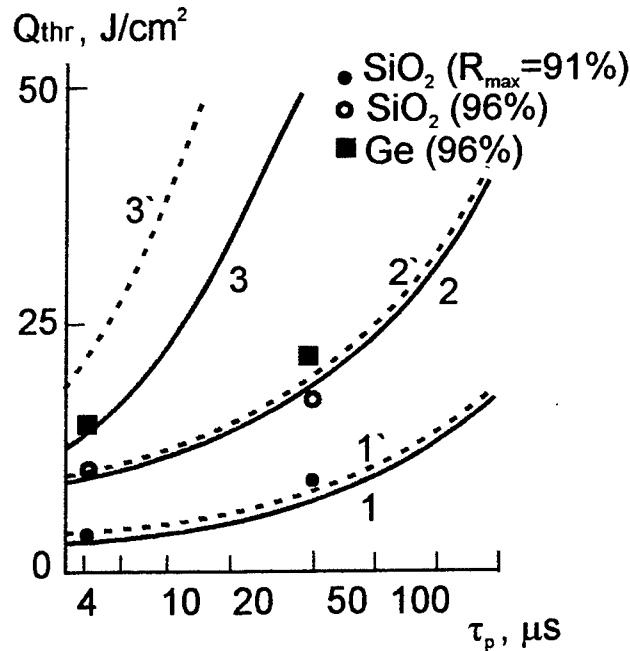


Fig.2. The influence of pulse duration on damage threshold of VO₂-mirrors. 1, 1' - quartz glass substrate, R_{max} = 91 %; 2, 2' - quartz glass substrate, R_{max} = 96 %; 3, 3' - germanium substrate, R_{max} = 96%. Dashed curves - calculation without taking into account of temperature influence on parameters of materials.

On Fig.2 for a comparison the calculated results also are shown without taking into account of a temperature modification thermal parameters of layers of a mirror (dashed curves). It follows from Figure, that this factor poorly influences on the results of calculations for a mirror on a substrate with a low thermal conductivity, but it appears essential in case of a high thermal conductivity of a substrate. The reason it is that in the first case the influence of a substrate on the temperature of an interference system is not enough and modification of a thermal conductivity of layers reduces only in redistribution of heat in layers. In the second case the heat release into a substrate becomes the essential factor, and the effectiveness of a heat rejection is determined not only thermal conductivity of a substrate, but also thermal conductivity of interference layers.

At pulse - periodic condition of action in characteristics of radiation stability of VO₂-mirrors enters not only damage threshold, but also the stability of modulation characteristics from pulse to pulse. So, at high intensities and pulse-repetition frequency, the efficiency of heat release from interference layers in a substrate can appear insufficient, therefore to a moment of arrival of the next pulse, the temperature of a VO₂ film will exceed temperature of a beginning of phase transition, that will be exhibited in a diminution of modulation of a reflection coefficient. Moreover, at rather high repetition frequencies the temperature of a VO₂ film, to a moment of arrival of the next pulse, can exceed temperature of completion of phase transition (T = 70°C), that will reduce in full vanishing of modulation. (This effect is reversible, as after an extinction of radiation action radiation and cooling of a mirror the modulation is restored.) In this connection it is necessary to determine conditions, at which the loss by a VO₂-mirror of modulating properties can be minimized or is eliminated.

At the analysis of pulse - periodic action of a radiation on VO₂-mirrors, two basic parameters describing the result of this action can be used. At first, pulse temperature of a surface of a mirror at the end of *i*-th pulse of a radiation - Tⁱ_{max}. This temperature characterizes maximum temperature of a mirror and determines maximum admissible power and temporal parameters of a radiation, setting their upper bound - damage threshold. Secondly, the pulse temperature of a surface of a mirror before the beginning *i*-th pulse of a radiation - Tⁱ_{min}. This temperature characterizes minimum temperature and sets the second upper bound of admissible power and temporal parameters of a radiation - from a point of view of a range of a modification of a reflection coefficient of a mirror at it switching.

At duration of pulse - periodic action exceeding the part of second, the thermal model of a mirror should take into account a thickness it of a substrate and heat exchange with an environment. Therefore, during radiation pulse the simulation was carried out on the considered above model (see expression (3)), and in gaps between pulses the model of a homogeneous slice having parameters of a substrate was used.

Within the framework of such a model the modification of temperature of a mirror in a point z ($0 < z < l$) after pulse can be represented as⁹:

$$T(t,z) = 2 \sum_{n=1}^{\infty} \exp(-a\zeta_n^2 t) \cdot \frac{(\zeta_n^2 + g^2) \cdot \cos(\zeta_n z)}{(\zeta_n^2 + g^2) \cdot l + g} \cdot \int_0^l T(0,u) \cdot \cos(\zeta_n u) du \quad (4)$$

Here $T(0, u)$ - distribution of temperature in a substrate at the moment of a termination of action pulse, $g = a/H$, H - factor of heat exchange depending on properties of a cooling medium, l - thickness of a substrate, a - temperature conductivity of a substrate, $(\zeta_n - n$ -th solution of an equation $\zeta_n \operatorname{tg}(\zeta_n l) - 1/h = 0$). The characteristic temperatures T_{\max}^i and T_{\min}^i are determined by expressions:

$$T_{\max}^i = \sum_{m=1}^i T_m + T^* \quad , \quad T_{\min}^i = \sum_{m=1}^i T_m \quad (5)$$

Here T_m - the temperature assigned to expression (4) for $z = 0$ and t , equal to the interval between m -th and i -th pulses ($1 < m < i$), T^* - temperature of a surface of a mirror in an extremity of action of a single radiation pulse.

Fig.3a shows the calculated temperature via time of radiation action for a VO_2 -mirror ($dR/dT > 0$) on a Ge substrate (cooling by air) for pulse - periodic action of a radiation with $\tau_p = 1 \mu\text{s}$, $t = 5 \text{ s}$ and $f = 1 \text{ kHz}$. On the Figure it is shown, that at energy densities of a radiation in each pulse $Q_0 = 0.5 \text{ J/cm}^2$ during action maximum temperature does not reach the magnitude appropriate to a damage threshold. At the same time, T_{\min} becomes more than 70°C already through 1.5 s after the beginning of the action, that indicates the full extinction of modulation of a radiation by a mirror. The calculations show, that for cooling of a VO_2 -mirror by air and fixed magnitudes of τ_p and t the optimization of a radiation load on a mirror is possible at the expense of a variation of magnitudes Q_0 and f , permitting to eliminate the reach of damage threshold and, at the same time, to ensure a conditions of maximum modulation during all time of action. However, for high pulse-repetition frequencies ($f \geq 1 \text{ kHz}$) the optimum energy densities of a radiation thus do not exceed 5 mJ/cm^2 .

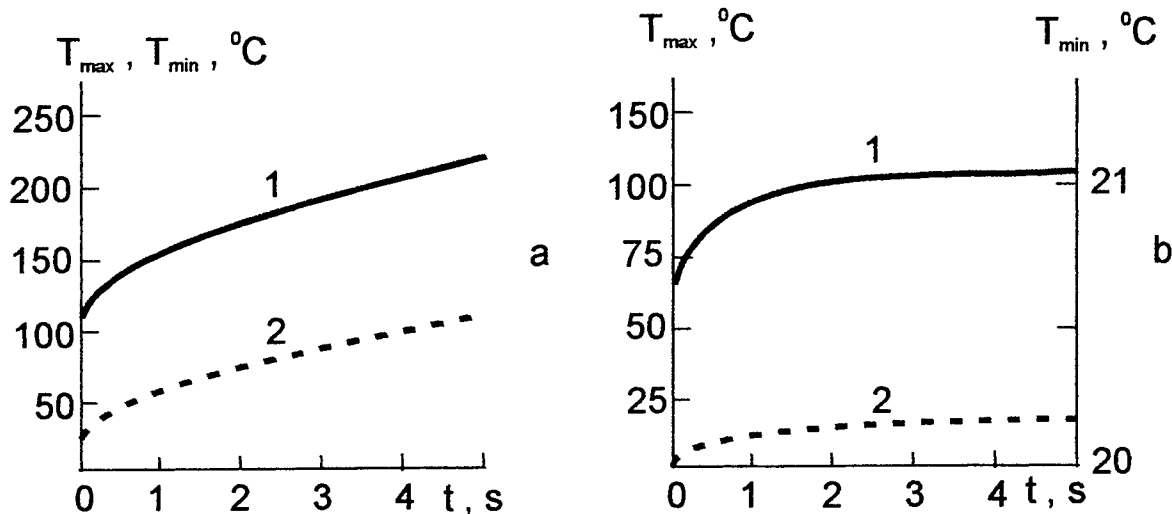


Fig.3. The change of temperature of a VO_2 -mirror surface in pulse - periodic action conditions and cooling: by air (a) and by water (b). $\tau_p = 1 \mu\text{s}$, $f = 1 \text{ kHz}$, $Q_0 = 0.5 \text{ J/cm}^2$, $l = 10 \text{ mm}$. a - Ge substrate, b - Cu substrate. 1 - T_{\max} , 2 - T_{\min} .

Fig.3b shows the time dependent T_{\max} and T_{\min} for a VO_2 -mirror ($dR/dT > 0$) on a copper substrate with forced cooling by water for $\tau_p = 1 \mu\text{s}$, $f = 1 \text{ kHz}$ and $Q_0 = 0.5 \text{ J/cm}^2$. It follows from the Figure, that the fast modification of temperature of a mirror surface happens only on an initial stage of action, and at $t > 0.3 \text{ s}$ temperature varies very slowly. As for the given condition of mirror cooling the magnitude T_{\min} poorly depends on time of action, the magnitude of a damage threshold will be approximately equal to magnitude of a damage threshold for a mono pulse condition of action. The difference between temperature T_{\min} and temperature of cooling fluid, in this case, is determined by a thickness and thermal conductivity of a substrate and in a considered example is $\sim 0.2^\circ\text{C}$. The calculation shows, that for the considered conditions of action the energy density of a radiation, at which the maximum modulation is saved, can be increased up to $1-1.5 \text{ J/cm}^2$.

4. CONCLUSION

The represented results show, that for VO₂-mirrors intended for mid IR-region, in the pulse - periodic (at duration of a radiation exceeding 0.5 μs) and continuous conditions, the mechanism of destruction of mirrors by a radiation has mainly thermal character. The damage threshold of mirrors by a radiation can exceed 3 kW/cm², that allows to use such mirrors for radiation control of high-power lasers, and also in limiters of intensity of a laser radiation. Further magnification of damage threshold can be possible at the expense of use highly pure materials for manufacture of mirrors, choice of materials with a minimum difference of coefficients of thermal expansion and diminution of a thickness of an interference system of a mirror. Interference systems with a small amount of layers described in¹ in the latter case can be used.

5. ACKNOWLEDGEMENTS

This work was supported by DERA (United Kingdom).

6. REFERENCES

1. O.P.Konovalova, A.I.Sidorov, I.I.Shaganov, "Interference systems of controlled mirrors on base of vanadium dioxide for a spectral range 0,6-10,6 μm", *J.Opt.Techn.* **66**, N 5, 13-21, 1999.
2. A.A.Bugaev, B.P.Zacharchenia, F.A.Chudnovsky, *Phase transition metal - semiconductor and its application*, 183 p., Nauka, Leningrad, 1979.
3. A.B.Welch, B.Burzlaff, W.Cunningham, "Electronically scanned coherent CO₂ laser radar techniques", *Proc. SPIE*, **300**, 153-167, 1981.
4. O.B.Danilov, V.V.Danilov, A.I.Sidorov et al, "Intracavity wide-angle beaming in mid-IR gas lasers", *Conf. Photonics West.*, USA, San-Jose., 1998.
5. A.I.Sidorov, E.N.Sosnov, "Shaping of leading edge of generation pulse in the laser with a VO₂-mirror", *Quantum Electronics*, **25**, N 6, 522-525, 1998.
6. O.B.Danilov, V.P.Belousov, I.M.Belousova et al, "Nonlinear optical limiters of laser radiation on base of reverse saturable absorption and stimulated reflection", *Conf. Photonics West.* USA, San-Jose., 1998.
7. M.Mansuripur, G.A.N.Connel., J.W.Goodman., "Laser induced local heating of multilayers", *Appl. Opt.*, **21**, N6, 1106-1114, 1982.
8. B.A.Grigoriev *Pulse heating by radiations.* Science, Moskow, v.2, 727 p., 1974.
9. H.S.Carlsaw, J.S.Jaeger *Conduction of heat in solids*, Clarendon Press, Oxford, 487 p., 1959.

EFFICIENT INTRACAVITY FREQUENCY DOUBLING OF CO₂ LASER IN NONLINEAR CRYSTALS

Vladimir O. Petukhov^a, Vadim A. Gorobets^a, Sergei Ya. Tochitsky^a, Konstantin V. Kozlov^b

^aB.I. Stepanov Institute of Physics, NASB, Scaryna Ave.68, 220072, Minsk, Belarus

^bJoint Stock Company "Peleng", Makayonok Str. 23, 220032, Minsk, Belarus

ABSTRACT

Several original schemes for intracavity frequency doubling of CO₂ laser radiation (TEA and cw systems) in AgGaSe₂ nonlinear crystals have been proposed and studied experimentally. Computer modeling was used for optimization of the optical schemes and cavity parameters. The enhancement by several fold in conversion efficiency was achieved for intracavity SHG in comparison with traditional schemes. A 60% peak power efficiency and 15% energy conversion efficiency has been obtained with a TEA CO₂ laser. More than 100 mW at 5 μm was generated in the crystal with $L=17$ mm, which is a record output for SHG of a cw CO₂ laser. This output is more than 10 times higher than 5 μm power measured with standard focusing the CO₂ laser beam.

Keywords: CO₂ laser, efficient intracavity frequency doubling, nonlinear crystals.

1. INTRODUCTION

Second Harmonic Generation (SHG) in nonlinear materials is an important process for the extension of the wavelength range accessible with available laser sources because of its simple, reliable application. It is widely used in different spectral ranges. In the 4-5 μm spectral range a frequency-doubled CO₂ laser has the potential for providing an optimum combination of spectral control and frequency stability. AgGaSe₂ is an efficient nonlinear material for phase matching frequency conversion of a CO₂ laser. However, in spite of efficient SHG reported for high-peak power CO₂ laser pulses in AgGaSe₂, for continuous-wave (cw) CO₂ lasers the output is too low for real applications. Resonance enhancement is a powerful means to improve the frequency-doubling efficiency if sufficient laser power is not available. It can be realized either by placing a crystal inside of the laser cavity. This method puts forward very strict requirements on both the nonlinear crystal and the laser. For example, it is necessary to eliminate Fresnel losses introduced by the crystal and to optimize the harmonic output coupling. Especially important is to use a nonlinear crystal of high optical quality in which residual absorption is minimized. In this paper results on the optimization of output power at 5 μm using different schemes are presented.

2. OPTICAL PROPERTIES OF AgGaSe₂ CRYSTALS

The AgGaSe₂ crystals examined here are two samples, 10x12x14 mm³ and 3.5x8x17 mm³. These crystals were grown in the Institute of Solid State and Semiconductors of the National Academy of Sciences of Belarus by Dr. V.N. Jakimovich¹. They were cut at an angle $\theta=55^\circ$ ($\varphi=45^\circ$) to the *c* axis corresponding to phase matching at 10.6 μm. All the samples were subjected to mechanical polishing; no antireflection coatings were deposited. Characterization of low-absorption AgGaSe₂ crystals is a quite complicated issue in relatively short samples. Infrared transmission measurements in the 2-12 μm region using spectrophotometers do not give conclusive results. For accurate evaluation, direct measurements of the absorption coefficients were undertaken based on the transmission of a focussed CO₂ laser beam after allowance for the Fresnel reflection. Another important issue that powerful, focused laser probe beam could bring multiphoton absorption to light. A stabilized, computer tunable cw CO₂ laser was used for these measurements. The laser beam was attenuated from ~5 W to 100 mW and focussed on the crystal. A calorimeter power meter measured transmitted radiation. The crystal was mounted on a specially designed optical table that allowed fast, backlash-free translation of the sample in and out of the laser beam. An interleaving procedure was adopted recording the laser power alternately with and without crystal. To avoid systematic problems, and to have some estimate of inherent random fluctuations, we made many such cycles and averaged data. The measured value of transmission exhibited error of 0.5 %. After allowance for the Fresnel reflection the estimated total experimental uncertainty in α_ω determination was 0.003 cm⁻¹. The absorption coefficients for ordinary polarization in the 9.2-10.8 μm range are found to be 0.006±0.003 cm⁻¹ for the second sample. The first sample has absorption factor 0.02±0.003 cm⁻¹. In addition careful mapping of a cross section of the crystals absorption was performed. The samples through the cross section had a high optical homogeneity.

3. EXPERIMENTAL STUDY OF DIFFERENT SCHEMES OF SHG WITH A TEA CO₂ LASER

A detailed study on frequency doubling of a TEA CO₂ laser with AgGaSe₂ crystal using traditional external focussing and intracavity schemes was carried out. It is known, that in the case of high power 10 μm laser pulses, the SHG efficiency is limited by the surface damage threshold of a crystal. Two schemes enhancing the SHG efficiency in nonlinear crystals were studied experimentally. First, the intracavity frequency doubling, for which the efficient interaction length is larger, was tested. Such a scheme was previously tested with Tl₃AsSe₃ crystals². Second a scheme using a nonlinear output coupler made of AgGaSe₂ was studied. This new technique for SHG was first proposed by us and proof-of-principle experiments were reported earlier³.

Figure 1 (a) shows a schematic diagram of the experimental set up and an external scheme of SHG. Two optical schemes used for intracavity SHG of CO₂ laser radiation are presented in figures 1 (b) and 1 (c). A 70 cm x 3 cm x 2 cm, UV preionized TEA CO₂ laser was used⁴. The cavity was formed by a rear curved mirror ($r=2.5$ m) and an output coupler. The cavity length was 1.25 m. To control mode quality and the radiation flux in the cavity, an iris was placed just before the output coupler. Energy for both the pump and the second harmonic was recorded by an IKT-1N calorimeter. Fast detectors either a FPU-500 photon drug detector or a cryogenically cooled FSG-22A photoresistor were utilized to measure the peak power and the pulse shape. Temporal resolution of a detector-digital scope detection chain was better than 25 ns. A 15-mm LiF filter blocked the CO₂ laser radiation.

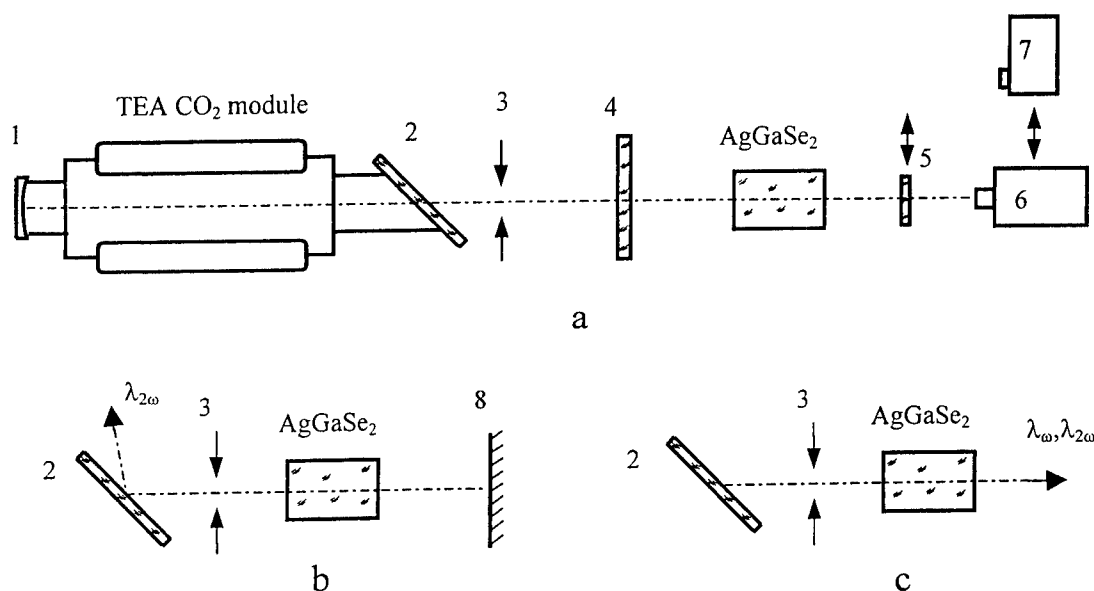


Fig. 1. Experimental arrangement of the components in the TEA CO₂ laser optical resonator: base-made laser system setup (a) and variations of optical resonator schemes (b, c).

1- nontransmitting mirror ($R=2.5$ m); 2- ZnSe Brewster window; 3- diaphragm (\varnothing 8 mm); 4- output mirror (Ge etalon); 5- LiF plate; 6- IKT-1N calorimeter; 7- Ge:Au photodetector; 8- reflector mirror ($R=\infty$).

The AgGaSe₂ crystal examined here is a 14-mm long sample with a 12-mm x 10-mm aperture. The parallelism of working optical surfaces was better than 20".

When the TEA CO₂ laser was filled with a gas mixture CO₂:N₂:He=1:1:6, a Ge etalon (reflectivity ~ 75%) was utilized as an output coupler and the output energy reached ~ 1 J. The laser oscillated on the 10P(20) line. The beam diameter was approximately 7 mm with a homogeneous spatial distribution of energy providing the fluence of 2.6 J/cm². Typical traces observed for the 10 μm and 5 μm pulses with an external focusing scheme are shown in fig. 2a and 2b, respectively. For these measurements radiation was attenuated to the level of 2 J/cm² providing conditions for use of the crystal without any damage. Note that the surface damage threshold for AgGaSe₂ is 2.7 J/cm²⁵. The peak power conversion efficiency was ~15% and the energy conversion efficiency – 2%. Analysis of temporal dynamics of the 10 μm and 5 μm pulses showed that the pump pulse profile is not optimal for nonlinear frequency conversion. Low intensity tail of the CO₂ pulse practically does not contribute in SHG. That is why we optimized gas mixture in the laser for SHG and decreased N₂ contamination in the mixture. Fig. 3a and 3b show the 10 μm pulse and the 5 μm pulse, correspondingly after optimization. At these conditions- gas mixture CO₂:N₂:He=7:1:25, discharge voltage of 24 kV- up to 6.5 mJ of energy was recorded for

the 5 μm pulse. It is important that energy fluence for this mixture was 1.5 times less than for the ordinary mixture without any change of the SHG efficiency.

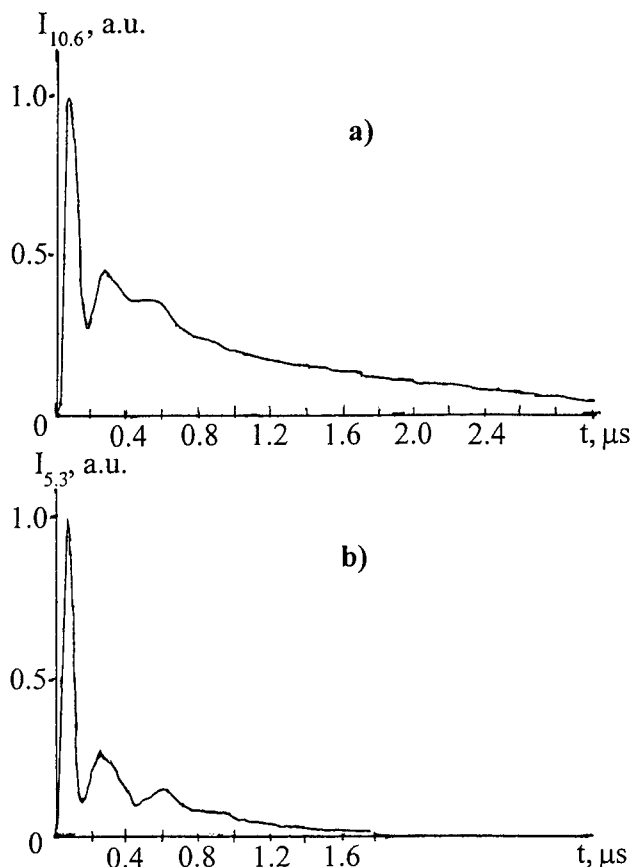


Fig. 2. Typical pulses of 10 μm (a) and 5 μm (b) when gas mixture was $\text{CO}_2:\text{N}_2:\text{He} = 1:1:6$.

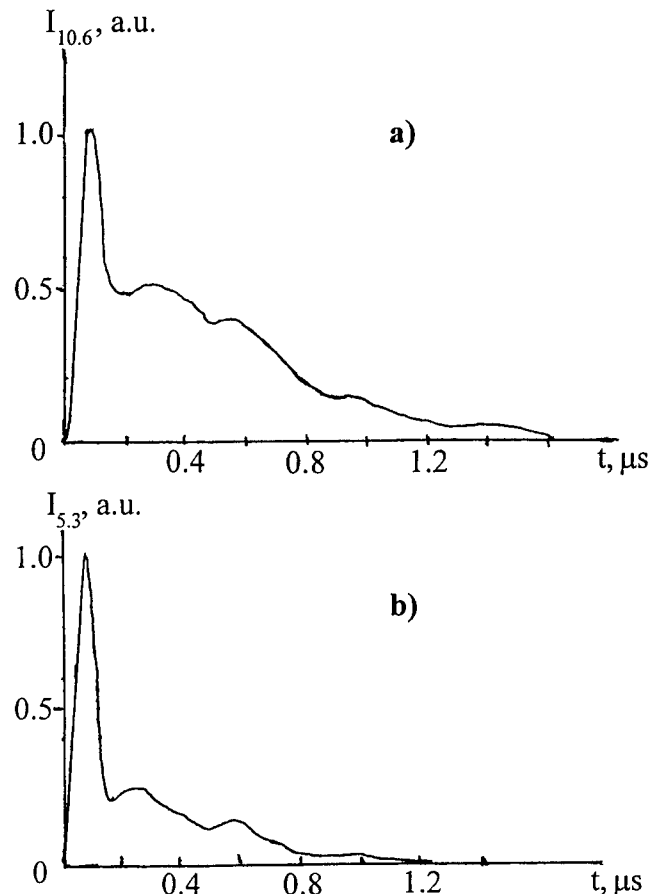


Fig. 3. Typical pulses of 10 μm (a) and 5 μm (b) when gas mixture was $\text{CO}_2:\text{N}_2:\text{He} = 7:1:25$.

Intracavity SHG (see fig. 1b) allowed to increase the harmonic output to 13.5 mJ. This output was obtained at the incident fluence approximately equal to the fluence for the external frequency conversion. It was achieved by placing a multilayer attenuator made of plastic film inside the cavity. The observed gain in the SHG efficiency is attributed with a double pass through the crystal. A s-polarized 5 μm beam was coupled through a Brewster window of the TEA CO_2 module. It should be noted that the coupling efficiency in our case was $\sim 60\%$ and part of 5 μm radiation is trapped in the cavity. If we assume that all 5 μm radiation is extracted from the cavity (a Ge Brewster window could provide the coupling efficiency of 90%), then up to 22 mJ of the second harmonic could be generated.

The most efficient SHG was obtained in a nonlinear output coupler made of AgGaSe_2 . Since nonlinear optical materials in the mid-IR region (AgGaSe_2 , ZnGeP_2) have high refractive indices, it is possible to use a nonlinear element simultaneously as an optimal output coupler and a frequency converter. For this configuration (see fig. 1 c) 52 mJ of energy at 5 μm was measured. At the same time the CO_2 laser produced 370 mJ of 10 μm radiation. If we define the external SHG efficiency in a usual manner as a ratio between energies or powers of the second harmonic and the fundamental radiation, then the energy conversion efficiency reached 15% and the peak power conversion efficiency – 60 %.

Thus, intracavity SHG is an efficient tool to enhance conversion efficiency of a TEA CO_2 laser. Especially promising in terms of the SHG efficiency is a novel technique using an output coupler made of nonlinear optical material. At comparable level of the pump pulse the conversion efficiency in the nonlinear output coupler is several times higher than for traditional external and intracavity SHG schemes.

4. INTRACAVITY SHG OF A CW CO_2 LASER RADIATION

We tested several different configurations for intracavity SHG in AgGaSe_2 . All experiments were performed with a sealed-off cw CO_2 laser⁶ with an active length 1.2 m. The laser oscillated on the 10P(20) line and produced up to 8 W in

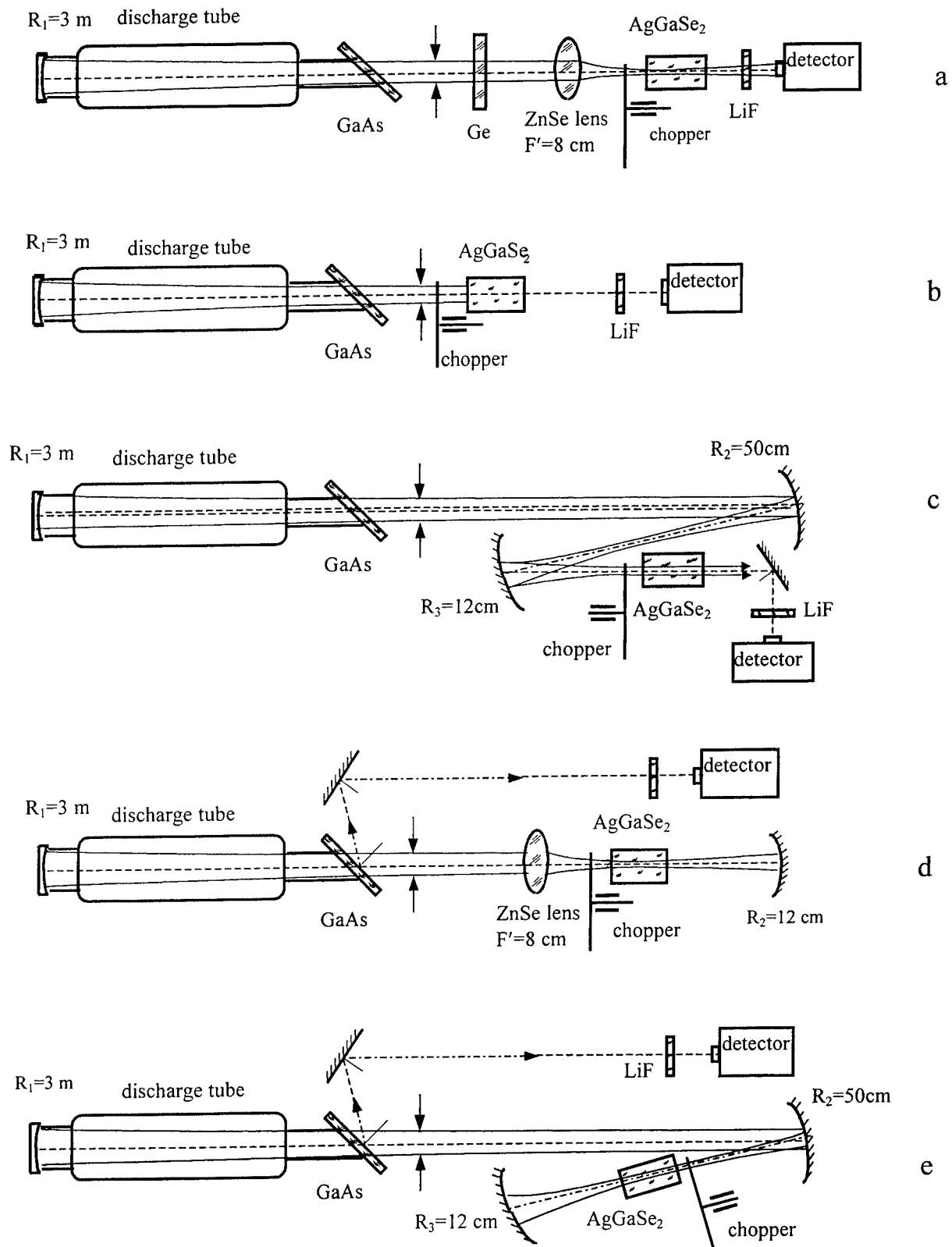


Fig. 4. Experimental arrangement of the components in the cw CO₂ laser system.

TEMoo mode. We utilized the 17 mm AgGaSe₂ crystal for SHG. The crystal was manufactured with a parallelism better than 4". This made it possible to practically use the nonlinear element as a Fabri-Perot etalon.

First, SHG was obtained using the AgGaSe₂ crystal as a nonlinear output coupler of the CO₂ laser (Fig. 4 b). This technique was successfully applied earlier for a high-power TEA CO₂ laser but its potential is not studied for a low-power cw laser. By replacing an output coupler of the laser with the nonlinear crystal, we were able to convert frequency to the second harmonic. The microwatt level of 5 μm power was measured when the beam diameter on the crystal was approximately 8 mm. Another factor, additionally to low-power pump, limiting the SHG efficiency in our experiment, is connected with the mismatch between the cut angle of the crystal and the 10P(20) line. Experimentally, we found that the optimal wavelength for SHG at normal incidence in the sample was 10.61 μm (the 10P(22) line). To increase the SHG efficiency, we modified the CO₂ laser cavity. A mirror telescope was placed in the cavity (fig. 4 c) to decrease the diameter of beam size on the crystal and, therefore, to increase pump intensity. An OPAL-PC (developed by SOI, St. Petersburg) computer program was used to optimize the radius of curvature for two mirrors, while maintaining the small spot size in a collimated beam (telescope worked as a beam compressor). At the beam diameter of $2w_0 \approx 0.9$ mm, the measured output was 1-1.5 W and 1-2 mW at 10 μm and 5 μm, respectively. This corresponds to a rather high efficiency of SHG for a relatively low-power cw CO₂ laser beam. Careful optimization of the laser parameters (the discharge current, active medium composition, etc) would result in up to 1% efficiency of SHG for this promising scheme.

Kilohertz amplitude-modulated signals in mid-IR are needed for spectroscopic applications. To this end, we demonstrated the first acousto-optic modulation of light in a AgGaSe₂ nonlinear crystal. Piezoceramic plates made of CTS-19 were attached to the crystal sides, and a sinusoidal signal with frequency from 10-200 kHz was used to power the modulator. The nonlinear crystal served three purposes: output coupler, nonlinear frequency converter, and AO modulator. Preliminary results showed that acoustic modulation is efficient despite the small dimensions of the crystal. We observed 100 % modulation of both 10 μm and 5 μm radiation in the range of modulation frequency of 10-60 kHz. The SHG efficiency increased several times because of higher peak power of pump radiation. Note that nonlinear dynamics of this system is interesting to study, since a transition to period doubling of the laser output was observed around the modulation frequency of 40 kHz.

The best results on intracavity SHG in AgGaSe₂ (Fig. 4 d and 4 e) were demonstrated in a two-mirror cavity. An optical scheme of this configuration is presented below (Fig.4 a). Here the nonlinear element was placed normally to the cavity axis in the focus of an intracavity lens. A s-polarized 5 μm beam was coupled through a GaAs Brewster window and recorded by a detector. Estimations showed that intensities close to 100 kW/cm² could be reached at the focus. To prevent damage of AgGaSe₂ and formation of thermal lenses, an intracavity chopper with 3% duty cycle was mounted in front of the crystal. To avoid Q-switch regime, the chopper's slot was made 10 times larger than the beam diameter. More than 100 mW at 5 μm was generated in AgGaSe₂, which is a record output for SHG of a cw CO₂ laser. This output is more than 10 times higher than 5 μm power measured with standard focussing of the CO₂ laser beam (Fig.4 a).

5. ACKNOWLEDGEMENTS

We are grateful to Dr. V.N. Yakimovich for samples of crystals were given for this investigations. This work was partially supported by INTAS grant No 97-0515.

6. REFERENCES

1. V.O.Petukhov, V.A.Gorobets, S.Ya.Tochitsky, V.N.Jakimovich, V.I. Konstantinov, "Effective frequency conversion in nonlinear crystals for lasers of middle infrared range", *Proceedings of SPIE* (in press)
2. R.L. Pastel, "Intracavity doubling of a CO₂ TEA laser with thallium-arsenic-selenide crystal", *Applied Optics*, 26 (9), pp.1574-1576, 1987.
3. V.A.Gorobets, V.O.Petukhov, S.Ya.Tochitsky, V.V.Churakov, A.I.Fomin and V.N.Jakimovich, "CO₂ laser with frequency doubling in the nonlinear output mirror", *Proceedings of SPIE*, v. 2773, pp. 45-51, 1996.
4. V.A.Gorobets, V.O.Petukhov, S.Ya.Tochitsky, V.V.Churakov, "Transversely excited CO₂ lidar laser tunable over lines of regular and nontraditional bands", *Quantum Electronics* 25 (4), pp.489-493, 1995.
5. V.A.Gorobets, V.O.Petukhov, S.Ya.Tochitsky, V.V.Churakov, "Research of the nonlinear optical characteristics of IR crystals for frequency conversion of TEA CO₂ laser radiation", *Journal of Optical Technology*, 66 (1), pp. 62-67, 1999.
6. V.A.Gorobets, V.O.Petukhov, S.Ya.Tochitsky, V.V.Churakov. "Stabilized CW CO₂ (CO) laser with automatic tuning over oscillation lines for monitoring of air pollutants", *Proceedings of SPIE*, 2370, pp.640-644, 1995.

Stochastic and order phase structures in active medium flow of gas-dynamic laser

Valery O. Kovalevsky, Vitaly V. Lobachev*

The Institute of Laser Technique and Technology, Baltic State Technical University "VOENMEKH" named after D.F. Ustinov, 1, 1-st Krasnoarmeyskaya St., St.Petersburg 198005, Russia

ABSTRACT

Detail analysis of active medium flow structure is presented. Schlieren method photography of flow is processed to reconstruct parameters both stochastic and order phase components. Properties of random part including correlation function, spectrum of spatial frequency, scale of turbulence, are determined by digital filtering. It was possible to compare influence of random and regular phase distortions on radiation divergence structure.

Keywords: power spectral density; correlation function; directional radiation pattern; wave front order (regular, static) component; wave front stochastic (statistical, fluctuation) component.

1. INTRODUCTION

Lasers called forth appearance of different tasks related to radiation propagation through optically inhomogeneous mediums mostly because the latter significantly influence on quality of laser radiation. As a rule inhomogeneity is a perturbation of index of refraction of radiation medium due to variation of its density and/or composition. These perturbations result in the end in beam squinting, flicker effect, diffusion, angle of divergence enlargement and in other undesirable effects. In the aggregate this leads to intensity abatement of focused laser beam or of beam that is transported to long distances.

In this case one can consider not only heterogeneity that are situated on the laser beam way from exit aperture to target such as atmospheric turbulence or gas curtain that separate resonator cavity and exterior atmosphere, etc. Active medium (AM) fluctuations also should be taken into account. AM disturbances in gas flow lasers have the most considerable influence on beam quality due to diversity and complexity of processes leading to optical irregularity.

It is quite clear that gas-dynamic perturbations can be subdivided into regular (static, order) and stochastic (fluctuation) components, and actual field of phase disturbances corresponds to their superposition. Inasmuch as the former component corresponds to nonuniform distribution of average flow gas-dynamic parameters, it is consistent to assume that these distributions remain during laser generation. A result of such perturbations is radiation wave front (WF) transformation in laser exit aperture with all the undesirable consequences affecting beam haulage to target.

The second component corresponds to pulsating turbulent disturbances and has spatially irregular and, in general, time-varying character. This component being averaged in time that is comparable to generation time does not lead to serious distortion of WF, but is the origin of radiation spatial coherence losses and, in the end, of integral beam quality degradation.

Since there are obvious physical distinctions in the nature of above-mentioned gas-dynamic field components, one also has to expect essential difference in their influence on laser radiation parameters. Therefore, the models of their influence also will differ fundamentally. Thus, scalar diffraction theory is more common for modeling of light propagation with order phase field, whereas issues of optical waves coherence theory are needed for the description of effect of stochastic component.

It should be noted that the problem of air-optics as such was subject of comprehensive research in a number of treatises¹. But some of its aspects are still insufficiently examined due to their excessive complexity. And this may turn out to be substantial restriction in search of other ways of efficiency advancement of gas flow laser. That is why the goals of this paper are detail analysis of gas-dynamic field phase disturbances structures of GDL AM, revelation of nature of this disturbances and exposure of relations between basic structure components and also reliable prognosis of extent of disturbances influence on laser radiation integral quality that is estimated by directional characteristic.

2. FUNDAMENTALS AND METHOD OF INVESTIGATION

A set of restrictive hypotheses should be assumed in order to obtain detail information on local disturbances structure, especially statistical ones. This approach proves to be quite valid because analysis of dynamics of statistical assemblies appears to bring considerable difficulties even for numerical simulation. And test data as a rule have limited character that

* Correspondence: Email: office@iltt.spb.ru; Telephone: +007 (812) 2512162; Fax: +007 (812) 2512240

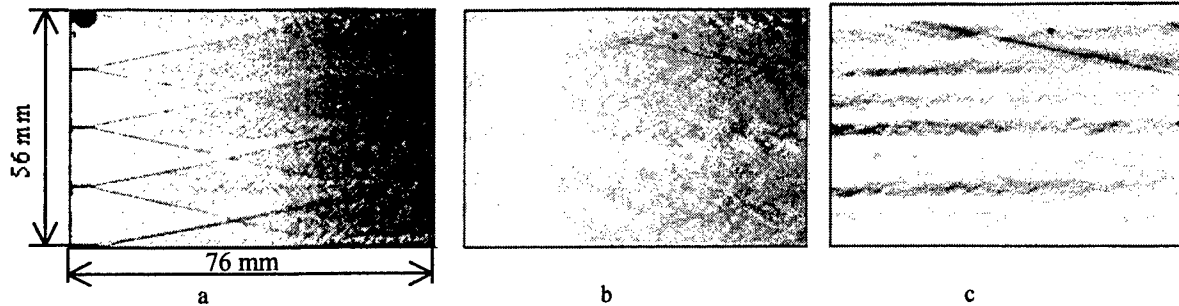


Fig. 1. Schlieren-pictures of AM flow (flow direction is horizontal from left to right); a,b – the optical knife is vertical, c – the optical knife is horizontal; a – near nozzle bank region, b,c – far wake gasdynamic field 160 mm distance from nozzle bank

does not allow to track simultaneously all the local relations of gas-dynamic field structure. The more traditional hypothesizes are the following:

1. Recorded signal consists of two components: order and random. The first component is reproduced from test to test, while the second one repeats oneself statistically with allowance for its ergodicity.
2. Examined gas flow has two-dimensional (flat) character since the screen of flat nozzles and the wind channel of a rectangular profile were used in experiment.
3. Random part statistical parameters vary slowly, consequently it can be assumed that the stochastic process is in wide sense spatially homogeneous on a bounded patch of wave surface.
4. By means of spatially averaging stochastic part of the signal with provision for its quasihomogeneity one can estimate averaged-out statistical characteristics as function of position along and across a flow.
5. Random process due to refraction (density) fluctuations induced by turbulence is considered spatially homogeneous and isotropic in flow orthogonal plane. This assumption permits to proceed to analysis of radiation parameters in the line perpendicular to nozzle slits.
6. Laser generation or gain time is supposed to be in orders of magnitude greater than characteristic temporal scales of turbulence and this dictates the necessity of application of coherence theory issues for modeling and analysis of the directional radiation pattern.
7. Contribution of order and stochastic components to distortion of initially flat WF propagated through gas flow can be considered separately. In which connection in case of order component geometrical optics approach is suitable but for the evaluation of diffusion conditioned by stochastic component small disturbance solution method of Maxwell's equations should be applied in order to take account of diffraction and flickering.

As one must obtain parameters of laser radiation that traversed through phase nonhomogeneous AM, it is expedient to use optical probing for measuring of such parameters. This method ensures integration of disturbances 3D-structure along optical path. In this case WF of probing beam in exit aperture bears information on integral along the way of probing structure of AM heterogeneity.

Technique of optical visualization of supersonic flow (Mach number ~ 5) should guarantee high spatio-temporal resolution and ability of adequate quantitative information restoration on distribution of WF local angles of slope or magnitudes proportional to phase incursion. One of the most convenient methods of noncontact optical probing of spatially multi-scale gas flow disturbances is schlieren method². Its field resolution is defined by the forming optical system, resolution dynamic range of the recording device. And temporal resolution in its turn is defined by pulse duration of probing radiation.

On Fig.1. you can see three schlieren pictures of gas flow behind the GDL nozzle screen design features of which are considered at large in³. It is only important to notice that in aperture sight there is supersonic flow with order structure of shock waves and wakes formed by three nozzle vanes. Schlieren pictures are distinguished by knife orientation relative to flow direction and also by the location of the probing beam aperture downstream. Air was used for lancing in experiments with the following deceleration parameters: pressure $P_0=25 \times 10^5$ Pa, temperature $T_0=300$ K. For schlieren picture acquisition spark source of achromatic light was used with the pulse duration $\sim 10^{-6}$ s.

It is known from the theory² that schlieren method in paraxial approximation of geometrical optics secures recording of the

intensity variation in every point of plane of observation that will be proportional to the WF angle of slope ε in the object plane orthogonal to knife edge.

$$\varepsilon = -\frac{2a}{f_1} \cdot \frac{I - I_0}{I_{00}}$$

Where I is intensity distribution in observation plane; I_0 is intensity distribution in observation plane without distortions introduced by object that is being investigated i.e. without it; I_{00} is intensity distribution in the observation plane without knife and object; $f_1=1600$ mm is main objective lens focal distance; $a=0,25$ mm is slit half-width. For high spatial resolution support over all the probing area ($\sim 76 \times 56$ mm) photometric fields registration was effected on special photographic film that was then digitized by high spatial resolution scanner.

It should be particularly noticed that schlieren pictures were taken in identical conditions but actually in different tests. That means that one can talk for certain about reproduction (with allowance for spatial affixment) of only order component of phase perturbation corresponding to averaged flow. But for the stochastic part of the signal conditioned by turbulent irregularity there are various member functions i.e. about these member functions one can talk in statistical sense.

Combined analysis of two records of wake far field (b) and (c) that differentiate by mutually orthogonal knife orientation in relation to flow direction is mostly interesting (take into consideration that left edge of both pictures was based on the distance of 160 mm from the nozzle screen). As namely on these two pictures there is reproducible disturbances order part we succeeded to part order and stochastic components i.e. completely reconstruct order component using two orthogonal WF angles of slope (ε_x and ε_y) and one-dimensional rows of cuts of stochastic component along and across a flow.

Let us consider technique of components isolation in more detail. For two schlieren being studied there can be written:

$$\varepsilon_x = \frac{dL_{reg}}{dx} + \frac{dL_{md}^I}{dx} = \varepsilon_{x-reg} + \varepsilon_{x-md}^I$$

$$\varepsilon_y = \frac{dL_{reg}}{dy} + \frac{dL_{md}^{II}}{dy} = \varepsilon_{y-reg} + \varepsilon_{y-md}^{II}$$

x and y indices are in accord with knife edge orientation orthogonal and parallel to gas flow; L – optical path difference, upper indices accentuate the fact of availability of two different member functions of the stochastic process associate with turbulence. Lower indices *reg* and *rnd* denote quantities related to regular and fluctuation components of recorded signal respectively. Hence it is obvious that isolation of order and fluctuation components should be performed in advance for WF deviations matrix (discrete representation of optical path differences field) recovery because otherwise WF gradient integrating cannot be performed correctly due to availability of different member functions of the stochastic component.

Random component overlay order one additively, hence application of linear filtration procedure is rational for components isolation⁴. Eventually the task comes to construction of linear transformation of angles-of-slope matrices that enables to depress (average) stochastic component and to preserve order component changeless. Invariant under shift (and equally effecting both components of the signal) filter can be used since for the far wake field within the aperture parameters of order component and statistical parameters of random component vary slowly.

Order part of disturbances in this area of gas flow is conditioned mainly by developed wake structure and featured by averaged profiles of flow gas-dynamic parameters. Due to their slight transformation downstream (in any case within limits of chosen aperture), significant simplification of digital filter is possible. Let us assume the numerical sequence that is determined as follows as pulse-response characteristic of our filter:

$$h(i, j) = \text{rect}\left(\frac{i}{nh}\right) \cdot \text{rect}\left(\frac{j}{mh}\right)$$

But even in this case estimation of nh and mh parameters by means of analyzing spectrum of input signal turns out to be extremely difficult due to considerable mutual penetration and overlapping of spectrums of fluctuation and order components.

Analysis of the signal for filter parameters estimation was effected only in spatial domain. First of all it should be noticed that space average as well as assembly average stochastic component a priori equals to zero. Hence maximum filter window sizes (along x and y axes) can be fitted at which order component still can be considered linear within the filter window and influence of fluctuation component would be reduced to null as a consequence of its complete averaging within limits of the

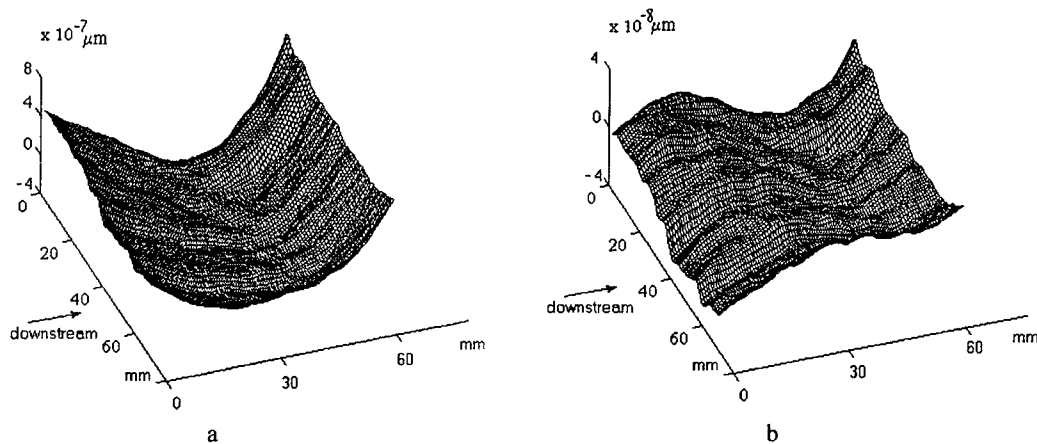


Fig.2. Regular component of WF distortion; a – original structure, b – without linear and spherical distortions

same window. Then for the central sample of such window one can get best estimate of magnitude of order distortion.

Search for nh and mh parameters was effected independently since filter is invariant under shift and separable. Choice of window size of optimal filter was based on window size dependence of certain criterion. Such criterion should feature at first quality of averaging of stochastic component inside the window and secondly degree of linearity of order component inside the same window. Local dispersion of window averaged along x -axis signal could be computed for each parallel to y -axis cut and assumed as such criterion (one can analogously calculate this dispersion for y window size). But as order component changes weakly within the limits of aperture, dispersion values computed all over the aperture were accepted as criterion.

Schlieren pictures (Fig.1.6.c) processing after component isolation showed up the fact that standard deviation of WF angles of slope ϵ of order component for longitudinal and transverse (to gas flow) WF gradients amount to 25 and 55 μrad respectively. And standard deviation of WF angles of slope of fluctuation component in the same directions amount to 19 and 9 μrad . Therefore decisive anisotropy of WF angles of slope occurs for these mutually orthogonal directions. In which connection standard deviation for transverse direction of order component is almost factor of two higher than standard deviation for longitudinal direction. And this is vice versa for fluctuation component. Its standard deviation for longitudinal direction is half as large again as for transverse direction.

One also cannot ignore the character of influence of shock waves that are one of constituents of regular structure. It is well known that gas-dynamic parameters including density (and therefore refraction) vary abruptly through shock wave. Presence of shock waves leads to extremely great WF gradients that result in impulse distortions on schlieren pictures (see Fig.1.a). Impulse distortions as it is known have continuous frequency spectrum that ranges from lowest to highest frequencies. That is why technique of signal component isolation being used is unable to isolate completely such impulse "hindrance". Although shock wave by its nature is an element of order structure.

As a result shock waves prove to be out of further detail analysis although this is not so great problem. Output beam shaping is used in the line of orthogonal to nozzle vanes direction for working elimination of influence of shock wave structure in AM flow. This method secures practically complete averaging of shock wave structure to an accuracy of wedge phase aberration. Besides AM GDL beam shaping can be effected in the range that is somewhat distant downstream from nozzle vanes where shock waves intensity becomes inappreciable and population inversion still retain acceptable level³. Though there are strong distortions caused by wakes in this area. This distortions determine level of AM optical quality.

Order component of WF corresponding to flow area on Fig.1.b,c is shown on Fig.2.a. It was recovered under combined schlieren pictures processing and filtration. Order component contains small wedge aberration apart from transverse periodic disturbances that are caused by wakes. Its nature is quite explainable by occurrence of intensive dissipative processes in the turbulent areas of gas flow causing flow deceleration and some accretion of density (refraction) background level. Since wedge aberration does not result in angular redistribution of laser beam energy, this constituent was eliminated out of further discussion.

More detail analysis showed that changing of density downstream is of nonlinear nature so long as WF of order component contains quadratic constituent that resembles two-dimensional lens (along a flow). This aberration impacts radiation divergence but does not disturb directional radiation pattern. Lens aberration compensation is also absolutely feasible by

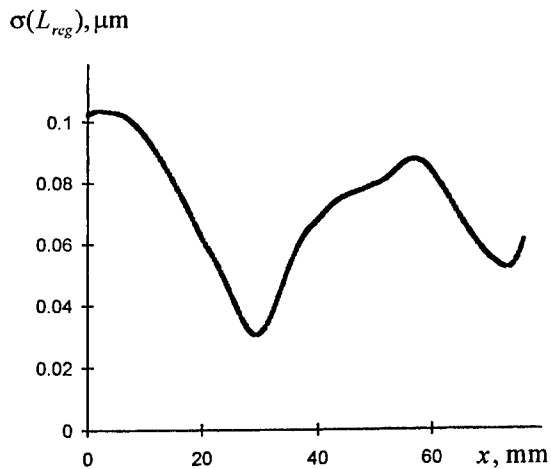


Fig.3. Dependence of root-mean-square of regular part phase aberration in transverse cuts on downstream distance

means of oversimplified methods.

Isometric of WF order component without wedge and lens constituents is displayed on Fig.2.b. This aberration through its heterogeneous structure directly impacts the level of radiation quality and structure of directional radiation pattern. Absolute phase differential) $\max(L_{reg}) - \min(L_{reg}) = 0,6 \mu\text{m}$, and WF root-mean-square deviation amounts to $\sigma(L_{reg}) = 0,1 \mu\text{m}$.

Structure of downstream alteration of root-mean-square deviation of WF order component (as function of longitudinal X -coordinate) for each cross is shown on Fig.3.

Let's now proceed to analysis of fluctuation component of optical path difference. As it was noticed formerly one can get information on WF stochastic component only for rows of one-dimensional cuts that are parallel or orthogonal to gas flow. Two-dimensional stochastic process behavior can be forecasted basing on statistical appraisal of each row. Root-mean-square deviation of random part of phase incursion in cuts is represented as function of cuts position in aperture for the cases of longitudinal and transverse gradients (see

Fig.4). One can see from these plots that dispersion level of stochastic component in transverse cuts slowly dropping downstream and in longitudinal cuts there is periodic increasing but no more than 30-40% in the areas of wake axes. This suggests that hypothesis of quasihomogeneity of stochastic component is quite valid. As a result estimates of mean values of root-mean-square deviation of WF stochastic component are obtained: $\sigma_x = 0,018 \mu\text{m}$ - for longitudinal cuts and $\sigma_y = 0,009 \mu\text{m}$ for transverse cuts. As for angles of slope differentials of WF, double difference in phase incursions for orthogonal gradients can be related to.

Now one can perform direct comparison of degree of influence of WF order and stochastic components. On the ground of found estimates root-mean-square deviation of order component is factor of 11 higher than deviation of random component for transverse cuts and factor of 5 higher than deviation of random component for longitudinal cuts! In other words there is significant difference in levels between regular and stochastic components and significant anisotropy of distortions in mutually orthogonal directions. Found estimates are of principle since different nature of regular and stochastic fluctuations implicates different methods of their compensation or correction.

At present one can consider characteristics of stationary stochastic process related to turbulent disturbances in more detail by

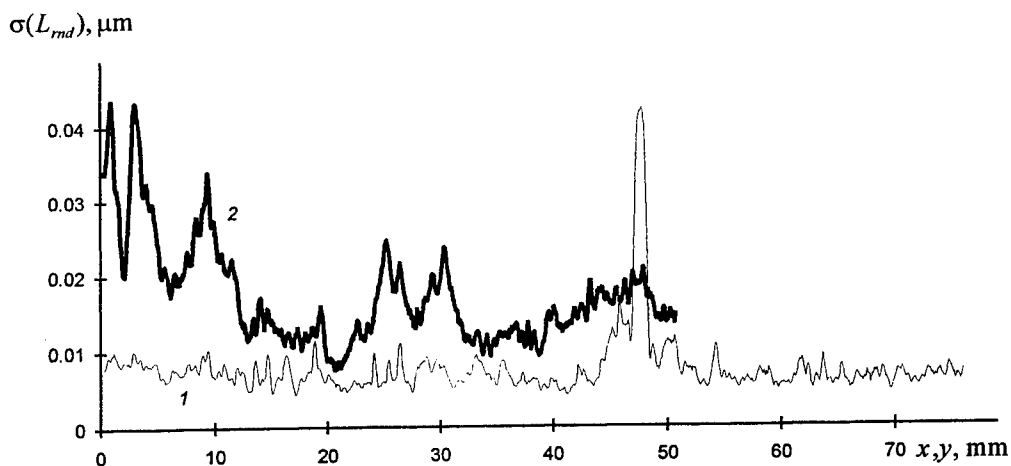


Fig.4. Dependence of root-mean-square of random part phase aberration in transverse - 1 and downstream - 2 cuts on downstream - x and transverse - y distances

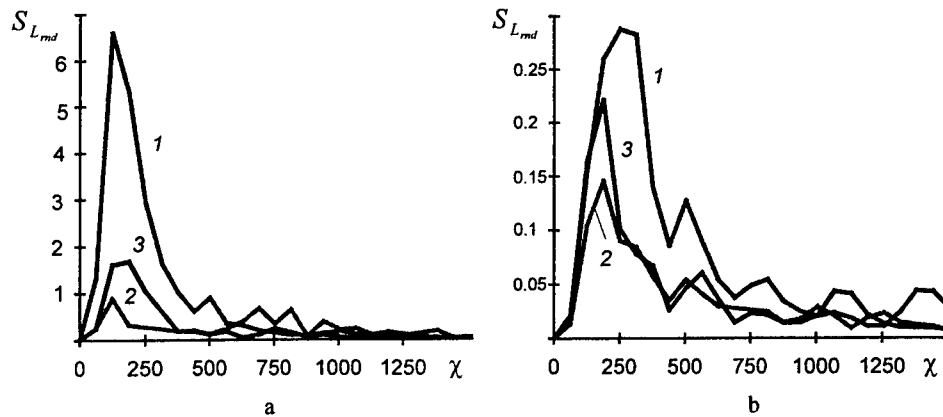


Fig.5. Spectrum of random component in few cuts for downstream (a) and transverse (b) directions; S_L in sign unit; $\chi=2\pi v$ - wavenumber m^{-1} ; 1,3 - boundary cuts, 2 - central cut

means of retrieval of its second-order statistics. These are power spectral density and correlation function. One-dimensional power spectral densities of WF fluctuations for directions in the line of x and y axes can be estimated for each cut. For numerical sequence of digitized WF power spectral density $S_{L_{rnd}}(\nu)$ is determined in the following discrete-spatial form⁴:

$$S_{L_{rnd}}(\nu) = \lim_{N \rightarrow \infty} E \left[\frac{R}{(2N+1)} \left| \frac{1}{R} \sum_{n=-N}^N L_{rnd}(n) \exp \left[-j \frac{2\pi\nu n}{R} \right] \right|^2 \right]$$

In this formula R is spatial resolution of digitized signal; N - number of samples; ν, m^{-1} - spatial frequency. With neglect of calculation operation of ensemble expectation and by taking finite number of samples N (i.e. we have data sequence $L_{rnd}(0), \dots, L_{rnd}(N-1)$), one can compute sample spectrum using finite data sequence:

$$\tilde{S}_{L_{rnd}}(\nu) = \frac{R}{N} \left| \sum_{n=0}^{N-1} L_{rnd}(n) \exp \left(-j \frac{2\pi\nu n}{R} \right) \right|^2,$$

This expression for sample spectrum is initial nonmodified form of so called periodogram estimate of power spectral density. It is simple to demonstrate, that sample spectrum $\tilde{S}_{L_{rnd}}(\nu)$ yields statistically invalid estimates of power spectral density since operation of ensemble expectation calculation was neglected. That is why ensemble pseudoaveraging should be used for graduation (smoothing) of periodogram. This can be done by means of technique analogous to Bartlett's method⁴.

Ensemble averaging is effected by means of sample spectrums averaging in the neighborhood of selected one with provision for quasihomogeneity of the stochastic process. Samples spectrums are computed by Fourier transform of WF cuts. It is reasonable to take for the sizes of averaging window the extents of filter window that was used for isolation of WF components. For assurance of statistically consistent estimate of power spectral density WF cuts should be statistically independent within the limits of averaging window. In our case this condition is met well mainly by reason of deficiency of information on second gradient of stochastic WF.

For degree of interdependence estimation of fluctuations in neighboring cuts maximum (for all frequencies) cross-correlation coefficient as function of distance between cuts was computed. It is found that longitudinal and transverse WF cuts that are 1 mm apart do not correlate. And with provision for Gaussian distribution of WF fluctuations these cuts are statistically independent. Since averaging window size tuned out to be factor of 6 higher than this distance power spectral density estimates found by means of averaging within the limits of such window can be considered statistically consistent. Power spectral density estimate for several longitudinal and transverse cuts is represented on Fig.5. Root-mean-square error of these estimates does not exceed 7% of estimated mean value in each cut.

It is easy to see that power spectral densities for transverse cuts differentiate each from other no more than at the value of root-mean-square error of estimate. This allows considering of gas flow as homogeneous in transverse direction all over the aperture. Power spectral densities of longitudinal cuts on the contrary significantly vary over the aperture because of transformation of wake turbulence downstream.

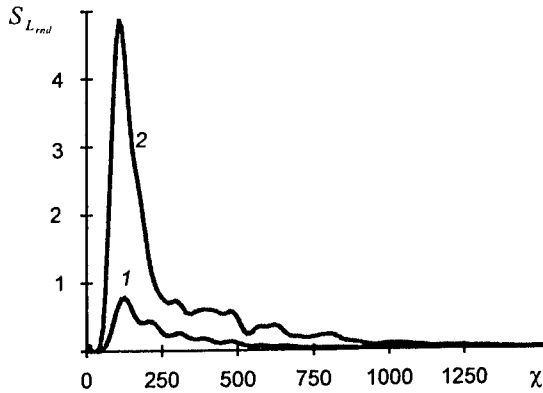


Fig.6. Mean aperture spectrum of random component; 1 - downstream direction, 2 - transverse direction, S_L in sign unit; χ - wavenumber m^{-1}

occurrence also cannot be explained by discreteness and finite frequency resolution because width of some modes significantly exceeds minimum size of frequency resolution cell of the digitized signal. While classical theory forecasts mode character of turbulence⁵.

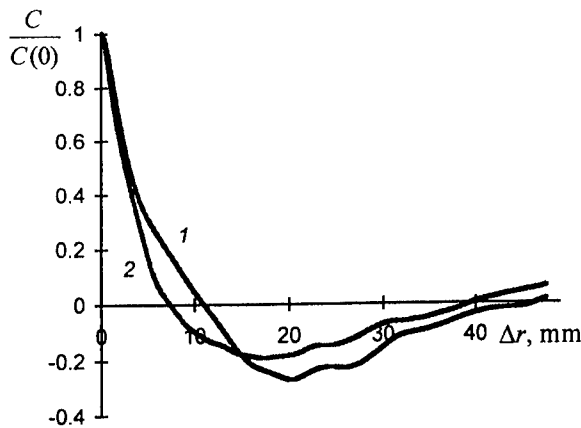


Fig.7. Mean aperture spatial correlation function of random component; 1 - downstream direction, 2 - transverse direction

However it was showed in paper¹ that even substantial inhomogeneity of parameters of stochastic WF within the aperture does not effect significantly far-field radiation characteristics as compared to homogeneous disturbance with the same dispersion. Therefore by spreading averaging window size to the limits of aperture one can compute space average power spectral density of WF fluctuations in the lines of X - and Y -directions. Aperture average power spectral densities of stochastic component and associate correlation functions for transverse and longitudinal directions are displayed on Fig.6 (power spectral density and correlation function are related by Wiener-Khinchin theorem through Fourier transform⁴).

It is obvious that average power spectral densities are not monotonic. A number of separate modes is distinctly seen towering over continuous spectrum. Their occurrence cannot be related to possible estimate error since spike magnitudes significantly exceed root-mean-square error of spectrum estimate. These modes

Space average autocorrelations $C(\rho)$ as functions of distance difference ρ along and across a flow are also displayed on Fig.7. Possessing of this data one can estimate integral scale of WF fluctuations that is surely correlated to integral scale of turbulent pulsation. Integral scale can be considered as parameter featuring correlation distance of WF stochastic component

$$\Lambda = \frac{\int_0^{\infty} C(\rho) d\rho}{C(0)}$$

As a result it was obtained that absolute integral scale amounts to $\Lambda_x=9,5$ mm along a flow and $\Lambda_y=7,1$ mm across a flow. It is curious that relative (i.e. related to aperture size) integral scales for both orthogonal directions amount to 0,13. Since integral scale in the line of gas flow turned out to be $\sim 1,3$ times greater than integral scale cross flow one can conclude that average turbulent eddy is oblong in the line of gas flow. The latter absolutely is in agreement with results of investigation⁵.

The most complex and most practically important as well is the question of ability of forecasting of laser radiation quality (or optical quality of AM) even if for single-pass laser amplifier for perpendicular to edges of nozzle vane direction. The ability of adequate transfer of obtained results to large-length in the line of amplification AM and ability of information recovery for working GDL wavelength is also important.

Since above considered results correspond to short propagation lengths in AM, phase screen approach is valid. For change to long propagation distances working wavelength mechanism of radiation interaction with randomly nonhomogeneous medium should be considered at large. This problem was discussed in much detail in⁶. Let us apply small disturbance solution method of Maxwell's equations with provision for Ritov transformation for electromagnetic field in random nonhomogeneous medium. This approach accounts for diffraction and flicker effect. There is relation between power spectral density of index of refraction $\Phi(\chi_3)$ and power spectral density of WF phase fluctuations $S(\chi, l)$, in which connection the latter represents recorded signal and can be expressed by the formula:

$$S(\chi, l) = \pi k^2 \left[1 + \frac{k}{l \cdot \chi^2} \sin\left(\frac{l \cdot \chi^2}{k}\right) \right] \cdot \Phi(\chi_3),$$

$\chi = \sqrt{\chi_x^2 + \chi_y^2} = \sqrt{(2\pi v_x)^2 + (2\pi v_y)^2}$ is a cyclic frequency of WF disturbances in aperture plane; $\chi_3 = \sqrt{\chi_x^2 + \chi_y^2 + \chi_z^2}$ – spatial cyclic frequency of index of refraction disturbances; l – propagation length in AM. k – radiation wave number (e.g. wave number of probing beam). On the other hand power spectral density $S(\chi, l)$ is estimated under the assumption of separation of variables for given propagation length l

$$S(\chi_x, \chi_y, l) = \frac{S_x(\chi_x) \cdot S_y(\chi_y)}{\sqrt{\sigma_x^2 \cdot \sigma_y^2}}$$

$\sigma^2 = \int_{-\infty}^{\infty} S(v) dv$ is estimate of dispersion of WF stochastic component (it was obtained above for x and y directions).

Aggregation of last two equations enables estimation of effect of random nonhomogeneous index of refraction field as new power spectral density $S_{new}(v_x, v_y, l_{new})$ for either propagation length l_{new} and for either radiation wavelength featured by wave number k_{new}

$$S_{new}(\chi, l_{new}) = \frac{k_{new}^2 l_{new}}{2k^2 l} \left[1 + \frac{k_{new}}{\chi^2 l_{new}} \sin\left(\frac{\chi^2 l_{new}}{k_{new}}\right) \right] S(\chi, l)$$

Now degree of transformation of directional radiation pattern can be appraised for flat monochromatic wave propagation through medium containing order and stochastic components of disturbances with newly estimated parameters and structure. Let us apply Shell theorem from coherence theory⁶ (equation for far-field intensity distribution) for quasi-monochromatic illuminant

$$I(x, y) = \iint_{-\infty}^{\infty} P(\Delta\zeta, \Delta\eta) \mu_{12}(\Delta\zeta, \Delta\eta) \exp\left[-j \frac{2\pi}{\lambda z} (x\Delta\zeta + y\Delta\eta)\right] d\Delta\zeta d\Delta\eta$$

$P(\Delta\zeta, \Delta\eta) = \iint_{\omega} p\left(\zeta - \frac{\Delta\zeta}{2}, \eta - \frac{\Delta\eta}{2}\right) p\left(\zeta + \frac{\Delta\zeta}{2}, \eta + \frac{\Delta\eta}{2}\right) d\zeta d\eta$ – aperture autocorrelation function; $\mu(\zeta, \eta) = \exp[-j\varphi(\zeta, \eta)]$ –

aperture function for the case of uniform intensity distribution over the aperture; $\varphi(\zeta, \eta)$ – order WF component distribution. Complex coherence ratio $\mu_{12}(\Delta\zeta, \Delta\eta)$ for the case of Gaussian probability density function is determined by the equation

$$\mu_{12}(\rho_1, \rho_2) = \exp[-\sigma^2 + C(\rho_1, \rho_2)],$$

here σ^2 is dispersion of phase fluctuations; $C(\rho_1, \rho_2)$ – phase fluctuations autocorrelation function.

One-dimensional central cuts of directional radiation patterns computed under Shell theorem are showed on Fig.8. These cuts demonstrate the degree of directional radiation patterns transformation compared to the case of ideal diffraction. On the cut of directional radiation pattern containing results of effect of both disturbance components one can see very small noncoherent halo conditioned by stochastic component of WF disturbances. One also can see ratio of abatement of

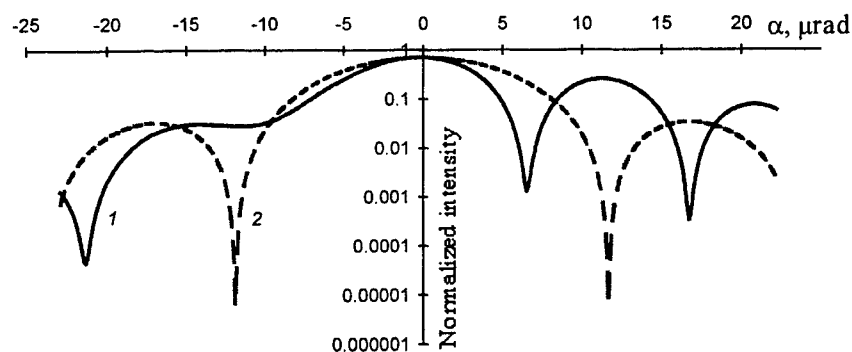


Fig.8. Orthogonal cuts of angle radiation pattern;
1 - downstream direction, 2 - transverse direction

maximum intensity of radiation propagated through optically nonhomogeneous medium. This ratio is accepted as integral criterion of AM optical quality or radiation quality (though it is obvious that there could be accepted any other set of conventional indicators). Maximum intensity in far-field region in normalized form is well known Strehl number Sh .

Schlieren pictures complex processing (under above considered method) was performed for several cases of radiation propagation through AM, including orthogonal to nozzle vanes propagation and for 1 meter propagation length. The results are brought together in the table.

Case	Sh		
	Sh_{all}	Sh_{reg}	Sh_{rnd}
Cold blowing; wavelength: $\lambda=0,5\mu\text{m}$; probing parallel to nozzle vanes; propagation length: $l=56\text{ mm}$	0,39	0,4	0,98
Cold blowing; wavelength: $\lambda=0,5\mu\text{m}$; lasing orthogonal to nozzle vanes; propagation length: $l=56\text{ mm}$	0,51	0,52	0,98
Cold blowing; wavelength: $\lambda=10,6\mu\text{m}$; lasing orthogonal to nozzle vanes; propagation length: $l=1\text{ m}$	0,77	0,79	0,99
Hot blowing (density level is reduced by factor of 10); wavelength: $\lambda=10,6\mu\text{m}$; lasing orthogonal to nozzle vanes; propagation length: $l=1\text{ m}$	0,99	0,99	1,00

It is obvious that for all cases the effect of WF order component on level of AM optical quality is prevailing. Fraction of random component effect on Strehl number turned out to be inappreciable even for conventional lasing direction (orthogonal to nozzle vanes). This result is unexpected because it somewhat contradicts to accepted assessment about practically complete integral averaging of order disturbances in the line of laser generation. It is commonly assumed that cardinal contribution to structure of radiation divergence is diffusion on turbulent pulsation of density (in the area of far wake at any rate).

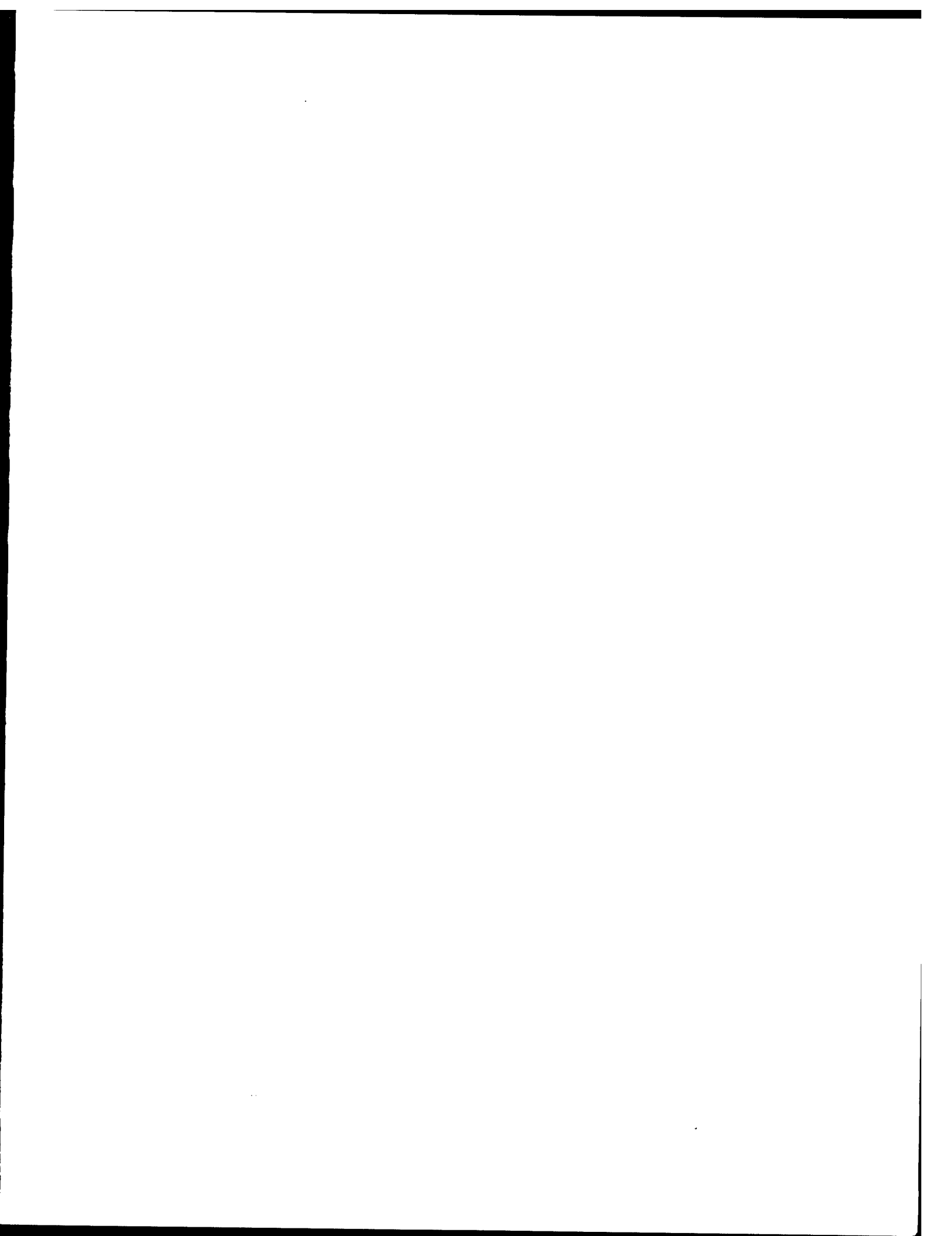
As for prediction of real AM behavior with braking temperature $\sim 2000\text{ K}$, one should not expect substantial difference in structure of order disturbances since anyway there are wakes and shock waves (in some areas) in gas flow. Differences can be in absolute levels of disturbances. As for stochastic component, absolute values of statistical parameters vary due to change in basic gas flow criterions (such as Reynolds number, etc.). Temperature dependent viscosity increase is also the origin of more fast compensation of gas-dynamic parameters Therefore found estimates should be considered worst cases.

ACKNOWLEDGMENTS

Authors are grateful to V.M.Mal'kov for provided set of high quality schlieren pictures that were used for processing and analysis.

REFERENCES

1. G.W.Sutton, J.E.Pond, R.Snow, Y.Hwang, "Hypersonic Interceptor Aero-Optics Performance Predictions", *J. of Spacecraft and Rockets*, **31**, № 4, 1994
2. H. Wolter, "Schlieren-, Phasenkontrast- und Lichtschnittverfahren", in *Hand-buch der physic*, **B 24**, Springer, Berline, 555–641, 1956
3. M.G.Khtalkerman, V.M.Mal'kov, "Aero-optics of nozzle banks of gasdynamic lasers", *J. of Applied Mechanics and Technical Physics (Rus.)*, **34**, № 6, 20–28, 1993
4. L.A.Zalmanzon, *Fourier, Wolsh, Haar transforms and its application in control, connection an other areas*, Nauka, Moscow, 1989
5. J.O.Hinze, *Turbulence: an introduction to its mechanism and theory*, McGRAW-HILL Book Company, New York, 1959
6. A.Isimaru, *Propagation and scattering of wave in rundo-ihomogeneity medium*, Mir, Moscow, 1981



Author Index

- Algatti, M. A., 117
Ariantsev, S. V., 8
Ashurkov, Roman I., 141
Babin, S. A., 48
Bagrov, Ig. V., 86
Bakaev, Valerii G., 8
Baranov, Igor Ya., 99
Barmashenko, B. D., 72
Belousov, Vldilen P., 92
Belousova, Inna M., 92
Bertsev, V. V., 29
Bocharov, V. N., 29
Boreisho, Anatoly S., 134
Bruins, E., 72
Burtsev, Andrei P., 29
Carroll, David L., 60
Cruz Orea, Alfredo, 117
Danilov, Oleg B., 86, 92, 164
Dutov, Alexander I., 104
Fockler, L. A., 60
Fokanov, V. P., 19
Fomin, Sergei G., 123
Furman, D., 72
Gorobets, Vadim A., 159, 171
Grigorev, Vladimir A., 92
Gurashvili, Victor A., 110
Ivanov, Nikolai G., 1
Jiménez Pérez, Jose L., 117
Kablukov, S. I., 48
Khailov, V. M., 134
Khorev, S. V., 48
Korolenko, Pavel V., 110
Kovalevsky, Valery O., 176
Kozlov, Boris A., 123, 141
Kozlov, Konstantin V., 159, 171
Kris'ko, A. V., 92
Kuleshov, Alexei A., 104
Kurbasov, Sergey V., 40
Kuzyakov, Boris A., 151
Lobachev, Vitaly V., 176
Losev, Valery F., 1
Mak, Artur A., 92
Mendoza-Alvarez, Julio G., 117
Morozov, N. V., 34
Motovilov, Sergei A., 104
Napartovich, Anatoly P., 110
Novoselov, N. A., 104
Orlov, N. L., 104
Panchenko, Yu. N., 1
Pavlov, A. B., 19
Pavlov, S. P., 110
Petukhov, Vladimir O., 159, 171
Podivilov, E. V., 48
Potapov, V. V., 48
Rantsev, O. V., 8
Rodin, Anatoly V., 110
Rosenwaks, Salman, 72
Rybalkin, V., 72
Sarkarov, Nidjef E., 110
Semenov, Victor E., 104
Sergeev, Paul B., 34, 40
Sericov, R. I., 134
Shapiro, D. A., 48
Sidorov, Aleksandr I., 164
Sokolov, A. A., 104
Solomon, Wayne C., 60
Sosnov, Eugene N., 92
Stepanov, M. G., 48
Stromberg, D. S., 60
Sychugov, Gleb V., 8
Titterton, David H., 164
Tochitsky, Sergei Ya., 171
Trilis, A. V., 134
Tserkovnikov, A. Yu., 8
Tul'skii, Stanislav A., 86, 164
Yachnev, Igor L., 164
Yastremsky, Arkadi G., 1
Zalesskiy, V. Yu., 92
Zhevlakov, Aleksandr P., 86, 164
Zotov, A. M., 110
Zvorykin, Vladimir D., 8